Научном већу Института за физику у Београду,

Предлог за Студентску награду Института за физику у Београду

Поштовани,

Велико ми је задовољство да предложим **др Иву Бачић** за Студентску награду Института за физику у Београду за докторску дисертацију под називом "*Self-organization in coupled excitable systems: interplay between multiple timescale dynamics and noise*", коју је одбранила 27. новембра 2020. године на Физичком факултету Универзитета у Београду.

Др Ива Бачић се у оквиру докторских студија бавила областима теорије нелинеарне динамике и стохастичких процеса, специјално истраживањем самоорганизације у спрегнутим ексцитабилним системима услед садејства шума и динамике која се одвија на на више карактеристичних временских скала.

Ексцитабилност је заједничка карактеристика великог броја разнородних неравнотежних система, укључујући биолошке системе, ласере, као и моделе хемијске кинетике, социјалних интеракција и климатске динамике. Ексцитабилност је нелинеаран *threshold-like* одговор система на пертурбације. Са становишта нелинеарне динамике, ексцитабилни системи се налазе у близини бифуркације између стационарног и осцилаторног режима, и издвојени су као засебна класа динамичких система. Комплексна динамика у ексцитабилним системима је често повезана са сингуларним бифуркацијама, које укључују оштро раздвајање карактеристичних временских скала на нивоу појединачних јединица и/или услед интеракција. Међу најважнијим примерима је концепт адаптивности, типичан за неуронске системе, где је динамика интеракција много спорија од коеволуирајуће локалне динамике јединица. Поред тога, ексцитабилни системи, као изразито неравнотежни системи, су изузетно осетљиви на пертурбације, па последично и на деловање шума. Под утицајем шума, системи у близини бифуркационог прага могу да манифестују резонантне феномене, који подразумевају нелинеаран одговор система на шум, као последицу тога што шум индукује нову карактеристичну временску скалу у динамици система. Најважнији примери укључују феномене резонанце кохеренције и инверзне стохастичке реакције.

Др Ива Бачић је проширила појам ексцитабилности на спрегнуте системе, разматрајући примере малог мотива сачињеног од локално ексцитабилних јединица и популације стохастичких неуронских мапа. У случају мотива, класификовано је више различитих врста ексцитабилних одговора и показано шта одређује праговско понашање, применивши елементе теорије сингуларних пертурбација. У случају популације, уведен је концепт макроскопске ексцитабилности, феномена при коме се цела популација ексцитабилних јединица понаша као ексцитабилни елемент. Анализа стабилности и стохастичких бифуркација режима макроскопске ексцитабилности, као и одређивање кривих фазног одговора макроскопских варијабли на пертурбацију, извршена је увођењем ефективног модела колективне динамике, развијеног применом методе средњег поља (*mean-field method*) заснованог на гаусијанској апроксимацији.

Други сегмент истраживања др Иве Бачић био је фокусиран на расветљавање механизама стохастичких флуктуација (енг. *switching* динамике) између метастабилних стања. Специјално,

УНИВЕРЗИТЕТ У БЕОГРАДУ
ИНСТИТУТ ЗА ФИЗИКУ БЕОГРАД
ИНСТИТУТ ОД НАЦИОНАЛНОГ ЗНАЧАЈА ЗА РЕПУБЛИКУ СРБИЈУ

Прегревица 118, 11080 Земун - Београд, Република Србија
Телефон: +381 11 3713000, Факс: +381 11 3162190, www.ipb.ac.rs
ПИБ: 100105980, Матични број: 07018029, Текући рачун: 205-66984-23

спроводећи анализу на два парадигматска модела, кандидаткиња је показала да коефекти шума и великог, али коначног раздвајања временских скала доводе до две врсте алтернирајуће динамике: спорих стохастичких флуктуација и стохастичког бурстовања. У разматрању мотива који се састоји од два спрегнута активна ротора, показано је да форма спорих флуктуација квалитативно зависи од раздвајања скала. У случају активног ротатора са споро адаптирајућом повратном спрегом, показано је да се *switching* између метастабилних стања изведених из детерминистичких атрактора манифестује као режим бурстовања, чије границе стабилности су израчунате користећи нови метод стохастичког усредњавања. Овим је кандидаткиња допринела проширењу теорије сингуларних пертурбација на стохастичке системе са *multiscale* динамиком.

Кандидаткиња је дала допринос уочавању и објашњењу два генеричка механизама инверзне стохастичке резонанце у спрегнутим екситабилним системима на вишеструким временским скалама. Феномен инверзне стохастичке резонанце, где фреквенција осцилација пертурбованих шумом постаје минимална на преферентном интензитету шума, је тек недавно откривен, тако да услови за његову појаву у спрегнутим системима, као и одговарајући генерички механизми досад нису били утврђени. Специјално, разматрајући утицај шума на парадигматски модел две јединице са екситабилном или осцилаторном локалном динамиком, идентификована су два генеричка сценарија за појаву инверзне стохастичке резонанце: један заснован на неуравнотеженом *switching*-у, а други повезан са стабилизацијом детерминистички нестабилне фиксне тачке шумом. Поред тога, кандидаткиња је допринела развоју новог метода контроле резонанце кохеренције у системима у близини бифуркације између стационарног и осцилаторног режима, показавши како се резонантни ефекат може појачати или сузбити прилагођавањем јачине споро адаптирајуће повратне спреге.

Др Бачић се у току докторских студија бавила и карактеризацијом утицаја структуре комплексних мрежа на процес уређивања кинетичког Изинговог (Глауберовог) модела, као и анализом структуре неуређених конфигурација. Експлицитно је показано да *small-world* топологија у термодинамичком лимесу онемогућава уређивање, при чему се неуређене конфигурације састоје од два домена који одговарају мулти-кластер структурама на почетној регуларној решетци.

Кандидаткиња је ове резултате приказала детаљно у оквиру докторске дисертације под називом "*Self-organization in coupled excitable systems: interplay between multiple timescale dynamics and noise*", која је написана на енглеском језику. Радови кандидаткиње у којима су објављени представљени резултати су:

1. **I. Bačić**, and I. Franović, *Two Paradigmatic Scenarios for Inverse Stochastic Resonance*, Chaos 30, 033123 (2020) [ISSN: 1054–1500, IF2019: 2.983]

2. **I. Bačić**, V. Klinshov, V. Nekorkin, M. Perc, and I. Franović, *Inverse stochastic resonance in a system of excitable active rotators with adaptive coupling*, Europhys. Lett. 124, 40004 (2018) [ISSN: 0295-5075, IF2015: 1.963]

УНИВЕРЗИТЕТ У БЕОГРАДУ

ИНСТИТУТ ЗА ФИЗИКУ БЕОГРАД

ИНСТИТУТ ОД НАЦИОНАЛНОГ ЗНАЧАЈА ЗА РЕПУБЛИКУ СРБИЈУ

Прегревица 118, 11080 Земун - Београд, Република Србија
Телефон: +381 11 3713000, Факс: +381 11 3162190, www.ipb.ac.rs
ПИБ: 100105980, Матични број: 07018029, Текући рачун: 205-66984-23

3. **I. Бачић**, S. Yanchuk, M. Wolfrum, and I. Franović, *Noise-induced switching in two adaptively coupled excitable systems*, Eur. Phys. J. - Spec. Top. 227, 1077 (2018) [ISSN: 1951-6355, IF2017: 1.947]

4. I. Franović, S. Yanchuk, S. R. Eydam, **I. Бачић**, and M. Wolfrum, *Dynamics of a Stochastic Excitable System with Slowly Adapting Feedback*, Chaos 30, 083109 (2020) [ISSN: 1054–1500, IF2019: 2.983]

5. I. Franović, O. V. Maslennikov, **I. Бачић**, and V. I. Nekorkin, *Mean-field dynamics of a population of stochastic map neurons*, Phys. Rev. E 96, 012226 (2017) [ISSN: 1539-3755, IF2016: 2.366]

У прилогу је дат комплетан списак публикација кандидаткиње. До сада, др Ива Бачић има 3 саопштења са међународних скупова штампаних у изводу (М34) и 6 радова објављених у међународним часописима, од којих су 2 рада категорије М21а, 3 рада су категорије М21, а 1 рад је категорије М22. Рад *Disordered configurations of the Glauber model in two-dimensional networks*, објављен у часопису *EPL (Europhysics Letters)*, истакнут је у *Research Highlights* тог часописа за 2018. годину и представљен на *Europhysics News*.

Укупан импакт фактор ових радова је 14,205. Према бази *Web of Science*, њени радови су цитирани 12 пута (без аутоцитата), уз h=3, док је према бази *Google Scholar*, укупан број цитата 20. Кандидаткиња је била рецензенткиња два рада у часопису *Chaos*.

Др Ива Бачић је била у локалном организационом одбору конференције *COST XLIC WG2 Expert meeting on biomolecules*, одржане 2015. године на Фрушкој Гори, Србија. Кандидаткиња је такође дугогодишња стручна сарадница Семинара физике у Истраживачкој станици Петница где је одржала низ предавања из математике и физике и менторисала два полазничка пројекта који су успешно завршени презентацијама полазница на годишњој конференцији ИС Петница „Корак у науку“ и објављивањем у зборницима радова полазника „Петничке свеске“.

Кандидаткиња задовољава и све формалне услове да буде предложена за Студентску награду у складу са Правилником о наградама: теза је одбрањена током претходне календарске године, истраживање је у целости спроведено на Институту за физику у Београду, а резултати истраживања су представљени на онлајн семинару Лабораторије за примену рачунара у науци 5. новембра 2020. године.

Имајући све наведено у виду, са задовољством предлажем др Иву Бачић за Студентску награду Института за физику у Београду за најбољу докторску тезу одбрањену током 2020. године.

У Београду,
26. 04. 2021. године

др Александра Алорић,
научни сарадник,
Институт за физику у Београду

СТРУЧНА БИОГРАФИЈА

Др Ива Бачић рођена је у Суботици 12. јуна 1992. године, где је завршила природни смер Гимназије „Светозар Марковић“. Након тога, уписала је 2010. године основне академске студије на Физичком факултету Универзитета у Београду, смер Теоријска и експериментална физика, где је дипломирала 2014. године са просечном оценом 9.44/10. Исте године је уписала мастер академске студије на Физичком факултету, смер Теоријска и експериментална физика, које је завршила 2015. године са просечном оценом 9.67/10. У току мастер студија, Ива је посетила синхротрон SOLEIL у Француској, у склопу израде мастер рада на тему *Inner-Shell Action Spectroscopy of Trapped Substance P Peptide Ions and their Nanosolvated Complexes* под менторством др Александра Милосављевића, научног саветника Института за физику у Београду. Истраживања су рађена у оквиру COST акције CM1204 (*XUV/X-ray light and fast ions for ultrafast chemistry (XLIC)*), при чему је такође била чланица локалног организационог одбора конференције *COST XLIC WG2 Expert meeting on biomolecules*, одржане 2015. године на Фрушкој Гори, Србија.

Новембра 2015. године уписала је докторске академске студије на Физичком факултету, ужа научна област Физика кондензоване материје и статистичка физика. Под менторством др Игора Франовића, вишег научног сарадника из Лабораторије за примену рачунара у науци (Scientific Computing Laboratory) Института за физику у Београду, Ива се у склопу докторских академских студија бавила коефектима шума и вишеструких временских скала у системима спрегнутих екситабилних јединица, одбранивши дисертацију под називом *Self-organization in Coupled Excitable Systems: Interplay Between Multiple Timescale Dynamics and Noise* новембра 2020. године. Завршила је докторске студије са просечном оценом 10/10. Од марта 2016. године, др Бачић је запослена на Институту за физику у Београду у Лабораторији за примену рачунара у науци. Била је ангажована на пројекту основних истраживања ОН171017 *Моделирање и нумеричке симулације сложених вишечестичних система* Министарства просвете, науке и технолошког развоја Републике Србије. Поред тога, учествовала је и на DAAD билатералном пројекту између Републике Србије и СР Немачке *Emergent dynamics in systems of coupled excitable units* 2017. и 2018. године, у склопу чега је посетила *Weierstrass Institute* у Берлину неколико пута, као и у COST акцији CA17120 (*Chemobrionics*), 2018 – .

Октобра 2020. годие започела је постдокторско усавршавање при Централно-Европском Универзитету у Будимпешти, Мађарска, где учествује на ERC Synergy пројекту *Dynamics and Structure of Networks (DYNASNET)* посвећеном повезивању теорије графова и комплексних мрежа, под руководством др Алберта-Ласла Барабашија и др Мартона Пошфаија. Др Бачић је на Централно-Европском Универзитету била асистенткиња на предмету *Scientific Python* у току зимског семестра академске *2020/21* године.

Др Бачић је до сада је објавила шест научних радова (2 категорије М21а, 3 категорије М21 и 1 рад категорије М22) и неколико саопштења са међународних скупова штампана у изводу. Укупан импакт фактор ових радова је 14, 205. Према бази *Web of Science*, њени радови су цитирани 12 пута (без аутоцитата), уз h=3, док је према бази *Google Scholar*, укупан број цитата 20. Рад *Disordered configurations of the Glauber model in two-dimensional networks*, објављен у часопису *EPL (Europhysics Letters)*, истакнут је у *Research Highlights* за 2018. годину и представљен на *Europhysics News*. Своје резултате је до сада представила на више међународних конференција, и била је учесница неколико школа за усавршање младих научника, укључујући *1st Complexity Science Hub Vienna Winter School* (Обергургл, Аустрија), *School and Workshop on Patterns of Synchrony: Chimera States and Beyond* (ICTP, Трст, Италија), *Dynamics of Coupled Oscillator Systems* (Берлин, Немачка), и *20. симпозијум физике кондензоване материје* (Београд, Србија). Била је позвана на престижну летњу школу *Complex Systems Summer School 2020* Санта Фе института (Њу Мексико, САД), као и на *Spring College on the Physics of Complex Systems* (ICTP, Трст, Италија) где је требало да асистира др Сидни Реднеру на курсу „Статистичка физика из кинетичке перспективе“, али су ти догађаји отказани услед пандемије. Др Бачић је руководила двама средњошколским пројектима семинара физике у Истраживачкој станици Петница, представљеним на конференцијама „Корак у науку“ 2019. и 2020. годне. Била је рецезенткиња два рада у часопису *Chaos* 2020. године.

Поред матерњег, Ива говори два светска језика, енглески и немачки.

Списак публикација др Иве Бачић

Радови објављени у међународним часописима изузетних вредности (категорија М21а):

1. **I. Bačić**, and I. Franović, *Two Paradigmatic Scenarios for Inverse Stochastic Resonance*, Chaos 30, 033123 (2020) [ISSN: 1054–1500, IF2019: 2.983]
2. I. Franović, S. Yanchuk, S. R. Eydam, **I. Bačić**, and M. Wolfrum, *Dynamics of a Stochastic Excitable System with Slowly Adapting Feedback*, Chaos 30, 083109 (2020) [ISSN: 1054–1500, IF2019: 2.983]

Радови објављени у врхунским међународним часописима (категорија М21):

1. **I. Bačić**, V. Klinshov, V. Nekorkin, M. Perc, and I. Franović, *Inverse stochastic resonance in a system of excitable active rotators with adaptive coupling*, Europhys. Lett. 124, 40004 (2018) [ISSN: 0295-5075, IF2015: 1.963]
2. I. Franović, O. V. Maslennikov, **I. Bačić**, and V. I. Nekorkin, *Mean-field dynamics of a population of stochastic map neurons*, Phys. Rev. E 96, 012226 (2017) [ISSN: 1539-3755, IF2016: 2.366]
3. **I. Bačić**, I. Franović, and M. Perc, *Disordered Confgurations of the Glauber Model in Two-dimensional Networks*, Europhys. Lett. 120, 68001 (2017) [ISSN: 0295-5075, IF2015: 1.963]

Радови објављени у истакнутим међународним часописима (категорија М22):

1. **I. Bačić**, S. Yanchuk, M. Wolfrum, and I. Franović, *Noise-induced switching in two adaptively coupled excitable systems*, Eur. Phys. J. - Spec. Top. 227, 1077 (2018) [ISSN: 1951-6355, IF2017: 1.947]

Саопштења са међународног скупа штампана у изводу (категорија М34):

1. **I. Bačić**, M. Lj. Ranković, F. Canon, V. Cerovski, C. Nicolas, A. Giuliani, and A. R. Milosavljević, *Gas-phase X-ray action spectroscopy of protonated nanosolvated substance P peptide around O K-edge,* WG2 Expert Meeting on Biomolecules, 27-30 April 2015, Fruška gora, Serbia.
2. **I. Bačić**, *Inverse stochastic resonance in a system of active rotators with adaptive coupling*, Dynamics of Coupled Oscillator Systems, 19-21 November 2018, WIAS Berlin, Germany.
3. **I. Bačić**, I. Franović, and M. Perc, *Disordered Configurations Of The Glauber Model On Two-Dimensional Networks*, The 20th Symposium on Condensed Matter Physics - SFKM 2019, 7-11 October 2019, Belgrade, Serbia.

Одбрањена докторска дисертација (категорија М70):

1. **I. Вачић**, *Self-organization in Coupled Excitable Systems: Interplay Between Multiple Timescale Dynamics and Noise (Самоорганизација у спрегнутим ексцитабилним системима: садејство вишеструких временских скала и шума),* Универзитет у Београду – Физички факултет, Београд, 2020.

Web of Science

Clarivate
Analytics

Search   Search Results   Tools ▾   Searches and alerts ▾   Search History   Marked List   7

Citation report for 6 results from Web of Science Core Collection between [2017 ▾] and [2021 ▾] [Go]

You searched for: **AUTHOR:** (Bacic, Iva) ...More

This report reflects citations to source items indexed within Web of Science Core Collection. Perform a Cited Reference Search to include citations to items not indexed within Web of Science Core Collection.

Export Data: [Save to Excel File ▾]

Total Publications	h-index	Sum of Times Cited	Citing articles
6 Analyze	**3**	**13**	**13** Analyze
	Average citations per item	Without self citations	Without self citations
2001 — 2020	**2.17**	**12**	**12** Analyze

Sum of Times Cited per Year
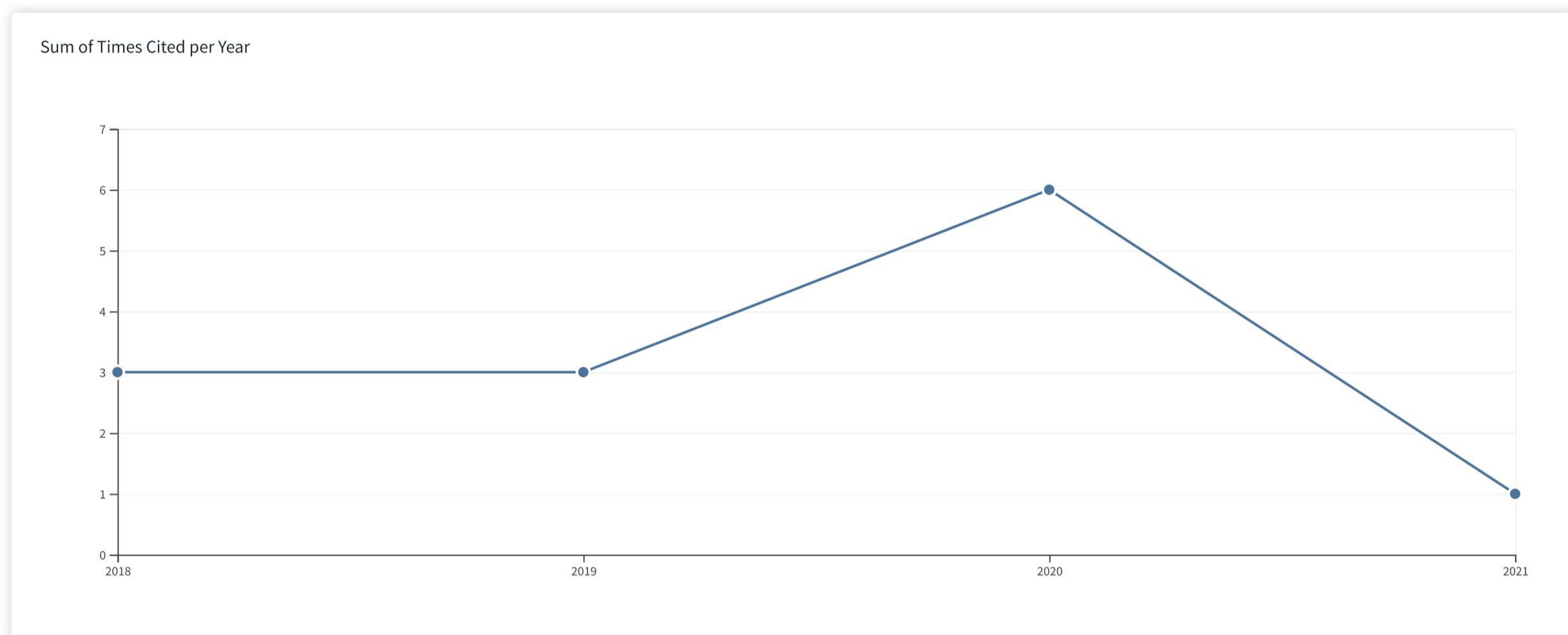
Sort by: Times Cited ⬇ | Date | More ▾   ◀ 1 of 1 ▶

ⓘ How are these totals calculated?

	2017 ◀	2018	2019	2020	2021 ▶	Total	Average Citations per Year
Use the checkboxes to remove individual items from this Citation Report or restrict to items published between [2017 ▾] and [2021 ▾] [Go]	0	3	3	6	1	13	3.25
1. **Inverse stochastic resonance in a system of excitable active rotators with adaptive coupling** By: Bacic, Iva; Klinshov, Vladimir; Nekorkin, Vladimir; et al. EPL Volume: 124 Issue: 4 Article Number: 40004 Published: NOV 2018	0	0	1	3	0	4	1.00
2. **Noise-induced switching in two adaptively coupled excitable systems** By: Bacic, Iva; Yanchuk, Serhiy; Wolfrum, Matthias; et al. EUROPEAN PHYSICAL JOURNAL-SPECIAL TOPICS Volume: 227 Issue: 10-11 Pages: 1077-1090 Published: NOV 2018	0	2	2	0	0	4	1.00
3. **Mean-field dynamics of a population of stochastic map neurons** By: Franovic, Igor; Maslennikov, Oleg V.; Bacic, Iva; et al. PHYSICAL REVIEW E Volume: 96 Issue: 1 Article Number: 012226 Published: JUL 27 2017	0	1	0	2	0	3	0.60
4. **Two paradigmatic scenarios for inverse stochastic resonance** By: Bacic, Iva; Franovic, Igor CHAOS Volume: 30 Issue: 3 Article Number: 033123 Published: MAR 2020	0	0	0	0	1	1	0.50
5. **Disordered configurations of the Glauber model in two-dimensional networks** By: Bacic, Iva; Franovic, Igor; Perc, Matjaz EPL Volume: 120 Issue: 6 Article Number: 68001 Published: DEC 2017	0	0	0	1	0	1	0.20
6. **Dynamics of a stochastic excitable system with slowly adapting feedback** By: Franovic, Igor; Yanchuk, Serhiy; Eydam, Sebastian; et al. CHAOS Volume: 30 Issue: 8 Article Number: 083109 Published: AUG 2020	0	0	0	0	0	0	0.00

☐ Select Page   🖨 ✉   [Save to Excel File ▾]

Sort by: Times Cited ⬇ | Date | More ▾   ◀ 1 of 1 ▶

6 records matched your query of the 13,326,295 in the data limits you selected.

Iva Bačić

Central European University; Institute of
Physics Belgrade

complex networks
nonlinear dynamics
complex systems
bifurcation analysis

	All	Since 2016
Citations	20	20
h-index	3	3
i10-index	0	0

0 articles   3 articles

not available   available

Based on funding mandates

TITLE	CITED BY	YEAR
Noise-induced switching in two adaptively coupled excitable systems I Bačić, S Yanchuk, M Wolfrum, I Franović The European Physical Journal Special Topics 227 (10), 1077-1090	7	2018
Inverse stochastic resonance in a system of excitable active rotators with adaptive coupling I Bačić, V Klinshov, V Nekorkin, M Perc, I Franović EPL (Europhysics Letters) 124 (4), 40004	5	2018
Mean-field dynamics of a population of stochastic map neurons I Franović, OV Maslennikov, I Bačić, VI Nekorkin Physical Review E 96 (1), 012226	5	2017
Dynamics of a stochastic excitable system with slowly adapting feedback I Franović, S Yanchuk, S Eydam, I Bačić, M Wolfrum Chaos: An Interdisciplinary Journal of Nonlinear Science 30 (8), 083109	1	2020
Two paradigmatic scenarios for inverse stochastic resonance I Bačić, I Franović Chaos: An Interdisciplinary Journal of Nonlinear Science 30 (3), 033123	1	2020
Disordered configurations of the Glauber model in two-dimensional networks I Bačić, I Franović, M Perc EPL (Europhysics Letters) 120 (6), 68001	1	2018
Self-organization in coupled excitable systems: interplay between multiple timescale dynamics and noise I Bačić Универзитет у Београду		2020
Highlights from the previous volumes I Bačić, J Hindes, IB Schwartz, M Schäfer, MM Doria, A Perali EPL (Europhysics Letters) 122 (1), 00000		2018

Two paradigmatic scenarios for inverse stochastic resonance

Iva Bačić and Igor Franović[a] (ID)

AFFILIATIONS

Scientific Computing Laboratory, Center for the Study of Complex Systems, Institute of Physics Belgrade, University of Belgrade, Pregrevica 118, 11080 Belgrade, Serbia

[a]**Author to whom correspondence should be addressed:** franovic@ipb.ac.rs

ABSTRACT

Inverse stochastic resonance comprises a nonlinear response of an oscillatory system to noise where the frequency of noise-perturbed oscillations becomes minimal at an intermediate noise level. We demonstrate two generic scenarios for inverse stochastic resonance by considering a paradigmatic model of two adaptively coupled stochastic active rotators whose local dynamics is close to a bifurcation threshold. In the first scenario, shown for the two rotators in the excitable regime, inverse stochastic resonance emerges due to a biased switching between the oscillatory and the quasi-stationary metastable states derived from the attractors of the noiseless system. In the second scenario, illustrated for the rotators in the oscillatory regime, inverse stochastic resonance arises due to a trapping effect associated with a noise-enhanced stability of an unstable fixed point. The details of the mechanisms behind the resonant effect are explained in terms of slow–fast analysis of the corresponding noiseless systems.

Published under license by AIP Publishing. https://doi.org/10.1063/1.5139628

The effects of noise may generically be classified into two groups: on the one hand, the noise may enhance or suppress certain features of deterministic dynamics by acting on the system states in an inhomogeneous fashion, while on the other hand, it may give rise to novel forms of behavior, associated with crossing of thresholds and separatrices or to a stability of deterministically unstable states. The constructive role of noise has been evinced in a wide range of real-world applications, from neural networks and chemical reactions to lasers and electronic circuits. The classical examples of stochastic facilitation concern the resonant phenomena, including stochastic resonance, where noise of appropriate intensity may induce oscillations in bistable systems that are preferentially locked to a weak periodic forcing, and coherence resonance, where an intermediate level of noise may trigger coherent oscillations in excitable systems. Recently, a novel form of nonlinear response to noise, called inverse stochastic resonance (ISR), has been discovered while studying individual neural oscillators and models of neuronal populations. It has come to light that noise may reduce the intrinsic spiking frequency of neuronal oscillators, transforming the tonic firing into a bursting-like activity or even quenching the oscillations. Within the present study, we demonstrate two paradigmatic mechanisms of inverse stochastic resonance, one based on biased switching

between the metastable states, and the other associated with a noise-enhanced stability of an unstable fixed point. We show that the effect is robust, in a sense that it may emerge in coupled excitable and coupled oscillatory systems, and both in cases of Type I and Type II oscillators.

I. INTRODUCTION

Noise in excitable or multistable systems may fundamentally change their deterministic dynamics, giving rise to qualitatively novel forms of behavior, associated with crossing of thresholds and separatrices, or stabilization of certain unstable structures.[1,2] The emergent dynamics may involve noise-induced oscillations and stochastic bursting,[3–5] switching between metastable states,[6,7] or noise-enhanced stability of metastable and unstable states,[8–12] to name but a few. In neuronal systems, the phenomena reflecting the constructive role of noise are collected under the notion of stochastic facilitation,[13–15] which mainly comprises the resonant effects. The most prominent examples concern coherence resonance,[16–20] where the regularity of noise-induced oscillations becomes maximal at a preferred noise level, and stochastic resonance,[13,21] where the sensitivity of a system to a subthreshold periodic stimulation becomes

maximal at an intermediate noise level. Recent studies on the impact of noise in neuronal oscillators have revealed that the noise may also give rise to an inhibitory effect, which consists in reducing the intrinsic spiking frequency such that it becomes minimal at an intermediate noise intensity.[14,22–30] This effect has been called inverse stochastic resonance (ISR), but in contrast to stochastic resonance, it concerns autonomous rather than periodically driven systems. Apart from reports in models of neurons and neuronal populations, ISR has recently been evinced for cerebellar Purkinje cells *in vitro*,[28] having shown how the lifetimes of the so-called UP states with elevated spiking activity and the DOWN states of relative quiescence[7,31–33] depend on the noise intensity.

The studies of the mechanism behind ISR have so far mostly been focused on Type II neural oscillators with bistable dynamics poised close to a subcritical Hopf bifurcation,[14,23–25] considering Hodgkin–Huxley and Morris–Lecar models. Under the influence of noise, such systems exhibit switching between the two metastable states, derived from the periodic and the stationary attractor of the deterministic dynamics. At an intermediate noise level, one observes that the switching rates become strongly asymmetric, with the system spending substantially more time in a quasi-stationary state. This is reflected in a characteristic non-monotone dependence of the spiking frequency on noise, which is a hallmark of ISR.

Nevertheless, a number of important issues on the mechanism giving rise to ISR have remained unresolved. In particular, is the effect dependent on the type of neuronal excitability? Also, can there be more than a single mechanism of ISR? And finally, how does the effect depend on the form of couplings and whether it can be robust for adaptively changing couplings, typical for neuronal systems?

To address these issues, we invoke a simple, yet paradigmatic model that combines the three typical ingredients of neuronal dynamics, including excitability, noise, and coupling plasticity. In particular, we consider a system of two identical, adaptively coupled active rotators[6,29,34] influenced by independent Gaussian white noise sources

$$\dot\varphi_i = I_0 - \sin\varphi_i + \kappa_i \sin(\varphi_j - \varphi_i) + \sqrt{D}\xi_i(t),$$
$$\dot\kappa_i = \varepsilon(-\kappa_i + \sin(\varphi_j - \varphi_i + \beta)). \tag{1}$$

The indices $i, j \in \{1, 2\}, i \neq j$ denote the particular units, described by the respective phases $\{\varphi_1, \varphi_2\} \in S^1$, which constitute the fast variables and the slowly varying coupling weights $\{\kappa_1, \kappa_2\} \in \mathcal{R}$. The scale separation between the characteristic timescales is set by the small parameter $\varepsilon \ll 1$ that defines the adaptivity rate. The local dynamics is controlled by the excitability parameter I_0 such that the saddle-node of infinite period (SNIPER) bifurcation at $I_0 = 1$ mediates the transition between the excitable ($I_0 \lesssim 1$) and the oscillatory regimes ($I_0 > 1$). The excitable units may still exhibit oscillations, induced either by the action of the coupling (*emergent oscillations*) and/or evoked by the stochastic terms (noise-induced oscillations). The noiseless coupled system (1) is invariant with respect to exchange of the units' indices such that all the stationary or the periodic solutions always appear in pairs connected by the Z_2 symmetry. Given the similarity between the active rotators and the theta neurons, which also conform to Type I excitability, system (1) may be considered qualitatively analogous to a motif of two adaptively coupled neurons,[37] influenced by an external bias current

I_0 and the synaptic noise. Adaptivity is modeled in terms of phase-dependent plasticity[36,38–40] of coupling weights, having the modality of the plasticity rule adjusted by parameter β. This form of plasticity has already been shown to be capable of qualitatively reproducing the features of some well-known neuronal plasticity rules.[39,40] In particular, for $\beta = 3\pi/2$, one recovers Hebbian-like learning,[41] where the synaptic potentiation promotes phase synchronization, while for $\beta = \pi$, adaptation acts similarly to spike-timing-dependent plasticity (STDP),[42–46] whose typical form[35,45] favors a causal relationship between the pre- and post-synaptic neuron firing times.[39,40]

II. INVERSE STOCHASTIC RESONANCE DUE TO A BIASED SWITCHING

The first generic scenario for ISR we demonstrate is based on *biased switching* between the metastable states associated with coexisting stationary and periodic attractors of the corresponding deterministic system. As an example, we consider the noise-induced reduction of frequency of emergent oscillations on a motif of two adaptively coupled stochastic active rotators with excitable local dynamics ($I_0 = 0.95$). To elucidate the mechanism behind the effect, we first summarize the details of the noise-free dynamics and then address the switching behavior. A complete bifurcation analysis of the noiseless version of (1) with excitable local dynamics has been carried out in Refs. 6 and 29, having shown (i) how the number and stability of the fixed points depends on the plasticity rule, characterized by β, as well as (ii) how the interplay between β and the adaptivity rate, controlled by the small parameter ε, gives rise to limit cycle attractors. Our focus is on the interval $\beta \in (3.298, 4.495)$, which approximately interpolates between the limiting cases of Hebbian-like and STDP-like plasticity rules. There, the system exhibits two stable equilibria born from the symmetry-breaking pitchfork bifurcation and has four additional unstable fixed points. For the particular case $\beta = 4.2$ analyzed below, the two stable equilibria, given by EQ1:= $(\varphi_1^*, \varphi_2^*, \kappa_1^*, \kappa_2^*)$ = $(1.2757, 0.2127, -0.0078, -0.8456)$ and EQ2:= $(\varphi_1^*, \varphi_2^*, \kappa_1^*, \kappa_2^*)$ = $(0.2127, 1.2757, -0.8456, -0.0078)$, have been shown to manifest excitable behavior.[6]

The onset of emergent oscillations, as well as the coexistence between the stable stationary and periodic solutions in the noiseless version of (1), is illustrated in Fig. 1. The maximal stability region of the two Z_2 symmetry-related periodic solutions is indicated in Fig. 1(a), which shows the variation of κ_1 variable, $\sigma_{\kappa_1} = \max(\kappa_1(t)) - \min(\kappa_1(t))$, in the (β, ε) parameter plane. The scan was performed by the method of numerical continuation starting from a stable periodic solution such that the initial conditions for an incremented parameter value are given by the final state obtained for the previous iteration step. One finds that for a given β, there exists an interval $\varepsilon \in (\varepsilon_{\min}, \varepsilon_{\max})$ of intermediate scale-separation ratios supporting the oscillations, cf. the highlighted region in Fig. 1(b). In particular, the two Z_2-symmetry related branches of stable periodic solutions emanate from the fold of cycles bifurcations, denoted by FC in Fig. 1(b) such that the associated threshold scale-separation $\varepsilon_{\min}(\beta)$ decreases with β. The two branches of oscillatory solutions merge around $\varepsilon \approx 0.06$, where the system undergoes an inverse pitchfork bifurcation (PFC) of limit cycles. The incipient stable limit cycle acquires the anti-phase space–time symmetry

$\varphi_1(t) = \varphi_2(t + T_{osc}/2), \kappa_1(t) = \kappa_2(t + T_{osc}/2)$, with T_{osc} denoting the oscillation period.[6] An example illustrating the basins of stability of stationary and oscillatory solutions for $\varepsilon = 0.1$, obtained by fixing the initial values of phases and varying the initial coupling weights within the range $\kappa_{i,ini} \in (-1, 1)$, is shown in Fig. 1(c). In the presence of noise, the coexisting attractors of the deterministic system turn to metastable states, which are connected by the noise-induced switching.

Inverse stochastic resonance manifests itself as the noise-mediated suppression of oscillations, whereby the frequency of noise-perturbed oscillations becomes minimal at an intermediate noise level. For the motif of two adaptively coupled excitable active rotators, such characteristic non-monotone dependence on noise is generically found for intermediate adaptivity rates supporting multistability between the stationary and the oscillatory solutions. A family of curves illustrating the dependence of the oscillation frequency on noise variance $\langle f \rangle(D)$ for a set of different ε values is shown in Fig. 2(a). The angular brackets $\langle \cdot \rangle$ refer to averaging over an ensemble of a 100 different stochastic realizations, having fixed a set of initial conditions within the basin of attraction of the limit cycle attractor. Nonetheless, qualitatively analogous results are recovered if for each realization of the stochastic process, one selects a set of random initial conditions lying within the stability basin of a periodic solution. In Ref. 29, we have shown that the noise-induced switching gives rise to a bursting-like behavior, where the spiking is interspersed by the quiescent episodes which correspond to the system residing in the vicinity of the quasi-stationary metastable states. Such episodes become prevalent at the noise levels around the minimum of $\langle f \rangle(D)$. For weaker noise $D \lesssim 10^{-3}$, the frequency of emergent oscillations remains close to the deterministic one, whereas for a much stronger noise, it increases above that of unperturbed oscillations. One observes that the suppression effect of noise depends on the adaptivity rate such that it is enhanced for faster adaptivity, see Ref. 29 for a more detailed analysis. In order to illustrate how the ISR effect is reflected at the level of the dynamics

of coupling weights, in Figs. 2(b)–2(d) are shown the stationary distributions $P(\kappa_1)$ for the noise levels below, at, and above the resonant level. To provide a reference to the deterministic case, we have denoted by the dashed-dotted lines the weight levels associated with the two equilibria EQ1 and EQ2, while the blue shading indicates the variation σ_κ of the stable limit cycle. Note that the stable periodic solution is unique because for the considered ε value, the deterministic system lies above the pitchfork of cycles bifurcation, cf. PFC in Fig. 1(b). The stationary distribution $P(\kappa_1)$ at the resonant noise expectedly shows a pronounced peak at one of the quasi-stationary states, while the distributions below or above the resonant noise level indicate a high occupancy of the oscillatory metastable state.

In order to elucidate the mechanism behind ISR, we have calculated how the fraction of the total time spent at the oscillatory metastable states, T_{osc}/T_{tot}, changes with noise. In terms of numerical experiments, the quasi-stationary and the oscillatory metastable states can readily be distinguished by considering the corresponding $\kappa_i(t)$ series, using the fact that the typical distance $|\kappa_1(t) - \kappa_2(t)|$ is much larger for the quasi-stationary than the oscillatory solutions. This has allowed us to employ a simple threshold method to identify the particular system's states and trace the associated transitions. Figure 3(a) indicates a non-monotone dependence of $T_{osc}/T_{tot}(D)$, implying that the switching process around the resonant noise level becomes strongly biased toward the quasi-stationary state, even more so for a faster adaptivity. The biased switching is facilitated by the geometry of the phase space, featuring an asymmetrical structure with respect to the separatrix between the coexisting attractors such that the limit cycle lies much closer to the separatrix than the stationary states.

The nonlinear response to noise may be understood in terms of the competition between the transition processes from and to the limit cycle attractor. These processes are characterized by the transition rates from the stability basin of the limit cycle attractor to that of the stationary states $\gamma_{LC \to FP}$ and vice versa, $\gamma_{FP \to LC}$, which are numerically estimated as the reciprocal values of the corresponding

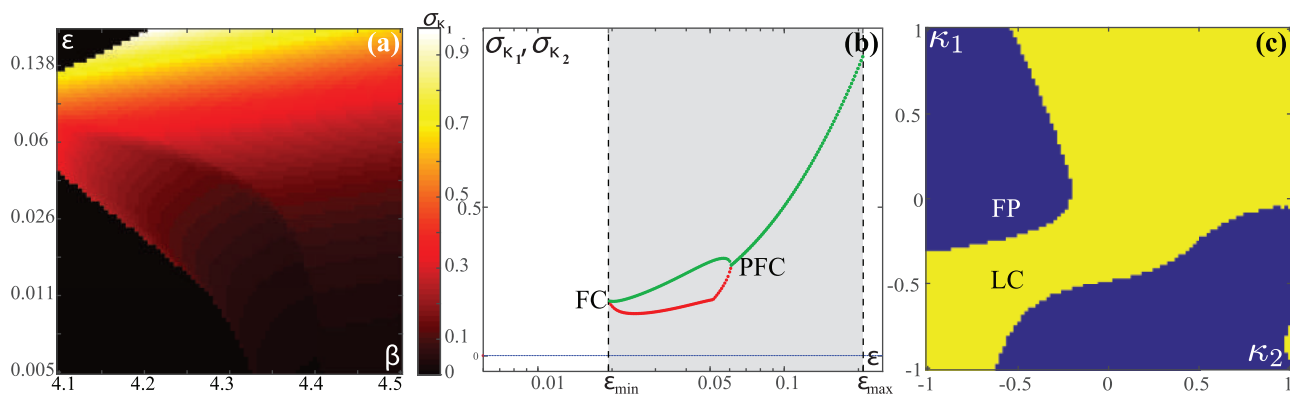**FIG. 1.** Emergent oscillations in (1) for $I_0 = 0.95, D = 0$. (a) Variation σ_{κ_1} of the coupling weight κ_1 in the (β, ε) plane. (b) Dependencies $\sigma_{\kappa_i}(\varepsilon), i \in \{1, 2\}$ for the representative stationary (blue) and oscillatory solution (red and green refer to the two units) at fixed $\beta = 4.2$. Shading indicates the ε interval that supports multistability between the two symmetry-related stable equilibria and the limit cycle attractor(s). FC and PFC denote the ε values where the fold of cycles and pitchfork of cycles occur. (c) Basins of stability of the stationary (FP, blue) and oscillatory solutions (LC, yellow) in the (κ_1, κ_2) plane, obtained by fixing the initial phases to $(\varphi_1, \varphi_2) = (1.32, 0.58)$. The remaining parameters are $\beta = 4.2, \varepsilon = 0.1$.
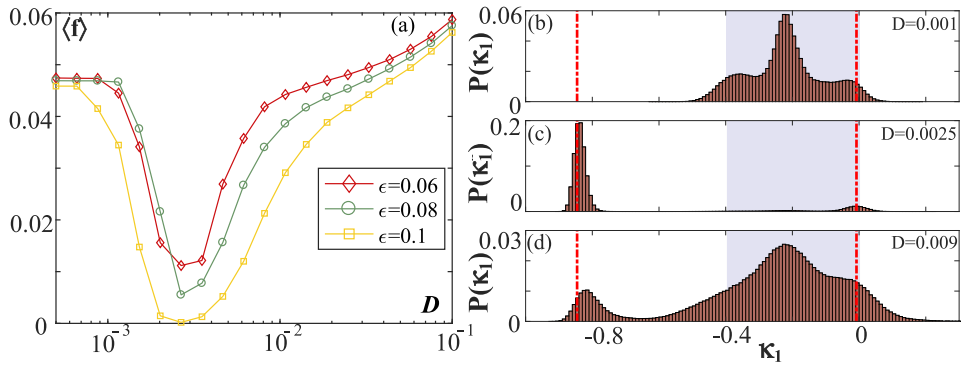
FIG. 2. (a) Dependencies of the mean oscillation frequency on noise for scale separation $\varepsilon = 0.06$ (diamonds), $\varepsilon = 0.08$ (circles) and $\varepsilon = 0.1$ (squares), obtained for fixed $I_0 = 0.95$, $\beta = 4.2$. Averaging has been performed over an ensemble of 100 different stochastic realizations. (b)–(d) show the stationary distributions $P(\kappa_1)$ below ($D = 0.001$), at ($D = 0.0025$), and above ($D = 0.009$) the resonant noise intensity for $\varepsilon = 0.1$. The dashed-dotted lines denote the κ_1 levels associated with the two stable equilibria, $\kappa_1^*(EQ1)$ and $\kappa_1^*(EQ2)$, while the blue shaded interval indicates the variation σ_{κ_1} of the unique stable periodic solution.

mean first-passage times.[47] In Figs. 3(b) and 3(c) is illustrated the qualitative distinction between the noise-dependencies of the transition rates: while $\gamma_{LC \to FP}$ displays a maximum at the resonant noise level, $\gamma_{FP \to LC}$ just increases monotonously with noise. For small noise $D \lesssim 10^{-3}$, one observes virtually no switches to the quasi-stationary state, as evinced by the fact that the corresponding oscillation frequency is identical to the deterministic one. For increasing noise, the competition between the two processes is resolved in such a way that at an intermediate/large noise, the impact of $\gamma_{LC \to FP}/\gamma_{FP \to LC}$ becomes prevalent. The large values of $\gamma_{FP \to LC}$ found for quite strong noise $D \gtrsim 0.04$ reflect the point that the system there spends most of the time in the oscillatory metastable state, making only quite short excursions to the quasi-stationary state.

Though ISR is most pronounced for intermediate ε, it turns out that an additional subtlety in the mechanism of biased switching may be explained by employing the singular perturbation theory to

the noiseless version of (1). In particular, by combining the critical manifold theory[48] and the *averaging* approach,[49] one may demonstrate the *facilitatory role of plasticity* in enhancing the resonant effect, showing that the adaptation drives the fast flow toward the parameter region where the stationary state is a focus rather than a node.[29] The response to noise in multiple timescale systems has already been indicated to qualitatively depend on the character of the stationary states, yielding fundamentally different scaling regimes with respect to noise variance and the scale-separation ratio.[50–52] Intuitively, one expects that the resonant effects should be associated with the quasi-stationary states derived from the focuses rather than the nodes[50] because the local dynamics then involves an eigenfrequency.

The fast–slow analysis of (1) for $I_0 = 0.95$ has been carried out in detail in Refs. 6 and 29 such that here we only summarize the main results concerning the associated layer and reduced
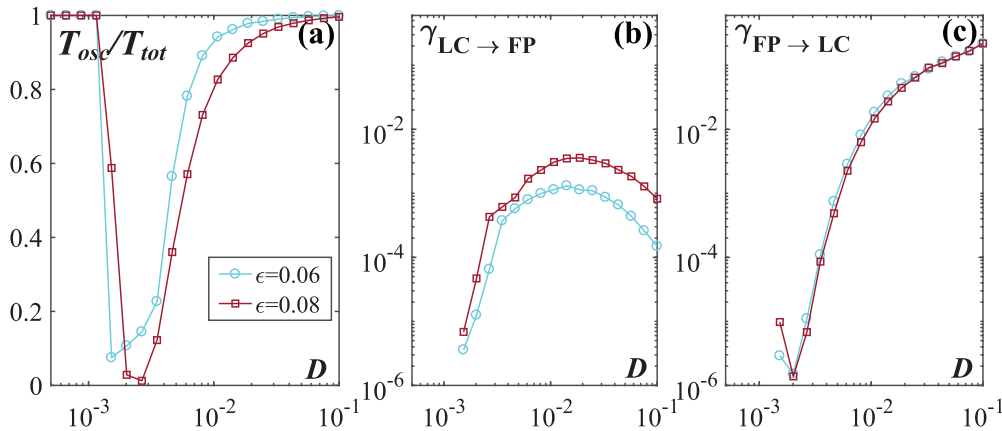

FIG. 3. (a) Fraction of the time spent at the oscillatory metastable state T_{osc}/T_{tot} as a function of noise for $\varepsilon = 0.06$ (circles) and $\varepsilon = 0.08$ (squares). (b) and (c) Numerically estimated transition rates from the oscillatory to the quasi-stationary metastable states, $\gamma_{LC \to FP}(D)$ and vice versa, $\gamma_{FP \to LC}(D)$. The remaining parameters are $I_0 = 0.95$, $\beta = 4.2$.
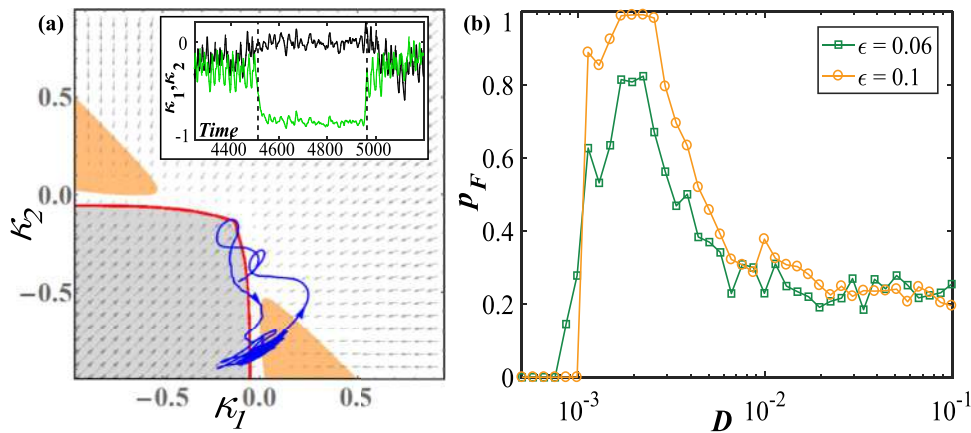
FIG. 4. (a) Fast–slow analysis of (1) for $I_0 = 0.95, D = 0$. The fast flow exhibits a periodic attractor (grey shaded region) and a stable equilibrium (white region), with two branches of SNIPER bifurcations (red lines) outlining the boundary between them. The arrows indicate the vector fields corresponding to the stable sheets of the slow flow. The inset shows $\kappa_i(t)$ series corresponding to a switching episode from the oscillatory to the stationary state and back, obtained for $\varepsilon = 0.06, \beta = 4.2$. The corresponding $(\kappa_1(t), \kappa_2(t))$ orbit is indicated by the blue line. Within the two orange regions, the two stable equilibria are focuses rather than the nodes. (b) Conditional probability $p_F(D)$ of having the crossing of SNIPER bifurcation followed by a visit to the orange-shaded region from (a), obtained for $\varepsilon = 0.06$ (squares) and $\varepsilon = 0.1$ (circles).

problems.[48] Within the layer problem, the fast flow dynamics

$$\dot{\varphi}_1 = I_0 - \sin\varphi_1 + \kappa_1 \sin(\varphi_2 - \varphi_1),$$
$$\dot{\varphi}_2 = I_0 - \sin\varphi_2 + \kappa_2 \sin(\varphi_1 - \varphi_2) \tag{2}$$

is considered by treating the slow variables $\kappa_1, \kappa_2 \in [-1, 1]$ as additional system parameters. Depending on κ_1 and κ_2, the fast flow dynamics is found to be almost always *monostable*, exhibiting either a stable equilibrium or a limit cycle attractor, apart from a small region of bistability between the two.[6,29] The maximal stability region of the oscillatory regime, encompassing both the domain where the oscillatory solution is monostable and where it coexists with a stable equilibrium, is indicated by the gray shading in Fig. 4(a). The latter has been determined by the method of numerical continuation, starting from a periodic solution. The thick red lines outlining the region's boundaries correspond to the two branches of SNIPER bifurcations.[6] Note that for each periodic solution above the main diagonal $\kappa_1 = \kappa_2$, there exists a Z_2 symmetry-related counterpart below the diagonal.

By averaging over the different attractors of the fast flow dynamics, we have obtained multiple stable sheets of the slow flow.[49] The explicit procedure consists in determining the time average $\langle\varphi_2 - \varphi_1\rangle_t = h(\kappa_1, \kappa_2)$ by iterating (2) for each fixed set (κ_1, κ_2)[6,49] and then substituting these averages into the equations of the slow flow

$$\kappa'_1 = [-\kappa_1 + \sin(h(\kappa_1, \kappa_2) + \beta)],$$
$$\kappa'_2 = [-\kappa_2 + \sin(-h(\kappa_1, \kappa_2) + \beta)], \tag{3}$$

where the prime refers to a derivative over the rescaled time variable $T := t/\varepsilon$. The arrows in Fig. 4(a) show the vector fields on the two stable sheets of the slow flow (3) associated with the stationary and the periodic attractors of the fast flow.

The performed fast–slow analysis has allowed us to gain a deeper insight into the facilitatory role of adaptivity within the

ISR. In particular, in the inset of Fig. 4(a) are extracted the time series $(\kappa_1(t), \kappa_2(t))$, which (from left to right) illustrate the switching episode from an oscillatory to the quasi-stationary metastable state. The triggering/termination of this switching event is associated with an inverse/direct SNIPER bifurcation of the fast flow. Note that for (κ_1, κ_2) values immediately after the inverse SNIPER bifurcation, the stable equilibrium of the fast flow is a node. Nevertheless, for the noise levels corresponding to the most pronounced ISR effect, the coupling dynamics guides the system into the triangular orange-shaded regions in Fig. 4(a), where the equilibrium is a stable focus rather than a node. We have verified that this feature is a hallmark of ISR by numerically calculating the conditional probability p_F that the events of crossing the SNIPER bifurcation are followed by the system's orbit visiting the (κ_1, κ_2) regions with a focus equilibrium. The $p_F(D)$ dependencies for two characteristic ε values in Fig. 4(b) indeed show a maximum for the resonant noise levels, corresponding to the minima of the frequency dependencies in Fig. 2(a). The local dynamics around the focus gives rise to a *trapping* effect such that the phase variables remain for a longer time in the associated quasi-stationary states than in case where the metastable states derive from the nodes of the fast flow. Small noise below the resonant values is insufficient to drive the system to the regions featuring focal equilibria, whereas for too strong noise, the stochastic fluctuations completely take over, washing out the quasi-stationary regime. The trapping effect is enhanced for the faster adaptivity rate, as evinced by the fact that the curve $p_F(D)$ for $\varepsilon = 0.1$ lies above the one for $\varepsilon = 0.06$.

III. INVERSE STOCHASTIC RESONANCE DUE TO A TRAPPING EFFECT

As the second paradigmatic scenario for ISR, we consider the case where the oscillation frequency is reduced due to a noise-induced trapping in the vicinity of an *unstable* fixed point of the
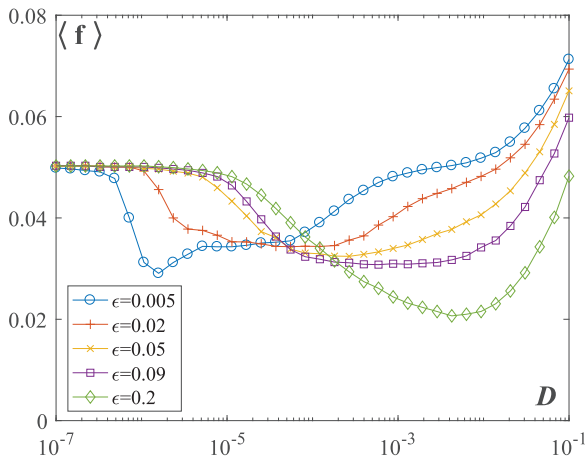
FIG. 5. Family of dependencies $\langle f \rangle (D)$ for scale separations $\varepsilon \in \{0.005, 0.02, 0.05, 0.09, 0.2\}$ at fixed $I_0 = 1.05$, $\beta = \pi$. Stochastic averaging has involved an ensemble of 100 different process realizations.

noiseless system. Such a trapping effect may be interpreted as an example of the phenomenon of *noise-enhanced stability* of an unstable fixed point.[8–12] This mechanism is distinct from the one based on biased switching because there the quasi-stationary states derive from the *stable* equilibria of the noise-free system such that the noise gives rise to crossing over the separatrix between the oscillatory and the quiescent regime. Nevertheless, in the scenario below, noise induces "tunneling" through the bifurcation threshold, temporarily stabilizing an unstable fixed point of the deterministic system.

In particular, we study an example of a system (1) comprised of two adaptively coupled active rotators in the *oscillatory*, rather than the excitable regime, setting the parameter $I_0 = 1.05$ close to a bifurcation threshold. The plasticity parameter is fixed to $\beta = \pi$ such that the modality of the phase-dependent adaptivity resembles the STDP rule in neuronal systems. One finds that this system exhibits a characteristic non-monotone response to noise, with the oscillation frequency of the phases $\langle f \rangle$ displaying a minimum at an intermediate noise level (see Fig. 5). In contrast to the mechanism described in Sec. II, the onset of ISR here does not qualitatively depend on the adaptivity rate. One only finds a quantitative dependence of the system's nonlinear response to noise on ε, in a sense that the resonant noise level shifts to larger values with increasing ε. Our exhaustive numerical simulations indicate that the ISR effect persists for slow adaptivity rates, cf. the example of the $\langle f(D) \rangle$ for $\varepsilon = 0.005$ in Fig. 5, and the results of the fast–slow analysis below will further show that all the ingredients required for the ISR effect remain in the singular perturbation limit $\varepsilon \to 0$. The persistence of the ISR effect has also been numerically confirmed for faster adaptivity rates $\varepsilon \sim 0.1$. In this case, we have observed that the minima of the $\langle f(D) \rangle$ curves become deeper with ε, suggesting that the ISR becomes more pronounced for higher adaptivity rates.

To elucidate the mechanism behind ISR, we again perform the fast–slow analysis of the corresponding noise-free system. Prior to this, we briefly summarize the results of the numerical bifurcation analysis for the noiseless system in the case of finite scale

separation. First note that selecting a particular plasticity rule $\beta = \pi$ confines the dynamics of the couplings to a symmetry invariant subspace $\kappa_1(t) = -\kappa_2(t) \equiv \kappa(t)$. Due to this, the noiseless version of the original system (1) can be reduced to a three-dimensional form

$$
\begin{aligned}
\dot{\varphi}_1 &= I_0 - \sin\varphi_1 + \kappa \sin(\varphi_2 - \varphi_1), \\
\dot{\varphi}_2 &= I_0 - \sin\varphi_2 + \kappa \sin(\varphi_2 - \varphi_1), \\
\dot{\kappa} &= \varepsilon(-\kappa - \sin(\varphi_2 - \varphi_1)).
\end{aligned}
\tag{4}
$$

By numerically solving the eigenvalue problem, we have verified that (4) possesses no stable fixed points, but rather a pair of saddle nodes and a pair of saddle focuses. Also, we have determined that the maximal real part of the eigenvalues of the focuses displays a power-law dependence on the scale separation, tending to zero in the singular limit $\varepsilon \to 0$. Concerning the oscillatory states, our numerical experiments show that (4) exhibits multistability between three periodic solutions, whereby two of them are characterized by the non-zero couplings and a constant phase-shift between the fast variables, whereas the third solution corresponds to a case of effectively uncoupled units [$\kappa(t) = 0$] and the fast variables synchronized in-phase.

A deeper understanding of the ingredients relevant for the trapping mechanism can be gained within the framework of the fast–slow analysis, considering the layer problem

$$
\begin{aligned}
\dot{\varphi}_1 &= I_0 - \sin\varphi_1 + \kappa \sin(\varphi_2 - \varphi_1), \\
\dot{\varphi}_2 &= I_0 - \sin\varphi_2 + \kappa \sin(\varphi_2 - \varphi_1).
\end{aligned}
\tag{5}
$$

Treating $\kappa \in [-1, 1]$ as an additional system parameter, we first look for the stationary and periodic attractors of the fast flow. It is convenient to apply the coordinate transformation $(\varphi_1, \varphi_2) \mapsto (\Phi, \delta\varphi) = (\frac{\varphi_1 + \varphi_2}{2}, \frac{\varphi_1 - \varphi_2}{2})$, rewriting (5) as

$$
\begin{aligned}
\delta\dot{\varphi} &= -\sin\delta\varphi \cos\Phi, \\
\dot{\Phi} &= I_0 - \cos\delta\varphi(\sin\Phi + 2\kappa \sin\delta\varphi).
\end{aligned}
\tag{6}
$$

From the second equation, one readily finds that the fast flow cannot possess any fixed points on the synchronization manifold $\delta\varphi = 0$ because $I_0 > 1$ such that the stationary solutions derive only from the condition $\cos\Phi = 0$. A numerical analysis shows that, depending on κ, the fast flow for $I_0 \gtrsim 1$ can exhibit two or no fixed points. For the particular value $I_0 = 1.05$, one finds that two fixed points, namely, a saddle and a *center*, exist within the interval $\kappa \in [-0.1674, 0.1674]$. The appearance of a center point is associated with the time-reversal symmetry of the fast flow (5). Indeed, one may show that the fast flow is invariant to a symmetry-preserving map R of the form

$$
R = \begin{cases}
\varphi_1 \to \pi - \varphi_2, \\
\varphi_2 \to \pi - \varphi_1, \\
t \to -t.
\end{cases}
\tag{7}
$$

Note that in case of the finite scale separation, the counterpart of the center point of the fast flow is a weakly unstable focus of the complete system (4).

The structure of the fast flow is organized around the saddle-center bifurcation, which occurs at $\kappa = \kappa_{SC} = -0.1674$. There, the
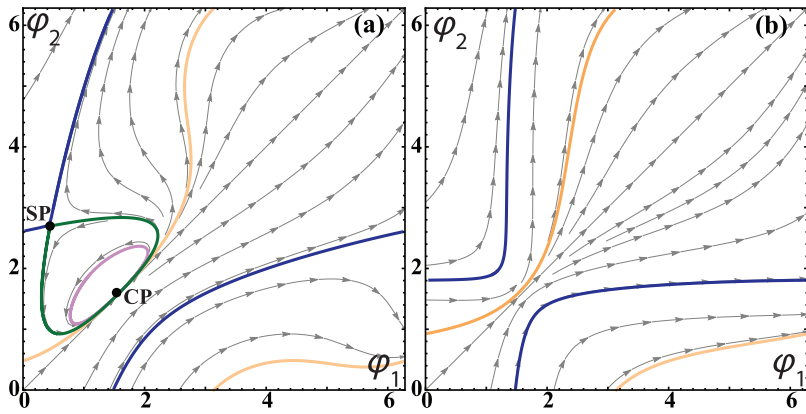
FIG. 6. Typical dynamics of the fast flow (5) for $I_0 = 1.05$ below ($\kappa = -0.8$) and above the saddle-center bifurcation ($\kappa = -0.08$) are illustrated in (a) and (b), respectively. In (a), the system possesses two unstable fixed points, a saddle (SP) and a center (CP), and exhibits three types of closed orbits: a limit cycle attractor (orange), homoclinic connections to SP (blue and green), and subthreshold oscillations around the center (purple). In (b), the system exhibits bistability between two oscillatory states, shown in orange and blue.

two fixed points get annihilated as a homoclinic orbit associated with the saddle collapses onto the center. To gain a complete picture of the dynamics of the fast flow, we have shown in Figs. 6(a) and 6(b) the illustrative examples of the phase portraits and the associated vector fields for $\kappa < \kappa_{SC}$ and $\kappa > \kappa_{SC}$, respectively. For $\kappa \in [-1, \kappa_{SC})$, the fast flow possesses a limit cycle attractor, essentially derived from the local dynamics of the units, cf. the orbit indicated in red in Fig. 6(a). Apart from an attracting periodic orbit, one observes two additional types of closed orbits, namely, the homoclinic connections to the saddle point (SP), shown by blue and

green, as well as the periodic orbits around the center point (CP), an example of which is indicated in orange. For $\kappa > \kappa_{SC}$, the fast flow exhibits bistability between two oscillatory solutions, such that there is a coexistence of a limit cycle inherited from the local dynamics of units and the limit cycle associated with the former homoclinic orbits, cf. Fig. 6(b).

In the presence of noise, the described attractors of the fast flow turn to metastable states. Nevertheless, in contrast to the case of two adaptively coupled excitable units, the slow stochastic fluctuations here do not only involve switching between the metastable
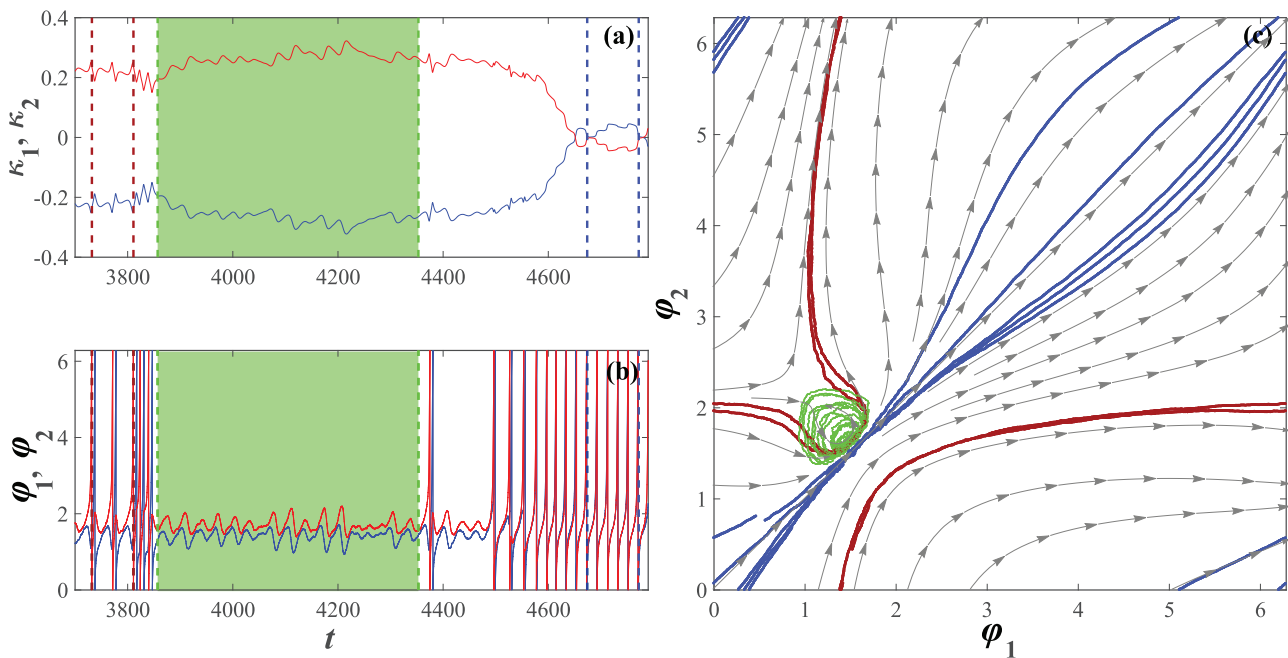
FIG. 7. (a) and (b) show the time traces of $\kappa_i(t)$ and $\varphi_i(t)$, respectively, with an episode where the system remains in the vicinity of an unstable fixed point highlighted in green. The parameters are $I_0 = 1.05$, $\varepsilon = 0.035$, $\beta = \pi$, $D = 10^{-4}$. (c) The orbits conforming to the two metastable states characterized by large-amplitude oscillations of phases are shown in red and blue, whereas the subthreshold oscillations are indicated in green. Superimposed is the vector field of the fast flow, corresponding to the limit $\varepsilon \to 0$.

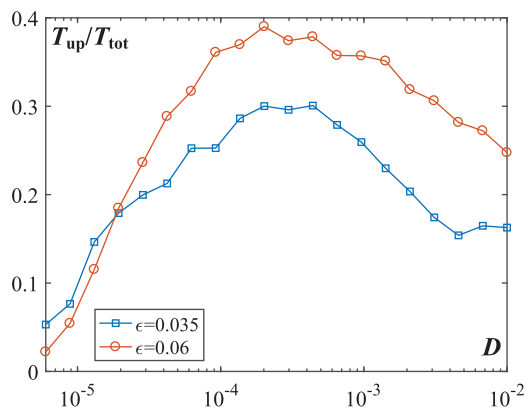**FIG. 8.** Numerically estimated fraction of time spent in the vicinity of the unstable fixed point T_{up}/T_{tot} as a function of noise for $\varepsilon = 0.035$ (squares) and $\varepsilon = 0.06$ (circles). Note that the positions of the maxima coincide with the corresponding resonant noise levels from Fig. 5. Remaining system parameters are $l_0 = 1.05, \beta = \pi$.

states but also comprise the *subthreshold oscillations* derived from the periodic orbits around the center point. These subthreshold oscillations provide for the trapping effect, which effectively leads to a reduced oscillation frequency. An example of the time series $\kappa_i(t)$ and $\varphi_i(t), i \in \{1, 2\}$ obtained for an intermediate $\varepsilon = 0.035$ in Figs. 7(a) and 7(b) indeed shows three characteristic episodes, including visits to two distinct oscillatory metastable states and an extended stay in the vicinity of the center, cf. the stochastic orbits

$(\varphi_1(t), \varphi_2(t))$ and the vector field of the fast flow in Fig. 7(c). In the case of finite scale separation, the trapping effect is manifested as the noise-enhanced stability of an unstable fixed point. The prevalence of subthreshold oscillations changes with noise in a non-monotone fashion, see the inset in Fig. 7(c), becoming maximal around the resonant noise level where the frequency dependence on noise exhibits a minimum, cf. Figs. 5 and 8. The fraction of time spent in the metastable state corresponding to subthreshold oscillations has been estimated by the numerical procedure analogous to the one already described in Sec. II.

IV. TWO MECHANISMS OF ISR IN CLASSICAL NEURONAL MODELS

So far, we have demonstrated the two paradigmatic scenarios for ISR considering the examples of coupled Type I units, whose local dynamics is close to a SNIPER bifurcation, be it in the excitable or the oscillatory regime. Nevertheless, the onset of ISR and the specific mechanisms of the phenomenon do not depend on the excitability class of local dynamics. In particular, we have recently demonstrated that a single Type II Fitzhugh–Nagumo relaxation oscillator exhibits qualitatively the same form of non-monotone dependence on noise,[30] with the mechanism involving noise-induced subthreshold oscillations that follow the maximal canard of an unstable focus. In that case, it has been established that the trapping effect and the related subthreshold oscillations are triggered due to a phase-sensitive excitability of a limit cycle. Moreover, we have verified that the same model of neuronal dynamics, set to different parameter regimes, may exhibit two different scenarios of ISR. In particular, by an appropriate selection of the system
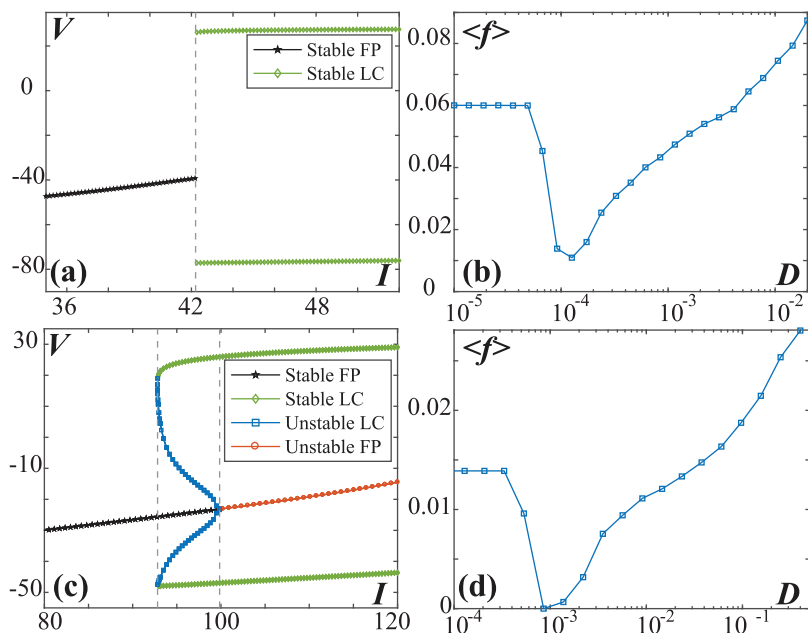

FIG. 9. (a) Bifurcation diagram showing the dependence of the amplitudes of the membrane potential V on the external bias current I for the version of Morris–Lecar model exhibiting a supercritical Hopf bifurcation. (b) illustrates the $\langle f \rangle(D)$ dependence for the Morris–Lecar neural oscillator in close vicinity of the supercritical Hopf bifurcation. (c) $V(I)$ bifurcation diagram for the setup where the Morris–Lecar model displays a subcritical Hopf bifurcation. (d) Characteristic non-monotone dependence $\langle f \rangle(D)$ for the Morris–Lecar model from (c), with the bifurcation parameter $I = 95$ set in the bistable regime. The two sets of parameters putting the Morris–Lecar model in the vicinity of a supercritical or a subcritical Hopf bifurcation are specified in the main text.

parameters, the Morris–Lecar neuron model

$$C\frac{dv}{dt} = -g_{fast}m(v)(v - E_{Na}) - g_{slow}W(v - E_K)$$
$$- g_{leak}(v - E_{leak}) + I,$$
$$\frac{dv}{dt} = \phi\frac{W_\infty(v) - W}{\tau(v)},$$
$$m(v) = 0.5\left[1 + \tanh\left(\frac{v - \beta_m}{\gamma_m}\right)\right], \tag{8}$$
$$W_\infty(v) = \left[1 + \tanh\left(\frac{v - \beta_w}{\gamma_w}\right)\right],$$
$$\tau(v) = 1/\cosh\left(\frac{v - \beta_w}{2\gamma_w}\right),$$

where v and W, respectively, denote the membrane potential and the slow recovery variable, can be placed in the vicinity of a supercritical or a subcritical Hopf bifurcation,[53] with the external bias current I being the bifurcation parameter. In the first case, obtained for $E_{Na} = 50$ mV, $E_K = -100$ mV, $E_{leak} = -70$ mV, $g_{fast} = 20$ mS/cm^2, $g_{slow} = 20$ mS/cm^2, $g_{leak} = 2$ mS/cm^2, $\phi = 0.15$, $C = 2\,\mu$F/cm^2, $\beta_m = -1.2$ mV, $\beta_w = -13$ mV, $\gamma_m = 18$ mV, $\gamma_w = 10$ mV, the model is monostable under the variation of I, and the ISR is observed slightly above the Hopf bifurcation $(I = 43\,\mu$A/cm$^2)$ due to a noise-enhanced stability of an unstable fixed point, cf. Figs. 9(a) and 9(b). In the second case, conforming to the parameter set $E_{Na} = 120$ mV, $E_K = -84$ mV, $E_{leak} = -60$ mV, $g_{fast} = 4.4$ mS/cm^2, $g_{slow} = 8$ mS/cm^2, $g_{leak} = 2$ mS/cm^2, $\phi = 0.04$, $C = 20\,\mu$F/cm^2, $\beta_m = -1.2$ mV, $\beta_w = 2$ mV, $\gamma_m = 18$ mV, $\gamma_w = 30$ mV, the model displays bistability between a limit cycle and a stable equilibrium in a range of I just below the Hopf threshold. There, ISR emerges due to a mechanism based on biased switching, see the bifurcation diagram $V(I)$ in Fig. 9(c) and the dependence of the oscillation frequency on noise for $I = 95\,\mu$A/cm^2 in Fig. 9(d).

V. DISCUSSION AND OUTLOOK

Considering a model which involves the classical ingredients of neuronal dynamics, such as excitable behavior and coupling plasticity, we have demonstrated two paradigmatic scenarios for inverse stochastic resonance. By one scenario, the phenomenon arises in systems with multistable deterministic dynamics, where at least one of the attractors is a stable equilibrium. Due to the structure of the phase space, and, in particular, the position of the separatrices, the switching dynamics between the associated metastable states becomes biased at an intermediate noise level such that the longevity of the quasi-stationary states substantially increases or they may even turn into absorbing states. In the other scenario, an oscillatory system possesses a weakly unstable fixed point, whose stability is enhanced due to the action of noise. The latter results in a trapping effect such that the system exhibits subthreshold oscillations, whose prevalence is noise-dependent and is found to be maximal at the resonant noise level. Both scenarios involve classical facilitatory effects of noise, such as crossing the separatrices or stochastic mixing across the bifurcation threshold, which should warrant the

ubiquity of ISR. In terms of the robustness of the effect, we have demonstrated that the onset of ISR is independent on the excitability class of local dynamics, and moreover, that the same model of neuronal dynamics, depending on the particular parameters, may display two different scenarios for ISR.

Given that ISR has so far been observed at the level of models of individual neurons,[23,24,26,30] motifs of units with neuron-like dynamics[22,29] and neural networks,[27] it stands to reason that the phenomenon should be universal to neuronal dynamics, affecting both the emergent oscillations and systems of coupled oscillators. The explained mechanisms appear to be generic and should be expected in other systems comprised of units with local dynamics poised close to a bifurcation threshold. Inverse stochastic resonance should play important functional roles in neuronal systems, including the reduction of spiking frequency in the absence of neuromodulators, the triggering of stochastic bursting, i.e., of on–off tonic spiking activity, the suppression of pathologically long short-term memories,[14,24,26,28] and most notably, may contribute to generation of UP–DOWN states, characteristic for spontaneous and induced activity in cortical networks.[31,32]

REFERENCES

[1] B. Lindner, J. García-Ojalvo, A. Neiman, and L. Schimansky-Geier, Phys. Rep. **392**, 321 (2004).
[2] E. Forgoston and R. O. Moore, SIAM Rev. **60**, 969 (2018).
[3] B. Neiman and D. F. Russell, Phys. Rev. Lett. **88**, 138103 (2002).
[4] L. Ryashko and E. Slepukhina, Phys. Rev. E **96**, 032212 (2017).
[5] C. Zheng and A. Pikovsky, Phys. Rev. E **98**, 042148 (2018).
[6] I. Bačić, S. Yanchuk, M. Wolfrum, and I. Franović, Eur. Phys. J. Spec. Top. **227**, 1077 (2018).
[7] I. Franović and V. Klinshov, Chaos **28**, 023111 (2018).
[8] A. Fiasconaro, B. Spagnolo, and S. Boccaletti, Phys. Rev. E **72**, 061110 (2005).
[9] R. N. Mantegna and B. Spagnolo, Phys. Rev. Lett. **76**, 563 (1996).
[10] S. Ciuchi, F. de Pasquale, and B. Spagnolo, Phys. Rev. E **47**, 3915 (1993).
[11] N. V. Agudov, A. A. Dubkov, and B. Spagnolo, Physica A **325**, 144 (2003).
[12] G. Augello, D. Valentia, and B. Spagnolo, Eur. Phys. J. B **78**, 225 (2010).
[13] M. D. McDonnell and L. M. Ward, Nat. Rev. Neurosci. **12**, 415 (2011).
[14] B. A. Schmerl and M. D. McDonnell, Phys. Rev. E **88**, 052722 (2013).
[15] A. Destexhe and M. Rudolph-Lilith, *Neuronal Noise* (Springer, New York, 2012).
[16] A. S. Pikovsky and J. Kurths, Phys. Rev. Lett. **78**, 775 (1997).
[17] B. Lindner and L. Schimansky-Geier, Phys. Rev. E **60**, 7270 (1999).
[18] V. A. Makarov, V. I. Nekorkin, and M. G. Velarde, Phys. Rev. Lett. **86**, 3431 (2001).
[19] A. Zakharova, A. Feoktistov, T. Vadivasova, and E. Schöll, Eur. Phys. J. Spec. Top. **222**, 2481 (2013).
[20] N. Semenova, A. Zakharova, V. Anishchenko, and E. Schöll, Phys. Rev. Lett. **117**, 014102 (2016).
[21] L. H. Gammaitoni, P. Hänggi, P. Jung, and F. Marchesoni, Rev. Mod. Phys. **70**, 223 (1998).
[22] B. S. Gutkin, J. Jost, and H. C. Tuckwell, Eur. Phys. Lett. **81**, 20005 (2008).
[23] H. C. Tuckwell, J. Jost, and B. S. Gutkin, Phys. Rev. E **80**, 031907 (2009).

[24] M. Uzuntarla, J. R. Cressman, M. Ozer, and E. Barreto, Phys. Rev. E **88**, 042712 (2013).

[25] M. Uzuntarla, Phys. Lett. A **377**, 2585 (2013).

[26] M. Uzuntarla, J. J. Torres, P. So, M. Ozer, and E. Barreto, Phys. Rev. E **95**, 012404 (2017).

[27] M. Uzuntarla, E. Barreto, and J. J. Torres, PLoS Comput. Biol. **13**, e1005646 (2017).

[28] A. Buchin, S. Rieubland, M. Häusser, B. S. Gutkin, and A. Roth, PLoS Comput. Biol. **12**, e1005000 (2016).

[29] I. Bačić, V. Klinshov, V. I. Nekorkin, M. Perc, and I. Franović, Eur. Phys. Lett. **124**, 40004 (2018).

[30] I. Franović, O. E. Omel'chenko, and M. Wolfrum, Chaos **28**, 071105 (2018).

[31] T. T. G. Hahn, J. M. McFarland, S. Berberich, B. Sakmann, and M. R. Mehta, Nat. Neurosci. **15**, 1531 (2012).

[32] V. V. Vyazovskiy and K. D. Harris, Nat. Rev. Neurosci. **14**, 443 (2013).

[33] I. Franović and V. Klinshov, Eur. Phys. Lett. **116**, 48002 (2016).

[34] J. A. Kromer, R. D. Pinto, B. Lindner, and L. Schimansky-Geier, Eur. Phys. Lett. **108**, 20007 (2014).

[35] L. Lücken, O. V. Popovych, P. A. Tass, and S. Yanchuk, Phys. Rev. E **93**, 032210 (2016).

[36] D. Kasatkin, S. Yanchuk, E. Schöll, and V. Nekorkin, Phys. Rev. E **96**, 062211 (2017).

[37] P. O. Sporns and R. Kotter, PLoS Biol. **2**, e369 (2004).

[38] Y. L. Maistrenko, B. Lysyansky, C. Hauptmann, O. Burylko, and P. Tass, Phys. Rev. E **75**, 066207 (2007).

[39] T. Aoki and T. Aoyagi, Phys. Rev. Lett. **102**, 034101 (2009).

[40] T. Aoki and T. Aoyagi, Phys. Rev. E **84**, 066109 (2011).

[41] D. O. Hebb, *The Organization of Behavior: A Neuropsychological Approach* (John Wiley and Sons, New York, 1949).

[42] S. Song, K. D. Miller, and L. F. Abbott, Nat. Neurosci. **3**, 919 (2000).

[43] R. C. Froemke and Y. Dan, Nature **416**, 433 (2002).

[44] H.-X. Wang, R. C. Gerkin, D. W. Nauen, and G.-Q. Bi, Nat. Neurosci. **8**, 187 (2005).

[45] A. Morrison, M. Diesmann, and W. Gerstner, Biol. Cybern. **98**, 459 (2008).

[46] O. V. Popovych, S. Yanchuk, and P. A. Tass, Sci. Rep. **3**, 2926 (2013).

[47] P. Hänggi, P. Talkner, and M. Borkovec, Rev. Mod. Phys. **62**, 251 (1990).

[48] C. Kuehn, *Multiple Time Scale Dynamics* (Springer International Publishing, Switzerland, 2015).

[49] A. Shilnikov, Int. J. Bifurcat. Chaos **18**, 2141 (2008).

[50] N. Berglund and B. Gentz, *Noise-Induced Phenomena in Slow-Fast Dynamical Systems* (Springer, Berlin, 2006).

[51] *Stochastic Methods in Neuroscience*, edited by C. Laing and G. J. Lord (Oxford University Press, London, 2009).

[52] J. Touboul and G. Wainrib, Physica D **307**, 42 (2015).

[53] H. Wang, L. Wang, L. Yu, and Y. Chen, Phys. Rev. E **83**, 021915 (2011).

Dynamics of a stochastic excitable system with slowly adapting feedback

Igor Franović, Serhiy Yanchuk, Sebastian Eydam, Iva Bačić, and Matthias Wolfrum
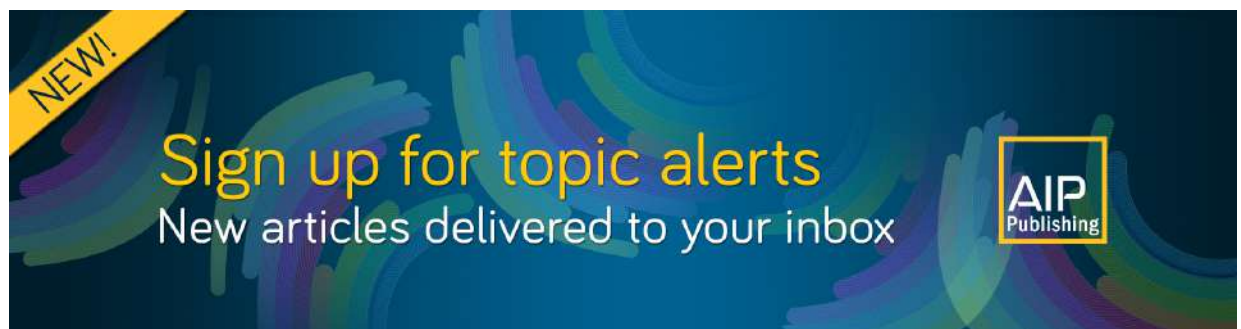
View Online   Export Citation   CrossMark

Dynamics of a stochastic excitable system with slowly adapting feedback

View Online   Export Citation   CrossMark

Igor Franović,[1,a] Serhiy Yanchuk,[2,b] Sebastian Eydam,[3,c] Iva Bačić,[1,d] and Matthias Wolfrum[3,e]

AFFILIATIONS

[1] Scientific Computing Laboratory, Center for the Study of Complex Systems, Institute of Physics Belgrade, University of Belgrade, Pregrevica 118, 11080 Belgrade, Serbia
[2] Institut für Mathematik, Technische Universität Berlin, Straße des 17. Juni 136, 10623 Berlin, Germany
[3] Weierstrass Institute, Mohrenstrasse 39, 10117 Berlin, Germany

[a] **Author to whom correspondence should be addressed:** franovic@ipb.ac.rs
[b] **Electronic mail:** yanchuk@math.tu-berlin.de
[c] **Electronic mail:** sebastian.eydam@gmail.com
[d] **Electronic mail:** iva@scl.rs
[e] **Electronic mail:** wolfrum@wias-berlin.de

ABSTRACT

We study an excitable active rotator with slowly adapting nonlinear feedback and noise. Depending on the adaptation and the noise level, this system may display noise-induced spiking, noise-perturbed oscillations, or stochastic bursting. We show how the system exhibits transitions between these dynamical regimes, as well as how one can enhance or suppress the coherence resonance or effectively control the features of the stochastic bursting. The setup can be considered a paradigmatic model for a neuron with a slow recovery variable or, more generally, as an excitable system under the influence of a nonlinear control mechanism. We employ a multiple timescale approach that combines the classical adiabatic elimination with averaging of rapid oscillations and stochastic averaging of noise-induced fluctuations by a corresponding stationary Fokker–Planck equation. This allows us to perform a numerical bifurcation analysis of a reduced slow system and to determine the parameter regions associated with different types of dynamics. In particular, we demonstrate the existence of a region of bistability, where the noise-induced switching between a stationary and an oscillatory regime gives rise to stochastic bursting.

Published under license by AIP Publishing. https://doi.org/10.1063/1.5145176

Recent years have witnessed a rapid expansion of stochastic models for a wide variety of important physical and biological phenomena, from sub-cellular processes and tissue dynamics, over large-scale population dynamics and genetic switching to optical devices, Josephson junctions, fluid mechanics, and climatology. These studies have demonstrated that the effects of noise manifest themselves on a broad range of scales but, nevertheless, display certain universal features. In particular, the effects of noise may generically be cast into two groups. On the one hand, the noise may enhance or suppress the features of deterministic dynamics, while on the other hand, it may give rise to novel forms of behavior, associated with the crossing of thresholds and separatrices or with stabilization of deterministically unstable states. The constructive role of noise has been evinced in diverse applications, from neural networks and chemical reactions to lasers and electronic circuits. Classical examples of stochastic facilitation in neuronal systems concern resonant phenomena, such as coherence resonance, where an intermediate level of noise may trigger coherent oscillations in excitable systems, as well as spontaneous switching between the coexisting metastable states. In the present study, we show how the interaction of noise and multiscale dynamics, induced by slowly adapting feedback, may affect an excitable system. It gives rise to a new mode of behavior based on switching dynamics, namely, the stochastic bursting and allows for an efficient control of the properties of coherence resonance.

I. INTRODUCTION

Multiscale dynamics is ubiquitous in real-world systems. In neuron models, for instance, the evolution of recovery or gating variables is usually much slower than the changes of the

membrane potential.[1,2] At the level of neural networks, certain mechanisms of synaptic adaptation, such as the spike timing-dependent plasticity,[3–5] are slower than the spiking dynamics of individual neurons. When modeling the dynamics of semiconductor lasers,[6–8] one similarly encounters at least two different timescales, one related to the carriers' and the other to the photons' lifetime, whereby their ratio can span several orders of magnitude. Investigating the dynamics of such multiscale systems has led to the development of a number of useful asymptotic and geometric methods, see Refs. 9–13, to name just a few.

Another ingredient inevitable in modeling real-world systems is noise, which may describe the intrinsic randomness of the system and the fluctuations in the embedding environment or may derive from coarse-graining over the degrees of freedom associated with small spatial or temporal scales.[14,15] For instance, neuronal dynamics is typically influenced by intrinsic sources of noise, such as the random opening of ion channels, and by external sources, like the synaptic noise.[16] In chemical reactions, noise comprises finite-size effects, while the stochasticity in laser dynamics reflects primarily quantum fluctuations. In general, the impact of noise can manifest itself by modification of the deterministic features of the system or by the emergence of qualitatively novel types of behavior, induced by the crossing of thresholds or separatrices.[17]

In the present paper, we study the effects of slowly adapting feedback and noise on an excitable system. Excitability is a general nonlinear phenomenon based on a threshold-like response of a system to perturbation.[1,15,18,19] An excitable system features a stable "rest" state intermitted by excitation events (firing), elicited by perturbations. In the absence of a perturbation, such a system remains in the rest state and a small perturbation induces a small-amplitude linear response. If the perturbation is sufficiently strong, an excitable system reacts by a large-amplitude nonlinear response, such as a spike of a neuron. When an excitable system receives additional feedback or a stochastic input or is coupled to other such systems, new effects may appear due to the self- or noise-induced excitations, as well as excitations from the neighboring systems. Such mechanisms can give rise to different forms of oscillations, patterns, propagating waves, and other phenomena.[15,20–28]

Our focus is on a stochastic excitable system subjected to a slow control via a low-pass filtered feedback

$$\dot{v}(t) = f(v(t), \mu(t)) + \sqrt{D}\xi(t), \tag{1}$$

$$\dot{\mu}(t) = \varepsilon(-\mu(t) + \eta g(v(t))), \tag{2}$$

where $\varepsilon \gtrsim 0$ is a small parameter that determines the timescale separation between the fast variable $v(t)$ and the slow feedback variable $\mu(t)$. The fast dynamics $\dot{v}(t) = f(v(t), 0)$ is excitable and is influenced by the Gaussian white noise $\xi(t)$ of variance D. Moreover, the slow feedback variable μ controls its excitability properties. The parameter η is the control gain such that for $\eta = 0$, one recovers a classical noise-driven excitable system.[15] An important example of a system conforming to (1) and (2) for $\eta \neq 0$ is the Izhikevich neuron model,[29] where the stochastic input to the fast variable would describe the action of synaptic noise.

Here, we analyze a simple paradigmatic example from the class of systems (1) and (2), where the excitable local dynamics is represented by an active rotator

$$\dot{\varphi}(t) = I - \sin\varphi(t) \quad \text{with} \quad \varphi \in [0, 2\pi).$$

The latter undergoes a saddle-node infinite period (SNIPER, sometimes also called SNIC – saddle node on invariant circle) bifurcation at $|I| = 1$, turning from excitable ($|I| \lesssim 1$) to oscillatory regime $|I| > 1$, see Ref. 30. The adaptation is represented by a positive periodic function $g(\varphi) = 1 - \sin\varphi$ such that the complete model reads

$$\dot{\varphi}(t) = I_0 + \mu(t) - \sin\varphi(t) + \sqrt{D}\xi(t), \tag{3}$$

$$\dot{\mu}(t) = \varepsilon(-\mu(t) + \eta(1 - \sin\varphi(t))). \tag{4}$$

In the presence of feedback, the noiseless dynamics of the active rotator depends now on $I = I_0 + \mu(t)$ involving the control variable $\mu(t)$, which can induce switching between the excitable equilibrium and the oscillatory regime. This adaptation rule provides a positive feedback for the spikes and oscillations, since $\mu(t)$ increases when $\varphi(t)$ is oscillating and drives the system toward the oscillatory regime, while in the vicinity of the equilibrium ($\sin\varphi \approx 1$) the control signal effectively vanishes.

We examine how the behavior of (3) and (4) is influenced by the noise level D and the control gain η, determining the phase diagram of dynamical regimes in terms of these two parameters. The first part of our results in Sec. II concerns the noise-free system $D = 0$, where we employ a combination of two multiscale methods, namely, adiabatic elimination in the regime where the fast subsystem has stable equilibrium and the averaging approach when the fast subsystem is oscillatory. As a result, we obtain a reduced slow system that is capable of describing both the slowly changing fast oscillations and the slowly drifting equilibrium, as well as the transitions between these regimes. The bifurcation analysis of this slow system reveals the emergence of bistability between the fast oscillations and the equilibrium for sufficiently large η.

The second part of our results, presented in Sec. III, addresses the multiscale analysis of the dynamics in the presence of noise ($D \neq 0$). Instead of deterministic averaging, we apply the method of *stochastic averaging*,[25,31–34] where the distribution density for the fast variable obtained from a stationary Fokker–Plank equation is used to determine the dynamics of the slow flow. In this way, we obtain a deterministic slow dynamics for which one can perform a complete numerical bifurcation analysis with respect to D and η. In Sec. IV, we investigate the effects of stochastic fluctuations on the slow dynamics, which vanish in the limit of infinite timescale separation $\varepsilon \to 0$ employed in Sec. III. The effect of a slowly adapting feedback on the coherence resonance is shown by extracting from numerical simulations the coefficient of variation of the spike time distribution in the excitable regime. In particular, we compare the results for small positive ε with the case of infinite time scale separation, where we use the stationary but noise dependent μ obtained in Sec. III. The noise-induced switching dynamics in the bistability region is demonstrated by numerical simulations showing an Eyring–Kramers type of behavior.

In terms of the different dynamical regimes, our study of stochastic dynamics reveals three characteristic (D, η) regions featuring noise-induced spiking, noise-perturbed spiking, and stochastic busting (see Fig. 1). We show that by varying the control gain
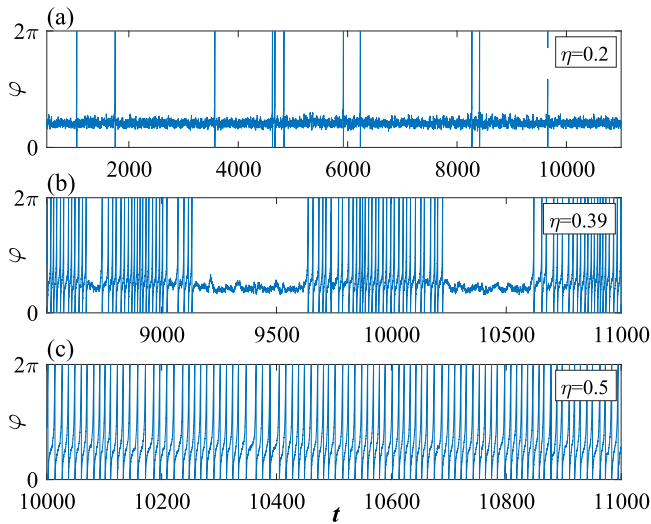
FIG. 1. Different dynamical regimes in the stochastic excitable system subjected to a slow control via a low-pass filtered feedback (3) and (4) with $\varepsilon = 0.005$, $D = 0.008$ and different choices of the control gain η: noise-induced spiking (a), stochastic bursting (b), and noise-perturbed spiking (c).

within the region of noise-induced spiking, one can enhance or suppress the coherence resonance, while within the bistability region, one can efficiently control the properties of stochastic bursting. Sections II–IV provide a detailed analysis of the described phenomena.

II. SLOW–FAST ANALYSIS OF THE DETERMINISTIC DYNAMICS

In this section, we analyze the systems (3) and (4) in the absence of noise ($D = 0$)

$$\dot{\varphi}(t) = I_0 - \sin \varphi(t) + \mu(t), \tag{5}$$

$$\dot{\mu}(t) = \varepsilon \left(-\mu(t) + \eta \left(1 - \sin \varphi(t)\right)\right), \tag{6}$$

considering the limit $\varepsilon \to 0$ within the framework of singular perturbation theory. The fast subsystem

$$\dot{\varphi}(t) = I_0 + \mu - \sin \varphi(t), \tag{7}$$

often called a "layer equation" describes the dynamics on the fast timescale and is obtained from (5) and (6) by setting $\varepsilon = 0$, whereby μ acts as a parameter.

A. Dynamics for $\mu < 1 - I_0$: Adiabatic elimination

In the case $\mu < 1 - I_0$, the fast subsystem (7) possesses two equilibria

$$\varphi_+(\mu) = \arcsin(I_0 + \mu), \quad \varphi_-(\mu) = \pi - \varphi_+(\mu), \tag{8}$$

where φ_+ is stable and φ_- is unstable. Considering them as functions of the parameter μ, the equilibria give rise to two branches, which

merge in a fold at $\mu = 1 - I_0$ (see Fig. 2). Equivalently, the set of equilibria of the fast subsystem

$$\{(\varphi, \mu) : \sin \varphi = I_0 + \mu\} \tag{9}$$

comprises the critical manifold of (5) and (6), with the stable part $\varphi_+(\mu)$ and the unstable part $\varphi_-(\mu)$.

Hence, for $\mu < 1 - I_0$, the trajectories are rapidly attracted toward the stable branch of the critical manifold, along which for positive ε they slowly drift. In order to describe this slow dynamics, we rescale time $T = \varepsilon t$ and obtain

$$\varepsilon \varphi'(T) = I_0 + \mu(T) - \sin \varphi(T), \tag{10}$$

$$\mu'(T) = -\mu(T) + \eta(1 - \sin \varphi(T)), \tag{11}$$

where the prime denotes the derivative with respect to the slow time T. Setting $\varepsilon = 0$, we can directly eliminate the term $\sin \varphi(T) = I_0 + \mu(T)$ and obtain the equation for the slow dynamics on the critical manifold

$$\mu'(T) = -\mu(T) + \eta(1 - I_0 - \mu(T)). \tag{12}$$

B. Dynamics for $\mu > 1 - I_0$: Averaging fast oscillations

For $\mu > 1 - I_0$, there is no stable equilibrium of the fast subsystem (7) (see Fig. 2). Instead, one finds periodic oscillations

$$\varphi_\mu(t) = 2 \arctan \frac{1 + \Omega(\mu) \tan \frac{t}{2} \Omega(\mu)}{I_0 + \mu}, \tag{13}$$

with the μ-dependent frequency

$$\Omega(\mu) = \sqrt{(I_0 + \mu)^2 - 1}.$$

In this case, the fast oscillations $\varphi_\mu(t)$ should be averaged in order to obtain the dynamics of the slow variable $\mu(T)$, see Refs 35

FIG. 2. Critical manifold and fast dynamics of systems (5) and (6). For $\mu < 1 - I_0$, the fast dynamics converges to the stable branch of the critical manifold, while for $\mu > 1 - I_0$, it is oscillatory with periodic rotation of the phase φ.

and 36. A rigorous formal derivation is provided in Appendix A, finally arriving at

$$\mu'(T) = -\mu(T) + \eta(1 - I_0 - \mu(T) + \Omega(\mu(T))). \quad (14)$$

Here, we give a simplified explanation of the averaging procedure. First, we substitute the fast-oscillating solution $\varphi = \varphi_\mu(t)$ of the fast subsystem into the equation for the slow variable (11),

$$\mu'(T) = -\mu(T) + \eta(1 - \sin \varphi_\mu(t)).$$

Since the term $\sin(\cdot)$ is fast oscillating, the last equation can be averaged over the fast timescale t, which leads to

$$\mu'(T) = -\mu(T) + \eta \left(1 - \langle \sin \varphi_\mu(t) \rangle_t \right). \quad (15)$$

The average $\langle \sin \varphi_\mu(t) \rangle_t$ can be found by integrating (7) over the period, which gives

$$\langle \dot{\varphi}(t) \rangle_t = \Omega(\mu) = I_0 + \mu - \langle \sin \varphi_\mu(t) \rangle_t. \quad (16)$$

Hence, by substituting

$$\langle \sin \varphi_\mu(t) \rangle_t = I_0 + \mu(T) - \Omega(\mu(T))$$

into (15), we obtain the slow averaged dynamics (14).

C. Combined dynamics of the slow variable

Summarizing the results so far, Eq. (12) describes the dynamics of the slow variable for $\mu < 1 - I_0$, while Eq. (14) holds for $\mu > 1 - I_0$. These two equations can be conveniently combined into a single equation of the form (14) by extending the definition of the frequency $\Omega(\mu)$ as follows:

$$\Omega(\mu) = \begin{cases} 0, & \mu < 1 - I_0, \\ \sqrt{(I_0 + \mu)^2 - 1}, & \mu > 1 - I_0. \end{cases} \quad (17)$$

Hence, the slow dynamics is described by the scalar ordinary differential equation on the real line (14), and, as a result, the only possible attractors are fixed points, which are given by the zeros of the right-hand side as

$$\Omega(\mu) = \frac{\eta + 1}{\eta}\mu + I_0 - 1. \quad (18)$$

Geometrically, they are points of intersection of the frequency profile $\Omega(\mu)$ with the line $\frac{\eta+1}{\eta}\mu + I_0 - 1$ [see Fig. 3(a)]. In particular, one can check that there is always one fixed point

$$\mu_1 = \frac{\eta(1 - I_0)}{1 + \eta} < 1 - I_0, \quad (19)$$

for which $\Omega(\mu_1) = 0$ such that it corresponds to a pair of equilibria on the critical manifold (9). Since μ_1 is stable for the slow dynamics, the point $(\varphi_+(\mu_1), \mu_1)$ is also a stable equilibrium for original systems (5) and (6) with small ε. The other two fixed points of the slow
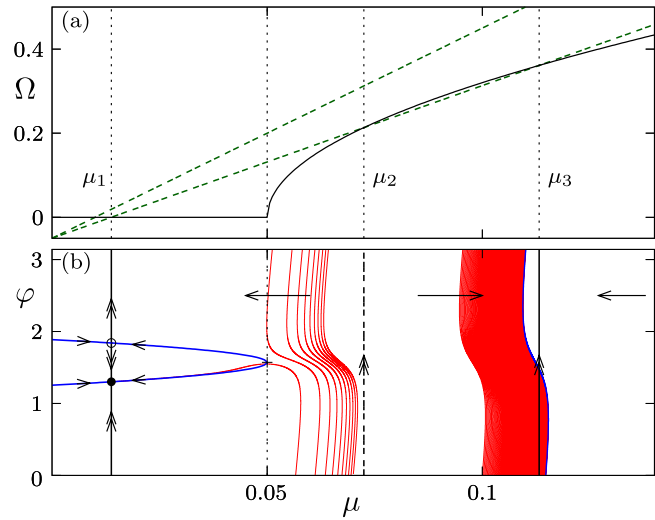

FIG. 3. (a) Graphical solution of the fixed point Eq. (18): $\Omega(\mu)$ according to (17) (black) and the right-hand side of (18) for different choices of η. One finds from one to three fixed points depending on η. (b) Scheme of the slow–fast dynamics of systems (5) and (6) with parameters $I_0 = 0.95$ and $\eta = 0.38$ and the numerical sample trajectories for $\varepsilon = 0.005$ (red). For $\mu < 1 - I_0$, trajectories are attracted to the stable branch of the slow manifold (blue curve) and subsequently slowly drift toward the stable fixed point $(\varphi_+(\mu_1), \mu_1)$ (black dot). For $\mu > 1 - I_0$, the sample trajectories show fast oscillations in φ with a slow average drift in μ in the direction indicated by the arrows.

equation

$$\mu_{2,3} = \frac{\eta\left(1 + \eta - I_0 \mp \sqrt{(\eta + I_0)^2 - 1 - 2\eta}\right)}{1 + 2\eta}, \quad (20)$$

with $\Omega(\mu_{2,3}) > 0$ appear in a saddle-node bifurcation at

$$\eta_{sn} = 1 - I_0 + \sqrt{2(1 - I_0)} \quad (21)$$

and correspond to a pair of periodic orbits of fast subsystem (7).

In Fig. 3(b) we show schematically the results of our slow–fast analysis for $I_0 = 0.95$ and $\eta = 0.38$. For the chosen parameter values there are two stable regimes: the fixed point $(\varphi_+(\mu_1), \mu_1)$ and a fast oscillation with $\langle \mu(t) \rangle_t \approx \mu_3$.

Finally, Fig. (4) presents the bifurcation diagram of the fixed points of the slow dynamics with respect to the control gain η. One observes that there is always one branch of stable fixed points corresponding to the steady state and two stable fixed points corresponding to fast oscillations for $\eta > \eta_{sn}$. For our choice of $I_0 = 0.95$, we obtain $\eta_{sn} \approx 0.3662$.

III. SLOW–FAST ANALYSIS OF THE DYNAMICS WITH NOISE

In this section, we consider the dynamics of systems (3) and (4) in the presence of noise ($D > 0$). In analogy to the noise-free case,
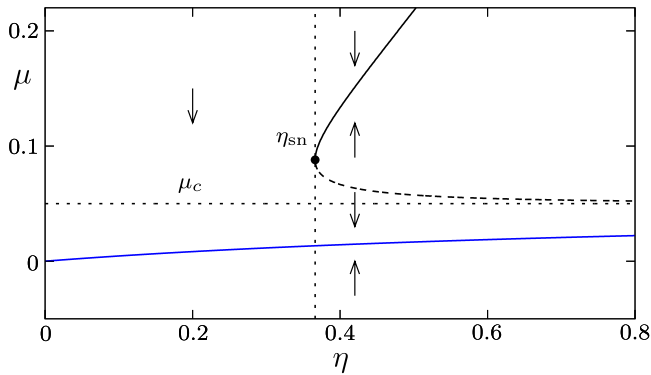
FIG. 4. Fixed points of the slow dynamics (14) for varying control gain η. The values $\mu_{2,3}$ on the upper branch (black curve) correspond to periodic orbits of the fast subsystem (7), while μ_1 (blue curve) is the branch of fixed points; solid and dashed lines indicate stable and unstable solutions, respectively. The direction of the motion in $\mu(T)$ is indicated by the arrows. The dotted lines indicate the onset of bistability for $\eta = \eta_{\mathrm{sn}}$ and the transition at $\mu_c = 1 - I_0$ from equilibria to periodic orbits.

one can use the limit $\varepsilon \to 0$ and employ the *stochastic average*

$$\langle \sin \varphi(t) \rangle_t = \lim_{t \to \infty} \frac{1}{t} \int_0^t \sin \varphi(t) \mathrm{d}t',$$

for solutions of the stochastic fast equation

$$\dot{\varphi}(t) = I_0 + \mu - \sin \varphi(t) + \sqrt{D}\xi(t) \qquad (22)$$

to approximate the slow dynamics in (11) by

$$\mu'(T) = -\mu(T) + \eta(1 - \langle \sin \varphi(t) \rangle_t). \qquad (23)$$

To this end, we consider the *stationary probability density distribution* $\rho(\varphi; \mu, D)$ for the fast noisy dynamics (3), which for fixed control μ and noise intensity D is given as a solution to the stationary Fokker–Planck equation

$$\frac{D}{2}\partial_{\varphi\varphi}\rho - \partial_\varphi\left[(I_0 + \mu - \sin \varphi)\rho\right] = 0, \qquad (24)$$

together with the periodic boundary conditions $\rho(0) = \rho(2\pi)$ and the normalization

$$\int_0^{2\pi} \rho(\varphi; \mu, D)\mathrm{d}\varphi = 1. \qquad (25)$$

From this, we can calculate the average

$$\langle \sin \varphi(t) \rangle_t = \int_0^{2\pi} \rho(\varphi; \mu, D) \sin \varphi \mathrm{d}\varphi \qquad (26)$$

and obtain the mean frequency

$$\Omega_D(\mu) = I_0 + \mu - \langle \sin \varphi(t) \rangle_t, \qquad (27)$$

which depends via (26) both on D and μ. Taking into account (23) and (27), the equation for the slow dynamics of $\mu(T)$ reads

$$\mu'(T) = -\mu(T) + \eta(1 - I_0 - \mu + \Omega_D(\mu(T))), \qquad (28)$$
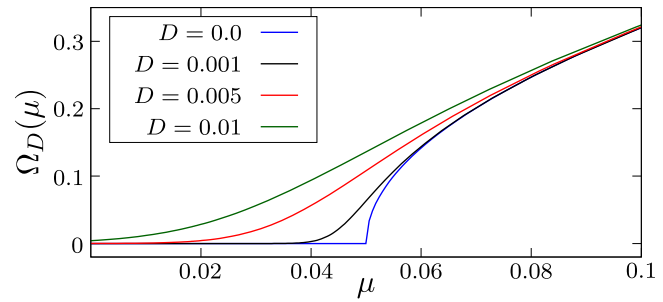

FIG. 5. Average frequency of the fast dynamics (3) given by (26) and (27) using numerical solutions of the stationary Fokker–Planck Eq. (24), where μ acts as a time independent parameter and fixed $I_0 = 0.95$.

i.e., it is of the same form as in the deterministic case (14). The corresponding fixed point equation for the stationary values of μ with respect to the slow dynamics is given by (18).

The stationary Fokker–Planck Eq. (24) can be solved directly by integral expressions [see Appendix B]. In particular, for $D = 0$, we readily recover the results for periodic averaging from Sec. II. However, for small non-vanishing D, the integrals become difficult to evaluate numerically, and we preferred to solve (24) as a first-order ODE boundary value problem with software AUTO,[37] which provides numerical solutions to boundary value problems by collocation methods together with continuation tools for numerical bifurcation analysis.

In Fig. 5 are shown the numerically obtained effective frequencies $\Omega_D(\mu)$ for different noise levels D. Solving the stationary Fokker–Planck Eq. (24) together with the fixed point equation for $\mu(T)$ (18), we obtain for fixed values of D and varying control gain η branches of stationary solutions $(\mu^*, \rho(\varphi; \mu^*, D))$ [see Fig. 6(a)]. For small noise intensities, these branches are folded, which indicates the coexistence of up to three stationary solutions, similarly as in the noise-free case. Alternatively, we can also fix η and obtain branches for varying D [see Fig. 6(c)]. For small η they are monotonically increasing, while for larger η they are folded. For $\eta_{\mathrm{sn}} < \eta$ there are two separate branches, emanating from the three solutions of (18) at $D = 0.6$

Numerical continuation of the folds in the (η, D) parameter plane provides the curves outlining the boundaries of the bistability region. Figure 6(b) shows that the two branches of folds meet at a cusp point $(\eta_{\mathrm{cu}}, D_{\mathrm{cu}})$. One of the branches approaches for $D \to 0$ the value $\eta = \eta_{\mathrm{sn}}$, which we have calculated in (21), while the other one diverges to infinite values of η. From our numerics for different values of I_0, we observe that closer to the critical value $I_0 = 1$, the cusp point shifts to a smaller noise intensity D such that the region of bistability decreases.

Note that for $D > 0$, all the average frequencies satisfy $\Omega_D > 0$ such that a clear distinction between the stationary and the oscillatory regime of the fast dynamics is no longer possible. However, one can compare the critical value of the deterministic fast dynamics
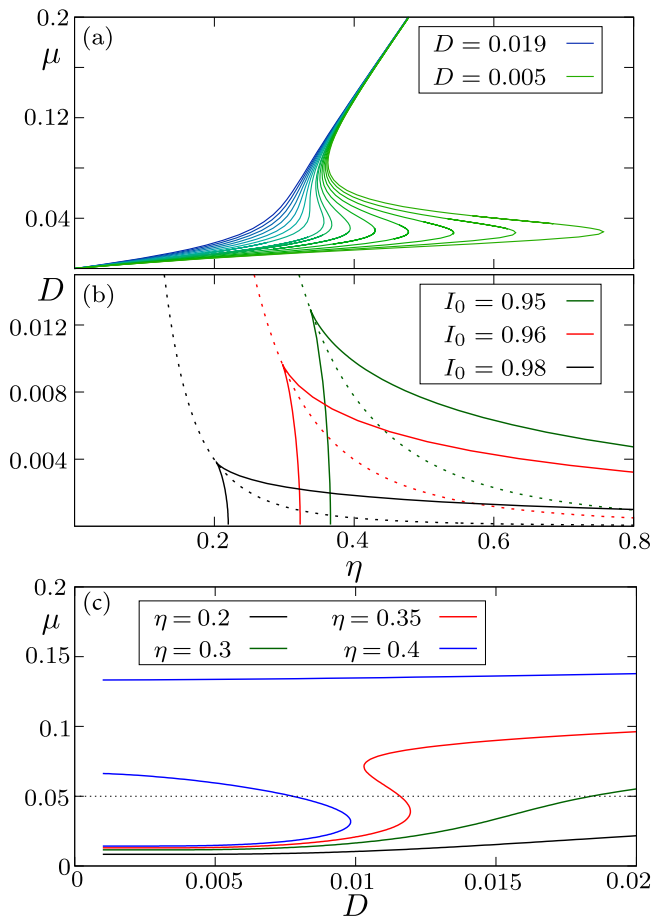
$$\mu_c = 1 - I_0, \qquad (29)$$

FIG. 6. Panels (a) and (c): Branches of fixed points μ^* of the slow dynamics (28) calculated at $I_0 = 0.95$ from (18) together with the stationary Fokker–Planck Eq. (24). (a) Branches $\mu^*(\eta)$ for noise values $D = 0.005, 0.006, \ldots, 0.019$ and (b) two-dimensional bifurcation diagrams in terms of η and D for three different values of I_0 show the curves of fold bifurcations, which meet at the cusp point. Dashed curves indicate the case where $\mu^* = \mu_c = 1 - I_0$. (c) Branches $\mu^*(D)$ for control gain values $\eta \in \{0.2, 0.3, 0.35, 0.4\}$.

with the corresponding stationary value μ^* of the slow variable from (28) to distinguish between the regime of $\mu^* < \mu_c$, where the oscillations are induced by the noisy fluctuations of $\mu(t)$ and have the form of rare spikes [see Fig. 1(a)], and the regime $\mu^* > \mu_c$ where the oscillatory behavior is already induced by the stationary value of μ^* [see Fig. 1(c)].

Our numerical bifurcation analysis shows that the curves where the stationary values of μ satisfy the condition $\mu = \mu_c$, shown as dashed line in Fig. 6(b), pass exactly through the corresponding cusp points and inside the bistability region refer to the unstable solutions given by the middle part of the S-shaped curves in Fig. 6(a). From this, we conclude that changing the parameters across this line outside the bistability region results in a gradual transition between the regime of fluctuation-induced oscillations and the oscillations induced by the stationary value of μ^*, while at the boundary of the

bistability region, a hysteretic transition between the two regimes is obtained. Moreover, for finite timescale separation $\varepsilon > 0$, there can also be transitions between the two stable regimes within the bistability region, which are induced as well by the stochastic fluctuations. In Sec. IV, we study in detail how the region of bistability found for the singular limit $\varepsilon \to 0$ also affects the dynamics of the original system in the case of finite timescale separation.

IV. EFFECTS OF FLUCTUATIONS AND FINITE TIMESCALE SEPARATION

The two basic deterministic regimes of the fast dynamics, which are the excitable equilibrium, and the oscillations induce in a natural way the two corresponding states of the system with noise and small $\varepsilon > 0$, namely,

- noise-induced spiking, characterized by a Poisson-like distribution of inter-spike intervals (ISIs) [see Fig. 7(a)] and
- noisy oscillations, involving a Gaussian-like distribution of the ISIs, centered around the deterministic oscillation period [see Fig. 7(b)].

These states are found for sufficiently small or large values of η, respectively, where only a corresponding single branch of the deterministic system is available and the fluctuations of μ around its average value have no substantial impact on the dynamics, cf. the blue and orange distributions in Fig. 7. For sufficiently large noise levels above the cusp ($D > D_{cu}$) and intermediate values of η, one observes a gradual transition between these two regimes. However, for smaller noise $D < D_{cu}$, allowing for the existence of the region
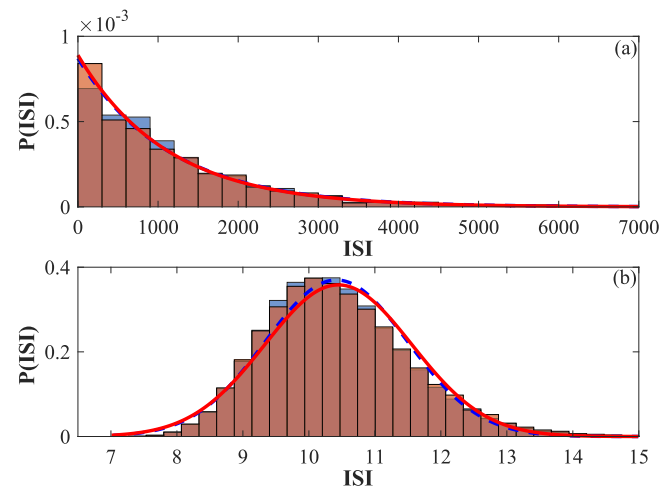

FIG. 7. Histograms of inter-spike intervals of the phase variable for control gain $\eta = 0.2$ (top panel) and $\eta = 0.5$ (bottom panel) obtained from numerical simulations of full systems (3) and (4) with $\varepsilon = 0.005$ (orange) and in the limit of infinite timescale separation (blue), using (22) with the stationary $\mu(T) \equiv \mu_D$ determined from the stationary Fokker–Planck Eq. (24). Solid red and dashed blue curves represent fits to an exponential decay (a) and a Gaussian (b) for the histograms concerning the full system and the limit of infinite scale separation, respectively.

of bistability [cf. Fig. 6(b)], new regimes of stochastic dynamics can emerge, namely,

- enhanced coherence resonance, where a noise-induced dynamical shift of the excitability parameter $I_0 + \mu_D$ is self-adjusted close to criticality and
- noise-induced switching between the two coexisting regimes in the bistability region [see Fig. 1(b)].

A. Enhanced coherence resonance

The phenomenon of coherence resonance,[20,38,39] where the regularity of noise-induced oscillations becomes maximal at an intermediate noise level, is well-known for noisy excitable systems such as the fast Eq. (22) without adaptation, i.e., for $\eta = 0$ and therefore also $\mu = 0$. For values of the control gain $0 < \eta < \eta_{cu}$ below the region of bistability, the control leads to a substantially enhanced coherence resonance. This effect can be quantified by studying the noise dependence of the coefficient of variation of the inter-spike intervals. For a given noisy trajectory of (22), the spiking times t_k are defined as the first passage times $\varphi(t_k) = 2\pi k, k \in \mathbb{N}$ with corresponding inter-spike intervals $\tau_k = t_k - t_{k-1}$. The coefficient of variation of their distribution is defined as

$$R(D) = \frac{\sqrt{\langle \tau_k^2 \rangle - \langle \tau_k \rangle^2}}{\langle \tau_k \rangle}. \tag{30}$$

For (22) with a fixed μ, the latter can be determined from direct numerical simulations. However, inserting for μ the corresponding stochastic averages $\mu^*(D; \eta)$ obtained in the section shows a strong nonlinear dependence both on η and D [see also Figs. 6(a) and 6(c)]. In particular, the strong nonlinear dependence on D for η slightly below the cusp value η_{cu} has a substantial impact on the resonant behavior reflected in the form of $R(D)$. In Fig. 8, we show the $R(D)$ dependence for different values of the control gain η, comparing the numerical results for the fast subsystem (22) with inserted stationary values $\mu^*(D; \eta)$ to numerical simulations of (3) and (4) for $\varepsilon = 0.005$. For $0 < \eta < \eta_{cu}$, one finds that the coherence resonance can be substantially enhanced, cf., for example, the $R(D)$ dependencies for $\eta = 0$ and $\eta = 0.3$. On the other hand, introducing negative values of the control gain η, the resonant effect can be readily suppressed. This implies that the adaptive feedback we employ provides an efficient *control of coherence resonance*. Such an effect has already been demonstrated in Refs. 40, 41, and 42 by using a delayed feedback control of Pyragas type. However, this control method requires the feedback delay time as an additional control parameter to be well adapted to the maximum resonance frequency.

B. Bursting behavior due to noise-induced switching

For parameter values (η, D) within the bistable region and finite timescale separation $\varepsilon > 0$, the coexisting states of excitable equilibrium and fast oscillations turn into metastable states of full systems (3) and (4). Based on our slow–fast analysis, the corresponding dynamics can be understood as follows. The noisy fluctuations of $\varphi(t)$ around its average distribution, given by the stationary Fokker–Planck Eq. (24), induces fluctuations of $\langle \sin \varphi(t) \rangle_t$, and hence also of μ, around their stationary average values calculated
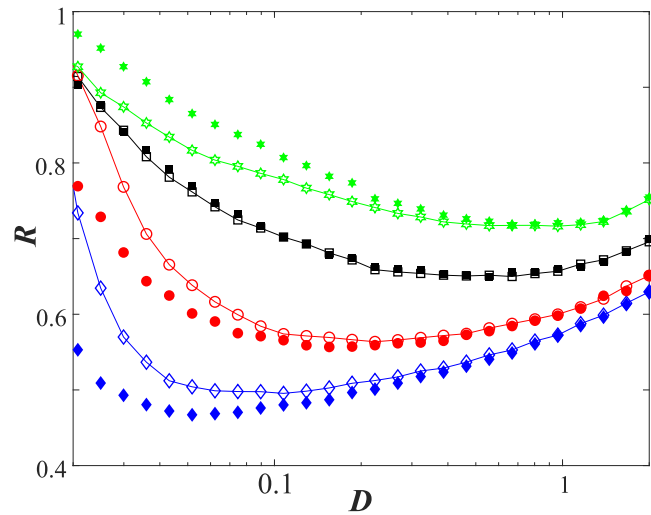
FIG. 8. Enhancement or suppression of coherence resonance by a slowly adapting feedback control. The connected lines with empty symbols refer to $R(D)$ dependencies for full systems (3) and (4) at different values of the control gain: $\eta = -0.2$ (green hexagonals), $\eta = 0$ (black squares), $\eta = 0.2$ (red circles), and $\eta = 0.3$ (blue diamonds), having fixed $I_0 = 0.95$, $\varepsilon = 0.005$. The unconnected filled symbols indicate the corresponding $R(D)$ dependencies obtained from numerical simulations of the fast subsystem 22 with stationary $\mu^*(D)$.

above. For small ε, the corresponding distribution of μ is centered in narrow peaks at the stable stationary values. However, with increasing ε, the nonlinear filtering induces a strong skewness of each peak in the distribution, and their overlapping indicates the possibility of noise-induced transitions between the two metastable states. Figure 9 shows the distribution for $\varepsilon = 0.005$ and different values of the η within the bistability region. These transitions can be understood in analogy to the Eyring–Kramers process in a double well potential. In the generic case of different energy levels for the two potential wells, transitions in one of the directions occur at a higher rate and the system stays preferably in the state associated with the global minimum of the potential. Such behavior of biased switching is very pronounced closed to the boundaries of the bistability region, where a switching to the state close to the fold has a much lower probability than switching back.

In Fig. 10 are shown the numerical time averages $\langle \mu(T) \rangle$ for varying control gain η. One can see that for most values of η, the long-time behavior is dominated by one of the two metastable states, which indicates a biased switching process. Nevertheless, at an intermediate value of η, we find a balanced switching, where transitions in both directions occur at an almost equal rate. A corresponding time trace is shown in Figs. 11 and 1(b). For $\varepsilon \to 0$, the switching rate decreases to zero exponentially and the switching bias in the unbalanced regime increases. This leads to the characteristic steplike behavior of the averages observed in Fig. 10 for smaller ε.

The noise-induced switching shown in Figs. 11 and 1(b) resembles the regime of bursting in neuronal systems. Here, it emerges by an interplay of slow adaptation and noise. In the present setup,
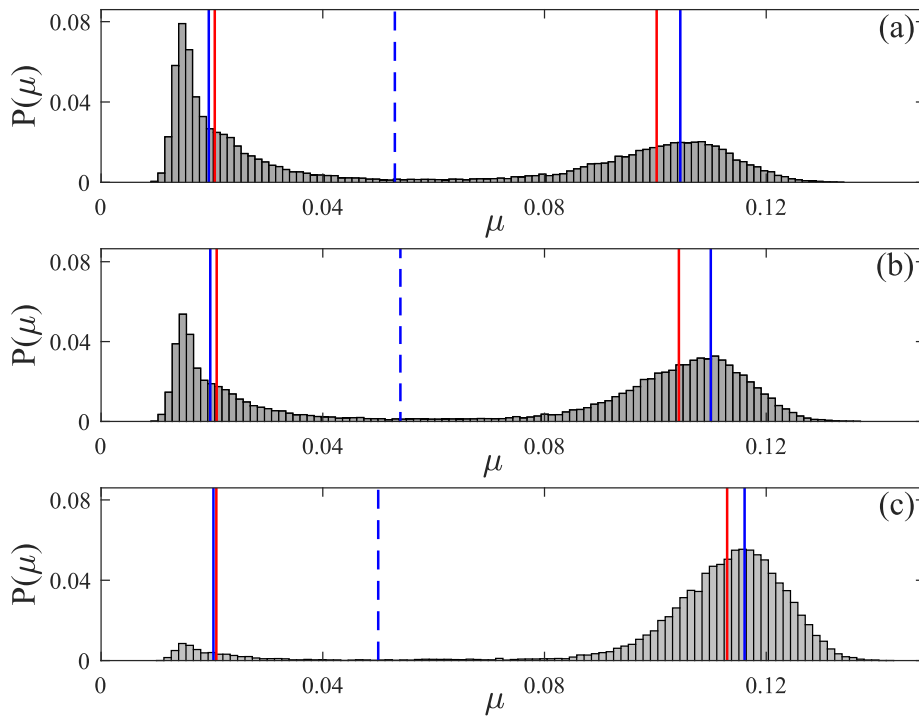
FIG. 9. Stationary distributions $P(\mu)$, sampled from numerical simulations of (3) and (4) with $\varepsilon = 0.005$. Parameters $\eta = 0.37$ in (a), $\eta = 0.373$ in (b) and $\eta = 0.38$ in (c) and fixed noise level $D = 0.009$ lie inside the bistability region from Fig. 6(b). Blue vertical lines indicate the fixed points of μ from the stationary Fokker–Planck Eq. (24) together with the fixed point Eq. (18) of the slow dynamics. Red vertical lines indicate the mean values of all μ in $P(\mu)$ below and of all μ above the unstable fixed point in the middle (dashed blue lines).

the bursts are triggered just by the stochastic fluctuations. However, in regime $\eta > \eta_{cu}$, the system is also quite susceptible to external inputs, which could initiate the bursts even without any intrinsic noise.

V. DISCUSSION AND OUTLOOK

Our model provides a novel perspective on how the dynamics of an excitable system is influenced by the interaction of a slowly adapting feedback and noise. The feedback is taken from a low-pass
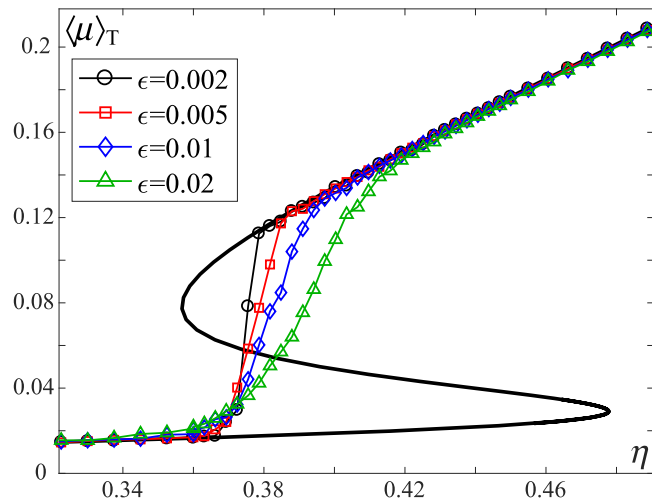
FIG. 10. Long-time averages $\langle\mu\rangle_T$ from numerical simulations of (3) and (4) with fixed noise intensity $D = 0.008$ and varying control gain η at different values of $\varepsilon \in \{0.002, 0.005, 0.01, 0.02\}$. The black curve represents the corresponding result for the infinite timescale separation [cf. Fig. 6(a)].
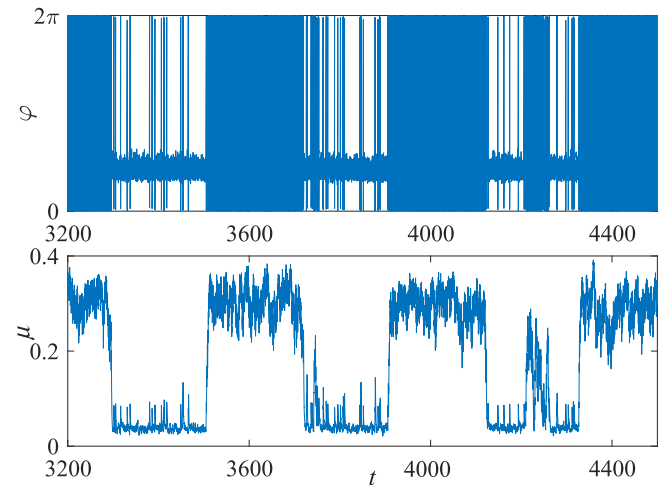
FIG. 11. Time series $\varphi(t)$ (top panel) and $\mu(t)$ (bottom panel) illustrating the regime of balanced switching. The system parameters are $\eta = 0.38$, $D = 0.008$, $l_0 = 0.95$, $\varepsilon = 0.01$.
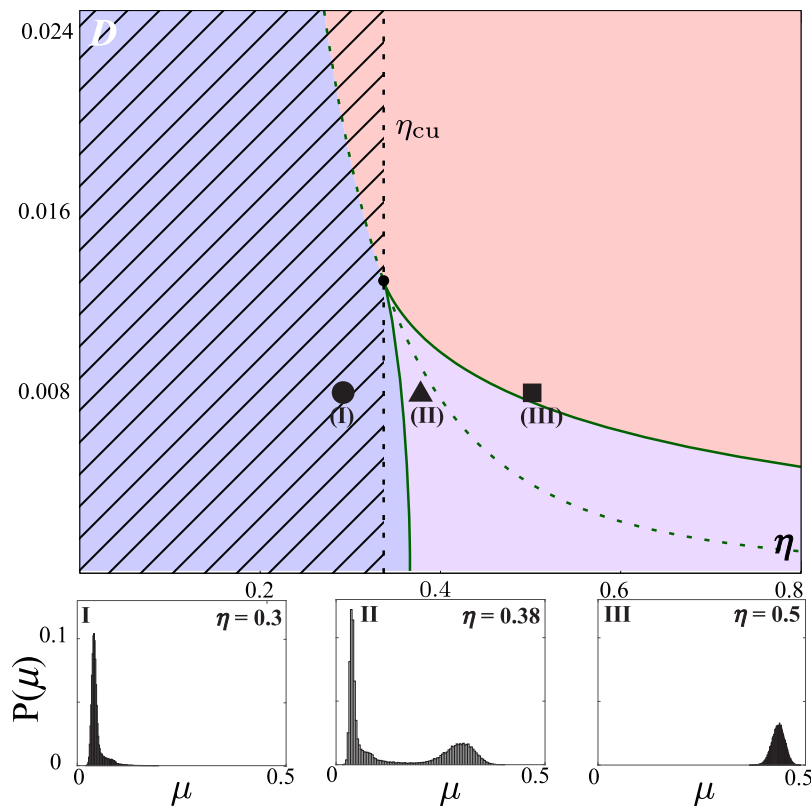
FIG. 12. Upper panel: parameter regions for different dynamical regimes: noise-induced spiking (blue), noise-perturbed oscillations (red), and noise-induced bursting (violet). Enhanced coherence resonance can be found in the hatched region. Symbols indicate the parameter values associated with the histograms $P(\mu)$ shown below. Lower panels: sampled distributions of $\mu(T)$ from numerical solutions with $\varepsilon = 0.005$, $D = 0.008$, and $\eta \in 0.3, 0.38, 0.5$.

filter of a function that gives a positive feedback to the oscillations by pushing the excitability parameter toward the oscillatory regime. Since excitability, feedback, and noise are typical ingredients of neural systems, we believe that the application of our results to a specific neural model would be a next natural step, aiming to gain a deeper understanding of the onset of different dynamical regimes, as well as the means of controlling their properties and the emerging resonant effects. In Fig. 12 are summarized our main results. In particular, the multiple timescale analysis for the limit of infinite timescale separation has allowed us to perform a numerical bifurcation analysis providing the parameter regions for the different dynamical regimes illustrated in Fig. 1. Numerical simulations for finite values of ε (lower panels in Fig. 12) show that the slowly varying control variable $\mu(T)$ is distributed around the stationary values from the limiting problem $\varepsilon = 0$ [see also Fig. 9]. Moreover, we have demonstrated that the filtered feedback in our model provides an efficient control of the effect of coherence resonance, which can be substantially enhanced or suppressed by a corresponding choice of the feedback gain. In the regime where the limiting problem $\varepsilon = 0$ indicates bistability between the equilibrium and a fast oscillation, the stochastic fluctuations at finite values of ε give rise to switching between the associated metastable states. However, our analysis shows that for sufficiently high noise intensity, this bistability vanishes and the two different deterministic states can no longer be distinguished.

From the point of view of the theory of multiscale systems, the deterministic part of the presented model provides one of the simplest examples combining the regimes of stable equilibrium and oscillations within the fast subsystem. A rigorous mathematical treatment of the dynamical transitions between the two regimes and the corresponding reductions by the standard adiabatic elimination and the averaging technique is still missing. Also, our approach to analysis of stochastic dynamics in multiscale systems by introducing a stationary Fokker–Planck equation for the fast dynamics leads to important questions concerning the limiting properties of the trajectories and the specific implications of the fluctuations. Nevertheless, we have considered only the case when the noise acts in the fast variable. An open problem is to study how the obtained results are influenced by the noise in the slow variable, where interesting new effects can be expected.[43]

ACKNOWLEDGMENTS

APPENDIX A: MULTISCALE AVERAGING IN THE REGIME OF FAST OSCILLATIONS

In this appendix, we provide a rigorous formal derivation of the slow averaged Eq. (14) for the case of periodic dynamics in the fast layers.

We apply the following general multiscale ansatz:

$$\varphi = \bar{\varphi}(t, \varepsilon t) + \varepsilon \hat{\varphi}(t, \varepsilon t),$$

$$\mu = \bar{\mu}(t, \varepsilon t) + \varepsilon \hat{\mu}(t, \varepsilon t).$$

Substituting this ansatz into (3) and (4), one obtains up to the terms of the order ε,

$$\partial_1 \bar{\varphi} + \varepsilon \partial_2 \bar{\varphi} + \varepsilon \partial_1 \hat{\varphi} = I_0 - \sin\left(\bar{\varphi} + \varepsilon \hat{\varphi}\right) + \bar{\mu} + \varepsilon \hat{\mu},$$

$$\partial_1 \bar{\mu} + \varepsilon \partial_2 \bar{\mu} + \varepsilon \partial_1 \hat{\mu} = \varepsilon \left(-\bar{\mu} - \varepsilon \hat{\mu} + \eta \left(1 - \sin\left(\bar{\varphi} + \varepsilon \hat{\varphi}\right)\right)\right),$$

where subscripts 1 and 2 refer to partial derivatives with respect to t and εt, respectively. Collecting the terms of order $\mathcal{O}(1)$, one finds

$$\partial_1 \bar{\varphi} = I_0 - \sin \bar{\varphi} + \bar{\mu}, \tag{A1}$$

$$\partial_1 \bar{\mu} = 0. \tag{A2}$$

Equation (A2) implies that $\bar{\mu} = \bar{\mu}(\varepsilon t)$ depends only on the slow time and acts as a parameter in (A1). For $\bar{\mu} > 1 - I_0$, Eq. (A1) has the oscillating solution $\bar{\varphi} = \varphi_{\bar{\mu}}(t)$ given by (13). Note that the parameters of this solution can depend on the slow time.

As a next step, we consider the terms of order ε,

$$\partial_2 \bar{\varphi} + \partial_1 \hat{\varphi} = -\hat{\varphi} \cos \bar{\varphi} + \hat{\mu}, \tag{A3}$$
$$\partial_2 \bar{\mu} + \partial_1 \hat{\mu} = -\bar{\mu} + \eta \left(1 - \sin \bar{\varphi}\right).$$

We rewrite Eq. (A3) as

$$\partial_2 \bar{\mu} + \bar{\mu} = -\partial_1 \hat{\mu} + \eta \left(1 - \sin \bar{\varphi}\right), \tag{A4}$$

where the left-hand side depends only on the slow time. Hence, the solvability condition for (A4) is the requirement that its right-hand side is independent on the fast time t, i.e.,

$$-\partial_1 \hat{\mu} + \eta \left(1 - \sin \bar{\varphi}\right) = u(T), \tag{A5}$$

with some function $u(T)$, where $T = \varepsilon t$ is the slow time. By integrating (A5) with respect to the fast time, we obtain

$$\hat{\mu}(t) = \hat{\mu}(0) + \eta \left(t - \int_0^t \sin \bar{\varphi} \, dt\right) - t u(T). \tag{A6}$$

The integral in (A6) can be computed using (A1),

$$\int_0^t \sin \bar{\varphi} dt = t I_0 + t \bar{\mu} - \bar{\varphi}(t) + \bar{\varphi}(0),$$

such that

$$\hat{\mu}(t) = \hat{\mu}(0) + t \left[\eta \left(1 - I_0 - \bar{\mu} + \frac{\bar{\varphi}(t) - \bar{\varphi}(0)}{t}\right) - u(T)\right].$$

Taking into account that

$$\frac{\bar{\varphi}(t) - \bar{\varphi}(0)}{t} = \Omega(\bar{\mu}) + \mathcal{O}\left(\frac{1}{t}\right),$$

we obtain the expression for $\hat{\mu}$,

$$\hat{\mu}(t) = \hat{\mu}(0) + t \left[\eta \left(1 - I_0 - \bar{\mu} + \Omega(\bar{\mu})\right) - u(T)\right] + \mathcal{O}(1),$$

where the linearly growing term must vanish for $\hat{\mu}(t)$ to be bounded. Setting such a secular term to zero (even without computing explicitly $\hat{\mu}$), we have

$$u(T) = \eta \left(1 - I_0 - \bar{\mu} + \Omega(\bar{\mu})\right)$$

and, hence, taking into account (A4) and (A5), the equation for the leading order approximation of the slow variable reads

$$\partial_2 \bar{\mu} + \bar{\mu} = \eta \left(1 - I_0 - \bar{\mu} + \Omega(\bar{\mu})\right).$$

Since $\bar{\mu}$ is the function of the slow time only, we have $\partial_2 \bar{\mu} = \bar{\mu}'$, which results in the required averaged Eq. (14).

APPENDIX B: EXPLICIT SOLUTION OF THE STATIONARY FOKKER–PLANCK EQUATION

Here, we present the analytic solution of the stationary Fokker–Planck Eqs. (24) and (25). By integrating Eq. (24) once, one obtains

$$\frac{D}{2} \partial_\varphi \rho - \left(I_0 + \mu - \sin \varphi\right) \rho = C, \tag{B1}$$

with a constant C to be determined. Solving (B1), and taking into account the normalization (25) and the boundary condition $\rho(0) = \rho(2\pi)$, we arrive at

$$\rho(\varphi; \mu, D) = \frac{1}{g_\Lambda} \Lambda(\varphi),$$

where

$$\Lambda(\varphi) = \int_0^{2\pi} \frac{\Psi(\varphi)}{\Psi(\varphi + \xi)} d\xi,$$

$$g_\Lambda = \int_0^{2\pi} \Lambda(\varphi) d\xi,$$

$$\Psi(\varphi) = \exp\left\{\frac{2}{D} \left[(I_0 + \mu)\varphi + \cos\varphi - 1\right]\right\}.$$

DATA AVAILABILITY

The data that support the findings of this study are available from the corresponding author upon reasonable request.

REFERENCES

[1] E. M. Izhikevich, *Dynamical Systems in Neuroscience: The Geometry of Excitability and Bursting* (The MIT Press, 2007), ISBN: 9780262090438.

[2] W. Gerstner, W. M. Kistler, R. Naud, and L. Paninski, *Neuronal Dynamics: From Single Neurons to Networks and Models of Cognition* (Cambridge University Press, 2014), ISBN: 9781107447615.

[3] L. F. Abbott and P. Dayan, *Theoretical Neuroscience* (The MIT Press, 2005).

[4] C. Clopath, L. Büsing, E. Vasilaki, and W. Gerstner, Nat. Neurosci. **13**, 344 (2010).

[5] O. Popovych, S. Yanchuk, and P. A. P. Tass, Sci. Rep. **3**, 2926 (2013).

[6] R. Lang and K. Kobayashi, IEEE J. Quantum Electron. **16**, 347 (1980).

[7] K. Lüdge, *Nonlinear Laser Dynamics* (Wiley-VCH Verlag GmbH & Co. KGaA, Weinheim, 2011), ISBN: 9783527639823.

[8] M. C. Soriano, J. García-Ojalvo, C. R. Mirasso, and I. Fischer, Rev. Mod. Phys. **85**, 421 (2013).

[9] M. Krupa, B. Sandstede, and P. Szmolyan, J. Differ. Equ. **133**, 49 (1997).

[10] M. Lichtner, M. Wolfrum, and S. Yanchuk, SIAM J. Math. Anal. **43**, 788 (2011).

[11] M. Desroches, J. Guckenheimer, B. Krauskopf, C. Kuehn, H. M. Osinga, and M. Wechselberger, SIAM Rev. **54**, 211 (2012).

[12] C. Kuehn, *Multiple Time Scale Dynamics* (Springer-Verlag GmbH, 2015), Vol. 191, ISBN: 978-3-319-12315-8.

[13] H. Jardon-Kojakhmetov and C. Kuehn, arxiv.org/abs/1901.01402 (2019).

[14] H. Haken, *Advanced Synergetics* (Springer, Berlin, 1985).

[15] B. Lindner, J. García-Ojalvo, A. Neiman, and L. Schimansky-Geier, Phys. Rep. **392**, 321 (2004).

[16] A. Destexhe and M. Rudolph-Lilith, *Neuronal Noise* (Springer, New York, 2012).

[17] E. Forgoston and R. O. Moore, SIAM Rev. **60**, 969 (2018).

[18] J. D. Murray, *Mathematical Biology*, Biomathematics Vol. 19 (Springer, New York, 1989), ISBN: 0-387-19460-6 (New York), 3-540-19460-6 (Berlin).

[19] A. T. Winfree, *The Geometry of Biological Time* (Springer, 2001), Vol. 12, ISBN: 978-1-4419-3196-2

[20] A. S. Pikovsky and J. Kurths, Phys. Rev. Lett. **78**, 775 (1997).

[21] V.-C. Oriol, M. Ronny, R. Sten, and L. Schimansky-Geier, Phys. Rev. E **83**, 036209 (2011).

[22] G. B. Ermentrout and D. Kleinfeld, Neuron **29**, 33 (2001).

[23] L. Lücken, D. P. Rosin, V. M. Worlitzer, and S. Yanchuk, Chaos **27**, 13114 (2017).

[24] I. Franović, O. E. Omel'chenko, and M. Wolfrum, Chaos **28**, 071105 (2018).

[25] I. Bačić, S. Yanchuk, M. Wolfrum, and I. Franović, EPJ ST **227**, 1077 (2018).

[26] I. Franović, K. Todorović, M. Perc, N. Vasović, and N. Burić, Phys. Rev. E **92**, 062911 (2015).

[27] I. Franović, M. Perc, K. Todorović, S. Kostić, and N. Burić, Phys. Rev. E **92**, 062912 (2015).

[28] S. Yanchuk, S. Ruschel, J. Sieber, and M. Wolfrum, Phys. Rev. Lett. **123**, 053901 (2019).

[29] E. M. Izhikevich, IEEE Trans. Neural Netw. **15**, 1063 (2004).

[30] S. H. Strogatz, *Nonlinear Dynamics and Chaos: With Applications to Physics, Biology, Chemistry, and Engineering* (Addison-Wesley, 1994).

[31] A. Shilnikov and M. Kolomiets, Int. J. Bifurc. Chaos **18**, 2141 (2008).

[32] G. Pavliotis and A. Stuart, *Multiscale Methods: Averaging and Homogenization* (Springer, Berlin, 2008).

[33] M. Galtier and G. Wainrib, Phys. Rev. E **2**, 13 (2012).

[34] L. Lücken, O. V. Popovych, P. A. Tass, and S. Yanchuk, Phys. Rev. E **93**, 32210 (2016).

[35] A. I. Neishtadt, J. Appl. Math. Mech **48**, 133 (1984).

[36] J. Guckenheimer and P. Holmes, *Nonlinear Oscillations, Dynamical Systems and Bifurcations of Vector Fields* (Springer-Verlag, New York, 1983).

[37] E. J. Doedel, R. C. Paffenroth, A. R. Champneys, T. F. Fairgrieve, Y. A. Kuznetsov, B. Sandstede, and X. Wang, *AUTO-07p: Continuation and Bifurcation Software for Ordinary Differential Equations* (Concordia University, Canada, 2007).

[38] B. Lindner and L. Schimansky-Geier, Phys. Rev. E **60**, 7270 (1999).

[39] V. A. Makarov, V. I. Nekorkin, and M. G. Velarde, Phys. Rev. Lett. **86**, 3431 (2001).

[40] R. Aust, P. Hövel, J. Hizanidis, and E. Schöll, Eur. Phys. J. Spec. Top. **187**, 77 (2010).

[41] N. Kouvaris, L. Schimansky-Geier, and E. Schöll, Eur. Phys. J. Spec. Top. **191**, 29 (2010).

[42] N. B. Janson, A. G. Balanov, and E. Schöll, Phys. Rev. Lett. **93**, 010601 (2004).

[43] P. H. Dannenberg, J. C. Neu, and S. W. Teitsworth, Phys. Rev. Lett. **113**, 020601 (2014).

Inverse stochastic resonance in a system of excitable active rotators with adaptive coupling

Iva Bačić[1], Vladimir Klinshov[2], Vladimir Nekorkin[2], Matjaž Perc[3] and Igor Franović[1(a)]

[1] *Scientific Computing Laboratory, Center for the Study of Complex Systems, Institute of Physics Belgrade,
University of Belgrade - Pregrevica 118, 11080 Belgrade, Serbia*
[2] *Institute of Applied Physics of the Russian Academy of Sciences - 46 Ulyanov Street,
603950 Nizhny Novgorod, Russia*
[3] *Faculty of Natural Sciences and Mathematics, University of Maribor - Koroška cesta 160,
SI-2000 Maribor, Slovenia*

Abstract – Inverse stochastic resonance is a phenomenon where an oscillating system influenced by noise exhibits a minimal oscillation frequency at an intermediate noise level. We demonstrate a novel generic scenario for such an effect in a multi-timescale system, considering an example of emergent oscillations in two adaptively coupled active rotators with excitable local dynamics. The impact of plasticity turns out to be twofold. First, at the level of multiscale dynamics, one finds a range of intermediate adaptivity rates that give rise to multistability between the limit cycle attractors and the stable equilibria, a condition necessary for the onset of the effect. Second, applying the fast-slow analysis, we show that the plasticity also plays a facilitatory role on a more subtle level, guiding the fast flow dynamics to parameter domains where the stable equilibria become focuses rather than nodes, which effectively enhances the influence of noise. The described scenario persists for different plasticity rules, underlying its robustness in the light of potential applications to neuroscience and other types of cell dynamics.

Introduction. – Noise in coupled excitable or bistable systems may induce two types of generic effects [1]. On the one hand, it can modify the deterministic behavior by acting non-uniformly on different states of the system, thus amplifying or suppressing some of its features. On the other hand, noise may give rise to completely novel forms of behavior, typically based on crossing the thresholds or separatrices, or involving enhanced stability of deterministically unstable structures. In neuronal systems, the constructive role of noise at different stages of information processing, referred to as "stochastic facilitation" [2,3], mainly comprises resonant phenomena. A classical example is the stochastic resonance [4], which allows for the detection of weak subthreshold periodic signals. A more recent development concerns the effect of inverse stochastic resonance (ISR) [3,5–12], where noise selectively reduces the spiking frequency of neuronal oscillators, converting the tonic firing into intermittent bursting-like activity or a short-lived transient followed

by a long period of quiescence. The name of the effect should be taken *cum grano salis*, because in contrast to stochastic resonance, it involves no additional external signal: one rather observes a non-monotonous dependence of the spiking rate on noise variance, whereby the oscillation frequency becomes minimal at a preferred noise level. Such an inhibitory effect of noise has recently been shown for cerebellar Purkinje cells [11], having explicitly demonstrated how the lifetimes of the spiking ("up") and the silent ("down") states [13–15] are affected by the noise variance. ISR has been indicated to play important functional roles in neuronal systems, including the reduction of spiking frequency in the absence of neuromodulators, suppression of pathologically long short-term memories, triggering of on-off tonic spiking activity and even optimization of information transfer along the signal propagation pathways [3,7,9,11].

So far, theoretical studies on ISR have mostly concerned the scenario where a single neuron exhibits bistable deterministic dynamics, featuring coexistence between a limit cycle and a stable equilibrium. Such bistability is

---
[(a)]E-mail: franovic@ipb.ac.rs

typical for Type-II neurons below the subcritical Hopf bifurcation, *e.g.*, classical Hodgkin-Huxley and Morris-Lecar models [3,6–8]. There, applying noise induces switching between the metastable states, but at an intermediate noise level, one surprisingly finds a strong asymmetry of the associated switching rates, which makes the periods spent in the vicinity of equilibrium much longer than the periods of spiking activity.

An important open problem concerns conditions giving rise to ISR in coupled excitable systems, where noise influences the emergent oscillations. Here we address in detail this issue, as it may be crucial to understanding the prevalence of the effect in neural networks, whose activity depends on the interplay of excitability, coupling properties and noise. Synaptic dynamics typically involves the plasticity feature, which makes self-organization in neuronal systems a multi-timescale process: the short-term spiking activity unfolds on a quasi-static coupling configuration, while the slow adjustment of coupling weights depends on the time-averaged evolution of units.

Motivated by the findings in neuroscience, we focus on the onset of ISR in a simplified, yet paradigmatic system of two adaptively coupled stochastic active rotators with excitable local dynamics. Active rotators are canonical for Type-I excitability and may be seen as equivalent to the theta-neuron model. Adaptivity is introduced in a way that allows continuous interpolation between a spectrum of plasticity rules, including Hebbian learning and spike-time-dependent plasticity (STDP) [16–18].

We demonstrate a generic scenario for the plasticity-induced ISR, where the system's multiscale structure, defined by the adaptivity rate, plays a crucial role. On a basic level, plasticity gives rise to multistable behavior involving coexisting stationary and oscillatory regimes. An additional subtlety, which we show by the fast-slow analysis, is that the plasticity promotes the resonant effect by guiding the fast flow toward the parameter region where the stable fixed points are focuses rather than nodes.

The paper is organized as follows. In the next section the details of the model and the numerical bifurcation analysis of the deterministic dynamics are presented. The third section contains the results on the ISR effect and the supporting conditions. In the fourth section the fast-slow analysis is applied to explain the mechanism by which plasticity enhances the system's non-linear response to noise. Apart from providing a brief summary, in the last section we also discuss the prevalence of the observed effect.

Model and bifurcation analysis of deterministic dynamics. – Our model involves two stochastic active rotators interacting by adaptive couplings [19–22],

$$
\begin{aligned}
\dot{\varphi}_1 &= I_0 - \sin \varphi_1 + \kappa_1 \sin(\varphi_2 - \varphi_1) + \sqrt{D}\xi_1(t), \\
\dot{\varphi}_2 &= I_0 - \sin \varphi_2 + \kappa_2 \sin(\varphi_1 - \varphi_2) + \sqrt{D}\xi_2(t), \\
\dot{\kappa}_1 &= \epsilon(-\kappa_1 + \sin(\varphi_2 - \varphi_1 + \beta)), \\
\dot{\kappa}_2 &= \epsilon(-\kappa_2 + \sin(\varphi_1 - \varphi_2 + \beta)),
\end{aligned}
\tag{1}
$$

where the phases $\{\varphi_1, \varphi_2\} \in S^1$, while the coupling weights $\{\kappa_1, \kappa_2\}$ are real variables.

The excitability parameters I_0, which one may interpret as external bias currents in the context of neuroscience, are assumed to be identical for both units. For such a setup, the deterministic version of (1) possesses a Z_2 symmetry, being invariant to the exchange of units' indices. The uncoupled units undergo a SNIPER bifurcation at $I_0 = 1$, with the values $I_0 < 1\,(I_0 > 1)$ corresponding to the excitable (oscillatory) regime. We consider the case of excitable local dynamics, keeping $I_0 = 0.95$ fixed throughout the paper, such that the oscillations may emerge only due to the coupling terms and/or noise. The scale separation between the fast dynamics of the phases and the slow dynamics of adaptation is adjusted by the parameter $\epsilon \ll 1$. The fast variables are influenced by independent white noise of variance D such that $\xi_i(t)\xi_j(t') = \delta_{ij}\delta(t - t')$ for $i, j \in \{1, 2\}$. Conceptually, adding stochastic input to the fast variables embodies the action of synaptic noise in neuronal systems [23].

The modality of the plasticity rule is specified by the parameter β, whose role may be understood by invoking the qualitative analogy between the adaptation dynamics in classical neuronal systems and the systems of coupled phase oscillators. This issue has first been addressed in [24–26], and a deeper analysis of the correspondence between the phase-dependent plasticity rules and the STDP has been carried out in [19]. In particular, it has been shown that the plasticity dynamics for $\beta = 3\pi/2$, where the stationary weights between the oscillators with smaller/larger phase differences increase/decrease, qualitatively resembles the Hebbian learning rule [25,26]. Nevertheless, when $\beta = \pi$, the coupling weights encode a causal relationship between the spiking of oscillators by changing in the opposite directions, in analogy to an STDP-like plasticity rule. Our interest lies with the β interval interpolating between these two limiting cases.

Using bifurcation analysis of the deterministic dynamics of (1), we first show how the modality of the plasticity rule influences the number of stationary states, and then explain how the onset of oscillations depends on adaptivity rate. The bifurcation diagram in fig. 1 indicates that the number and the stability of fixed points of (1) change with β in such a way that the system may possess two, four or six fixed points. Due to invariance to Z_2 symmetry, one always finds pairs of solutions sharing the same stability features. We consider the plasticity rules described by $\beta \in (3.298, 4.495)$, cf. the shaded region in fig. 1, where the system has two stable fixed points lying off the synchronization manifold $\varphi_1 = \varphi_2$, as well as four unstable fixed points. The bifurcations occurring at the boundaries of the relevant β interval are as follows. At $\beta = 3.298$, the system undergoes a supercritical symmetry-breaking pitchfork bifurcation giving rise to a pair of stable fixed points off the synchronization manifold. For $\beta = 4.495$, this pair of stable fixed points collides with a pair of unstable fixed points off
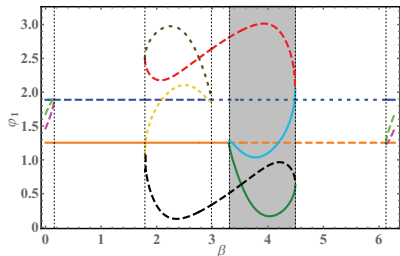
Fig. 1: (Color online) Bifurcation diagram for the fixed points of (1) with $D = 0$ under variation of β. Solid lines refer to stable fixed points, while dashed and dotted lines correspond to saddles of unstable dimension 1 and 2, respectively. Shading indicates the considered range of plasticity rules. The two fixed points independent on β belong to the synchronization manifold. The remaining parameters are $I_0 = 0.95, \epsilon = 0.05$.

Fig. 2: (Color online) Onset of oscillations in (1) for $D = 0$. (a) Variation σ_{κ_1} of the coupling weight κ_1 in the (β, ϵ)-plane. (b) Mean coupling weights $\langle \kappa_1 \rangle(\epsilon)$ and $\langle \kappa_2 \rangle(\epsilon)$ for oscillatory (thick lines) and stationary states (thin lines) at $\beta = 4.2$. (c) Variation $\sigma_{\kappa_1}(\epsilon)$ and $\sigma_{\kappa_2}(\epsilon)$, presented as in (b). Shading in (b) and (c) indicates the ϵ interval admitting the stable periodic solutions.

the synchronization manifold, getting annihilated in two symmetry- related inverse fold bifurcations. Note that the weight levels typical for the two stable stationary states support effective unidirectional interaction, in a sense that one unit exerts a much stronger impact on the dynamics of the other unit than vice versa. When illustrating the effect of ISR, we shall mainly refer to the case $\beta = 4.2$. For this β, the two stable focuses of (1) at $D = 0$ are given by $(\varphi_1, \varphi_2, \kappa_1, \kappa_2) = (1.177, 0.175, 0.032, -0.92)$ and $(\varphi_1, \varphi_2, \kappa_1, \kappa_2) = (0.175, 1.177, -0.92, 0.032)$. Within the considered β interval, the two stable fixed points of the coupled system exhibit excitable behavior, responding to external perturbation by generating either the successive spikes or synchronized spikes [21].

The onset of oscillations for the deterministic version of (1) relies on the interplay between the plasticity rule, controlled by β, and the adaptation rate, characterized by ϵ. In fig. 2(a) are shown the results of parameter sweep indicating the variation of κ_1 variable, $\sigma_{\kappa_1} = \max(\kappa_1(t)) - \min(\kappa_1(t))$, within the (β, ϵ) parameter plane. The sweep indicates the maximal stability region of the two emerging periodic solutions, related by the exchange symmetry of units indices. The data are obtained by numerical continuation starting from a stable periodic solution, such that the final state reached for the given parameter set is used as initial conditions of the system dynamics for incremented parameter values. One observes that for fixed β, there exists an interval of timescale separation ratios $\epsilon \in (\epsilon_{min}, \epsilon_{max})$ admitting oscillations, see fig. 2(b). Within the given ϵ range, the system exhibits multistability where periodic solutions coexist with the two symmetry-related stable stationary states. The lower threshold for oscillations, ϵ_{min}, reduces with β, whereas the upper boundary value, ϵ_{max}, is found to grow as β is enhanced. Note that the waveform of oscillations also changes as ϵ is increased under fixed β. In particular, for smaller ϵ, the waveforms corresponding to the two units are rather different. Nevertheless, around $\epsilon \approx 0.06$ the system undergoes a pitchfork bifurcation of limit cycles, such that
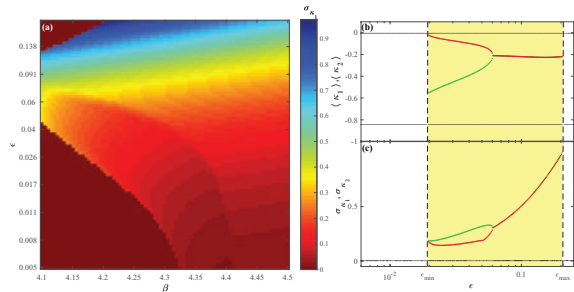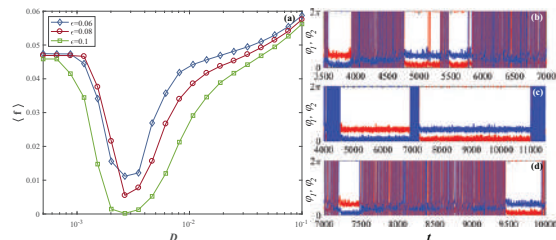

Fig. 3: (Color online) (a) Mean spiking rate $\langle f \rangle$ in terms of D for $\epsilon \in \{0.06, 0.08, 0.1\}$. The curves exhibit a characteristic minimum at an intermediate noise level. (b)–(d) Time traces $\varphi_1(t)$ and $\varphi_2(t)$ for noise levels below, at and above the resonant value. The remaining parameters are $I_0 = 0.95$, $\beta = 4.2, \epsilon = 0.06$.

the oscillatory solution gains the anti-phase space-time symmetry $\varphi_1(t) = \varphi_2(t + T/2), \kappa_1(t) = \kappa_2(t + T/2)$, where T denotes the oscillation period [21].

Numerical results on ISR. – Inverse stochastic resonance manifests itself as noise-mediated suppression of oscillations, whereby the frequency of noise-perturbed oscillations becomes minimal at a preferred noise level. For system (1), we find such an effect to occur generically for intermediate adaptivity rates, supporting multistability between the stationary and the oscillatory solutions, as described in the previous section. A family of curves describing the dependence of the oscillation frequency on noise variance $\langle f \rangle(D)$ for different ϵ values is shown in fig. 3. All the curves corresponding to $\epsilon \geq \epsilon_{min}(\beta)$ show a characteristic non-monotonous behavior, displaying a minimum at the optimal noise intensity. For weaker noise, the oscillation frequency remains close to the deterministic one, whereas for much stronger noise, the frequency increases above that of unperturbed oscillations. The displayed results are obtained by averaging over an ensemble of 1000 different stochastic realizations, having excluded the transient behavior, and having fixed a single set of initial conditions within the basin of attraction of the limit cycle attractor. Nevertheless, we have verified that the
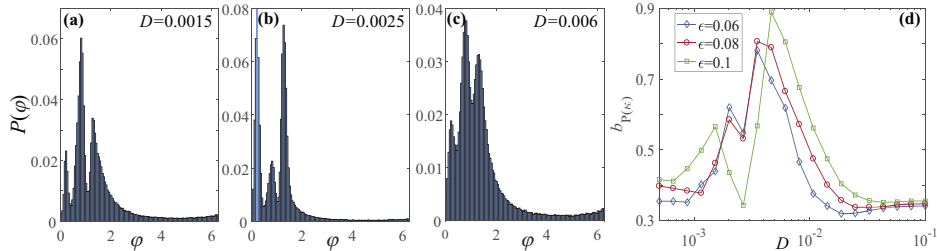
Fig. 4: (Color online) (a)–(c) Stationary distribution $P(\varphi_1)$ for the noise levels below, at and above the resonant value. System parameters are $I_0 = 0.95$, $\beta = 4.2$ and $\epsilon = 0.06$. From the three observable peaks, the middle one, prevalent in (a) and (c), refers to the metastable state associated to the oscillatory mode of (1) for $D = 0$. The two lateral peaks, dominant in (b), correspond to quasi-stationary states derived from the stable equilibria of the deterministic version of (1). (d) Bimodality coefficient for the stationary distribution of κ_1, $b_{P(\kappa_1)}$, as a function of D. The three curves refer to $\epsilon = 0.06$ (diamonds), $\epsilon = 0.08$ (circles) and $\epsilon = 0.1$ (squares).
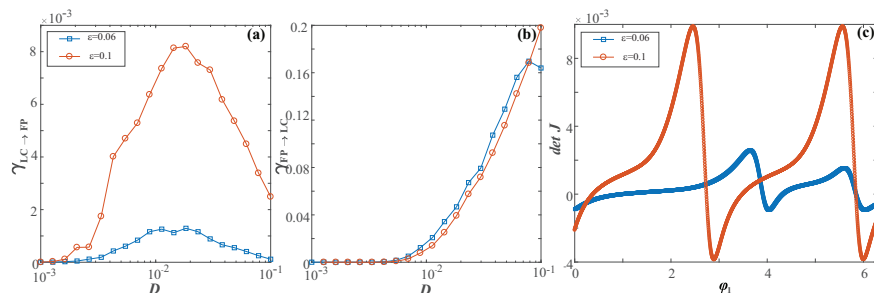
Fig. 5: (Color online) (a) and (b): transition rates from the stability basin of the limit cycle to the fixed point, $\gamma_{LC \to FP}(D)$ and vice versa, $\gamma_{FP \to LC}(D)$, numerically obtained for $\epsilon = 0.06$ (squares) and $\epsilon = 0.1$ (circles). The remaining parameters are $I_0 = 0.95, \beta = 4.2$. (c) Determinant of the Jacobian calculated along the limit cycle orbit as a function of the phase variable. The quantity provides an indication of the sensitivity of certain sections of the orbit to external perturbation. Blue and red colors correspond to $\epsilon = 0.06$ and $\epsilon = 0.1$, respectively.

qualitatively analogous results are obtained if for each realization of stochastic process one selects a set of random initial conditions lying within the stability basin of the periodic solution. The suppression effect of noise depends on the adaptivity rate, and is found to be more pronounced for faster adaptivity. Indeed, for smaller ϵ, $\varphi(t)$ series corresponding to the noise levels around the minimum of $\langle f \rangle(D)$ exhibit bursting-like behavior, whereas for larger ϵ, noise is capable of effectively quenching the oscillations, such that the minimal observed frequency approaches zero.

The core of the described effect concerns switching dynamics between the metastable states associated to coexisting attractors of the deterministic version of system (1). To illustrate this, in fig. 4 we have considered the stationary distributions of one of the phase variables, $P(\varphi)$, for the noise levels below, at and above the minimum of the $\langle f \rangle(D)$, having fixed the remaining parameters to $(\beta, \epsilon) = (4.2, 0.06)$. The distribution $P(\varphi)$ is characterized by two lateral peaks, reflecting the two symmetry-related quasi-stationary states, and the area around the central peak, corresponding to the oscillatory mode. For small noise $D = 0.0015$, see fig. 4(a), and very large noise $D = 0.006$, cf. fig. 4(c), the central peak of $P(\varphi)$ is expectedly prevalent compared to the two lateral peaks. Nevertheless, the switching dynamics for

$D = 0.0025$, the noise level about the minimum of $\langle f \rangle(D)$, is fundamentally different, and the corresponding distribution $P(\varphi)$ in fig. 4(b) shows that the system spends much more time in the quasi-stationary states than performing the oscillations. The onset of ISR in the dynamics of fast variables is accompanied by the increased bimodality of the stationary distribution of the couplings, see fig. 4(d).

In order to observe the non-monotonous response of the system's frequency to noise, the geometry of the phase space has to be asymmetrical with respect to the separatrix between the coexisting attractors in such a way that the limit cycle attractor lies much closer to the separatrix than the stationary states. Such structure of phase space gives rise to asymmetry in switching dynamics, whereby at the preferred noise level around the minimum of $\langle f \rangle(D)$, the transition rate from the stability basin of the limit cycle attractor to that of stationary states $\gamma_{LC \to FP}$ becomes much larger than the transition rate in the inverse direction, $\gamma_{FP \to LC}$. Figures 5(a) and (b) corroborate that the dependences $\gamma_{LC \to FP}(D)$ and $\gamma_{FP \to LC}(D)$ are qualitatively distinct: the former displays a maximum at the resonant noise level, whereas the latter just increases monotonously with noise. The fact that ISR is more pronounced for higher adaptivity rates is reflected in that the curve $\gamma_{LC \to FP}(D)$ for $\epsilon = 0.1$ lies substantially above that for $\epsilon = 0.06$, see fig. 5(a).

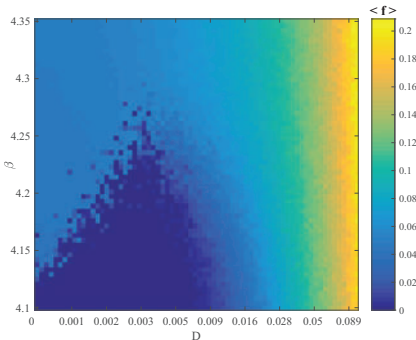Fig. 6: (Color online) Mean spiking rate $\langle f \rangle$ as a function of β and D for fixed $\epsilon = 0.05$. The results evince the robustness of the ISR effect with respect to different plasticity rules.

To understand why the interplay of adaptivity rate and noise yields a stronger resonant effect for larger ϵ, we have investigated the susceptibility of the limit cycle attractor to external perturbation. In particular, fig. 5(c) shows how the determinant of the Jacobian calculated along the limit cycle orbit change for $\epsilon = 0.06$ (blue line) and $\epsilon = 0.1$ (red line), respectively. For smaller ϵ, one may identify two particular points where the determinant of the Jacobian is the largest, *i.e.*, where the impact of external perturbation is felt the strongest. This implies that noise is most likely to drive the systems trajectory away from the limit cycle attractor around these two sections of the orbit, which should lie closest to the boundary to the stability basins of the stationary states. Such a physical picture is maintained for larger ϵ, but one should stress that the sensitivity of limit cycle attractor to external perturbation substantially increases along the entire orbit, cf. fig. 5(c). In other words, faster adaptivity enhances the impact of noise, contributing to a more pronounced ISR effect. This point is addressed from another perspective in the next section.

We also examine the robustness of ISR to different modalities of the plasticity rule specified by β. Figure 6 shows how the average oscillation frequency changes with β and D for fixed $\epsilon = 0.05$. The non-linear response to noise, conforming to a resonant effect with a minimum of oscillation frequency at an intermediate noise level, persists in a wide range of β, essentially interpolating between the Hebbian-like and the STDP-like adaptive dynamics.

Fast-slow analysis: role of plasticity in the resonant effect. – Though ISR is observed for intermediate ϵ, here we show that the fast-slow analysis may still be applied to demonstrate a peculiar feature of the mechanism behind the resonant effect. In particular, we find that the plasticity enhances the resonant effect by driving the fast flow dynamics toward the parameter domain where the stationary state is a focus rather than a node. It is well known that the response to noise in multi-timescale systems qualitatively depends on the character of stationary states. Indeed, by using the sample-paths approach and other advanced techniques, it has already been shown

that such systems may exhibit fundamentally different scaling regimes with respect to noise variance and the scale-separation ratio [27,28]. Moreover, the resonant effects may typically be expected in the case in which quasi-stationary states are focuses [27], essentially because the local dynamics around the stationary state then involves an eigenfrequency.

Within the standard fast-slow analysis, one may either consider the layer problem, defined on the fast timescale, or the reduced problem, concerning the slow timescale [29]. For the layer problem, the fast flow dynamics $\varphi_1(t; \kappa_1, \kappa_2), \varphi_2(t; \kappa_1, \kappa_2)$ is obtained by treating the slow variables κ_1 and κ_2 as system parameters, whereas in the case of the reduced problem, determining the dynamics of the slow flow $(\kappa_1(t), \kappa_2(t))$ involves time-averaging over the stable regimes of the fast flow of the layer problem. The fast flow can in principle exhibit several attractors, which means that multiple stable sheets of the slow flow may emerge from the averaged dynamics on the different attractors of the fast flow. Our key point concerns the dynamics of the slow flow, which requires us to first classify the attractors of the fast flow.

The fast flow dynamics is given by

$$
\begin{aligned}
\dot{\varphi}_1 &= I_0 - \sin\varphi_1 + \kappa_1 \sin(\varphi_2 - \varphi_1), \\
\dot{\varphi}_2 &= I_0 - \sin\varphi_2 + \kappa_2 \sin(\varphi_1 - \varphi_2),
\end{aligned}
\tag{2}
$$

where $\kappa_1, \kappa_2 \in [-1, 1]$ are considered as additional system parameters. One may formally obtain (2) by setting $\epsilon = 0$ in (1) with $D = 0$. We find that the fast flow is monostable for most of the (κ_1, κ_2) values, exhibiting either a stable equilibrium or a limit cycle attractor, see fig. 7(a). In general, the fast flow admits either two or four fixed points, and a more detailed physical picture, including the associated bifurcations, is presented in [21]. The stability region of the oscillatory regime, outlined by the red color, has been calculated by numerical continuation starting from a stable periodic solution. Bistability between a stable fixed point and a limit cycle is observed only in a small area near the main diagonal $\kappa_1 = \kappa_2$. Within the region featuring oscillatory regime, each periodic solution obtained for (κ_1, κ_2) above the main diagonal has a Z_2 symmetry-related counterpart below the diagonal. Typically, the periodic solutions emanate from SNIPER bifurcations, which make up two branches where either κ_1 or κ_2 are almost constant and close to zero.

Using the results from the analysis of the layer problem, our goal is to determine the vector fields corresponding to the stable sheets of the slow flow. We have numerically obtained the dynamics of the slow flow by a standard two-step approach [19,30]. First, for fixed values (κ_1, κ_2), we have determined the time-averaged dynamics of the fast flow (2), $\langle \varphi_2 - \varphi_1 \rangle_t = h(\kappa_1, \kappa_2)$, whereby the averaging $\langle \cdot \rangle_t$ is carried out over a sufficiently long time interval, having excluded the transient behavior. As already indicated, such an average depends on the attractor of the fast flow for the given (κ_1, κ_2). If the fast flow possesses
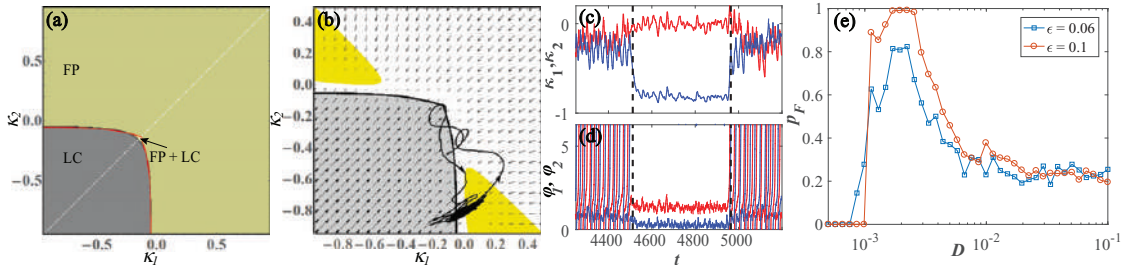
Fig. 7: (Color online) (a) Attractors of the fast flow (2) in terms of κ_1 and κ_2, now treated as free parameters. The fast flow is typically monostable, admitting either a stable fixed point (FP) or a stable limit cycle (LC), apart from a small region of bistability (FP+LC) around the main diagonal. (b) Vector field of the slow flow (3) determined by considering only the stable regimes of the fast flow for $\beta = 4.2, I_0 = 0.95$. Within the yellow-highlighted regions, the stable fixed point of the fast flow is a focus rather than the node. The displayed orbit $(\kappa_1(t), \kappa_2(t))$ corresponds to a switching episode from the oscillatory state to the quasi-stationary state and back (evolution direction indicated by arrows). Panels (c) and (d) show the time traces of phases and couplings during the switching episode. (e) Conditional probability $p_F(D)$ for $\epsilon = 0.06$ (blue squares) and $\epsilon = 0.1$ (red circles).

a stable fixed point, then $\langle \varphi_2 - \varphi_1 \rangle_t = \varphi_2^* - \varphi_1^*$, which corresponds to the slow critical manifold of the system. For (κ_1, κ_2) where the attractor of the fast flow is a periodic solution, $\langle \varphi_2 - \varphi_1 \rangle_t$ amounts to the time average over the period. Averaging over a periodic attractor of the fast flow is a standard approximation [30], quite natural when describing the influence of oscillations in the fast flow to the dynamics of the slow flow.

As the second step, the obtained time averages are substituted into the coupling dynamics

$$\begin{aligned}
\dot{\kappa}_1 &= \epsilon[-\kappa_1 + \sin(h(\kappa_1, \kappa_2) + \beta)], \\
\dot{\kappa}_2 &= \epsilon[-\kappa_2 + \sin(-h(\kappa_1, \kappa_2) + \beta)].
\end{aligned} \tag{3}$$

The system (3) allows one to determine the vector fields on the stable sheets of the slow flow, which correspond to the attractors of the fast flow. In fig. 7(b), the vector fields associated to each of the attractors (fixed point or limit cycle) are presented within its respective (κ_1, κ_2) stability region. In the small region of the (κ_1, κ_2)-plane supporting coexisting stable solutions of the fast flow, the corresponding vector field of the slow flow is given on multiple overlapping sheets, since the value of the average $f(\kappa_1, \kappa_2)$ depends on the initial conditions.

Within the above framework, one is able to explain a subtle influence of adaptivity on the mechanism behind the ISR. To this end, in fig. 7(b) we have projected a typical example of the $(\kappa_1(t), \kappa_2(t))$ trajectory of the full system (1) corresponding to a switching episode between the metastable states associated to a limit cycle attractor and a stable equilibrium of the deterministic system, see the time traces in figs. 7(c), (d). One observes that for the oscillating regime, the coupling dynamics always remains close to the SNIPER bifurcation of the fast flow, cf. fig. 7(a), which makes the oscillations quite susceptible to noise. Recall that the fast flow is typically monostable. Thus, switching events in the full system are naturally associated to the fast flow undergoing the SNIPER bifurcation: either a direct one, leading from the oscillatory to the stationary regime, or the inverse one, unfolding in the

opposite direction. For (κ_1, κ_2) values immediately after the SNIPER bifurcation toward the quiescent state, the stable equilibrium of the fast flow is a node. Nevertheless, for the noise levels where the effect of ISR is most pronounced, we find that the coupling dynamics guides the system into the region where the equilibrium is a stable focus rather than a node, see the yellow highlighted region in fig. 7(b). We have verified that this feature is a hallmark of the resonant effect by numerically calculating the conditional probability p_F that the events of crossing the SNIPER bifurcation are followed by the system's orbit visiting the (κ_1, κ_2) region where the stable equilibrium is a focus. The $p_F(D)$ dependences for two characteristic ϵ values at fixed $\beta = 4.2$ are plotted in fig. 7(e). One learns that $p_F(D)$ has a maximum for the resonant noise levels, where the corresponding curve $f(D)$ displays a minimum. In other words, the fact that the coupling dynamics drives the fast flow to the focus-associated regions of the (κ_1, κ_2)-plane results in trapping the phase variables for a longer time in the quasi-stationary (quiescent) state. Small noise below the resonant values is insufficient to drive the system to this region, whereas for too large a noise, the stochastic fluctuations completely take over, washing out the quasi-stationary regime. Note that for the faster adaptivity rate, the facilitatory role of coupling becomes more pronounced, as evinced by the fact that the curve $p_F(D)$ for $\epsilon = 0.1$ lies above the one for $\epsilon = 0.06$.

Discussion. – In the present paper, we have demonstrated a novel generic scenario for the onset of ISR, which involves an interplay between the local excitability feature and the adaptive dynamics of the couplings. For the example of two active rotators with coupling plasticity, we have shown that the spiking frequency corresponding to emergent oscillations varies non-monotonously with noise, displaying a minimum at a preferred noise level. Though the model *per se* is simplified, the underlying paradigm is relevant for combining the two core features of typical neuronal systems. The effect derives from the multi-timescale structure of the system, whereby the scale

separation between the local and the weight dynamics is tuned via adaptivity rate. Within a range of intermediate adaptivity rates, the deterministic dynamics of the full system exhibits multistability between the limit cycle attractors and the stable equilibria, each appearing in pairs due to the systems invariance to Z_2 symmetry. Applying the standard fast-slow analysis, we have shown that the resonant effect with noise is in fact plasticity-enhanced: plasticity promotes the impact of noise by guiding the fast flow toward the parameter domain where the stable equilibria become focuses instead of nodes. This mechanism increases the trapping efficiency by which the noise is able to deviate the systems trajectory from the metastable oscillatory states to the non-spiking regime. For faster adaptivity, the resonant effect is found to be more pronounced in a sense that the frequency dependence on noise shows deeper minima. Our scenario has proven to persist in a wide range of plasticity rules, interpolating between the cases analogous to Hebbian learning and STDP.

In earlier studies, observation of ISR has mostly been confined to Type-II neurons with intrinsic bistable dynamics, as in case of Hodgkin-Huxley or Morris-Lecar neurons near the subcritical Hopf bifurcation [3,6–9]. Even in case of networks, the macroscopic ISR effect has been linked to dynamical features of single units, only being modulated by the details of synaptic dynamics and the network topology [10]. In contrast to that, our results show that ISR may not rely on bistability of local dynamics, but may rather emerge due to the facilitatory role of coupling, here reflected in the interplay of multiscale dynamics and plasticity. Another distinction from most of the previous studies is that our scenario concerns Type-I units. For this class of systems, it is known that the dependence of the oscillating frequency of a single unit with noise is just monotonous [3,12], so that the resonant effect can only be observed in case of coupled units. So far, the latter case has been analyzed only once [5], but the underlying scenario is different from ours insofar as it involves static, rather than the adaptive couplings, and the effect *per se* is confined to a narrow region of the parameter space.

Quite recently, the onset of ISR has been reported for a single Fitzhugh-Nagumo oscillator [12], which is the first observation of the effect for Type-II neuron model in the vicinity of the supercritical Hopf bifurcation. Similar to the scenario we elaborated, ISR there also derives from the multiscale structure of the system. However, the actual mechanism behind the effect is associated to phase-sensitive (non-uniform) excitability of a limit cycle orbit conforming to relaxation oscillations [12]. These findings and the results here suggest that ISR may indeed provide a generic means of controlling and optimizing the firing rate in multi-timescale systems, which can be applied to neuronal activity, calcium signaling and other types of cell dynamics.

$$* * *$$

REFERENCES

[1] LINDNER B., GARCIA-OJALVO J., NEIMAN A. and SCHIMANSKY-GEIER L., *Phys. Rep.*, **392** (2004) 321.
[2] MCDONNELL M. D. and WARD L. M., *Nat. Rev. Neurosci.*, **12** (2011) 415.
[3] SCHMERL B. A. and MCDONNELL M. D., *Phys. Rev. E*, **88** (2013) 052722.
[4] GAMMAITONI L., HÄNGGI P., JUNG P. and MARCHESONI F., *Rev. Mod. Phys.*, **70** (1998) 223.
[5] GUTKIN B. S., JOST J. and TUCKWELL H. C., *EPL*, **81** (2008) 20005.
[6] TUCKWELL H. C., JOST J. and GUTKIN B. S., *Phys. Rev. E*, **80** (2009) 031907.
[7] UZUNTARLA M., CRESSMAN J. R., OZER M. and BARRETO E., *Phys. Rev. E*, **88** (2013) 042712.
[8] UZUNTARLA M., *Phys. Lett. A*, **377** (2013) 2585.
[9] UZUNTARLA M., TORRES J. J., SO P., OZER M. and BARRETO E., *Phys. Rev. E*, **95** (2017) 012404.
[10] UZUNTARLA M., BARRETO E. and TORRES J. J., *PLoS Comput. Biol.*, **13** (2017) e1005646.
[11] BUCHIN A., RIEUBLAND S., HÄUSSER M., GUTKIN B. S. and ROTH A., *PLoS Comput. Biol.*, **12** (2016) e1005000.
[12] FRANOVIĆ I., OMEL'CHENKO O. E. and WOLFRUM M., *Chaos*, **28** (2018) 071105.
[13] HAHN T. T. G., MCFARLAND J. M., BERBERICH S., SAKMANN B. and MEHTA M. R., *Nat. Neurosci.*, **15** (2012) 1531.
[14] FRANOVIĆ I. and KLINSHOV V., *Chaos*, **28** (2018) 023111.
[15] FRANOVIĆ I. and KLINSHOV V., *EPL*, **116** (2016) 48002.
[16] SONG S., MILLER K. D. and ABBOTT L. F., *Nat. Neurosci.*, **3** (2000) 919.
[17] FROEMKE R. C. and DAN Y., *Nature*, **416** (2002) 433.
[18] WANG H.-X., GERKIN R. C., NAUEN D. W. and BI G.-Q., *Nat. Neurosci.*, **8** (2005) 187.
[19] LÜCKEN L., POPOVYCH O. V., TASS P. A. and YANCHUK S., *Phys. Rev. E*, **93** (2016) 032210.
[20] KASATKIN D. V. and NEKORKIN V. I., *Radiophys. Quantum Electron.*, **58** (2016) 877.
[21] BAČIĆ I., YANCHUK S., WOLFRUM M. and FRANOVIĆ I., *Eur. Phys. J. ST*, **227** (2018) 1077.
[22] KASATKIN D., YANCHUK S., SCHÖLL E. and NEKORKIN V., *Phys. Rev. E*, **96** (2017) 062211.
[23] DESTEXHE A. and RUDOLPH-LILITH M., *Neuronal Noise* (Springer, New York) 2012.
[24] MAISTRENKO Y. L., LYSYANSKY B., HAUPTMANN C., BURYLKO O. and TASS P., *Phys. Rev. E*, **75** (2007) 066207.
[25] AOKI T. and AOYAGI T., *Phys. Rev. Lett.*, **102** (2009) 034101.
[26] AOKI T. and AOYAGI T., *Phys. Rev. E*, **84** (2011) 066109.
[27] BERGLUND N. and GENTZ B., *Noise-Induced Phenomena in Slow-Fast Dynamical Systems* (Springer, Berlin) 2006.
[28] LAING C. and LORD G. J. (Editors), *Stochastic Methods in Neuroscience* (Oxford University Press, London) 2009.
[29] KUEHN C., *Multiple Time Scale Dynamics* (Springer International Publishing, Switzerland) 2015.
[30] SHILNIKOV A., *Int. J. Bifurcat. Chaos*, **18** (2008) 2141.

Mean-field dynamics of a population of stochastic map neurons

Igor Franović,[1,*] Oleg V. Maslennikov,[2,†] Iva Bačić,[1] and Vladimir I. Nekorkin[2]

[1]*Scientific Computing Laboratory, Center for the Study of Complex Systems, Institute of Physics Belgrade,*
University of Belgrade, Pregrevica 118, 11080 Belgrade, Serbia
[2]*Institute of Applied Physics of the Russian Academy of Sciences, 46 Ulyanov Street, 603950 Nizhny Novgorod, Russia*

We analyze the emergent regimes and the stimulus-response relationship of a population of noisy map neurons by means of a mean-field model, derived within the framework of cumulant approach complemented by the Gaussian closure hypothesis. It is demonstrated that the mean-field model can qualitatively account for stability and bifurcations of the exact system, capturing all the generic forms of collective behavior, including macroscopic excitability, subthreshold oscillations, periodic or chaotic spiking, and chaotic bursting dynamics. Apart from qualitative analogies, we find a substantial quantitative agreement between the exact and the approximate system, as reflected in matching of the parameter domains admitting the different dynamical regimes, as well as the characteristic properties of the associated time series. The effective model is further shown to reproduce with sufficient accuracy the phase response curves of the exact system and the assembly's response to external stimulation of finite amplitude and duration.

I. INTRODUCTION

Gaining a comprehensive understanding of the emergent dynamics of neuronal populations and their interactions is a topical issue in neuroscience [1,2]. The acquired neurobiological data corroborate that the operational tasks at different levels of the brain's multiscale hierarchical organization are distributed across anatomically segregated, but functionally integrated, moduli [3–5]. Within theoretical studies, substantial attention have received the phenomena unfolding on the intermediate (mesoscopic) scale [6], whereby the considered models are supposed to reflect the behavior of assemblies comprising microcolumns or cortical columns [7–9]. The mesoscopic dynamics typically consists of oscillations of different frequencies and amplitudes, which may be interspersed by episodes of chaotic or pseudo-chaotic irregular behavior [7]. This can further be modulated via interplay with activity generated at other scales, primarily the stochastic fluctuations from the microscopic level and the slow rhythms derived from the macroscopic structures.

Conceptually, the given phenomena are often addressed by invoking a paradigm where each population exhibiting a collective mode is regarded as a large-scale oscillator, such that the assembly's response to external stimuli, noise, or collective oscillations from afferent populations may be examined using the methods of nonlinear dynamics [10]. The ensuing models of collective motion are developed using different forms of mean-field (MF) approximation, which mainly apply the bottom-up strategy [11] to build reduced and analytically tractable description of population behavior starting from the high-dimensional system of (stochastic) differential equations for the local neuron dynamics. An additional point that makes the mesoscopic circuits particularly suitable for the MF treatment is that the often used assumption on assembly homogeneity approximately holds at this scale

[12]. In terms of fashion by which the population dynamics is statistically characterized, one may classify the effective systems into neural mass or probability density models [8,13]. The former rely on the large coherence approximation and yield the mean-rate dynamics [14], whereas the latter involve the diffusion approximation, providing for the evolution of the assembly-averaged dynamics and the corresponding variance [15,16]. The MF approach and its generalization to spatially extended systems have become a standard tool for analyzing diverse problems in neuroscience and other fields [17–23].

Nevertheless, one should emphasize that the MF analysis has so far exclusively been applied to the class of continuous-time systems, while the effective models for assemblies of coupled maps have been lacking. In particular, the collective motion of spiking or bursting neurons influenced by noise has been extensively studied using different models of coupled discrete systems, such as Rulkov [24–31] or Izhikevich neuron maps [32,33], but this has not been complemented by an appropriate MF theory. The latter has likely been the consequence of inability to implement the Fokker-Planck formalism to discrete-time systems. In the present paper, we obtain for the first time the MF theory for a population of coupled stochastic neuronal maps. The derivation relies on Gaussian approximation, which is introduced within the framework of Gaussian closure hypothesis [34–40].

We apply the MF approach to systematically analyze the emergent behavior and the stimulus-response relationship of a population of stochastic map neurons, where the local dynamics can exhibit a variety of regimes, including excitability, subthreshold oscillations, regular and chaotic spiking or bursting, as well as mixed spiking-bursting oscillations [41–44]. The particular set of issues we address consists in establishing whether and how the MF model can be used to (i) qualitatively analyze the network stability and bifurcations of the exact system associated to emergence of generic collective regimes; (ii) provide adequate quantitative predictions in terms of bifurcation thresholds, and the average interspike intervals or bursting cycles of the exact system; as well as (iii) accurately anticipate the population's response
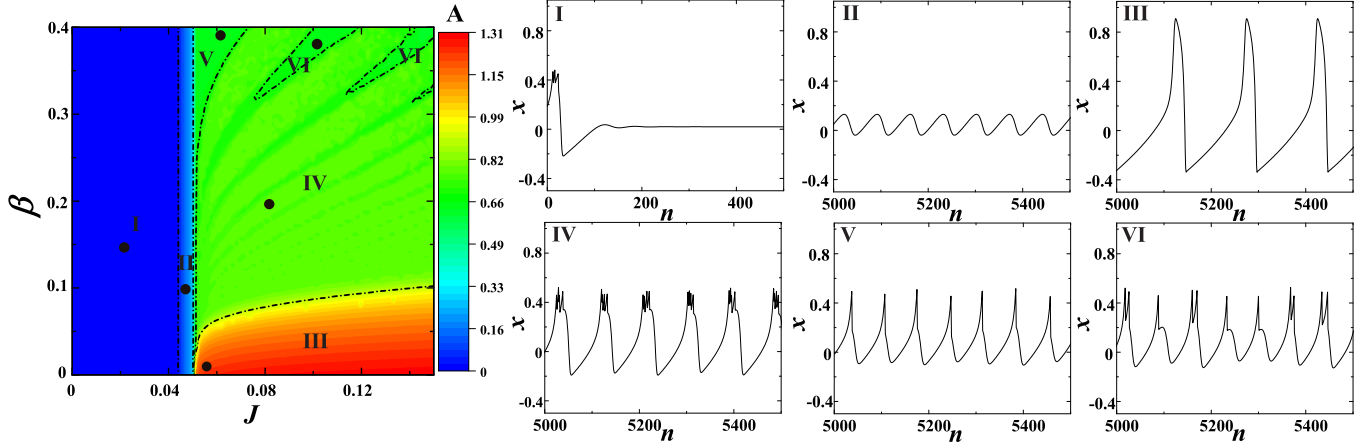
FIG. 1. Dynamical regimes exhibited by model (1). The heat map refers to variation of the amplitude of oscillations A of the x time series in the J-β plane. The wave forms shown in subfigures I–VI illustrate the different forms of neuron's behavior, including excitability (I), subthreshold oscillations (II), regular spiking (III), chaotic bursting (IV), chaotic spiking (V), as well as the mixed spike-burst activity (VI). The dots in the heat map indicate the particular (J,β) values where the representative wave forms are obtained.

to different forms of external stimuli. Within this context, it will be examined whether the effective model is capable of reproducing the properties of noise-activated, noise-induced, and noise-perturbed modes of collective behavior.

The paper is organized as follows. In Sec. II, we make an overview of the local map dynamics and introduce the population model. Section III outlines the ingredients most relevant for the derivation of the MF system, with the remaining technical details left for the Appendix. In Sec. IV, the qualitative and quantitative agreement between the dynamics of the exact and the MF model is illustrated by the appropriate bifurcation diagrams, as well as by comparing the characteristic features of the associated regimes. Section V concerns the assembly's stimulus-response relationship, first investigating the analogy between the respective phase-response curves (PRCs) of the exact system and the effective model in spiking and bursting regimes and then considering the extent to which the MF model reproduces the population's response to rectangular pulses of finite amplitude and duration. In Sec. VI, we provide a summary of our main results.

II. MAP NEURON DYNAMICS AND THE POPULATION MODEL

The dynamics of an isolated neuron conforms to a map model first introduced in Refs. [45,46], which is given by

$$x_{n+1} = x_n + G(x_n) - \beta H(x_n - d) - y_n,$$
$$y_{n+1} = y_n + \epsilon(x_n - J),$$

(1)

where n denotes the iteration step. The variable x_n qualitatively accounts for the membrane potential, whereas the recovery variable y_n, whose rate of change is set by a small parameter $\epsilon = 10^{-2}$, mimics the behavior of ion-gating channels. The parameters a, β, and d modify the profile of the ensuing oscillations, while J crucially influences the neural excitability, viz. the transitions from silence to active regimes.

The x_n evolution features two nonlinear terms, one being a FitzHugh-Nagumo-like cubic nonlinearity

$G(x_n) = x_n(x_n - a)(1 - x_n)$, which is complemented by a discontinuity term $-\beta H(x_n - d)$, where H stands for the Heaviside step function. The parameters $a = 0.1$ and $d = 0.45$ are kept fixed throughout the paper. The impact of discontinuity consists in making the fast subsystem [Eq. (1) with $\epsilon = 0$] a Lorenz-type map within certain parameter domains [46,47], which endows the model with the ability to generate chaotic spike or burst oscillations, otherwise lacking in the Fitzhugh-Nagumo type of systems.

Under variation of J and β, the map (1) may reproduce a rich repertoire of generic regimes displayed by the real neurons, as demonstrated in Fig. 1. In particular, the main frame shows amplitudes of the corresponding x time series for the given (J,β), while the remaining subfigures illustrate the characteristic wave forms pertaining to excitable regime (region I), subthreshold oscillations II), regular (III) or chaotic spiking (I), chaotic bursting (V), as well as the mixed chaotic spike-burst activity (VI). Some of the indicated boundaries, such as those involving domains IV, V, and VI should be understood as tentative, since the associated transitions are smooth and therefore difficult to discern.

The detailed phase plane analysis concerning the relevant unstable invariant curves and the mechanisms underlying transitions between the different dynamical regimes can be found in Ref. [48]. Here we briefly mention that under increasing J, the equilibrium loses stability via the Neimarck-Sacker bifurcation, which gives rise to subthreshold oscillations. Note that the latter may be considered an excitable state, in the sense that a strong-enough perturbation can elicit genuine spike, though the phase point does not relax to the equilibrium but rather to a closed invariant curve.

Adopting model (1) for local dynamics, we focus on an assembly of N stochastic neurons coupled in the all-to-all fashion via electrical synapses (diffusive couplings). Each neuron receives input from the units within the assembly and is further influenced by synaptic noise from the embedding environment. Note that it is quite common in two-dimensional neuron models with sharp separation of characteristic time scales to interpret the stochastic perturbation acting on the fast
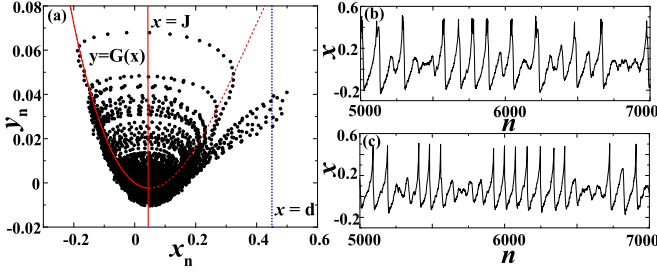
FIG. 2. Impact of noise on a single map neuron in the excitable regime. (a) The mechanism behind noise-induced spiking. The data are obtained for $J = 0.046$, $\beta = 0.4$, $\sigma = 0.005$. The equilibrium is deterministically stable given that the line $x = J$ intersects the invariant curve $y = G(x)$ below the curve's minimum. (b) The x_n series corresponding to noise-induced bursting ($J = 0.042$, $\beta = 0.2$, $\sigma = 0.008$), whereas (c) demonstrates stochastic spiking superimposed on subthreshold oscillations ($J = 0.048$, $\beta = 0.4$, $\sigma = 0.008$).

(slow) time scale as synaptic (intrinsic) noise [49–51]. The population activity is then described by the following system:

$$x_{i,n+1} = x_{i,n} + G(x_{i,n}) - \beta H(x_{i,n} - d) - y_{i,n} + I_{i,n}^{\text{syn}},$$
$$y_{i,n+1} = y_{i,n} + \epsilon(x_{i,n} - J), \tag{2}$$

$$I_{i,n}^{\text{syn}} = I_{i,n}^{\text{coup}} + I_{i,n}^{\text{rand}} = \frac{c}{N} \sum_{j=1, j \neq i}^{N} (x_{j,n} - x_{i,n}) + \sigma \xi_{i,n},$$

where i specifies the particular neuron. The synaptic currents $I_{i,n}^{\text{syn}}$ comprise two types of terms. The diffusive couplings $I_{i,n}^{\text{coup}}$ are characterized by the strength c, which is assumed to be uniform over the network and is set to $c = 1$ in the remainder of the paper. The random inputs $I_{i,n}^{\text{rand}}$ involve uncorrelated white noise [$E[\xi_{i,n}] = 0, E[\xi_{i,n}\xi_{j,n'}] = \delta_{ij}\delta(n - n')$] of intensity σ.

Confined to a single unit, the stochastic component may influence its dynamics either by perturbing the deterministic oscillatory regimes or by inducing oscillations in the excitable regime, cf. Fig. 2(b). The onset of noise-induced spiking or bursting within the parameter domain where the fixed point is deterministically stable (domain *I* in Fig. 1) corresponds to a phenomenon of stochastic bifurcation [39,52–55]. The latter are typically described phenomenologically, in a sense that certain time-averaged quantities, such as the asymptotic probability distributions of relevant variables or the associated power spectra, exhibit a qualitative change under variation of noise intensity. For instance, in continuous-time systems, it has been shown that the stochastic Hopf bifurcation from a stochastically stable fixed point to a stochastically stable limit cycle is accompanied by the loss of Gaussian property for the asymptotic distributions of the appropriate variables [56]. At variance with standard deterministic bifurcations, where one clearly observes a critical value of the control parameter, the change of system's behavior in noise-induced transitions is gradual [39]. Note that noise can also play an important part in the (J, β) region II where the deterministic map shows subthreshold oscillations. Here noise can give rise to a form of dynamics reminiscent of mixed-mode oscillations, cf. Fig. 2(c).

So far, models similar to (2) have been applied to address a number of problems associated to collective phenomena in

networks of coupled neurons, including synchronization of electrically coupled units with spike-burst activity [57,58], pattern formation in complex networks with modular architecture [41,42,59], transient cluster activity in evolving dynamical networks [44], as well as the basin stability of synchronization regimes in small-world networks [43]. Within this paper, the collective motion will be described in terms of the global variables $X_n = \frac{1}{N} \sum_{i=1}^{N} x_{i,n}$ and $Y_n = \frac{1}{N} \sum_{i=1}^{N} y_{i,n}$.

III. DERIVATION OF THE MEAN-FIELD MODEL

Considering a MF approximation, our main goal lies in deriving a reduced low-dimensional deterministic set of nonlinear difference equations whose dynamics is qualitatively analogous to the collective motion of the original system (2) composed of $2N$ coupled stochastic maps. In particular, the MF model should be able to generate all the regimes exhibited by the exact system, qualitatively reproducing the bifurcations that the latter undergoes. Also, applying the effective model, one should be capable of inferring with sufficient accuracy the parameter domains which admit the different collective states of the exact system, with the corresponding time series exhibiting similar characteristic quantitative features. Regarding the explicit effects of noise, the MF model is expected to account for the onset or suppression of different types of collective modes associated to macroscopic spiking or bursting activity, which are mediated by synchronization or desynchronization of individual neuron dynamics, respectively. The synchronization processes may be influenced by noise in a variety of ways, including the scenarios where noise acts as a perturbation to mainly deterministic (and chaotic) local oscillations, or the ones where noise plays a facilitatory role, in the sense that the collective mode emerges via synchronization of noise-induced local dynamics.

Given that we consider a system of discrete-time equations, one cannot adopt the usual method of deriving the MF model via Fokker-Planck formalism [40]. Nevertheless, an analytically tractable MF model may still be built by focusing on the evolution of cumulants [34–36,39], whereby the full density of states is factorized into a series of marginal densities. The advantage of such an approach is that the simplifying approximations aimed at truncating the underlying cumulant series can be introduced in a controlled fashion. Such approximations, stated in a form of closure hypothesis [34], are required due to nonlinearity of the original system, which causes the dynamics of cumulants of the given order to be coupled to those of the higher order.

In our case, the derivation of the effective model incorporates an explicit Gaussian closure hypothesis [34–36,39], by which all the cumulants above second order are assumed to vanish. The collective dynamics is then described by a set of five variables (the first- and second-order cumulants), including

(i) the means, given by $m_{x,n} = \lim_{N \to \infty} \frac{1}{N} \sum_{i=1}^{N} x_{i,n} \equiv \langle x_{i,n} \rangle$, $m_{y,n} = \lim_{N \to \infty} \frac{1}{N} \sum_{i=1}^{N} y_{i,n} \equiv \langle y_{i,n} \rangle$;

(ii) the variances, defined as $S_{x,n} = \langle x_{i,n}^2 \rangle - \langle x_{i,n} \rangle^2 = \langle x_{i,n}^2 \rangle - m_{x,n}^2$ and $S_{y,n} = \langle y_{i,n}^2 \rangle - \langle y_{i,n} \rangle^2 = \langle y_{i,n}^2 \rangle - m_{y,n}^2$;

(iii) the covariance $U_n = \langle x_{i,n} y_{i,n} \rangle - m_{x,n} m_{y,n}$.

The expressions for higher-order moments $\langle x_{i,n}^k \rangle$ in terms of the first- and second-order cumulants [60], such as

$$\langle x_i^3 \rangle = m_x^3 + 3m_x S_x$$
$$\langle x_i^4 \rangle = m_x^4 + 6m_x^2 S_x + 3S_x^2$$
$$\langle x_i^2 y_i \rangle = m_y S_x + m_y m_x^2 + 2m_x U$$
$$\langle x_i^3 y_i \rangle = 3S_x U + 3S_x m_x m_y + 3m_x^2 U + m_y m_x^3 \qquad (3)$$
$$\langle x_i^5 \rangle = m_x^5 + 15m_x S_x^2 + 10m_x^3 S_x$$
$$\langle x_i^6 \rangle = m_x^6 + 15S_x^3 + 15m_x^4 S_x + 45m_x^2 S_x^2,$$

can be derived using the closure hypothesis.

The Gaussian approximation effectively amounts to an assumption that the relation

$$\lim_{N \to \infty} \frac{1}{N} \sum_{i=1}^{N} x_{i,n}^k \approx E[x_{i,n}^k], \qquad (4)$$

holds, whereby E refers to expectation value obtained by averaging over an ensemble of different stochastic realizations. In other words, one supposes that the local variables are independent and are drawn from a normal distribution $\mathcal{N}(m_x, S_x)$. We do not know *a priori* whether such an assumption is fulfilled but can only judge on its validity by verifying the correctness of the predictions on the population dynamics provided by the MF model. Also note that the effective model concerns the assembly dynamics in the thermodynamic limit

$N \to \infty$. The stochastic terms in this case can be neglected, as one may show them to contribute to finite-size effects which scale as $1/N$. This means that the influence of noise in our MF model is felt only via the noise intensity, which assumes the role of an additional bifurcation parameter.

Let us illustrate the main technical points required for the derivation of the MF model. Our focus will lie with a couple of relevant examples, whereas the remaining details are provided in the Appendix. We begin by considering the dynamics of m_x, which is given by

$$m_{x,n+1} = m_{x,n} - m_{y,n} + \langle G(x_{i,n}) \rangle - \beta \langle H(x_{j,n} - d) \rangle. \quad (5)$$

It is easy to see that there is no contribution from the coupling term. As far as the third term on the right-hand side of Eq. (5) is concerned, using Eq. (3), one arrives at

$$\langle G(x_i) \rangle = \langle -x_i^3 + (1+a)x_i^2 - ax_i \rangle$$
$$= G(m_x) + S_x(1 + a - 3m_x). \qquad (6)$$

In the last expression, we have dropped the time index for simplicity and have introduced the shorthand notation $G(m_x) \equiv -m_x^3 + (1+a)(m_x^2 + S_x)$.

The key problem is how to treat the final term in the right-hand side of Eq. (5). Our approach consists in replacing the assembly average by the expectation value ($\langle H(x_i - d) \rangle \approx E[H(x_i - d)]$), obtained by assuming that the local variables at an arbitrary time moment are normally distributed according to $P(x_i) \sim \mathcal{N}(m_x, S_x)$. The expectation may then be evaluated as

$$E[-\beta \langle H(x_i - d) \rangle] = \int dx_1 \int dx_2 ... \int dx_N \left(-\frac{\beta}{N} \sum_i H(x_i - d) \right) p(x_1, x_2, ..., x_N)$$

$$= -\beta \int_{-\infty}^{\infty} dx_1 H(x_1 - d) p(x_1) = -\beta \int_d^{\infty} \frac{1}{\sqrt{2\pi S_x}} e^{-\frac{(x_1 - m_x)^2}{2S_x}} = -\frac{\beta}{2} \left(1 - \text{Erf}\left[\frac{d - m_x}{\sqrt{2S_x}} \right] \right), \qquad (7)$$

with the error function $\text{Erf}(x) = \frac{2}{\sqrt{\pi}} \int_0^x e^{-t^2} dt$. In the above calculation, we have explicitly used the assumption on the independence of distributions of local variables at any given moment of time.

In a similar fashion, one may consider the S_x dynamics, which constitutes the most demanding part of the derivation. In particular, proceeding from the S_x definition, we obtain

$$S_{x,n+1} = \langle x_{i,n+1}^2 \rangle - \langle x_{i,n+1} \rangle^2$$
$$= \langle [(1-c)x_{i,n} + G(x_{i,n}) - \beta H(x_{i,n} - d) - y_{i,n} + \xi_{i,n} + cm_{x,n}]^2 \rangle - [m_{x,n} - m_{y,n} + G(m_{x,n}) + S_{x,n}(1 + a - 3m_{x,n})$$
$$- \beta \langle H(x_{i,n} - d) \rangle]^2. \qquad (8)$$

As an illustration, let us evaluate one of the terms containing an average over the threshold function:

$$-2\beta E[\langle G(x_i)H(x_i - d) \rangle] = -2\beta \left[\int dx_1 G(x_1)H(x_1 - d)p(x_1) - \int dx_1 H(x_1 - d)p(x_1)[G(m_x) + S_x(1 + a - 3m_x)] \right]$$

$$\approx -2\beta \left[\int dx_1 [G(m_x) + G'(m_x)(x_1 - m_x) + \frac{1}{2}G''(m_x)(x_1 - m_x)^2]H(x_1 - d)p(x_1) \right.$$

$$\left. - \int dx_1 H(x_1 - d)p(x_1)[G(m_x) + S_x(1 + a - 3m_x)] \right] = ...$$

$$= -2\beta[(1+a)(m_x + d) - a - 3m_x d]\sqrt{\frac{S_x}{2\pi}} \exp\left[-\frac{(d - m_x)^2}{2S_x} \right]. \qquad (9)$$

Again, the time indexes have been suppressed to simplify the notation.

Leaving the remaining elements of the derivation for the Appendix, we now state the final equations of the MF model in the thermodynamic limit

$$m_{x,n+1} = m_{x,n} - m_{y,n} + G(m_{x,n}) + S_{x,n}(1 + a - 3m_{x,n}) - \frac{\beta}{2}\left(1 - \text{Erf}\left[\frac{d - m_{x,n}}{\sqrt{2S_{x,n}}}\right]\right)$$

$$m_{y,n+1} = m_{y,n} + \epsilon(m_{x,n} - J)$$

$$S_{x,n+1} = (1-c)^2 S_{x,n} + S_{y,n} + \sigma^2 - 2(1-c)U_n + S_{x,n}\left(-3m_{x,n}^2 + 2(1+a)m_{x,n} - a\right)^2$$

$$- 2(1-c)\left(3m_{x,n}^2 S_{x,n} + 3S_{x,n}^2 - 2(1+a)m_{x,n}S_{x,n} + aS_{x,n}\right) + 2(3S_{x,n}U_n + 3m_{x,n}^2 U_n - 2(1+a)m_{x,n}U_n)$$

$$- 2\beta[(1+a)(m_{x,n}+d) - a - 3dm_{x,n}]\sqrt{\frac{S_{x,n}}{2\pi}}\exp\left[-\frac{(d-m_{x,n})^2}{2S_{x,n}}\right] - 2\beta(1-c)\sqrt{\frac{S_{x,n}}{2\pi}}\exp\left[-\frac{(d-m_{x,n})^2}{2S_{x,n}}\right]$$

$$+ S_{x,n}^2\left[36m_{x,n}^2 - 24(1+a)m_{x,n} + 2(1+a)^2 + 6a\right] + 15S_{x,n}^3$$

$$S_{y,n+1} = S_{y,n} + \epsilon^2 S_{x,n} + 2\epsilon U_n$$

$$U_{n+1} = U_n - (a+c+\epsilon)U_n + \epsilon(1-c-a)S_{x,n} - S_{y,n} - (U_n + \epsilon S_{x,n})[3S_{x,n} + 3m_{x,n}^2 - 2(1+a)m_{x,n}]$$

$$- \beta\epsilon\sqrt{\frac{S_{x,n}}{2\pi}}\exp\left[-\frac{(d-m_{x,n})^2}{2S_{x,n}}\right]. \tag{10}$$

IV. ANALYSIS OF STABILITY AND BIFURCATIONS

In this section, our goal is to demonstrate the qualitative and quantitative analogies between the dynamics of the exact system and the MF model. To this end, we first examine the succession of macroscopic regimes in the J-β parameter plane for σ fixed at an intermediate value $\sigma = 0.002$, see Fig. 3. As in case of a single unit, changing J is relevant for the system's excitability, viz. the transitions from silent to active regimes, while β influences the wave forms of the active states (spiking, bursting, or mixed spike-bursting activity). The assembly is found to exhibit the collective modes which qualitatively correspond to the dynamics of a single unit illustrated in plates

III and VI of Fig. 1. The heat maps in the left column of Fig. 3 provide a comparison between the oscillation amplitudes A of the global variable X (top row) and the MF variable m_x (bottom row) for the given (J, β). The right column indicates how well are matched the average interspike interval (or the average bursting cycle) T of the exact system with the corresponding characteristics of the dynamics of the MF model (A1). In the given instances, exact system comprises an assembly of $N = 100$ neurons, having obtained A by averaging over a
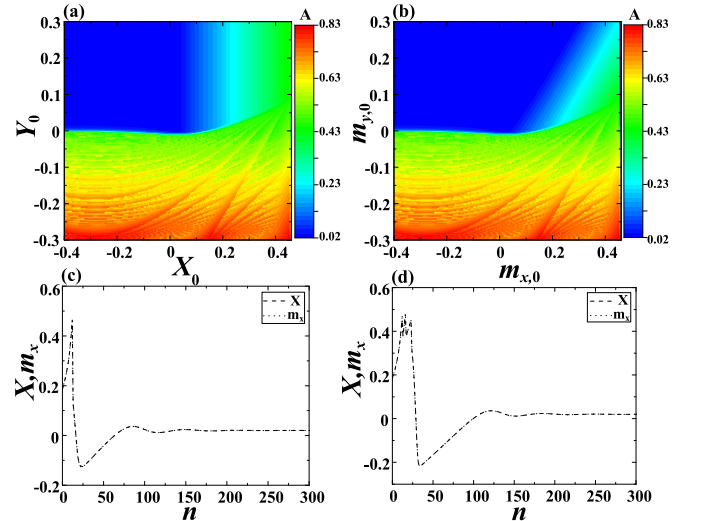

FIG. 3. Heat maps in (a) and (b) show the dependencies $A(J, \beta)$ and $T(J, \beta)$ obtained by stochastic averaging for a network of $N = 100$ neurons, respectively. Panels (c) and (d) illustrate the analogous results for the MF model. The noise intensity in all instances is $\sigma = 0.001$.

FIG. 4. Macroscopic excitability feature. In (a) and (b) are shown the maximum values of X and m_x reached within the time series of the exact and the MF system, starting from the analogous initial conditions (X_0, Y_0) and $(m_{x,0}, m_{y,0})$, respectively. The parameters are $J = 0.02, \beta = 0.4$. (c) Illustrates the case where a strong-enough perturbation elicits a single-spike response $(J = 0.02, \beta = 0.4)$, whereas (d) corresponds to a bursting response made up of three spikes $(J = 0.02, \beta = 0.15)$. In both instances, the time series of the MF model (dotted line) is indistinguishable from that of the exact system (dashed line).
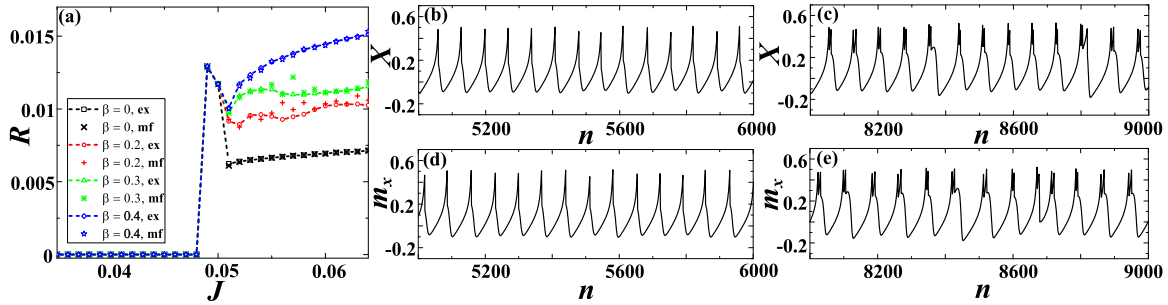
FIG. 5. (a) A family of $R(J)$ curves over β for a network of size $N = 100$ under fixed $\sigma = 0.001$. Superimposed are the results for the MF model, whereby the symbols $\times, +, *, \star$ correspond to cases $\beta = 0, 0.2, 0.3,$ and 0.4, respectively. Panels (b) and (c) illustrate the X series associated to the spiking and the bursting collective modes. The considered network is made up of $N = 100$ neurons, with the parameters set to $J = 0.06, \beta = 0.4, \sigma = 0.001$ in (b), and $J = 0.08, \beta = 0.2, \sigma = 0.001$ in (c). In (d) and (e) are provided the m_x series obtained for parameters from (b) and (c).

sufficiently long time series, whereas T is determined by taking average over an ensemble of 20 different stochastic realizations. With regard to T, we have selected a convenient threshold $\theta = 0.2$, which allows a clear detection of individual spikes and enables one to unambiguously discern the initiation stage of bursts, as required for calculating the length of the bursting cycle.

Let us begin the analysis by focusing on the domain of J values where the exact system exhibits the stochastically stable equilibrium, while the MF model has a stable stationary state. The stochastic stability physically implies that fluctuations around the deterministic fixed point are typically of the order of noise, though some rare spikes may still be evoked. For J sufficiently close to the region admitting the subthreshold oscillations, the population manifests macroscopic excitability. The term "macroscopic" here refers to a form of emergent assembly behavior rather than the characteristic spatial scale. To properly illustrate this feature, we have analyzed the assembly dynamics in the limit $\sigma = 0$, cf. Fig. 4. In particular, Figs. 4(a) and 4(b) show the maximum X and m_x values reached in the corresponding time series obtained for sets of different initial conditions (X_0, Y_0) and $(m_{x,0}, m_{y,0})$, respectively. The comparison between the two plots clearly corroborates that the boundary defining the domain of spiking response is appropriately anticipated by the MF model. An important remark is that for the given J, the assembly may exhibit different forms of macroscopic excitability, generating a single spike or a burst of spikes, as dependent on the value of β. This is demonstrated by the time series in Figs. 4(c) and 4(d). The former refers to a one-spike response in case of $\beta = 0.4$. For smaller β, one observes responses comprising two or more closely packed spikes, with Fig. 4(d) illustrating a three-spike burst encountered for $\beta = 0.25$. Note that the time series of the full system and the MF model are exactly matched in the limit $\sigma = 0$.

Next we address the noise-influenced transitions from silence to active regimes observed under increasing J. To do so, in Fig. 5(a) we have plotted the change of the firing (spiking or bursting) frequency R for an assembly consisting of $N = 100$ neurons. The average frequency is determined by considering an ensemble of 20 different stochastic realizations, having σ fixed to the moderate value from Fig. 4. The results from simulations of the full system (2) are compared against

the data obtained for the MF model. In this context, two points should be stressed. First, for moderate σ, note that the firing frequencies of the MF model lie in close agreement to those of the exact system. As a second point, one finds that such quantitative agreement extends to different forms of collective behavior, viz. it holds for different types of transitions from silent to active regimes. As already indicated, the wave forms pertaining to the active states depend on β, such that the associated transitions are mediated by the distinct synchronization processes. For instance, at $\beta = 0$, synchronization involves time series of single units that conform to spiking activity of type III from Fig. 1, which are quite resilient to impact of noise. On the other hand, for $\beta = 0.3$ or $\beta = 0.4$, the individual units exhibit chaotic bursting or spiking activity, respectively, such that the underlying synchronization process may be more susceptible to stochastic effects. The typical X time series illustrating the different collective modes are compared to the corresponding m_x series in Figs. 5(b)–5(e). The top (bottom) row concerns the data for the exact system (MF model).
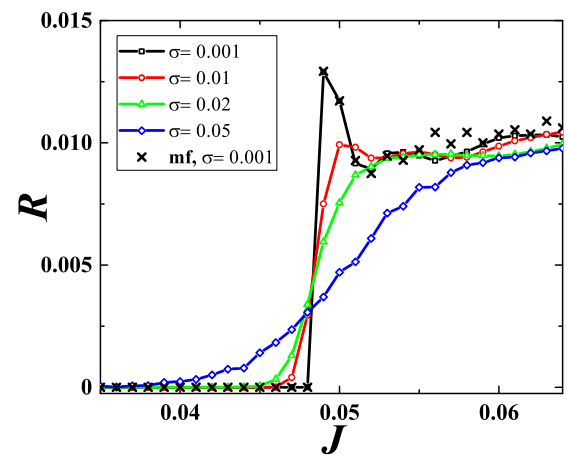

FIG. 6. Family of $R(J)$ curves over σ obtained for a network of $N = 100$ neurons under fixed $\beta = 0.2$. The different symbols correspond to cases $\sigma = 0.001$ (squares), $\sigma = 0.01$ (circles), $\sigma = 0.02$ (triangles), and $\sigma = 0.05$ (diamonds). The crosses connected by the dashed line highlight the $R(J)$ curve for the MF model at $\sigma = 0.001$.
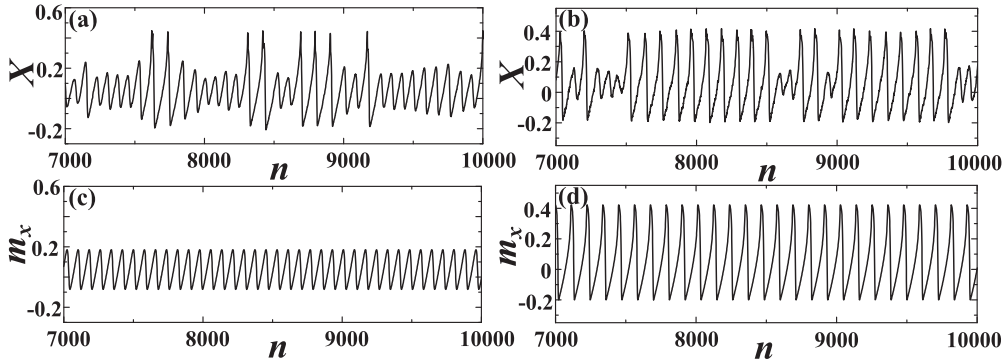
FIG. 7. Noise-induced phenomena within the J interval in vicinity of the deterministic threshold. X series in (a) shows the noise-induced spike-bursting activity on top of subthreshold oscillations ($J = 0.047$, $\beta = 0.2$, $\sigma = 0.02$). (b) Illustrates the "skipping" phenomenon where the stochastic effects occasionally suppress the large-amplitude oscillations of the X variable ($J = 0.058$, $\beta = 0.2$, $\sigma = 0.01$). In (c) and (d) are provided the m_x series corresponding to parameter sets from (a) and (b), respectively.

In order to investigate more closely the influence of noise for J interval in vicinity of the transition from silence to active regimes, we examine how the profiles of $R(J)$ curves change under increasing σ. The results shown in Fig. 6 refer to $\beta = 0.2$ and a population comprised of $N = 100$ neurons. As expected, the transition appears quite sharp for moderate noise $\sigma = 0.001$ but is considerably flattened for larger σ, e.g., $\sigma = 0.05$. The crosses indicate the firing frequencies predicted by the MF model for $\sigma = 0.001$.

For larger σ, the MF model fails to reproduce the behavior of the exact system in vicinity of threshold J, in the sense that it overestimates the maximal R value, as well as the actual critical J characterizing the transition. Viewed from another angle, one may infer that for sufficiently large σ and J below the threshold given by the MF model, the latter fails to capture the impact of synchronization processes taking place between the noise-induced oscillations of individual units. This especially refers to J interval where the spikes or bursts (depending on the given β) are superimposed on the background of subthreshold oscillations. An example of such a discrepancy between the behavior of the exact and the effective system is provided in Fig. 7, cf. Fig. 7(a) and Fig. 7(c). Also, for strong σ and J values above the transition, the firing frequencies anticipated by the effective model are typically higher than those of the exact system (not shown). Within this region, the stochastic effects suppress synchronization between the chaotic oscillations of single neurons, thereby reducing the corresponding R value. This is not accounted for with sufficient accuracy by the MF system. Note that such suppression of synchronization is reflected in the corresponding X series by the spike (burst) "skipping" mechanism, where the large-amplitude oscillations are occasionally replaced with subthreshold oscillations. For the associated J and σ values, such a phenomenon is absent in the dynamics of the effective model, cf. Fig. 7(b) and Fig. 7(d). In both of the scenarios illustrated in Fig. 7, the reason for the failure of MF model is that the Gaussian approximation breaks down due to large stochastic fluctuations.

The fashion in which the validity of the effective model's predictions deteriorates with increasing σ is made more explicit in Fig. 8, which shows the $A(J,\sigma)$ and $T(J,\sigma)$ dependencies for the exact and the approximate system at fixed $\beta = 0.4$. The considered size of the network is $N = 100$. Comparison between the respective A (left column) and T plots (right column) suggests that the range of σ values where the MF approximation applies is contingent on J. For instance, in the J region below the deterministic threshold, one may estimate this range by noting that the effective bifurcation diagram in Fig. 8(a) indicates that noise-induced macroscopic oscillations emerge for $\sigma \approx 0.003$. Since this point is not adequately represented by the effective model, cf. Fig. 8(c), one may state that the Gaussian approximation breaks down around $\sigma \approx 0.003$ within the given J region. Nevertheless, for J above the deterministic threshold, the validity of the MF model appears to depend rather strongly on particular J, with the σ values where the Gaussian approximation effectively fails spanning the range $\sigma \in (0.002, 0.006)$.
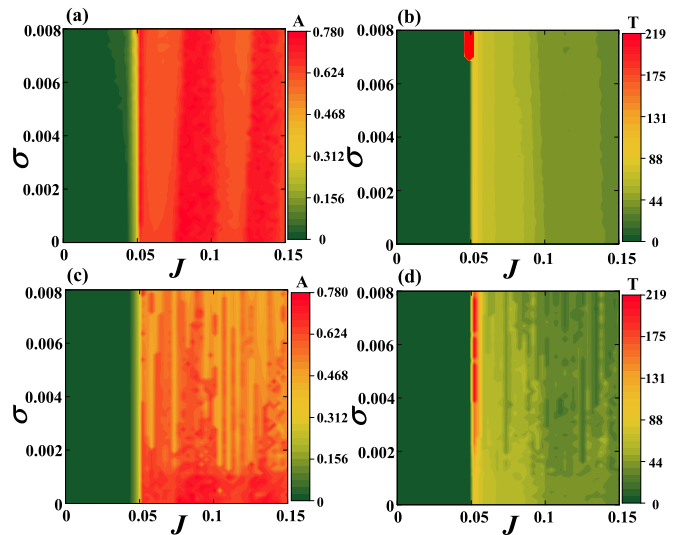

FIG. 8. Panels (a) and (b), respectively, refer to $A(J,\sigma)$ and $T(J,\sigma)$ dependencies for the network of $N = 100$ neurons under fixed $\beta = 0.4$. The results in (a) are obtained by averaging over a sufficiently long time series, whereas data in (b) derive from averaging over an ensemble of 20 different stochastic realizations. In (c) and (d) are provided the $A(J,\sigma)$ and $T(J,\sigma)$ dependencies determined by numerical simulations of the MF model.
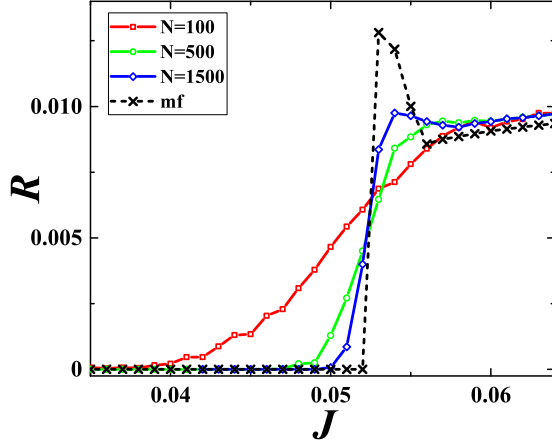
FIG. 9. $R(J)$ dependencies for increasing N under fixed $(\beta,\sigma) = (0.2,0.05)$. The squares, circles, and diamonds correspond to cases $N = 100$, $N = 500$, and $N = 1500$, respectively. The results predicted by the MF model are indicated by crosses connected via dashed line.

So far, we have investigated the impact of noise by comparing the results for the network of size $N = 100$ to those obtained for the effective system. Nevertheless, within Sec. III, it has already been emphasized that the MF model, deterministic in character, refers to the system's behavior in the thermodynamic limit $N \to \infty$, whereas the explicitly stochastic terms could only be incorporated as finite-size effects. This makes it relevant to examine how the behavior of the exact system within the J domain around deterministic threshold changes for large and fixed σ under increasing N. To this end, we have plotted in Fig. 9 the $R(J)$ curves calculated for $N = 100$ (squares), $N = 500$ (circles), and $N = 1500$ (diamonds) at fixed $\beta = 0.2,\sigma = 0.05$. The curve for $N = 100$ evinces that the given σ value is quite large in a sense of being sufficient to induce collective oscillations within the excitable regime. Apart from the dependencies for the full system, we also show the $R(J)$ curve associated to the MF model (dashed line with crosses). An interesting point regarding the latter is that the J threshold for the emergence of the collective mode is shifted toward a larger value compared to the case $\sigma \approx 0.01$. While the given transition itself appears quite sharp, the curves corresponding to the exact system approach it with increasing N, both in terms of the J threshold and the R values above the transition. This corroborates that the (J,σ) domain where the Gaussian approximation behind the MF model fails expectedly reduces with the increasing system size.

V. RESPONSE TO EXTERNAL STIMULI

The aim of this section is to investigate the extent to which the MF model can be used to predict the stimulus-response relationship of an assembly exhibiting different macroscopic regimes, including the excitable state, as well as the spiking and bursting collective modes. Let us first focus on the two latter instances and examine the sensitivity of a population to an external pulse perturbation within the framework of phase resetting theory [61–64]. In order to compare the behavior of the exact system and the effective model, we determine
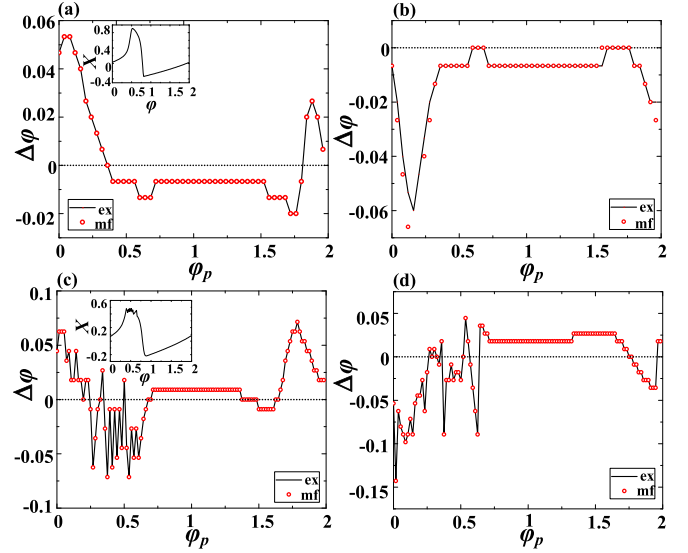

FIG. 10. Assembly phase resetting. Panels (a) and (b) show the PRCs for a population in spiking regime ($J = 0.055$, $\beta = 0$) under excitatory ($a = 0.008$) and inhibitory stimulation ($a = -0.008$), respectively. Results for the exact system ($N = 500$) are indicated by the solid line, whereas the data for the MF model are denoted by circles. The bottom row illustrates the PRCs for an assembly exhibiting macroscopic bursting ($J = 0.06$, $\beta = 0.1$), whereby (c) describes the effect of an excitatory ($a = 0.01$) and (d) of an inhibitory pulse perturbation ($a = -0.01$). The insets in (a) and (c) demonstrate how the phases are assigned to the points within the spiking and bursting cycles, respectively. Phase is expressed in units of π.

the corresponding PRCs, which describe the phase shift $\Delta\phi$, induced by the perturbation, in terms of the phase ϕ_p when the perturbation is applied. The considered stimulus has a form of a short pulse current $I_p = a_p H(n - n_i) H(n - n_f)$, whose magnitude a_p and width $\Delta = n_i - n_f$ are small compared to the amplitude and duration of the spiking (or bursting) cycle T_0, respectively. In case of the exact system, the same pulse current is delivered to each neuron i, adding the term I_p to x_i dynamics, whereas in the effective model, stimulation is administered via the m_x variable. The phase φ_p is defined in reference to T_0 by $\varphi_p = n_p/T_0$. The associated phase difference following the reset is calculated as $\Delta\varphi = 1 - T_1/T_0$, where T_1 denotes the duration of the perturbed spiking or bursting cycle.

The PRCs characterizing the assembly response in the spiking regime are provided in Fig. 10(a) and Fig. 10(b), whereby the former is obtained under the action of an excitatory ($a_p > 0$), and the latter under the influence of inhibitory stimulation ($a_p < 0$). We stress that, in both instances, the results derived from the effective model, denoted by circles, show excellent agreement with the data for the exact system (solid lines). In qualitative terms, one observes that excitatory stimulation may advance the phase of the spiking cycle if it arrives sufficiently close to the spike but still before the sharp rising stage. However, an excitatory perturbation acting during the spike or within the effective refractory period has a suppression effect, reflected in delaying of the next spike. In contrast to excitatory stimulation, the inhibitory pulse postpones the next firing time if it is introduced within the interval close to the rising stage of spike.
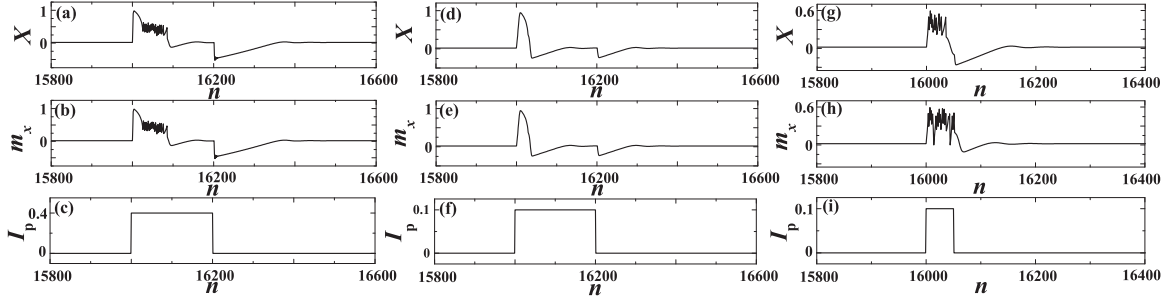
FIG. 11. Stimulus-response relationship in the excitable regime ($J = 0.02$). The top (middle) row refers to the response of the full system (MF model), whereas the bottom row shows the profile of the external stimulation. In panels (a)–(c), the system parameters are $\beta = 0.4$, $\sigma = 0$, while the perturbation is characterized by $a_p = 0.4, \Delta = 200$. Panels (d)–(f) concern the response of an assembly ($\beta = 0.1$, $\sigma = 0.001$) subjected to a rectangular pulse $a_p = 0.4$, $\Delta = 200$. Panels (g)–(i) illustrate the response of a population ($\beta = 0.4$, $\sigma = 0.001$) influenced by the external stimulation $a_p = 0.1, \Delta = 50$. The considered network is of size $N = 500$.

The PRCs determined for an assembly exhibiting collective bursting show qualitatively analogous effects to those described so far, see Fig. 10(c) and Fig. 10(d). This especially refers to impact of perturbation delivered sufficiently close to a moment of burst initiation. An apparent difference compared to Fig. 10(a) and Fig. 10(b) emerges during the bursting stage itself, where the associated PRCs expectedly exhibit strong fluctuations. Apart from that, one finds an interesting effect that both the excitatory and the inhibitory stimulation have a facilitatory role, i.e., cause phase advancement during the relaxation stage of the bursting cycle.

For a population in the excitable state, we consider scenarios where the system is influenced by a rectangular pulse perturbation of finite magnitude and duration, in a sense that the latter are comparable to corresponding features of typical spiking or bursting cycles. Note that the selected J value $J = 0.02$ lies sufficiently away from the interval admitting the subthreshold oscillations. Again, our objective is to determine whether the MF model correctly anticipates the response of the exact system, now in the presence of small to moderate noise. Some of the illustrative examples concerning the stimulus-response relationship under the finite perturbation are provided in Fig. 11. The top and the middle rows refer to X and corresponding m_x time series, respectively, while the bottom row shows the profile of the applied stimulus. We find that in the absence of noise or for sufficiently small σ, the effective model reproduces the evoked behavior of the full system quite accurately. This also refers to some highly complex forms of responses, as corroborated in Figs. 11(a)–11(c), which concern relatively large a_p and Δ. Under increasing σ, the ability of the MF model to predict the dynamics of the exact system gradually reduces but in a fashion that involves a nontrivial dependence on β. In particular, for smaller $\beta \approx 0.1$, which would facilitate macroscopic spiking mode for supercritical J, it turns out that the dynamics of the MF model lies in close agreement to the one of the exact system even for moderate noise $\sigma = 0.001$, cf. Figs. 11(d)–11(f). However, for higher β, such an analogy between the responses of the exact and the MF system is lost, see Figs. 11(g)–11(i). Naturally, the validity of the predictions given by the MF model deteriorates if the stimulation amplitude a_p and the duration Δ are large, especially in the presence of non-negligible noise.

VI. SUMMARY AND DISCUSSION

We have developed an MF approach in order to systematically analyze the emergent dynamics and the input-output relationship of a population of stochastic map neurons. The reduced low-dimensional model has been derived within the framework of Gaussian approximation, formally introduced in a form of a closure hypothesis. In physical terms, such an approximation suggests that the local variables at an arbitrary moment of time are independent and conform to a normal distribution centered about the assembly mean and characterized by the associated assembly variance. Validity of such an approximation cannot be established *a priori*, but has been systematically verified by numerically corroborating that the MF model reproduces the behavior of the exact system with sufficient accuracy.

In particular, we have first demonstrated that the effective model can qualitatively capture all the bifurcations of the exact system leading to the onset of different generic regimes of collective behavior. As far as the quantitative agreement is concerned, we have established substantial matching between the parameter domains admitting the respective dynamical regimes for the exact and the approximate system. Moreover, the typical features of the associated regimes, such as the average interspike interval or the average bursting cycle, exhibit analogous changes with parameter variation and in many parameter domains display numerically similar values.

An important issue has been to explicitly examine how the effects of noise are reflected in the behavior of the MF model. For the noise-perturbed activity, where the sufficiently small noise weakly influences the deterministic attractors of the system, the obtained results indicate that the Gaussian approximation holds. Nevertheless, the physical picture changes in case of noise-induced collective behavior. In particular, for different scenarios of stochastic bifurcations, typically corresponding to transitions from subthreshold oscillations, which involve generalized excitability feature, to spiking or bursting regimes, the exact system undergoes a gradual (smooth) change of collective dynamics, whereas the MF model exhibits a standard deterministic bifurcation with a sharp bifurcation threshold. In such instances, the collective variables of exact system manifest large fluctuations, which

explicitly violate the Gaussian approximation behind the effective model. Note that the loss of Gaussianity property for asymptotic distribution of relevant variables, which accompanies the described stochastic bifurcations, does not imply per se that our Gaussian approximation fails in the supercritical state. This point is evinced by the fact that the dynamics of the effective model shows qualitatively and quantitatively similar features to those of the exact system if the considered parameters lie sufficiently above the stochastic bifurcation. In fact, the Gaussian approximation applied in the derivation of the MF model breaks down only in vicinity of such transitions, where the finite-size effects neglected in Eq. (A1) become most prominent. We have numerically verified the prevalence of finite-size effects in these parameter domains, showing that the change of the appropriate order parameter, such as the spiking frequency, becomes sharper as the size of the neural assembly is increased. Nevertheless, the validity of Gaussian approximation is regained once the system is sufficiently above the bifurcation.

Apart from considering asymptotic dynamics, we have verified that the MF model is capable of capturing the stimulus-response features of the exact system. For short pulse-like perturbations, it has been found that the approximate system reproduces the PRCs of the exact system for both the spiking and bursting regimes of collective activity with high accuracy. Substantial analogies have also been observed in case of macroscopic excitable regime for scenarios where the assembly is stimulated by rectangular pulse perturbations of finite amplitude and duration.

Having developed a viable MF approach, the present research has set the stage for a more systematic exploration of collective dynamics of assemblies of map neurons by analytical means. We believe that the introduced techniques can be successfully applied for treating the emergent behavior of populations in case of chemically and delay-coupled neurons [41]. Moreover, the method may likely be used to explore the effects of parameter inhomogeneity, as well as to study the impact of complex network topologies [41,43]. Our ultimate goal will be to extend the MF approach to account for collective behavior of interacting populations of map neurons [41,42].

ACKNOWLEDGMENTS

APPENDIX

In the following, we provide the remaining details concerning the calculation of the S_x dynamics, which is the most complex part of the derivation of the effective model. Following some algebra, Eq. (9) can be transformed to

$$S_{x,n+1} = (1-c)^2 S_{x,n} + S_{y,n} + \sigma^2 - 2(1-c)U_n + \underbrace{(\langle G(x_{i,n})^2\rangle - \langle G(x_{i,n})\rangle^2)}_{\text{Var}(G(x_{i,n}))} + 2(1-c)(\langle x_{i,n}G(x_{i,n})\rangle - m_{x,n}\langle G(x_{i,n})\rangle)$$

$$- 2(\langle y_{i,n}G(x_{i,n})\rangle - m_{y,n}\langle G(x_{i,n})\rangle) - 2\beta(1-c)[\langle x_{i,n}H(x_{i,n}-d)\rangle - m_{x,n}\langle H(x_{i,n}-d)\rangle] - 2\beta(\langle G(x_{i,n})H(x_{i,n}-d)\rangle$$

$$- \langle G(x_{i,n})\rangle\langle H(x_{i,n}-d)\rangle) + \beta^2 \underbrace{(\langle H(x_{i,n}-d)^2\rangle - \langle H(x_{i,n}-d)\rangle^2)}_{\text{Var}(H(x_{i,n}-d)))}.$$
$$(A1)$$

The partial results required for completing the calculation are given by

$$\langle x_i G(x_i)\rangle - m_x\langle G(x_i)\rangle = G'(m_x)S_x - 3S_x^2$$
$$\langle y_i G(x_i)\rangle - m_y\langle G(x_i)\rangle = -3S_x U_{xy} - 3m_x^2 U_{xy} + 2(1+a)m_x U_{xy},$$
$$(A2)$$

where $G'(m_x) \equiv -3m_x^2 + 2(1+a)m_x - a$. Note that the time indexes have been omitted for simplicity. After some tedious work, it may also be shown that the expression for variance $\text{Var}(G(x_i))$ reads

$$\text{Var}(G(x_i)) = G'^2(m_x)S_x + S_x^2\big[36m_x^2 - 24(1+a)m_x + 2(1+a)^2 + 6a\big] + 15S_x^3.$$
$$(A3)$$

Let us now explicitly calculate the terms containing the threshold function. First, we have

$$-2\beta(1-c)[\langle x_i H(x_i - d)\rangle - \langle x_i\rangle\langle H(x_i - d)\rangle]$$

$$= -2\beta(1-c)\left[\int dx_1 dx_2...dx_N \frac{1}{N}\sum_i x_i H(x_i - d)p(x_1,...,x_N) - m_x \int dx_1 dx_2...dx_N \frac{1}{N}\sum_i H(x_i - d)p(x_1,...,x_N)\right] = ...$$

$$= -2\beta(1-c)\left[\int dx_1(x_1 - m_x)H(x_1 - d)p(x_1)\right] = -2\beta(1-c)\sqrt{\frac{S_x}{2\pi}}\exp\left[-\frac{(d-m_x)^2}{2S_x}\right].$$
$$(A4)$$

Note that the second term containing the threshold function has been evaluated in the main text, cf. Eq. (10).

Finally, let us address the term $\beta^2 \text{Var}[H(x_i - d)]$, which can be estimated by considering the associated expectation $\beta^2 \text{Var}[H(x_i - d)] \approx \beta^2 [\langle H(x_i - d)^2 \rangle - \langle H(x_i - d) \rangle^2]$. Applying the technique introduced in Sec. III, we obtain

$$E[\beta^2 H(x_i - d)^2] = \beta^2 \int dx_1 \int dx_2 ... \int dx_N \left[\frac{1}{N^2} \sum_i \sum_j H(x_i - d) H(x_j - d) \right] p(x_1, x_2, ..., x_N)$$

$$= \underbrace{\frac{\beta^2}{N^2} N \int dx_1 H(x_1 - d) p(x_1)}_{N \text{ cases where } i=j} + \underbrace{\frac{\beta^2}{N^2} N(N-1) \int dx_1 \int dx_2 H(x_1 - d) H(x_2 - d) p(x_1) p(x_2)}_{N(N-1) \text{ cases where } i \neq j}$$

$$= \frac{\beta^2}{2N} \left[1 - \text{Erf}\left(\frac{d - m_x}{\sqrt{2S_x}} \right) \right] + \frac{\beta^2}{4N^2} N(N-1) \left[1 - \text{Erf}\left(\frac{d - m_x}{\sqrt{2S_x}} \right) \right]^2. \tag{A5}$$

Given that $\beta^2 \langle H(x_i - d) \rangle^2 = \frac{\beta^2}{4} [1 - \text{Erf}(\frac{d - m_x}{\sqrt{2S_x}})]^2$, one arrives at

$$\beta^2 \text{Var}[H(x_i - d)] = \frac{\beta^2}{4N} \left[1 - \text{Erf}\left(\frac{d - m_x}{\sqrt{2S_x}} \right) \right] \left[1 + \text{Erf}\left(\frac{d - m_x}{\sqrt{2S_x}} \right) \right]. \tag{A6}$$

This shows that the variance of the threshold function ultimately contributes to a finite-size effect which can be neglected in the thermodynamic limit.

[1] G. Buzsáki, *Rhythms of the Brain* (Oxford University Press, Oxford, 2009).
[2] A. Destexhe and D. Contreras, Science **314**, 85 (2006).
[3] C. Zhou, L. Zemanová, G. Zamora, C. C. Hilgetag, and J. Kurths, Phys. Rev. Lett. **97**, 238103 (2006).
[4] E. Bullmore and O. Sporns, Nat. Rev. Neurosci. **10**, 186 (2009).
[5] O. Sporns, D. Chialvo, M. Kaiser, and C. C. Hilgetag, Trends Cogn. Sci. **8**, 418 (2004).
[6] W. J. Freeman, *Neurodynamics: An Exploration in Mesoscopic Brain Dynamics* (Springer-Verlag, London, 2000).
[7] H. Liljenström, Scholarpedia **7**, 4601 (2012).
[8] G. Deco, V. K. Jirsa, P. A. Robinson, M. Breakspear, and K. Friston, PLoS Comput. Biol. **4**, e1000092 (2008).
[9] J. L. P. Velazquez and R. Wennberg, *Coordinated Activity in the Brain: Measurements and Relevance to Brain Function and Behavior* (Springer, New York, 2009).
[10] Y. Baibolatov, M. Rosenblum, Z. Z. Zhanabaev, M. Kyzgarina, and A. Pikovsky, Phys. Rev. E **80**, 046211 (2009).
[11] W. Gerstner, H. Sprekeler, and G. Deco, Science **338**, 60 (2012).
[12] *Lectures in Supercomputational Neuroscience: Dynamics in Complex Brain Networks*, edited by P. beim Graben, C. Zhou, M. Thiel, and J. Kurths (Springer-Verlag, Berlin, 2008).
[13] M. Breakspear, Nat. Neurosci. **20**, 340 (2017).
[14] W. J. Freeman, *Mass Action in the Nervous System: Examination of the Neurophysiological Basis of Adaptive Behavior through the EEG* (Academic Press, London, 1975).
[15] N. Fourcaud and N. Brunel, Neural Comput. **14**, 2057 (2002).
[16] S. El Boustani, and A. Destexhe, Neural Comput. **21**, 46 (2009).
[17] S. E. Folias and P. C. Bressloff, Phys. Rev. Lett. **95**, 208107 (2005).
[18] S. E. Folias and P. C. Bressloff, SIAM J. Appl. Math. **65**, 2067 (2005).
[19] C. R. Laing, W. C. Troy, B. Gutkin, and G. B. Ermentrout, SIAM J. Appl. Math. **63**, 62 (2002).
[20] P. C. Bressloff, Phys. Rev. E **82**, 051903 (2010).
[21] M. A. Buice and J. D. Cowan, Phys. Rev. E **75**, 051919 (2007).
[22] N. Brunel and V. Hakim, Neural Comput. **11**, 1621 (1999).
[23] H. Hasegawa, Phys. Rev. E **67**, 041903 (2003).
[24] N. F. Rulkov, Phys. Rev. E **65**, 041922 (2002).
[25] N. F. Rulkov, I. Timofeev, and M. Bazhenov, J. Comput. Neurosci. **17**, 203 (2004).
[26] D. Q. Wei and X. S. Luo, Europhys. Lett. **78**, 68004 (2007).
[27] Q. Y. Wang, Z. Duan, M. Perc, and G. Chen, Europhys. Lett. **83**, 50008 (2008).
[28] C. A. S. Batista, A. M. Batista, J. A. C. de Pontes, R. L. Viana, and S. R. Lopes, Phys. Rev. E **76**, 016218 (2007).
[29] B. Ibarz, J. M. Casado, and M. A. F. Sanjuán, Phys. Rep. **501**, 1 (2011).
[30] I. Franović and V. Miljković, Europhys. Lett. **92**, 68007 (2010).
[31] I. Franović and V. Miljković, Commun. Nonlinear Sci. Numer. Simul. **16**, 623 (2011).
[32] E. M. Izhikevich, Neural Comput. **18**, 245 (2006).
[33] E. M. Izhikevich and G. M. Edelman, Proc. Natl. Acad. Sci. U.S.A. **105**, 3593 (2008).
[34] B. Lindner, J. Garcia-Ojalvo, A. Neiman, and L. Schimansky-Geier, Phys. Rep. **392**, 321 (2004).
[35] I. Franović, K. Todorović, N. Vasović, and N. Burić, Phys. Rev. E **89**, 022926 (2014).
[36] I. Franović, K. Todorović, N. Vasović, and N. Burić, Phys. Rev. E **87**, 012922 (2013).
[37] I. Franović, K. Todorović, N. Vasović, and N. Burić, Chaos **22**, 033147 (2012).
[38] V. Klinshov and I. Franović, Phys. Rev. E **92**, 062813 (2015).
[39] M. A. Zaks, X. Sailer, L. Schimansky-Geier, and A. B. Neiman, Chaos **15**, 026117 (2005).
[40] B. Sonnenschein, M. A. Zaks, A. B. Neiman, and L. Schimansky-Geier, Eur. Phys. J. Special Topics **222**, 2517 (2013).
[41] O. V. Maslennikov and V. I. Nekorkin, Phys. Rev. E **90**, 012901 (2014).

[42] O. V. Maslennikov, D. V. Kasatkin, N. F. Rulkov, and V. I. Nekorkin, Phys. Rev. E **88**, 042907 (2013).

[43] O. V. Maslennikov, V. I. Nekorkin, and J. Kurths, Phys. Rev. E **92**, 042803 (2015).

[44] O. V. Maslennikov and V. I. Nekorkin, Commun. Nonlinear Sci. Numer. Simul. **23**, 10 (2015).

[45] V. I. Nekorkin and L. V. Vdovin, Izv. Vyssh. Uchebn. Zaved. Prikladn. Nelinejn. Din. **15**, 36 (2007).

[46] M. Courbage, V. I. Nekorkin, and L. V. Vdovin, Chaos **17**, 043109 (2007).

[47] O. V. Maslennikov and V. I. Nekorkin, Chaos **23**, 023129 (2013).

[48] O. V. Maslennikov and V. I. Nekorkin, Map-based approach to problems of spiking neural network dynamics, in *Nonlinear Dynamics and Complexity*, edited by V. Afraimovich, A. C. J. Luo, and X. Fu (Springer International, Switzerland, 2014), pp. 143–161.

[49] A. Destexhe and M. Rudolph-Lilith, *Neuronal Noise* (Springer, New York, 2012).

[50] I. A. Khovanov, A. V. Polovinkin, D. G. Luchinsky, and P. V. E. McClintock, Phys. Rev. E **87**, 032116 (2013).

[51] I. Franović, K. Todorović, M. Perc, N. Vasović, and N. Burić, Phys. Rev. E **92**, 062911 (2015).

[52] L. Arnold, *Random Dynamical Systems* (Springer Verlag, Berlin, 1999).

[53] J. A. Acebrón, A. R. Bulsara, and W.-J. Rappel, Phys. Rev. E **69**, 026202 (2004).

[54] M. Gaudreault, J. M. Berbert, and J. Viñals, Phys. Rev. E **83**, 011903 (2011).

[55] P. Kaluza, C. Strege, and H. Meyer-Ortmanns, Phys. Rev. E **82**, 036104 (2010).

[56] S. Tanabe and K. Pakdaman, Phys. Rev. E **63**, 031911 (2001).

[57] V. I. Nekorkin and O. V. Maslennikov, Radiophys. Quantum Electron. (Engl. Transl.) **54**, 56 (2011).

[58] M. Courbage, O. V. Maslennikov, and V. I. Nekorkin, Chaos Soliton. Fract. **45**, 645 (2012).

[59] O. V. Maslennikov and V. I. Nekorkin, Radiophys. Quantum Electron. (Engl. Transl.) **55**, 198 (2012).

[60] C. W. Gardiner, *Handbook of Stochastic Methods for Physics, Chemistry and the Natural Sciences*, 3rd ed. (Springer-Verlag, Berlin, 2004).

[61] *Phase Response Curves in Neuroscience: Theory, Experiment, and Analysis*, edited by N. W. Schultheiss, A. A. Prinz, and R. J. Butera (Springer, New York, 2012).

[62] P. A. Tass, *Phase Resetting in Medicine and Biology: Stochastic Modeling and Data Analysis* (Springer, Berlin, 2007).

[63] E. M. Izhikevich, *Dynamical Systems in Neuroscience: The Geometry of Excitability and Bursting* (MIT Press, Cambridge, 2007), Chap. 10.

[64] C. C. Canavier, Scholarpedia **1**, 1332 (2006).

Disordered configurations of the Glauber model in two-dimensional networks

IVA BAČIĆ[1], IGOR FRANOVIĆ[1] and MATJAŽ PERC[2,3,4]

[1] *Scientific Computing Laboratory, Center for the Study of Complex Systems, Institute of Physics Belgrade,
University of Belgrade - Pregrevica 118, 11080 Belgrade, Serbia*
[2] *Faculty of Natural Sciences and Mathematics, University of Maribor - Koroška cesta 160,
SI-2000 Maribor, Slovenia*
[3] *CAMTP – Center for Applied Mathematics and Theoretical Physics, University of Maribor - Mladinska 3,
SI-2000 Maribor, Slovenia*
[4] *Complexity Science Hub - Josefstädterstraße 39, A-1080 Vienna, Austria*

Abstract – We analyze the ordering efficiency and the structure of disordered configurations for the zero-temperature Glauber model on Watts-Strogatz networks obtained by rewiring 2D regular square lattices. In the small-world regime, the dynamics fails to reach the ordered state in the thermodynamic limit. Due to the interplay of the perturbed regular topology and the energy neutral stochastic state transitions, the stationary state consists of two intertwined domains, manifested as multiclustered states on the original lattice. Moreover, for intermediate rewiring probabilities, one finds an additional source of disorder due to the low connectivity degree, which gives rise to small isolated droplets of spins. We also examine the ordering process in paradigmatic two-layer networks with heterogeneous rewiring probabilities. Comparing the cases of a multiplex network and the corresponding network with random inter-layer connectivity, we demonstrate that the character of the final state qualitatively depends on the type of inter-layer connections.

The interplay of local dynamics and the underlying network topology has been in the focus of research in physics and various interdisciplinary fields [1–3], having recently attracted considerable interest in the context of phase ordering processes [4–6]. The Ising-Glauber model [7] constitutes one of the paradigmatic models for analyzing such processes [8]. While it has been introduced to describe the nonequilibrium dynamical behavior of magnetic systems consisting of a large number of interacting particles, it has since been applied to a variety of other problems, including those in social sciences [9], geology [10], and electrochemistry [11].

Within the Glauber model, the spin variables can assume two discrete values, having the states of nodes evolve according to the local majority rule. The Glauber model was initially defined on a regular lattice [7]. Nevertheless, given that non-lattice topologies including random, scale-free [12] and small-world [13] networks are often better suited to describe real-world systems, the issue of Glauber dynamics on complex networks has been gaining

increasing attention [8,14–16]. Apart from such models, complexity of interactions in many real-world systems may also involve "networks of networks" featuring modular or multilayer architecture [17], the scenarios which have been much less explored in the framework of Glauber dynamics.

Our work addresses two problems of ordering in complex networks: i) the disordered states of the zero-temperature Glauber model on monolayer rewired networks, where we identify two types of disordered configurations, and ii) the ordering process on two-layer rewired networks, where we find that the ordering process is strongly affected by the type of inter-layer connections.

In case of the two-dimensional square lattice, when only interactions between four nearest neighbors are taken into account, see fig. 1(a), the zero-temperature Glauber dynamics is multistable [18]. In particular, the system either reaches the ground state for $\approx 2/3$ of all the process realizations, or ends up in the frozen striped state with probability $p_f \approx 1/3$. Concerning rewired square lattices with coordination number $\langle k \rangle = 4$, it has been shown that
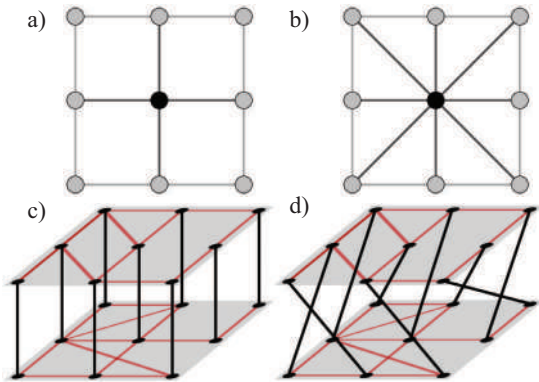
Fig. 1: (Color online) Considered network topologies. Panel (a) shows the scenario of a monolayer network with nearest-neighbor interactions ($k = 4$), whereas panel (b) shows the case where the next-nearest neighbor interactions are also included ($k = 8$). Panel (c) shows results for the multiplex two-layer network, whereas panel (d) shows results when there is random connectivity between the two layers.

the dynamics fails to reach the ground state [15,19], but little is known about the nature of the associated disordered configurations.

Our immediate goals are to understand why the Glauber model on small-world networks fails to reach ground state and to gain insight into the character of the disordered states on rewired networks with $\langle k \rangle = 4$ and $\langle k \rangle = 8$. We also study the ordering process on two-layer rewired networks with $\langle k \rangle = 4$, comparing the effects of different types of inter-layer connectivity, including multiplexing, see fig. 1(c), and the scenario with connections distributed between randomly selected pairs of nodes, cf. fig. 1(d).

Model. – In the Glauber model, the interactions are usually confined (but not necessarily restricted) to nearest-neighboring units. Incorporating higher-order competing (frustrated) interactions is one of the classical scenarios for the onset of new phases and potentially new types of phase transitions lying outside of Ising universality class. While the ferromagnetic interactions imposed by the model favor parallel alignment of spins, thermal noise prevents the system from reaching the ground state at any nonzero value of temperature. To avoid such stochastic effects which prevent full ordering, we consider systems quenched from an infinitely high temperature to absolute zero, in which spin states are initially uncorrelated and the net magnetization is vanishing. The Hamiltonian of the system is given by $H = -\sum_{\langle ij \rangle} J_{ij} S_i S_j$ where $S_i = \pm 1$ are Ising spin variables, the sum $\langle ij \rangle$ is over pairs of neighbors, and $J_{ij} > 0$ are ferromagnetic coupling constants, assumed to be uniform in our paper ($J_{ij} = J$). Each pair of parallel neighboring spins contributes $-J$ to the energy, while the contribution of antiparallel pairs is $+J$. Without loss of generality, we set $J = 1$ in the present study.

The state of the system evolves according to the majority rule applied to spins sequentially selected at random in each time step. This dynamical rule allows only energy lowering or the energy neutral state transitions. The former correspond to events where the spin variable is updated to the state prevalent in its local neighborhood, while the latter conform to scenario without a local majority, such that the given spin evolves stochastically with both orientations being equally likely.

Watts and Strogatz [13] have introduced an algorithm for generating small-world and random graphs by gradually rewiring a regular lattice. In their model, links from the regular lattice are chosen at random and replaced with new ones until a desired fraction of links p is rewired. Rewiring effectively introduces shortcuts between distant nodes, thereby drastically reducing the mean shortest path even in the limit $p \to 0$. By increasing the amount of disorder ($p \to 1$) one obtains a random network with the mean connectivity conserved. Small-world networks are generated by introducing an intermediate level of disorder ($0 < p \ll 1$), and are characterized by the high clustering coefficient and the short average path length. The former implies that neighboring nodes tend to group in well connected clusters, whereas the latter means that an arbitrary distant node can be reached by a small number of intermediate links.

We simulate Glauber dynamics of Ising spins on Watts-Strogatz rewired networks generated from two-dimensional regular $L \times L$ lattices with periodic boundary conditions. To understand the interplay between topological effects and the local majority dynamical rule, we vary several parameters in addition to L and the rewiring probability p, including the mean connectivity degree $\langle k \rangle$ and the initial magnetization m_0. As an additional ingredient, we also examine how the ordering process is affected by whether the Glauber dynamical rule allows for stochastic flipping or not. We refer to the rule without stochastic flipping as the modified Glauber rule.

To distinguish the influence of rewiring itself from the effect of connectivity of the network, we compare the results of simulations on networks with $\langle k \rangle = 4$ and $\langle k \rangle = 8$ in the small-world regime. We regard the next nearest neighbors as first neighbors in the topological sense by setting all interactions to be of equal strength. Assigning a finite value to the initial magnetization $m_0 \neq 0$ can be understood as introducing an initial bias toward local state clustering in the network. Modifying the Glauber dynamical rule by allowing state transitions only in the case of a strong local majority allows us to understand the effect of energy neutral processes on ordering in disordered topologies. In this scenario, nodes with an equal number of neighbors in both states are ignored when encountered during a trial rather than having their state determined stochastically. It turns out that the ground state is always reached on regular square lattices when a strong majority is necessary for state transition, *i.e.*, the striped state turns out to be the consequence of energy neutral stochastic flips.

To gain a more comprehensive insight into structure of the disordered configurations, we make a distinction between the domains comprised of topologically connected

nodes in the same state, and the clusters with respect to positions of the nodes on the original regular lattice. The lattice and the graph neighborhoods are always identical for spins placed on regular lattices. However, as the lattice structure is modified such that the links between neighbors are replaced by links to distant nodes, the lattice and the topological neighbors may not necessarily coincide, which results in rich patterns on the lattice. In order to investigate the crossover from frozen striped configurations occurring in regular lattices to disordered states occurring in the rewired lattices, we compare the correlation length ξ to characteristic graph length measures, namely the radius R, diameter D and the mean shortest path $\langle s \rangle$. The correlation length is defined as the decay rate of the two-point correlation function $G(l) = \langle S_i S_j \rangle - \langle S_i \rangle \langle S_j \rangle$ which measures the correlation of states as a function of the Manhattan distance l between the nodes. Note that ξ characterizes the competition between topology and dynamics on the state of distant nodes, while R, D and $\langle s \rangle$ are purely topological measures.

We also address the issue of how connecting two networks of the same size with different rewiring probabilities affects the ordering process. To do so, we compare the results obtained for the two-layer multiplex network (N bonds connecting nodes of two layers in one-to-one fashion) with the results for the case where the same number of inter-layer connections is distributed between randomly chosen pairs of nodes.

The main quantity of interest is the fraction of configurations that have not reached the ground state ("active configurations") f_a after a given simulation time T as a function of p. The absolute value of net magnetization $|m|$ is an order parameter for individual systems: $|m| = 1$ corresponds to the ground case, whereas $|m| = 0$ corresponds to the case in which there is an equal number of spins in both states. Thus, we measure the dependence of the final value of the magnetization $|m_f|$ in disordered configurations on p. However, $|m_f|$ contains no information about clustering in the network.

We simulate the dynamics on networks consisting of 50×50, 80×80 and 150×150 nodes for fixed values of N, $\langle k \rangle$, p and m_0. The total number of trials in each particular case is set to 1000. In summary, our numerical algorithm consists of the following steps:

I) *Regular network initialization.* Construct lattices with $k = 4$ or $k = 8$ as in fig. 1.

II) *Rewiring.* Following the method described in [15], our rewiring process ensures that there are no self-loops or multiple links between pairs of nodes, and that the minimal connectivity degree is 2. Bonds are sequentially selected at random and rewired with probability p until a desired fraction p of the total number of bonds is rewired.

III) *Spin state initialization.* The initial state is set by randomly putting each of the N spins into one of the possible states. If the initial magnetization is m_0, the state of each spin is set to $+1$ with the probability $p_{spin} = \frac{1+m_0}{2}$ and to -1 with probability $1 - p_{spin}$.

IV) *Glauber dynamics.* The evolution of the system is governed by the original or the modified (non-stochastic) Glauber dynamical rule, proceeding either until it reaches the ground state or until it fails to do so after a predetermined number of steps. We choose this value to be $T = 5000N$ (5000 attempted spin flips per node).

In what follows, we first analyze the case of a monolayer Watts-Strogatz network, and then consider the ordering process in paradigmatic two-layer networks with two types of inter-layer connections.

Monolayer networks. – Figure 2(a) shows how the fraction of active configurations f_a depends on p for Watts-Strogatz networks with local Glauber dynamics following a zero-temperature quench ($m_0 = 0$). The nonlinear dependence of f_a on p is observed regardless of $\langle k \rangle$, but turns out to be qualitatively different for the cases $\langle k \rangle = 4$ and $\langle k \rangle = 8$. When $\langle k \rangle = 8$, with increasing randomness ($p \gtrsim 0.5$), the dynamics leads to almost complete ordering. Nevertheless, when $\langle k \rangle = 4$, a finite fraction of configurations fails to reach the ground state in the thermodynamic limit over the whole range of p values. In the small-world regime, however, the ground state is not reached in the thermodynamic limit in either case. The result that ordering cannot be attained in small worlds when state transitions are governed by Glauber dynamics has been previously demonstrated for rewired rings ($d = 1$) and rewired square lattices ($d = 2$) with $\langle k \rangle = 4$ [15,19].

One infers that the local neighborhood majority rule with stochastic spin flips cannot lead to an ordered state on graphs with a perturbed regular topology. While the neighborhood from the regular lattice is mostly conserved in the small-world limit, R, D and $\langle s \rangle$ on the other hand monotonically decrease with p due to the presence of short-cuts (see fig. 3). Thus, it follows that perturbing the local neighborhood essentially leads to dynamical frustration of the local majority rule. A very small amount of topological disorder is sufficient to induce the critical slowing-down of dynamics, causing the disordered states to appear as deformed stripes on the lattice. Further deformation of the stripes leads to multiclustering on the lattice, which is reflected in the crossover effect [20]. We have established that this effect corresponds to the drop of ξ below the topological distances. At the same time, the low value of ξ indicates the absence of long-range ferromagnetic order. The two-point correlation function is found to satisfy an exponential scaling law $G(l) \propto e^{-\frac{l}{\xi}}$ over the whole range of p. Furthermore, depending on the p value, both ξ and R, D and $\langle s \rangle$ exhibit different scaling regimes.

In particular, in the small-world regime, $R, D, \langle s \rangle$ and ξ exhibit a power law dependence on p, $r \propto p^{-a}$ with $r \in \{R, D, \langle s \rangle, \xi\}$ and $a \in \{a_R, a_D, a_{\langle s \rangle}, a_\xi\}$. For 80×80
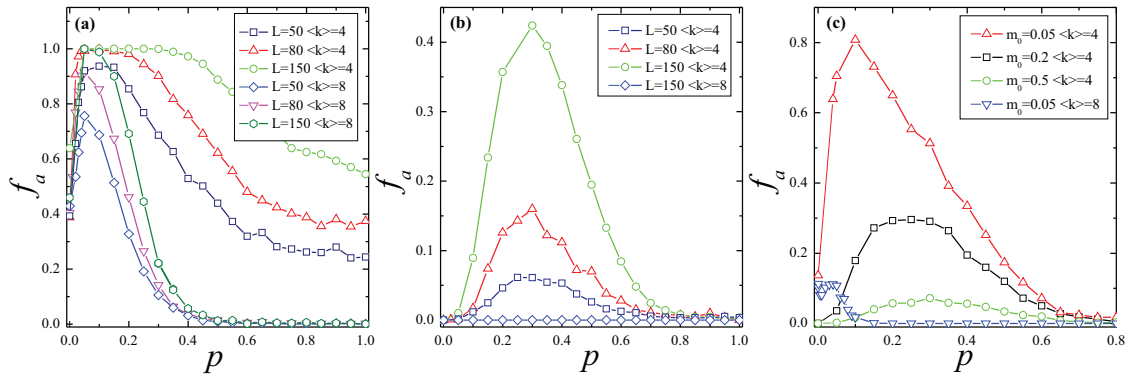
Fig. 2: (Color online) (a) Final fraction of active runs f_a in terms of rewiring probability p for the standard Glauber rule with $m_0 = 0$. The results are provided for networks with $\langle k \rangle = 4$ and $\langle k \rangle = 8$ neighbors and $L \in \{50, 80, 150\}$. Note that complete ordering is not observed in the small-world regime $0 < p \ll 1$ independent of $\langle k \rangle$. (b) Impact of modified Glauber rule: for $\langle k \rangle = 8$, the system reaches complete ordering (hence only the curve corresponding to $L = 150$ is shown), whereas for $\langle k \rangle = 4$, the frustration effect emerges at intermediate p, becoming more pronounced with the network size. Panel (c) displays f_a for systems governed by the standard Glauber rule starting from initial conditions $m_0 \neq 0$. The influence of small worldliness is such that it suppresses disorder regardless of $\langle k \rangle$ with increasing m_0, while it still promotes disorder at intermediate p range for $\langle k \rangle = 4$.
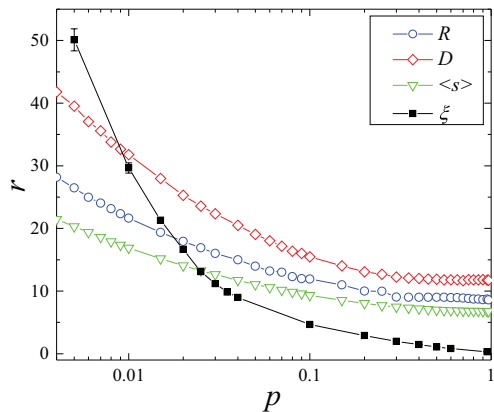
Fig. 3: (Color online) Correlation length ξ compared to graph distance measures (radius R, diameter D, and average path length $\langle s \rangle$) as functions of p. While ξ reflects the interplay between the dynamics and the network structure, the remaining quantities characterize purely topological features of the network. Crossing of $\xi(p)$ with other curves indicates the transition between the dynamics typical for the regular lattices and that for the rewired networks. Note that all four quantities exhibit a power law dependence $r \propto p^{-a}$ in the p region approximately coinciding with the small-world regime. The results refer to networks with 80×80 nodes and $\langle k \rangle = 4$.

networks, the following values for the exponent a are found: $a_R = -0.259 \pm 0.004$, $a_D = -0.296 \pm 0.005$, $a_{\langle s \rangle} = -0.25 \pm 0.003$ and $a_\xi = -0.77 \pm 0.01$. For larger values of p, the topological measures do not change significantly with increasing p indicating that topological effects remain the same after ≈ 0.5. Nevertheless, ξ decays to zero as $p \to 1$, which implies that the dynamics is sensitive to rewiring over the whole range of p, as corroborated by the growing number of "clusters" of decreased sizes in disordered configurations for large p, see fig. 4.

Interestingly, a deeper understanding of the difference in ordering efficiency in terms of p may be gained by

considering f_a for configurations governed by the modified Glauber rule. Evidently, the difficulty in attaining order subsides when stochasticity is eliminated from the dynamics in the small-world limit regardless of $\langle k \rangle$, see fig. 2(b). In other words, the ground state is reached with probability one if energy-neutral state transitions are not allowed. This always holds for $\langle k \rangle = 8$, and also for networks with $\langle k \rangle = 4$ in the limits $p \to 0$ and $p \to 1$. For intermediate p, ordering remains suppressed to a certain degree.

The next objective is to demonstrate that varying initial magnetization m_0 allows one to interpolate between the influences of dynamics and topology. Figure 2(c) shows f_a as a function of p for $m_0 \neq 0$ under the standard Glauber rule. While initial bias towards local clustering promotes complete ordering for regular networks, the dynamical outcome is different for rewired networks. In case $\langle k \rangle = 8$, small values of $m_0 \neq 0$ significantly increase ordering, whereby the position of the peak of $f_a(p)$ coincides with the peak value of $f_a(p)$ at $m_0 = 0$. Perturbing the quenched initial state on graphs in the small-world regime increases the prevalence of the ground state. Nevertheless, the peaks of $f_a(p)$ curves for $\langle k \rangle = 4$ networks in fig. 2(c) shift toward the peak value from fig. 2(b) as m_0 is increased. A fraction of configurations still fails to reach the ground state for some values of p, even for high values of m_0. The shift demonstrates that as the number of stochastic state transitions decreases due to the initial bias in clustering, the dynamical frustration is reduced. Nonetheless, the topological obstructions in networks with low $\langle k \rangle$ can suppress ordering even for high values of m_0.

Further insight on this issue can be gained by observing how $|m_f|$ averaged over active configurations depends on p, see fig. 5. The initial increase in magnetization corresponds to the divergence of relaxation time in the limit $p \to 0$, *i.e.*, the crossover from large-world to small-world behavior. Expectedly, there is a qualitative difference in
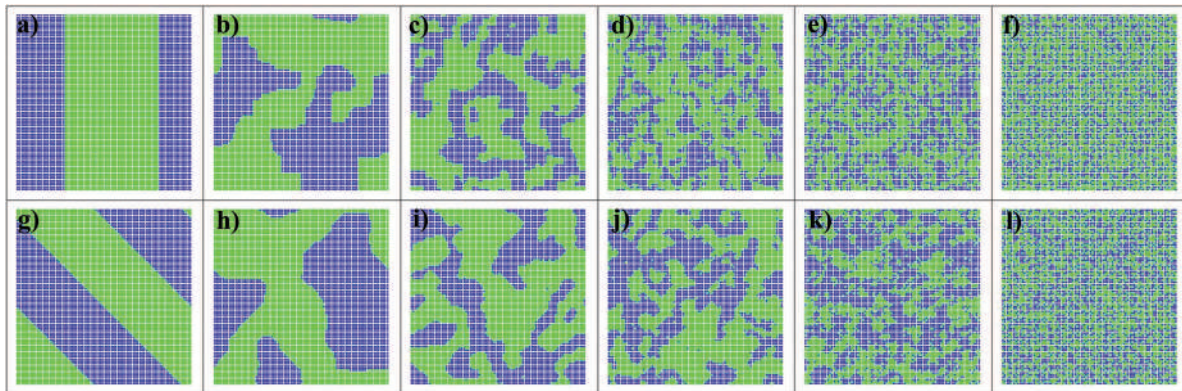
Fig. 4: (Color online) Snapshots of disordered configurations at $T = T_f$ on the lattice. The top (bottom) row refers to networks with $\langle k \rangle = 4$ ($\langle k \rangle = 8$). The rewiring probabilities are $p = 0$ in (a) and (g), $p = 0.02$ in (b) and (h), $p = 0.1$ in (c) and (i), $p = 0.3$ in (d) and (j), $p = 0.5$ in (e) and (k), as well as $p = 1$ in (f) and (l). The stripe structure is gradually lost with increasing p, giving way to the multiclustered states with respect to the original lattice. The number of domains increases with p as the network topology substantially departs from the lattice one. In terms of the network structure, each of the disordered configurations consists of two connected components. All the results are obtained for networks with 80×80 nodes.
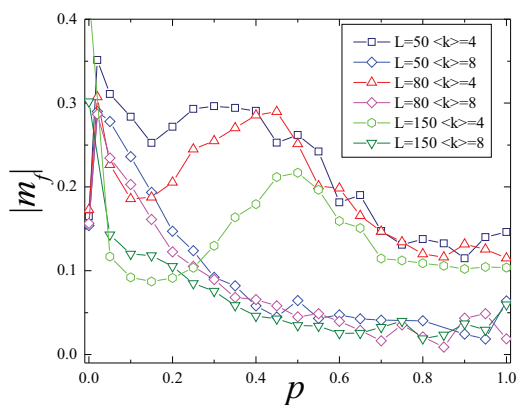
Fig. 5: (Color online) Final magnetization averaged over the ensemble of disordered configurations $|m_f|$ in dependence of p. For $\langle k \rangle = 8$, one finds approximately equal numbers of nodes in both states as $p \to 0$. For $\langle k \rangle = 4$, within the small-world regime, $|m_f|$ is reduced compared to the regular lattice, while for intermediate p, the droplet configurations lead to an increase of $|m_f|$. The peak of $|m_f|(p)$ gets shifted because the fraction of active runs is higher at a wider range of p values for larger networks, cf. fig. 2(a).

the $|m_f|(p)$ profile for different $\langle k \rangle$ under increasing p. The curves for $\langle k \rangle = 8$ monotonically decrease, indicating that the small number of configurations that does survive converges to a state consisting of a similar number of opposite spins in the limit $p \to 1$. In contrast, the initial decrease in $|m_f|$ for networks with $\langle k \rangle = 4$ is followed by the peak at intermediate values of p, associated to the presence of droplet configurations with $|m_f| \to 1$.

Moreover, we have verified that the disordered configurations in the small-world regime consist of two intertwined topological spin domains of almost similar size with stochastically fluctuating interfaces. An example of such a two-component state for $p = 0.1$ is provided in fig. 6, whereby the corresponding lattice domain configuration is shown in fig. 4(c). Blinkers that arise as a result of the
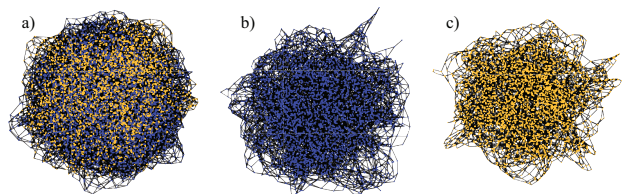
Fig. 6: (Color online) Example of a disordered configuration obtained for the network of size 80×80, with $\langle k \rangle = 4$ neighbors on average and $p = 0.1$ rewired links. (a) refers to the full configuration, whereas (b) and (c) show the larger component (3637 nodes) and the smaller component (2763 nodes), respectively. The final magnetization is $|m_f| \approx 0.14$. The nodes are separated into two domains of similar size, forming a multi-domain state on the lattice, cf. fig. 5(c).

long-range connections can be present along with stochastic flipping of interfaces on the lattice. Increasing p corresponds to the formation of domains with decreasing size with respect to the lattice. Several examples of configurations with two topological components for different p are shown in fig. 4. The number of these domains counted on the lattice grows exponentially with p (not shown). In the random network limit, as the fraction of links belonging to the original lattice $1 - p$ decreases, clusters become indistinguishable when observed on the lattice. Topologically, the two-domain configuration is reminiscent of the disordered configurations of the voter model on small-world networks [8,21]. Once the dynamics cannot cause further decrease in energy, the interface length reaches a constant value, as interface diffusion is no longer possible. In this scenario, while a fraction of nodes with even connectivity degrees continues to flip indefinitely with no energy cost, the states of the odd-degree nodes become stationary.

Nevertheless, the disordered configurations associated to the increase of f_a in fig. 2(b) for $\langle k \rangle = 4$ are frozen at very high values of $|m_f|$, viz. $|m_f| \to 1$ in
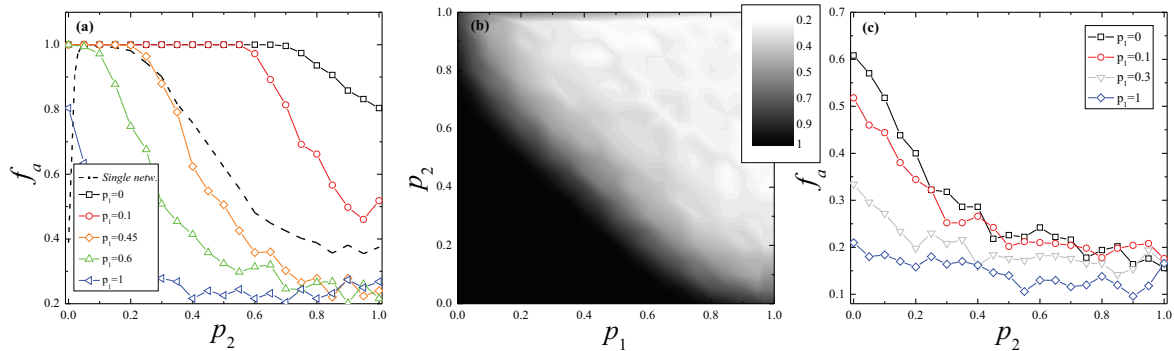
Fig. 7: (Color online) (a) Ordering in two-layer multiplex networks: f_a for the layer with rewiring probability p_1 (see the legend) in terms of the rewiring probability p_2 of the other layer. For comparison, the results for the single (monolayer) network are indicated by the dashed line. (b) f_a of a single layer of a multiplex network as a function of p_1 and p_2. The states of two layers are strongly correlated, but the ordering is completely inhibited in the small-world regime. (c) f_a of a layer of the network with random inter-layer connectivity. Ordering is significantly improved for all values of p. All the results are obtained for networks with 80×80 nodes and $\langle k \rangle = 4$.

the thermodynamic limit, and correspond to *absorbing* states of the network. These configurations result from low connectivity and consist of a tiny fraction of spins isolated in small domains surrounded by the "sea" of nodes of the opposite orientation. In this scenario, nodes with small k form stable droplets of opposing magnetization which cannot be dynamically influenced by the nodes from the rest of the network, preventing the system from reaching the full order. These droplets may appear on the remnants of the regular lattice, such that their interior consists of nodes connected by links from the regular lattice ($k = 4$), whereas their boundary is mainly comprised of nodes with one removed link ($k = 3$), thereby trapping the "interior" in the same state. Even-degree nodes that appear on the boundaries have more links with nodes within the droplet than with other neighbors, such that their state cannot be changed either. With further rewiring of the lattice, stable droplets may still form as even smaller groups of interconnected nodes with small degrees ($k = 2$ or $k = 3$), likewise disconnected from the rest of the network. The larger the network, the more likely becomes such a scenario. Also, for larger network sizes, a larger number of droplets may be present, which is the reason why a larger fraction of configurations fails to reach order. This peculiar frustration on the remnants of a regular lattice also accounts for the incomplete ordering of systems governed by the standard Glauber dynamics in rewired networks with $\langle k \rangle = 4$, and explains for the difference in the behavior in the limit $p \to 1$. Final configurations in networks with $\langle k \rangle = 4$ can consist of two large components and a few isolated droplets for p above the small-world regime, similar to final configurations obtained for $m_0 \neq 0$.

Two-layer networks. – We now address the ordering process in multilayer networks, focussing on the paradigmatic example of two coupled $\langle k \rangle = 4$ networks with different rewiring probabilities p_1 and p_2. By our

algorithm, the individual layers are rewired consecutively, after which N links are introduced between them, either at random or with the one-to-one correspondence between the layers' nodes. The simulation is terminated after $2T$ steps if order is not reached. Note that introducing new links effectively generates a large network with $\langle k \rangle = 5$ and $5N$ bonds.

Our findings indicate that both cases lead to highly correlated states of layers, which are simultaneously ordered/disordered and have $m_{f1} \approx m_{f2}$. For this reason, f_a of a single layer presents an appropriate quantity to characterize the ordering process. We find that the dependence of f_a on rewiring probability changes qualitatively depending on the nature of the inter-layer bonds, cf. fig. 7(a) and fig. 7(c). The multiplex configuration turns out to suppress ordering of both networks in the small-world regime, as indicated in fig. 7(a) and fig. 7(b). However, fig. 7(a) shows that ordering efficiency can be increased if at least one of the networks is "sufficiently random", with a smooth transition taking place at $0.35 \lesssim p \lesssim 0.45$. Interestingly, the other scenario, which involves placing the same number of bonds between randomly chosen pairs of nodes from both networks, promotes both ordering and correlation between the layer states. This is corroborated by fig. 7, suggesting that regardless of p_1 and p_2, ordering in this case is significantly improved compared to that on a single network and the multiplex network.

The curves obtained for multiplex networks resemble the ones obtained for the single network even for p as large as 0.6, while those obtained for random inter-layer connections are monotonically decreasing as p_2 is increased over the whole range of p. Even though in both cases networks become correlated in terms of m_f and ordering, multiplexing seems to preserve the type of dynamics obtained on small-world structures of one network, while introducing random bonds between the layers destroys the small-worldliness effect.

Conclusions. – We have analyzed ordering efficiency of the Glauber model of Ising spin kinetics on the Watts-Strogatz networks obtained by rewiring from the two-dimensional square lattices with coordination numbers $\langle k \rangle = 4$ and $\langle k \rangle = 8$. We have extended the previous results concerning the failure of such systems to reach the ground state in the small-world regime $0 < p \ll 1$, gaining insight into the associated disordered configurations. The fraction of active configurations exhibits a nonlinear dependence on the rewiring probability. It is interesting that a similar type of dependence has been observed in relation to the synchronization process on small-world networks [22]. It is found that the Glauber dynamics on small-world networks becomes stuck in metastable stationary active configurations, which consist of two intertwined domains of opposite spins, whereby the fraction of nodes on the interfaces flips indefinitely. This effect is manifested as clustering patterns in the lattice representation. The size of domains on the lattice becomes smaller as p is increased. We have demonstrated that the limiting value of p at which the number of lattice and topological domains is equal (to two) corresponds to the value where the correlation length ξ becomes smaller than the average path length in the network.

Our analysis shows that the active configurations in the small-world regime emerge when the perturbed regular topology constrains the number of possible energy lowering processes, while the stochastic energy-neutral spin-flipping processes contribute to dynamical frustration and trap the system in a set of metastable states with the same energy. While the ground state is not accessible because energy lowering processes are not possible, the energy-neutral processes allow for the transitions between states of the same energy. This is similar to what has been reported for Glauber dynamics on 3D regular lattices [23], Glauber dynamics on random graphs [8], and the voter model on small-world networks [21].

We have further demonstrated that there exists a finite probability of finding another type of disordered configuration in networks with low connectivity for intermediate values of p. These are frozen, almost completely ordered states with a few isolated droplets of opposing magnetization. For $\langle k \rangle = 8$, such configurations become unlikely due to the high average connectivity degree in the network, giving way to fully ordered states if p is sufficiently increased ($p > 0.5$). In networks with $\langle k \rangle = 4$, a certain fraction of configurations exists as a combination of these states, especially if an initial bias towards clustering ($m_0 \neq 0$) is introduced.

We have also examined the features of the ordering process in paradigmatic two-layer networks. It has been found that the structure of inter-layer connections strongly affects the ordering process. In particular, multiplexing decreases ordering efficiency in the small-world regime $0 < p \ll 1$, but improves it if the rewiring probability in both layers is sufficiently high. Nevertheless, random connectivity between the layers always promotes ordering, regardless of layer topology. In all the considered scenarios, the layers typically end up in highly correlated states.

We believe that the future research may be directed towards extending our findings on the dynamics of interacting rewired networks. In particular, it could be interesting to modify inter-layer coupling strengths, vary the number of connections between the layers or consider hierarchical networks and networks with a large number of layers.

$* * *$

REFERENCES

[1] STROGATZ S., *Nature*, **410** (2001) 268.
[2] ALBERT R. and BARABÁSI A.-L., *Rev. Mod. Phys.*, **74** (2002) 47.
[3] BOCCALETTI S., LATORA V., MORENO Y., CHAVEZ M. and HWANG D.-U., *Phys. Rep.*, **424** (2006) 175.
[4] BRAY A. J., *Adv. Phys.*, **51** (2002) 481.
[5] CASTELLANO C., *Rev. Mod. Phys.*, **81** (2009) 591.
[6] PASTOR-SATORRAS R., CASTELLANO C., VAN MIEGHEM P. and VESPIGNANI A., *Rev. Mod. Phys.*, **87** (2015) 925.
[7] KRAPIVSKY P. L., REDNER S. and BEN-NAIM E., *A Kinetic View of Statistical Physics* (Cambridge University Press, Cambridge) 2010.
[8] CASTELLANO C., LORETO V., BARRAT A., CECCONI F. and PARISI D., *Phys. Rev. E*, **71** (2005) 066107.
[9] STAUFFER D., *Am. J. Phys.*, **76** (2008) 470.
[10] GANGULY J., *Advances in Physical Geochemistry: Diffusion, Atomic Ordering, and Mass Transport* (Springer, New York) 2012.
[11] BOSCO E., *J. Electroanal. Chem.*, **346** (1993) 433.
[12] BARABÁSI A.-L. and ALBERT R., *Science*, **286** (1999) 509.
[13] WATTS D. J. and STROGATZ S. H., *Nature*, **393** (1998) 440.
[14] CASTELLANO C. and PASTOR-SATORRAS R., *J. Stat. Mech.* (2006) P05001.
[15] HERRERO C. P., *J. Phys. A: Math. Theor.*, **42** (2009) 415102.
[16] BAEK Y., HA M. and JEONG H., *Phys. Rev. E*, **85** (2012) 031123.
[17] BOCCALETTI S. *et al.*, *Phys. Rep.*, **544** (2014) 1.
[18] SPIRIN V., KRAPIVSKY P. L. and REDNER S., *Phys. Rev. E*, **65** (2001) 016119.
[19] BOYER D. and MIRAMONTES O., *Phys. Rev. E*, **67** (2003) 035102.
[20] BARTHÉLÉMY M. and AMARAL L. A. N., *Phys. Rev. Lett.*, **82** (1999) 3180.
[21] CASTELLANO C., VILONE D. and VESPIGNANI A., *Europhys. Lett.*, **63** (2003) 153.
[22] GRABOW C., HILL S. M., GROSSKINSKY S. and TIMME M., *Europhys. Lett.*, **90** (2010) 48002.
[23] SPIRIN V., KRAPIVSKY P. L. and REDNER S., *Phys. Rev. E*, **63** (2001) 036118.

THE EUROPEAN
PHYSICAL JOURNAL
SPECIAL TOPICS

Regular Article

Noise-induced switching in two adaptively coupled excitable systems

Iva Bačić[1], Serhiy Yanchuk[2], Matthias Wolfrum[3], and Igor Franović[1,a]

[1] Scientific Computing Laboratory, Center for the Study of Complex Systems, Institute of Physics Belgrade, University of Belgrade, Pregrevica 118, 11080 Belgrade, Serbia
[2] Institute of Mathematics, Technische Universität Berlin, Straße des 17. Juni 136, 10623 Berlin, Germany
[3] Weierstrass Institute, Mohrenstrasse 39, 10117 Berlin, Germany

Abstract. We demonstrate that the interplay of noise and plasticity gives rise to slow stochastic fluctuations in a system of two adaptively coupled active rotators with excitable local dynamics. Depending on the adaptation rate, two qualitatively different types of switching behavior are observed. For slower adaptation, one finds alternation between two modes of noise-induced oscillations, whereby the modes are distinguished by the different order of spiking between the units. In case of faster adaptation, the system switches between the metastable states derived from coexisting attractors of the corresponding deterministic system, whereby the phases exhibit a bursting-like behavior. The qualitative features of the switching dynamics are analyzed within the framework of fast-slow analysis.

1 Introduction

In many complex systems, ranging from biology, physics and chemistry to social sciences and engineering, the interaction patterns are not static, but are rather affected by the states of constituent units [1–4]. This gives rise to complex feedback mechanisms, where the coupling weights adapt to dynamical processes at the units, which in turn influences the evolution of units itself. Modeling of such systems is based on the paradigm of adaptive networks, where self-organization unfolds both at the level of coupling weights and the collective states of the units, typically involving a separation of characteristic timescales. The faster and the slower timescales are naturally associated to the dynamics of units and couplings, respectively, such that the short-term evolution of the units occurs on a quasi-static network, whereas the slow changes in coupling weights depend on the time-averaged dynamics of the units. An important example of adaptive connectivity is provided by neuronal systems, where the strength of synaptic couplings is adjusted to the underlying spiking activity via spike-time-dependent plasticity (STDP), a temporally asymmetric form of Hebbian learning [5],

---

[a] e-mail: franovic@ipb.ac.rs

promoting causal relationship between the spikes of pre- and postsynaptic neurons [6–8].

Motivated by the research on neuronal systems, in the present paper we study a simplified model which incorporates the basic ingredients of neurodynamics, such as excitability, plasticity and noise. The considered system consists of two adaptively coupled active rotators, whose intrinsic dynamics is set to excitable regime and subjected to noise. The plasticity rule is introduced in such a way that one may continuously interpolate between the coupling dynamics characteristic to Hebbian learning and STDP. We demonstrate that the interplay of plasticity and noise may facilitate two qualitatively different forms of slow stochastic fluctuations, depending on the adaptation rate. While for slower adaptation the self-organized dynamics consists of switching between the two modes of noise-induced oscillations, in case of faster adaptation, the switching dynamics comprises metastable states associated to attractors of the deterministic system.

In the context of neuroscience, one may compare the considered system to a binary neuron motif. It is well known that the same structural motif, defined at the level of anatomy, can support multiple functional motifs [9–12], characterized by different weight configurations and potentially distinct directions of information flow. In these terms, our study will show that the co-effect of plasticity and noise may (i) contribute to the emergence of different functional motifs on top of the given structural one and (ii) trigger slow alternation between the functional motifs.

So far, the co-effects of noise and the STDP plasticity rule have been analyzed in systems of two coupled neural oscillators, as well as in networks of oscillators. In case of two units, multistability between different weight configurations has been found, surprisingly indicating that noise may stabilize configurations of strong bidirectional coupling absent in the deterministic system [13]. At variance with this, our study concerns excitable local dynamics and explicitly addresses the slow stochastic fluctuations between metastable states. For networks of adaptively coupled neural or phase oscillators, the previous research has mainly focused on the impact of plasticity on the synchronization behavior. In the absence of noise, several generic forms of macroscopic dynamics have been identified, including desynchronized or partially synchronized states with weak couplings, as well as cluster states [14–18]. In presence of noise, an interesting effect of self-organized noise resistance to desynchronization has been reported in the case of a network of neural oscillators [19]. In networks of excitable units, the STDP rule has been shown to give rise to oscillating coupling configurations that facilitate switching between strongly and weakly synchronized states [20–22].

The paper is organized as follows. The details of the model are introduced in Section 2. An overview of the underlying deterministic dynamics, characterizing the impact of plasticity on the stationary states and the onset of emergent oscillations, is provided in Section 3. Section 4 is dedicated to a fast–slow analysis of the deterministic dynamics, whereas in Section 5 are explained the features of the two generic types of switching behavior. In Section 6 we provide a summary of our main results.

2 Model

We consider a system of two stochastic active rotators interacting by adaptive couplings, where the dynamics of the phases $\{\varphi_1(t), \varphi_2(t)\}$ and the coupling weights $\{\kappa_1(t), \kappa_2(t)\}$ is given by

$$
\begin{aligned}
\dot{\varphi_1} &= I_0 - \sin\varphi_1 + \kappa_1 \sin(\varphi_2 - \varphi_1) + \sqrt{D}\xi_1 \\
\dot{\varphi_2} &= I_0 - \sin\varphi_2 + \kappa_2 \sin(\varphi_1 - \varphi_2) + \sqrt{D}\xi_2 \\
\dot{\kappa_1} &= \epsilon(-\kappa_1 + \sin(\varphi_2 - \varphi_1 + \beta)) \\
\dot{\kappa_2} &= \epsilon(-\kappa_2 + \sin(\varphi_1 - \varphi_2 + \beta)),
\end{aligned}
\tag{1}
$$

where $\varphi_1, \varphi_2 \in S^1$, while κ_1 and κ_2 are real variables. The rotators are assumed to be identical, having their local dynamics governed by the excitability parameter I_0, which gives rise to a SNIPER bifurcation at $I_0 = 1$. We focus on the excitable regime, such that $I_0 = 0.95$ is kept fixed throughout the paper. In this case, the uncoupled system always converges to a steady state, whereas the collective dynamics emerges due to interaction and noise. The parameter $\epsilon \ll 1$ defines the scale separation between the fast dynamics of the phases and the slow dynamics of adaptation. White noise of variance D acts only within the subspace of fast variables, whereby the terms $\xi_1(t)$ and $\xi_2(t)$ are independent ($\langle \xi_i(t)\xi_j(t') \rangle = \delta_{ij}\delta(t - t')$ for $i, j \in \{1, 2\}$). In the context of neuroscience, I_0 can be interpreted as external bias current, whereas the impact of stochastic terms is analogous to that of synaptic noise. Note that the deterministic version of (1) is symmetric with respect to the exchange of indices $1 \leftrightarrow 2$.

The plasticity rule is controlled by the parameter β, which allows one to interpolate between the different adaptation modalities. The analogy between the adaptivity dynamics in classical neuronal systems and the systems of coupled phase oscillators has been addressed in [14,23,24], whereas a deeper analysis of the correspondence between the phase-dependent plasticity rules and the STDP has been provided in [13]. From these studies, it follows that the scenario found for $\beta = 3\pi/2$, where the stationary weights increase for smaller phase differences and decrease for larger ones ("like-and-like" form of behavior), qualitatively resembles the Hebbian learning rule [23,24]. Nevertheless, in the case $\beta = \pi$, the two coupling weights always change in opposite directions, which may be interpreted as promoting an STDP-like plasticity rule. In the present paper, we are interested in the β interval between these two limit cases, since it admits two coexisting excitable fixed points.

3 Deterministic dynamics of the full system

In this section, we analyze the details of the *deterministic* dynamics of the full system (1), considering first the stationary states and the associated excitability feature, and then focusing on the scenario that gives rise to emergent oscillations.

3.1 Stationary states and excitable dynamics

Fixed points $(\varphi_1^*, \varphi_2^*, \kappa_1^*, \kappa_2^*)$ of the complete system (1) for $D = 0$ are given by the solutions of the following set of equations:

$$\sin \varphi_1^* - \sin(\varphi_2^* - \varphi_1^* + \beta)\sin(\varphi_2^* - \varphi_1^*) = I_0,$$
$$\sin \varphi_2^* - \sin(\varphi_1^* - \varphi_2^* + \beta)\sin(\varphi_1^* - \varphi_2^*) = I_0, \qquad (2)$$

with

$$\kappa_1^* = \sin(\varphi_2^* - \varphi_1^* + \beta),$$
$$\kappa_2^* = \sin(\varphi_1^* - \varphi_2^* + \beta). \qquad (3)$$

Equation (2) can be solved numerically for any fixed parameter set, or numerical path-following can be applied in order to study the dependence of the fixed points on the parameters.

The bifurcation diagram in Figure 1 shows how the number and stability of fixed points of the full system change with β. In particular, depending on β, there may be two, four or six fixed points. Due to symmetry, the solutions always appear in pairs of points sharing the same stability features. Since our study concerns plasticity rules which support excitable fixed points, we have confined the analysis to the interval $\beta \in (3.298, 4.495)$, where the system has *two stable* fixed points, which lie off the synchronization manifold $\varphi_1 = \varphi_2$. Apart from that, there are also four unstable
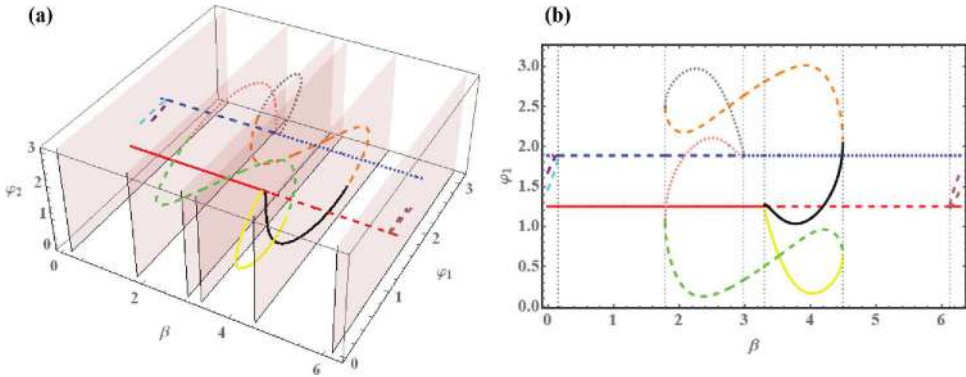
Fig. 1. (a) Bifurcation diagram for the fixed points of system (1) with $D = 0$ in the $(\beta, \varphi_1, \varphi_2)$ space. (b) Projection of the bifurcation diagram to (β, φ_1) plane. The two fixed points independent on β belong to the synchronization manifold: the red (blue) one is always longitudinally stable (unstable). The solid lines denote stable fixed points, whereas the dashed and dotted lines denote saddles of unstable dimension 1 and 2, respectively.

fixed points. The bifurcations associated to the boundaries of the given β interval are as follows: at $\beta = 3.298$ the system undergoes a supercritical symmetry-breaking pitchfork bifurcation where a symmetry related pair of two stable fixed points off the synchronization manifold is created, whereas at $\beta = 4.495$, this pair meets another pair of unstable fixed points off the synchronization manifold such that both are annihilated in symmetry related inverse saddle-node bifurcations. For instance, at $\beta = 4.1$, one finds the symmetry related pair of stable foci given by $(\varphi_1, \varphi_2, \kappa_1, \kappa_2) = (1.177, 0.175, 0.032, -0.92)$ and $(\varphi_1, \varphi_2, \kappa_1, \kappa_2) = (0.175, 1.177, -0.92, 0.032)$. Note that these weight levels support effective master-slave configurations, where one unit exerts a much stronger influence on the other unit than vice versa.

The two stable asymmetric fixed points in the interval $\beta \in (3.298, 4.495)$ are excitable, and may exhibit several different types of response to external perturbations, see the classification in Figure 2. Introducing the perturbations by setting different initial conditions, we plot in Figure 2 the phase dynamics in the fast subspace while keeping the weights (κ_1, κ_2) fixed. Note that in the case where both units respond with a single spike, the order of firing is such that the unit with larger initial phase $\varphi_i(0), i \in \{1, 2\}$ fires first.

3.2 Onset of oscillations

The onset of emergent oscillations in system (1) with $D = 0$ depends on the interplay between the plasticity rule, specified by β, and the speed of adaptation, characterized by ϵ. A parameter scan indicating the variation of κ_1, $A_{\kappa_1} = \max(\kappa_1(t)) - \min(\kappa_1(t))$ in terms of (β, ϵ) is shown in Figure 3a. The results are obtained by numerical continuation beginning from a stable periodic solution, such that the final state reached for a certain set of (β, ϵ) values provides the initial conditions for the simulation of the system at incremented parameter values. By this method, we have determined the maximal stability region of the periodic solution.

One finds that for a fixed β, there actually exists an interval of timescales separation $\epsilon \in (\epsilon_{min}, \epsilon_{max})$ admitting oscillations, cf. Figure 3b. The periodic solutions in this interval coexist with the two symmetry-related stable stationary states. One observes that the threshold ϵ_{min} reduces with β, whereas the upper boundary value ϵ_{max} grows with increasing β. The detailed bifurcation mechanisms behind the onset
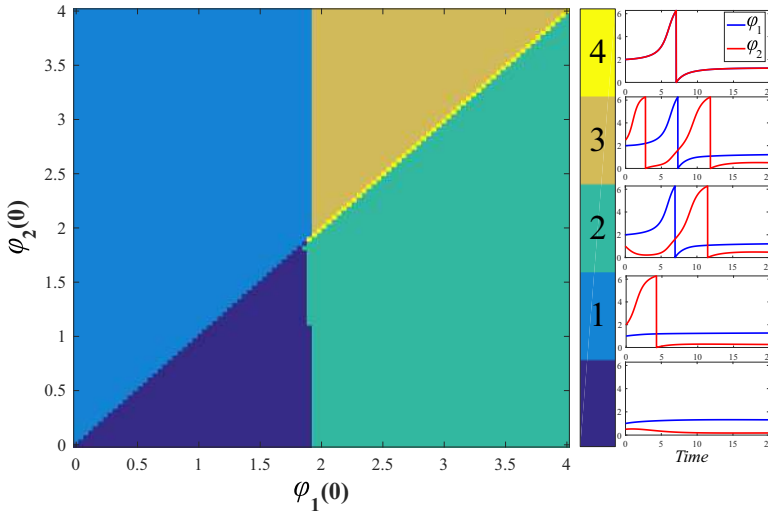
Fig. 2. Modalities of the response to external perturbation for system (1) with $D = 0$. The system parameters are $I_0 = 0.95$, $\epsilon = 0.01$ and $\beta = 4.212$, whereas the initial conditions for the coupling weights are set to $\kappa_1(0) = -0.0077$, $\kappa_2(0) = -0.846$. Depending on the initial phases $(\varphi_1(0), \varphi_2(0))$, one may observe the following regimes: (0) no spikes; (1) the unit with larger $\varphi(0)$ emits one spike and the other does not; (2) both units emit a single spike, with the unit with larger $\varphi(0)$ firing first; (3) the unit with larger $\varphi(0)$ emits two spikes and the other unit emits one; (4) both units spike synchronously.

of oscillations and multistability are beyond the scope of this paper, and essentially involve an interplay between the fast and slow variables.

Enhancing ϵ under fixed β gives rise to a supercritical symmetry-breaking pitchfork bifurcation of limit cycles, indicated by PFL in Figure 3b. Below the bifurcation, the phases $\varphi_1(t)$ and $\varphi_2(t)$ maintain a small phase-shift, while the oscillation profiles $\kappa_i(t), i \in \{1, 2\}$ are rather different, see Figures 3d and 3e, respectively. Above the bifurcation, the system gains the anti-phase space-time symmetry $\varphi_1(t) = \varphi_2(t + T/2), \kappa_1(t) = \kappa_2(t + T/2)$ where T denotes the oscillation period, cf. the associated waveforms in Figures 3g and 3f.

4 Slow-fast analysis of the deterministic dynamics

The deterministic dynamics in case of slow adaptation, corresponding to a strong timescale separation between the fast and slow variables, may be analyzed within the framework of standard fast-slow analysis. In general, one may either consider the layer problem, defined on the fast timescale, or the reduced problem, which concerns the slow timescale. Within the layer problem, the aim is to determine the fast flow dynamics $\varphi_1(t; \kappa_1, \kappa_2), \varphi_2(t; \kappa_1, \kappa_2)$ by treating the slow variables κ_1 and κ_2 as parameters, whereas the reduced problem consists in determining the dynamics of the slow flow $(\kappa_1(t), \kappa_2(t))$ (reduced flow) assuming that the fast flow of the layer problem is either at a stable equilibrium or at the averaged value of a stable regime.

In this section, we first investigate the fast layer problems. Depending on the values of the slow variables (κ_1, κ_2), the fast flow can exhibit several attractors, such that multiple sheets of the slow flow emerge from the averaged dynamics on the different attractors of the fast flow.
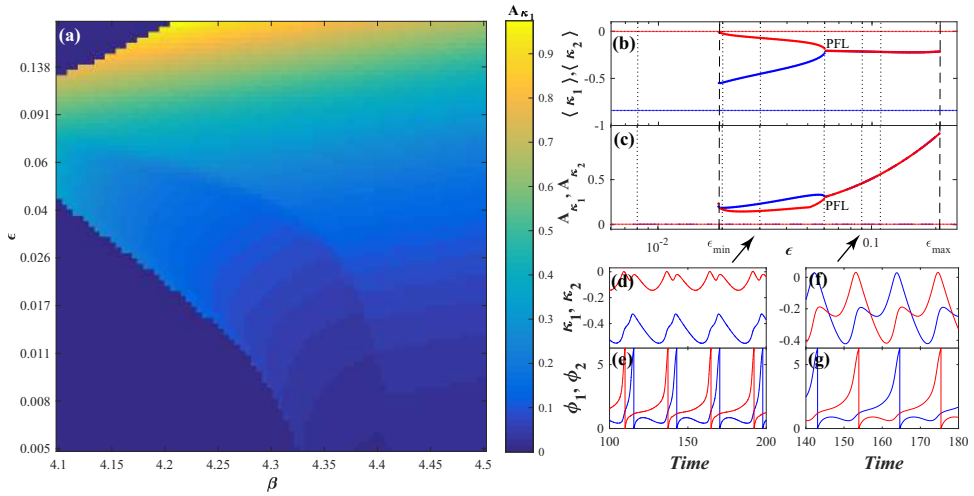
Fig. 3. Onset of oscillations in the full system (1) for $D = 0$. In panel (a) is shown how the variation A_{κ_1} of coupling weight κ_1 changes in the (β, ϵ) plane. Panel (b) shows how the mean coupling weights $\langle \kappa_1 \rangle$ and $\langle \kappa_2 \rangle$ of oscillatory states (thick lines) change with ϵ under fixed $\beta = 4.212$. The thin solid lines indicate the stationary state. In panel (c) are plotted the analogous dependencies for variation of the oscillation. The dotted lines in (b) and (c) indicate the ϵ values corresponding to the time traces in Figure 7, whereas the dashed lines indicate the boundaries of the ϵ region supporting the stable periodic solutions. The symmetry-breaking pitchfork bifurcation of limit cycles is denoted by PFL. In panels (d)–(g) are shown the waveforms of periodic solutions without and with the anti-phase space-time symmetry, obtained for $\epsilon = 0.03$ and $\epsilon = 0.09$, respectively (see the arrows). The excitability parameter is fixed to $I_0 = 0.95$.

4.1 Dynamics of the fast flow

Within the layer problem, one studies the dynamics of the fast variables

$$
\begin{aligned}
\dot{\varphi}_1 &= I_0 - \sin \varphi_1 + \kappa_1 \sin (\varphi_2 - \varphi_1) \\
\dot{\varphi}_2 &= I_0 - \sin \varphi_2 + \kappa_2 \sin (\varphi_1 - \varphi_2),
\end{aligned}
\tag{4}
$$

where $\kappa_1, \kappa_2 \in [-1, 1]$ are considered as additional system parameters. Formally, system (4) is obtained by setting $\varepsilon = 0$ in (1) for $D = 0$.

The numerically obtained bifurcation diagram in Figure 4a shows that the fast flow is monostable for most of the (κ_1, κ_2) values, possessing either an equilibrium or a limit cycle attractor. The stability boundary of the periodic solution (red curves) has been obtained by the method of numerical continuation where, beginning from a stable periodic solution, the initial conditions for incremented parameter values are given by the final state reached for the previous set of (β, ϵ) values. The coexistence between a stable fixed point, lying on the synchronization manifold, and a limit cycle is found within a small region near the diagonal, see Figure 4a. Let us first classify the fixed points of the fast flow and then examine the scenarios that give rise to oscillations.

It can be shown that the fast flow admits either two or four fixed points, with the associated regions indicated in Figure 4b. In particular, two fixed points FP1 and FP2 on the synchronization manifold are *independent* on κ_1 and κ_2. They are given by $(\varphi_1^*, \varphi_2^*) = (\arcsin I_0, \arcsin I_0)$ and $(\varphi_1^*, \varphi_2^*) = (\pi - \arcsin I_0, \pi - \arcsin I_0)$. One may also find two additional fixed points off the synchronization manifold, referred
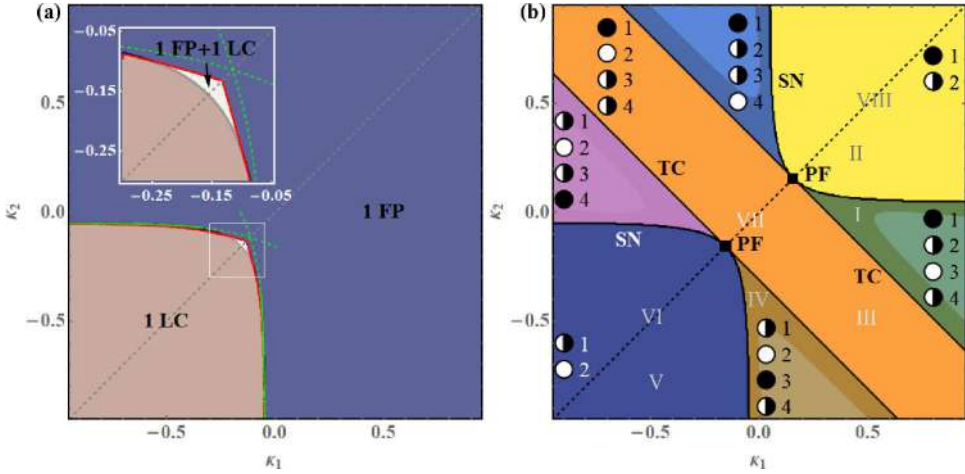
Fig. 4. (a) Attractors of the fast flow (4) in terms of κ_1 and κ_2, now considered as parameters. The fast flow is typically monostable, supporting either a stable fixed point (FP) or a stable limit cycle (LC), apart from a small region around the main diagonal, where it exhibits bistable behavior. The green dashed curves indicate approximations of two branches of SNIPER bifurcations, obtained by the method described in the text. The red lines correspond to the numerically determined stability boundaries of the oscillatory solution. (b) Classification of the fixed points of the fast flow (4). The fixed points are labeled the same way as in the main text, with their stability indicated as follows: full circles denote stable fixed points, semi-full circles represent saddle points and white circles correspond to doubly unstable fixed points. Within the four light-shaded triangular-shaped regions, the doubly unstable fixed point is a focus, rather than a node. The notation I–VIII refers to parameter values corresponding to the phase portraits in Figure 5.

to as FP3 and FP4 in Figure 4b. The bifurcations affecting the number and stability of the fixed points, beginning from the lower left region of the (κ_1, κ_2) plane, can be summarized as follows. Along the main diagonal $\kappa_1 = \kappa_2$, we find two points of supercritical pitchfork bifurcations (PF), where from the symmetric fixed points the saddles FP3 and FP4 appear and disappear. Off the main diagonal, the pitchforks are unfolded into curves of saddle-node (SN) and transcritical bifurcations (TC), see Figure 4b.

The (κ_1, κ_2) region featuring stable oscillations almost completely matches the lower left domain admitting two unstable fixed points. Within this region, each periodic solution obtained for (κ_1, κ_2) above the main diagonal $\kappa_1 = \kappa_2$ has a counterpart in the domain below the main diagonal, related to it by the exchange symmetry of units indices. Typically, the periodic solutions emerge via SNIPER bifurcations, comprising two branches where either κ_1 or κ_2 remain almost constant and close to zero. In both cases, the two fixed points that collide and disappear are FP3 and FP4. Nevertheless, such scenarios cannot be maintained in the small (κ_1, κ_2) region admitting coexistence between a fixed point and a limit cycle, because the SNIPER bifurcation is accompanied by a change in the number of fixed points. Our findings suggest that near the main diagonal, the limit cycle emerges via a heteroclinic bifurcation, where an orbit connects two saddles lying off the synchronization manifold (not shown). Note that the orbit of the limit cycle follows the unstable manifold of the saddle point FP2 on the synchronization manifold. To the left or the right of the main diagonal, instead of a heteroclinic bifurcation, one finds homoclinic bifurcations, whereby a saddle point, either FP3 or FP4, touches the limit cycle orbit. The schematic phase portraits indicating the stable and unstable manifolds of the fixed points and the limit
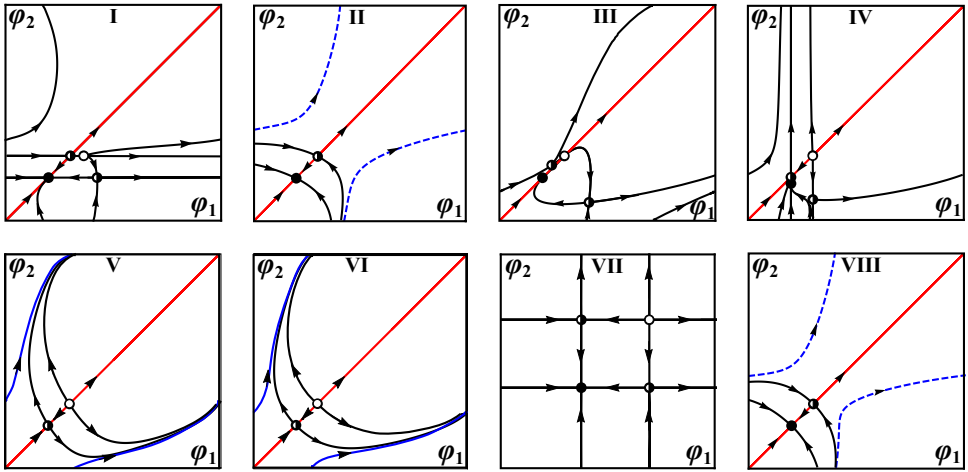
Fig. 5. Schematic phase portraits corresponding to the characteristic regimes of the fast flow. The panels I–VIII refer to representative parameter values indicated in Figure 4b. Also, the stability of fixed points is presented the same way as in Figure 4b. The invariant synchronization manifold is denoted by the red color, whereas the orbit of a stable/unstable limit cycle is indicated by the solid/dashed blue lines.

cycle for the characteristic regimes of the fast flow, denoted by I–VIII in Figure 4b, are illustrated in Figure 5.

The two branches of SNIPER bifurcations may readily be approximated for small values of κ_1 and κ_2 by a simple scheme, which amounts to reducing the fast flow to a normal form of saddle-node bifurcation. Suppose first that $\kappa_1 \ll 1$ and $I_0 - 1 \ll 1$. More specifically, let $\xi \ll 1$ be a small parameter such that $I_0 - 1 = \xi$ (close to the threshold) and $\kappa_1 = \gamma\xi$, i.e. γ is a rescaling parameter of κ_1, allowing for a zoom in the neighborhood of zero. Then, the steady states are given by the system

$$1 + \xi - \sin\varphi_1 + \xi\gamma\sin(\varphi_2 - \varphi_1) = 0,$$
$$1 + \xi - \sin\varphi_2 + \kappa_2\sin(\varphi_1 - \varphi_2) = 0. \tag{5}$$

The first equation in the zeroth order approximation leads to $\varphi_1 = \pi/2$. Hence, using the perturbation approach, we have

$$\varphi_1^* = \frac{\pi}{2} + \sqrt{\xi}\Psi_1 + \cdots ; \quad \varphi_2^* = \Psi_2 + \cdots , \tag{6}$$

where the $\sqrt{\xi}$ scaling follows from the Taylor expansion of the function $\sin\varphi_1$ at $\pi/2$. Inserting (6) into (5), one obtains the system of equations for Ψ_1 and Ψ_2

$$1 + \frac{1}{2}\Psi_1^2 - \gamma\cos\Psi_2 = 0,$$
$$1 - \sin\Psi_2 + \kappa_2\cos\Psi_2 = 0. \tag{7}$$

From system (7), it is not difficult to see that the saddle-node bifurcation takes place if the condition $1 - \gamma\cos\Psi_2 = 0$ is satisfied. This leads to the parametric representation $\kappa_1 = \xi\gamma = \frac{I_0 - 1}{\cos\Psi_2}, \kappa_2 = \frac{\sin\Psi_2 - 1}{\cos\Psi_2}$, of the saddle-node curve for small κ_1 values, where Ψ_2 plays the role of the parameter along the curve. An analogous approach may be used to capture the second branch of saddle-node bifurcations, cf. the green dashed lines in Figure 4a.

4.2 Dynamics of the slow flow

We have numerically obtained the dynamics of the slow flow by applying a two-step approach. First, for fixed values (κ_1, κ_2), we determine the time-averaged dynamics of the fast flow (4), $\langle \varphi_2 - \varphi_1 \rangle_t = f(\kappa_1, \kappa_2)$. Here, the averaging $\langle \cdot \rangle_t$ is performed over a sufficiently large time interval, having eliminated a transient. Hence, this average depends on the attractor of the fast flow for the given (κ_1, κ_2). In particular, if the fast flow possesses a stable fixed point, then $\langle \varphi_2 - \varphi_1 \rangle_t = \varphi_2^* - \varphi_1^*$, where $(\varphi_1^*, \varphi_2^*)$ is a solution of

$$
\begin{aligned}
I_0 - \sin \varphi_1^* + \kappa_1 \sin (\varphi_2^* - \varphi_1^*) = 0 \\
I_0 - \sin \varphi_2^* + \kappa_2 \sin (\varphi_1^* - \varphi_2^*) = 0.
\end{aligned}
\tag{8}
$$

This procedure just results in determining the slow critical manifold of the system. In case when the attractor of the fast flow is periodic, $\langle \varphi_2 - \varphi_1 \rangle_t$ presents the time average over the period. Averaging approximation in case of a periodic attractor of the fast flow constitutes a standard approach [13,25], rather natural for describing the influence of oscillations in the fast flow on the dynamics of the slow flow. At the second stage, the obtained time-averages are substituted into the dynamics of the weights

$$
\begin{aligned}
\dot{\kappa}_1 = \epsilon[-\kappa_1 + \sin(f(\kappa_1, \kappa_2) + \beta)] \\
\dot{\kappa}_2 = \epsilon[-\kappa_2 + \sin(-f(\kappa_1, \kappa_2) + \beta)].
\end{aligned}
\tag{9}
$$

The system (9) is used to determine the vector field of the slow flow by taking into account only the attractors of the fast flow, such that the vector field associated to each attractor is plotted within its respective stability region, cf. Figure 6.

In regions of the (κ_1, κ_2) plane where there are coexisting stable solutions of the fast flow, the corresponding vector field of the slow flow is given on multiple overlapping sheets, since the value of the average $f(\kappa_1, \kappa_2)$ depends on the initial conditions. In our case, this occurs only in a small region of coexistence between an equilibrium and a stable limit cycle.

One should single out two important features of the slow flow: (i) it exhibits two symmetry-related fixed points in the green and blue regions in Figure 6, and (ii) the slow vector field is pointed in opposite directions close to the boundary between the fast oscillatory regime (orange region) and the steady states of the fast flow (blue, green and white regions). The latter in particular implies that interesting effects occur close to the border of the oscillatory and the steady state regime of the fast flow. Moreover, adding noise gives rise to fluctuations around this boundary, which leads to switching between the quasi-stationary and the fast spiking dynamics. Such effects are studied in more detail within the next section.

5 Switching dynamics

Our main observation in this section is that the interplay of plasticity and noise induces slow stochastic fluctuations (switching dynamics), mediating two qualitatively different scenarios depending on the speed of adaptation. The latter include (i) switching between two modes of *noise-induced* oscillations for slower adaptation (small $\epsilon \simeq 0.01$) and (ii) switching between multiple coexisting attractors of the deterministic dynamics for faster adaptation (intermediate $\epsilon \simeq 0.05$).

In case (i), the impact of noise is twofold: on a short timescale, it gives rise to spiking dynamics, whereas on a long time scale, it induces random transitions between
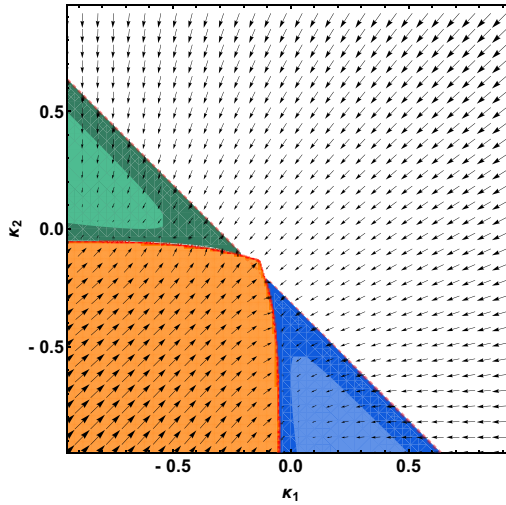
Fig. 6. Vector field of the slow flow obtained by taking into account only stable attractors of the fast flow for $\beta = 4.212, I_0 = 0.95$. The color coding is as follows: orange color denotes the region associated to the stable limit cycle of the fast flow, white stands for the stable fixed point of the fast flow FP1, whereas blue and green color correspond to the two stable fixed points FP3 and FP4. Within the light-shaded regions, FP3 and FP4 are foci rather than nodes, cf. Figure 4b.

the two oscillatory modes. In case (ii), the switching dynamics comprises metastable states derived from two fixed points, as well as two limit cycles associated to emergent oscillations of the corresponding deterministic system. The key difference between the effects (i) and (ii) is that for slower adaptation, the system switches between the oscillatory modes that do not exist as deterministic attractors. Moreover, the two generic types of switching are characterized by distinct phase dynamics: for slower adaptation, one finds alternation of patterns with different order of spiking between the units, whereas for faster adaptation, the phases effectively exhibit bursting behavior, involving a succession between episodes of spiking and relative quiescence. An overview on how the typical dynamics of couplings changes with ϵ at fixed β is provided in Figure 7. Note that the difference between the average coupling weights of the stable periodic solutions of the deterministic system are much smaller than a typical distance between the coupling levels for the stationary states. The prevalence of metastable states is affected by ϵ so that intermediate adaptation favors oscillatory modes, whereas the fast adaptation apparently promotes the two quasi-stationary states. In the next two subsections, we provide further insight into the mechanisms behind the switching dynamics using the results of the fast-slow analysis.

5.1 Switching dynamics under slow adaptation

As already indicated, ϵ is here taken sufficiently small, such that it cannot facilitate emergent oscillations in the full system (1). For $\epsilon \simeq 0.01$ and under appropriate noise levels, one observes noise-induced oscillations [26]. The latter arise via a scenario involving a multiple-timescale stochastic bifurcation, whereby noise acts only within the fast subsystem of (1). The onset of oscillations under increasing D occurs in two stages. In the first stage, the phase dynamics gradually exhibits more induced spikes,
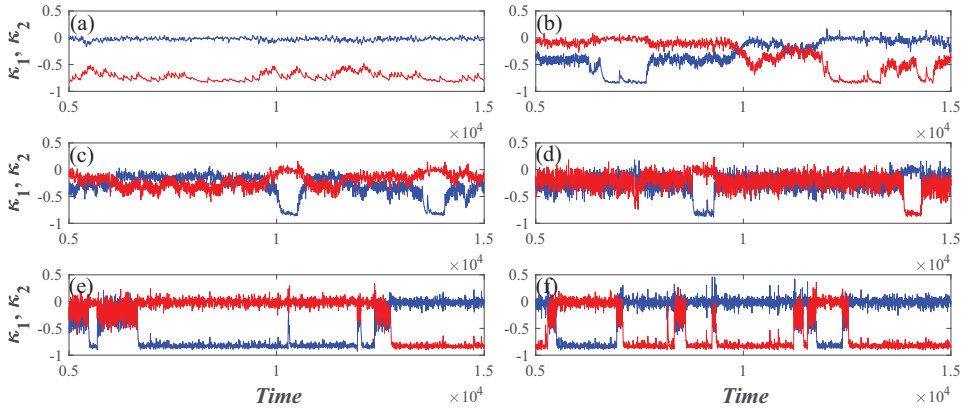
Fig. 7. Switching dynamics under variation of ϵ. The time traces $(\kappa_1(t), \kappa_2(t))$ are obtained for fixed $I_0 = 0.95$, $D = 0.006$, $\beta = 4.212$, whereas ϵ assumes the following values: (a) $\epsilon = 0.008$, (b) $\epsilon = 0.02$, (c) $\epsilon = 0.03$, (d) $\epsilon = 0.06$, (e) $\epsilon = 0.09$, (f) $\epsilon = 0.11$.
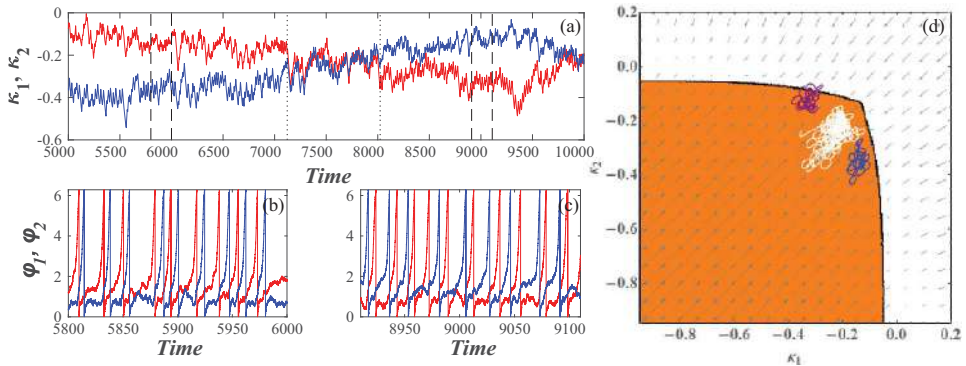
Fig. 8. Switching dynamics between the two modes of noise-induced oscillations. Time traces of the weights are shown in panel (a), whereas panel (b) and (c) display the corresponding time traces of the phases during the intervals between the dashed lines in panel (a). In panel (d), the $(\kappa_1(t), \kappa_2(t))$ projections of the orbits associated to each of the two modes (blue color), as well as the switching episode, shown in white, are superimposed to the vector field of the slow flow from Figure 6. The shaded area corresponds to the stable limit cycle. The system parameters are $I_0 = 0.95, \beta = 4.212, \epsilon = 0.01, D = 0.009$.

such that the stationary distributions of phases eventually acquire a longer tail reflecting the occurrence of spikes (not shown). Nevertheless, the stationary distributions $P(\kappa_i)$ change appreciably only at the second stage, which takes place for sufficiently large D. Such a change accompanies the emergence of coupling oscillations. Note that the system (1) actually exhibits *two modes* of noise-induced oscillations, characterized by the different order of firing between the two units, cf. the time traces of phase dynamics and the associated evolution of couplings in Figure 8a.

It is interesting to examine whether the vector field of the slow flow from Section 4.2 can be used to explain the slow stochastic fluctuations of the coupling weights. To this end, we have superimposed the $(\kappa_1(t), \kappa_2(t))$ orbits of the two noise-induced modes, as well as a switching episode, to a vector field of the slow flow from Figure 6. Note that the orbits typically lie close to the boundary outlining the transition between the two attractors of the fast flow, featuring non-negligible coupling weights. Moreover, the two modes are confined to small areas of the (κ_1, κ_2) plane
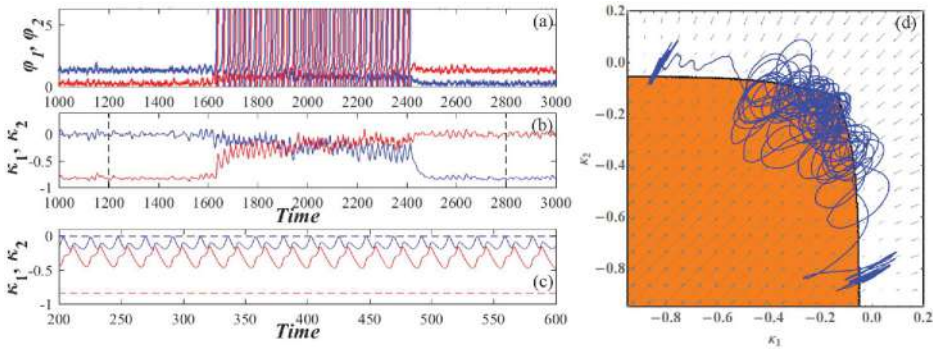
Fig. 9. Time traces of the phases (a) and weights (b) associated to noise-induced switching between the coexisting attractors of the deterministic system. The results are obtained for $I_0 = 0.95, \beta = 4.212, \epsilon = 0.05, D = 0.004$. In panel (c) is provided the deterministic dynamics of weights obtained for the same parameter values. In panel (d), the $(\kappa_1(t), \kappa_2(t))$ orbit corresponding to the interval between the dashed lines in (b) is super-imposed on the vector field of the slow flow cf. Figure 6.

symmetrical with respect to the main diagonal $\kappa_1 = \kappa_2$, whereas the switching episode virtually takes place on the diagonal. Apparently, the noise-induced modes occupy regions where the oscillations in the fast flow emerge via homoclinic bifurcations, rather than the SNIPER scenario. Nonetheless, the switching episode seems to involve the domain featuring coexistence of the two stable sheets of the slow vector field. Within these sheets, which correspond to two attractors of the fast flow (a stable node and a stable limit cycle), the vector fields are oriented in opposite directions, thereby contributing to switching.

5.2 Switching dynamics for faster adaptation

In case of faster adaptation associated to intermediate ϵ, the switching dynamics involves four metastable states, derived from the attractors of the deterministic system. The deterministic multistable behavior includes two symmetry-related stationary states, as well as two symmetry-related limit cycles. Note that while the two stable steady states exist for arbitrary small ϵ and are therefore visible in the slow flow in Figure 6, the oscillatory solutions disappear for small ϵ and hence cannot be observed in the slow flow. The two oscillatory regimes are characterized by the same phase shift, but the reverse order of firing between the two units. Influenced by noise, the phases effectively engage in bursting behavior, manifesting slow stochastic fluctuations between episodes of intensive spiking activity and periods of relative quiescence, see Figure 9a. For a fixed noise level, the prevalence of metastable states, defined by transition probabilities between them, changes with adaptation speed. One observes that for $\epsilon \simeq 0.05$, the oscillatory dynamics is preferred, whereas for $\epsilon \simeq 0.1$, the quasi-stationary states are more ubiquitous.

A comparison of the (κ_1, κ_2) orbits displaying switching dynamics and the vector field of the slow flow from Figure 6 again shows that the former is confined to the criticality region at the boundary between the stationary and oscillatory regimes in the fast flow, cf. Figure 9. One should remark on how the transitions between the different metastable states take place. In particular, from Figure 9b, it is clear that there can be no direct transitions between the two quasi-stationary states, but they rather have to be mediated by the system passing through the oscillatory states. Also, the transition from oscillatory to quasi-stationary states typically occurs

once the couplings approach a master-slave-like configuration, where the coupling in one direction is much stronger than the other one. This scenario coincides with the SNIPER bifurcation of the fast flow described in Section 4.1. The scenario of transition between the two metastable oscillatory states resembles closely the one from Section 5.2.

6 Summary

In the present study, we have analyzed a system of two adaptively coupled active rotators with excitable intrinsic dynamics, demonstrating that the interplay of plasticity and noise may give rise to slow stochastic fluctuations. Two qualitatively different types of self-organized behavior have been identified, depending on the adaptation speed. For slower adaptation, the switching dynamics consists of an alternation between two modes of noise-induced oscillations, associated to a preferred order of spiking between the two units. In this case, noise plays a twofold role: on one hand, it perturbs the excitable local dynamics giving rise to oscillations on a short timescale, whereas on the other hand, it elicits the alternation between the two oscillatory states on a long timescale. The underlying phase dynamics shows slow switching between two patterns distinguished by the different order in which the units are spiking. In case of faster adaptation, the coupling becomes capable of eliciting emergent oscillations in the deterministic system [27]. The latter then exhibits complex multistable behavior, involving two stationary and two oscillatory regimes. Under the influence of noise, the system undergoes switching between these four different metastable states, whose prevalence at fixed noise level depends on the speed of adaptation. The deterministic attractors associated to metastable states are related by the Z_2 symmetry. Thus, a mismatch in excitability parameters would lead to symmetry-breaking, whereby a small mismatch would induce a bias in switching dynamics, whereas a larger mismatch, corresponding to a scenario with one excitable and one oscillatory unit, would completely alter the observed dynamics.

Though the underlying phenomena are not found in the singular limit of infinite scale separation, the fast-slow analysis we have applied still allows one to explain the qualitative features of both considered types of switching behavior. Studying the layer problem, and in particular the vector field of the slow flow, has enabled us to gain insight into the metastable states and the transitions between them. It has been demonstrated that the coupling dynamics is always in a state of "criticality", being confined to the boundary between the stationary and oscillatory regimes of the fast flow.

Given that excitability, plasticity and noise are inherent ingredients of neuronal systems, the obtained results can be interpreted in the context of neuroscience. It is well known that the backbone of neural networks is made up of binary and ternary neuron motifs, whereby the structural motifs typically support multiple functional motifs, essentially characterized by the weight configuration and the underlying direction of the information flow. With this in mind, the scenario of switching under slow adaptation may be important, because it implies that a binary motif can display slow alternation between two effectively unidirectional weight configurations, promoting opposite direction of information flow. For faster adaptation, one finds multistability between unidirectional coupling and bidirectional coupling of moderate strength. Nonetheless, the underlying phase dynamics, if extended to networks, may be considered as a paradigm for UP-DOWN states, typical for cortical dynamics [28,29]. Thus, it would be of interest to examine the impact of plasticity in networks of noisy excitable units, where one may expect different types of emergent behavior, such as cluster, non-synchronized and partially synchronized states, depending on the frustration of local dynamics and the impact of noise.

Author contribution statement

I.F. and S.Y. conceived the model and defined the analysis of noise-induced switching as the main goal of the research. S.Y. and M.W. developed the general framework to investigating the deterministic fast-slow problem and the bifurcation analysis of the associated reduced systems. I.B. obtained all the numerical results, whereas I.B. and I.F. carried out the bifurcation analysis, identified the two types of noise-induced switching behavior and made the main contribution to writing the manuscript. All the authors discussed the findings and participated in interpretation of the results.

References

1. F. Sorrentino, E. Ott, Phys. Rev. Lett. **100**, 114101 (2008)
2. F. Vazquez, V.M. Eguiluz, M.S. Miguel, Phys. Rev. Lett. **100**, 108702 (2008)
3. N. Caporale, Y. Dan, Ann. Rev. Neurosci. **31**, 25 (2008)
4. C. Furusawa, K. Kaneko, Phys. Rev. Lett. **90**, 088102 (2003)
5. D.O. Hebb, *The Organization of Behavior: a Neuropsychological Approach* (John Wiley & Sons, New York, 1949)
6. S. Song, K.D. Miller, L.F. Abbott, Nat. Neurosci. **3**, 919 (2000)
7. R.C. Froemke, Y. Dan, Nature (London) **416**, 433 (2002)
8. H.-X. Wang, R.C. Gerkin, D.W. Nauen, G.-Q. Bi, Nat. Neurosci. **8**, 187 (2005)
9. O. Sporns, R. Kotter, PLoS Biol. **2**, e369 (2004)
10. I. Franović, V. Miljković, Chaos Soliton. Fract. **44**, 122 (2011)
11. I. Franović, V. Miljković, Chaos Soliton. Fract. **45**, 527 (2012)
12. I. Franović, V. Miljković, EPL **92**, 68007 (2011)
13. L. Lücken, O.V. Popovych, P.A. Tass, S. Yanchuk, Phys. Rev. E **93**, 032210 (2016)
14. Y.L. Maistrenko, B. Lysyansky, C. Hauptmann, O. Burylko, P.A. Tass, Phys. Rev. E **75**, 066207 (2007)
15. P. Seliger, S.C. Young, L.S. Tsimring, Phys. Rev. E **65**, 041906 (2002)
16. M. Li, S. Guan, C.-H. Lai, New J. Phys. **12**, 103032 (2010)
17. P.S. Skardal, D. Taylor, J.G. Restrepo, Physica D **267**, 27 (2014)
18. D. Kasatkin, S. Yanchuk, E. Schöll, V. Nekorkin, Phys. Rev. E **96**, 062211 (2017)
19. O.V. Popovych, S. Yanchuk, P.A. Tass, Sci. Rep. **3**, 2926 (2013)
20. K. Mikkelsen, A. Imparato, A. Torcini, Phys. Rev. Lett. **110**, 208101 (2013)
21. D. Millman, S. Mihalas, A. Kirkwood, E. Niebur, Nat. Phys. **6**, 801 (2010)
22. A. Levina, J.M. Hermann, T. Geisel, Phys. Rev. Lett. **102**, 118110 (2009)
23. T. Aoki, T. Aoyagi, Phys. Rev. Lett. **102**, 034101 (2009)
24. T. Aoki, T. Aoyagi, Phys. Rev. E **84**, 066109 (2011)
25. A. Shilnikov, Int. J. Bifurc. Chaos **18**, 2141 (2008)
26. S.-J. Wang, G. Ouyang, J. Guang, M. Zhang, Phys. Rev. Lett. **116**, 018101 (2016)
27. Q. Ren, K.M. Kolwankar, A. Samal, J. Jost, Phys. Rev. E **86**, 056103 (2012)
28. T.T.G. Hahn, J.M. McFarland, S. Berberich, B. Sakmann, M.R. Mehta, Nat. Neurosci. **15**, 1531 (2012)
29. V.V. Vyazovskiy, K.D. Harris, Nat. Rev. Neurosci. **14**, 443 (2013)

Inverse stochastic resonance in a system of active rotators with adaptive coupling

Iva Bačić

Institute of Physics Belgrade

Inverse stochastic resonance is a phenomenon where an oscillating system shows a nonlinear response to noise, displaying a minimal oscillation frequency at an intermediate noise level. Such an effect has been indicated to play important functional roles in neuronal systems, contributing to reduction of spiking frequency in the absence of neuromodulators or to triggering of the on-off tonic spiking activity. We demonstrate a novel generic scenario for such an effect in a multi-timescale system, considering the example of emergent oscillations in two adaptively coupled active rotators with excitable local dynamics. The fast-slow analysis we carry out indicates that the plasticity plays a facilitatory role by guiding the fast-flow dynamics to parameter domains where the stable equilibria change character from nodes to focuses, which ultimately enhances the influence of noise. The described scenario persists for different plasticity rules, underlying its robustness in light of potential application to neuronal systems.

Gas-phase X-ray action spectroscopy of protonated nanosolvated substance P peptide around O K-edge

I. Bačić[1], M. Lj. Ranković[1], F. Canon[2], V. Cerovski[1], C. Nicolas[3], A. Giuliani[3,4] and
A. R. Milosavljević[1]

[1] *Institute of Physics Belgrade, University of Belgrade, Pregrevica 118, 11080 Belgrade, Serbia*
[2] *INRA, UMR1324 Centre des Sciences du Goût et de l'Alimentation, F-21000 Dijon, France*
[3] *SOLEIL, l'Orme des Merisiers, St Aubin, BP48, 91192 Gif sur Yvette Cedex, France*
[4] *INRA, UAR1008, CEPIA, Rue de la Géraudière, BP 71627, 44316 Nantes, France*

We report preliminary results from unprecedented near edge X-ray absorption fine structure action spectroscopy of a gas-phase nanosolvated peptide ion. Doubly protonated substance P (Arg-Pro-Lys-Pro-Gln-Gln-Phe-Phe-Gly-Leu-Met-NH2) cations have been isolated in a linear ion trap and submitted to soft X-ray synchrotron radiation by means of coupling a commercial quadrupole ion trap mass spectrometer (Thermo Finningan LTQ XL) to the PLEIADES beamline at the SOLEIL synchrotron radiation facility (France) [1]. X-ray activation tandem mass spectra have been recorded for different photon energies, scanned over C, N and O K-edge ionization thresholds.

Figure 1 shows the photofragment ions yield corresponding to a total water loss (a normalized integral yield of all fragments corresponding to the loss of one or more water molecules) from the doubly protonated substance P cation nanosolvated with 11 water molecules $[M+2H+11H_2O]^{2+}$ upon soft X-ray irradiation. We observed that a resonant excitation of an O 1s electron to an unoccupied molecular orbital, following by a resonant Auger decay, induces an increased water detachment from the precursor.
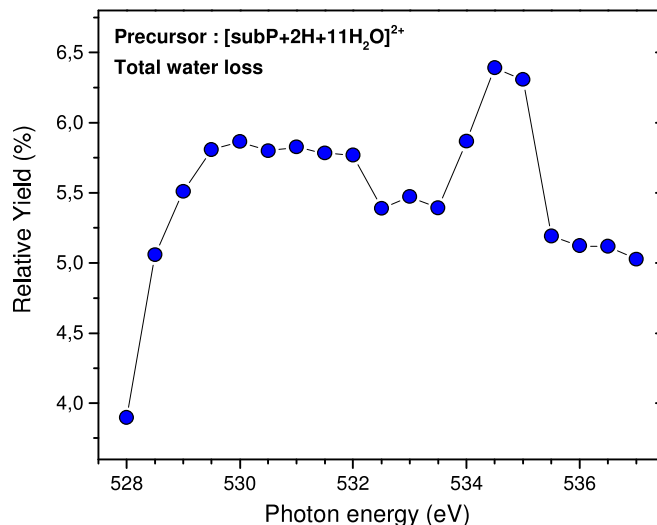
Fig.1. Photofragment ions yield that corresponds to a range m/z 674-766 (an integral yield of all fragments corresponding to the loss of one or more water molecules) from a doubly protonated nanosolvated substance P cation precursor $[M+2H+11H_2O]^{2+}$ (m/z 773.5).

REFERENCES

[1] A. R. Milosavljević et al., J. Phys. Chem. Letters 3, 1191 (2012).

Disordered Configurations of the Glauber Model on Two-Dimensional Networks

I. Bačić[a], I. Franović[a] and M. Perc[b, c, d]

[a]Scientific Computing Laboratory, Center for the Study of Complex Systems, Institute of Physics Belgrade - Belgrade, Serbia
[b]Faculty of Natural Sciences and Mathematics, University of Maribor - Maribor, Slovenia
[c]Center for Applied Mathematics and Theoretical Physics, University of Maribor - Maribor, Slovenia
[d]Complexity Science Hub - Vienna, Austria

Abstract. We analyze the ordering efficiency and the structure of disordered configurations for the zero-temperature Glauber model on Watts-Strogatz networks obtained by rewiring 2D regular square lattices. In the small-world regime, the dynamics fails to reach the ordered state in the thermodynamic limit. Due to the interplay of the perturbed regular topology and energy neutral stochastic state transitions, the stationary state consists of two intertwined domains, manifested as multi-cluster states on the original lattice. Moreover, for intermediate rewiring probabilities, one finds an additional source of disorder due to the low connectivity degree, which gives rise to small isolated droplets of spins. We also examine the ordering process in paradigmatic two-layer networks with heterogeneous rewiring probabilities. Comparing the cases of a multiplex network and the corresponding network with random inter-layer connectivity, we demonstrate that the character of the final state qualitatively depends on the type of inter-layer connections.
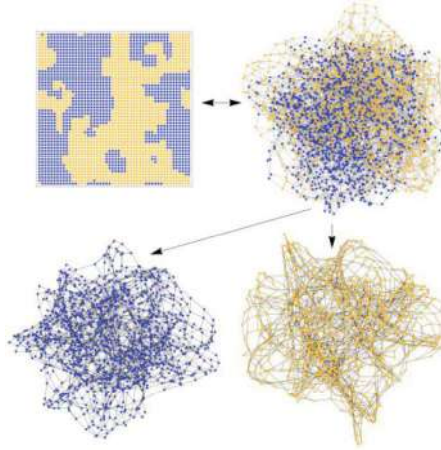
FIGURE 1. A disordered configuration with two domains comprises a multi-cluster state on the lattice.

REFERENCES

1. Bačić I., Franović I., and Perc M., *EPL* **120**, 68001 (2017).

UNIVERSITY OF BELGRADE

FACULTY OF PHYSICS

Iva Bačić

SELF-ORGANIZATION IN COUPLED EXCITABLE SYSTEMS: INTERPLAY BETWEEN MULTIPLE TIMESCALE DYNAMICS AND NOISE

Doctoral Dissertation

Belgrade, 2020

UNIVERZITET U BEOGRADU

FIZIČKI FAKULTET

Iva Bačić

SAMOORGANIZACIJA U SPREGNUTIM EKSCITABILNIM SISTEMIMA: SADEJSTVO VIŠESTRUKIH VREMENSKIH SKALA I ŠUMA

Doktorska disertacija

Beograd, 2020.

Thesis Defense Committee

Thesis advisor:
Dr. Igor Franović
Associate Research Professor
Institute of Physics Belgrade
University of Belgrade

Committee member:
Prof. Dr. Đorđe Spasojević
Professor
Faculty of Physics
University of Belgrade

Committee member:
Prof. Dr. Milan Knežević
Professor
Faculty of Physics
University of Belgrade

Committee member:
Dr. Antun Balaž
Research Professor
Institute of Physics Belgrade
University of Belgrade

"We can lift ourselves out of ignorance, we can find ourselves as creatures of excellence and intelligence and skill. We can learn to be free!"

Richard Bach, Seagull Jonathan Livingston

Acknowledgements

In addition to my own hard work and persistence, the completion of the present thesis would not have been possible without the immense support that I have received both professionally and privately.

I wish to express my appreciation to my supervisor for introducing me to the world of research, writing, and publishing, as well as for imparting his broad scientific expertise to me, providing me with the foundation upon which I will build my international scientific career. I would also like to express my gratitude to our senior collaborators from Berlin, Dr. Serhiy Yanchuk and Dr. Matthias Wolfrum, whose expertise and valuable insights, shared through numerous discussions, helped me broaden my scientific horizons. I also sincerely thank dr Antun Balaž, head of our lab, to whom I am indebted for his encouragement and assistance throughout all stages of my PhD studies.

Finally, I owe lots of gratitude to my friends and family. The support of every single one of you has been very valuable to my completion of this journey. I thank my father for teaching me the importance of erudition by setting his own example, and my mother for teaching me to aim for the stars while adamantly following my dreams.

Self-Organization in Coupled Excitable Systems: Interplay Between Multiple Timescale Dynamics and Noise

— Abstract —

The dynamics of complex systems typically involves multiple spatial and temporal scales, while emergent phenomena are often associated with critical transitions in which a small parameter variation causes a sudden shift to a qualitatively different regime. In the vicinity of such transitions, complex systems are highly sensitive to external perturbations, potentially resulting in dynamical switching between different (meta)stable states. Such behavior is typical for many biological systems consisting of coupled excitable units. In neuronal systems, for instance, self-organization is influenced by the interplay between noise from diverse sources and a multi-timescale structure arising from both local and coupling dynamics.

The present thesis is devoted to several types of self-organized dynamics in coupled stochastic excitable systems with multiple timescale dynamics. The excitable behavior of single units is well understood, in terms of both the nonlinear threshold-like response to external perturbations and the characteristic non-monotonous response to noise, embodied by different resonant phenomena. However, the excitable behavior of coupled systems, as a new paradigm of emergent dynamics, involves a number of fundamental open problems, including how interactions modify local dynamics resulting in excitable behavior at the level of the coupled system, and how the interplay of multiscale dynamics and noise gives rise to switching dynamics and resonant phenomena. This thesis comprises a systematic approach to addressing these issues, consisting of three complementary lines of research.

In particular, within the first line of research, we have extended the notion of excitability to coupled systems, considering the examples of a small motif of locally excitable units and a population of stochastic neuronal maps. In the case of the motif, we have classified different types of excitable responses and, by applying elements of singular perturbation theory, identified what determines the motif's threshold-like response. Regarding the neuronal population, we have established the concept of macroscopic excitability whereby an entire population of excitable units acts like an excitable element itself. To examine the stability

and bifurcations of the macroscopic excitability state, as well as the associated stimulus-response relationship, we have derived the first effective mean-field model for the collective dynamics of coupled stochastic maps.

The second line of research concerns switching dynamics induced by the interplay of noise and multiplicity of timescales in small systems of locally excitable units. Our analysis, carried out on two paradigmatic models, has revealed that the coaction of noise and a large, but finite timescale separation gives rise to two different types of switching dynamics, namely slow stochastic fluctuations and stochastic bursting. In the former case, demonstrated for a motif of two adaptively coupled stochastic units with excitable local dynamics, we have found that the fluctuation forms qualitatively depend on the scale separation. In one of the scenarios, noise induces two characteristic time scales, giving rise to switching between two modes of noise-induced oscillations. Concerning the latter, by introducing the model of a stochastic excitable unit with a slowly adapting feedback, we have demonstrated that switching between metastable states derived from deterministic attractors gives rise to a bursting regime, whose stability boundaries we have calculated by introducing a new stochastic averaging method which extends singular perturbation theory to stochastic multiscale systems.

Within the third line of research, we have studied resonant phenomena in coupled systems with local dynamics near the bifurcation threshold. By considering the influence of noise on a paradigmatic model of two units with excitable or oscillatory local dynamics, we have identified two generic scenarios for the onset of inverse stochastic resonance: one based on biased switching, and the other associated with the noise-enhanced stabilization of a deterministically unstable fixed point. We have also demonstrated a novel method of efficient control of coherence resonance, showing how the effect may be enhanced or suppressed by adjusting the strength of the slowly adapting feedback.

Keywords: excitability, noise, multiscale dynamics, macroscopic excitability, switching dynamics, resonant phenomena
Scientific field: Physics
Research area: Statistical physics
UDC number: 536

Samoorganizacija u spregnutim ekscitabilnim sistemima: sadejstvo višestrukih vremenskih skala i šuma

---
Sažetak

Dinamika kompleksnih sistema se tipično odigrava na nekoliko prostornih i vremenskih skala, pri čemu su emergentni fenomeni često povezani sa kritičnim prelazima, pri kojima mala promena vrednosti parametra izaziva naglu i kvalitativnu promenu dinamičkog režima. U blizini takvih prelaza, kompleksni sistemi su vrlo osetljivi na eksterne peturbacije, što može izazvati dinamiku alterniranja (*switching*) između različitih (meta)stabilnih stanja. Takvo ponašanje je tipično za mnoštvo bioloških sistema sačinjenih od spregnutih ekscitabilnih jedinica, među kojima su i neuronski sistemi, kod kojih na samoorganizaciju utiču koefekti šuma iz raznolikih izvora i višestrukosti vremenskih skala koja potiče od lokalne dinamike i dinamike interakcija.

Ova disertacija je posvećena proučavanju nekoliko vrsta samoorganizujuće dinamike u spregnutim stohastičkim ekscitabilnim sistemima sa dinamikom koja se odvija na višestrukim vremenskim skalama (*multiscale* dinamika). Ekscitabilno ponašanje pojedinačnih jedinica je detaljno istraženo, kako u pogledu nelinearnog pragovskog (*threshold-like*) odgovora na eksterne perturbacije, tako i u pogledu karakterističnog nemonotonog odgovora na šum, manifestovanog kroz razne rezonantne fenomene. Međutim, pri razmatranju ekscitabilnog ponašanja spregnutih sistema kao nove paradigme emergentne dinamike, na fundamentalnom nivou postoje brojna otvorena pitanja, uključujući kako interakcije modifikuju lokalnu dinamiku rezultujući ekscitabilnošću na nivou spregnutog sistema, kao i kako sadejstvo *multiscale* dinamike i šuma dovodi do *switching*-a i rezonantnih fenomena. U ovoj disertaciji, sačinjenoj od tri komplementarne linije istraživanja, sistematično pristupamo traženju odgovora na navedena pitanja.

U sklopu prve linije istraživanja, proširili smo koncept ekscitabilnosti na spregnute sisteme, razmatrajući primere malog motiva sačinjenog od lokalno ekscitabilnih jedinica i populacije stohastičkih neuronskih mapa. U slučaju motiva, klasifikovali smo različite vrste ekscitabilnih odgovora i pokazali šta određuje pragovsko ponašanje, primenivši elemente teorije singularnih perturbacija. U slučaju populacije, uveli smo koncept makroskopske

ekscitabilnosti pri kojoj se cela populacija eksitabilnih jedinica ponaša kao eksitabilni element. Kako bismo ispitali stabilnost i bifurkacije stanja makroskopske eksitabilnosti, kao i odgovor sistema na perturbaciju, izveli smo prvi efektivni model srednjeg polja (*mean-field*) za kolektivnu dinamiku spregnutih stohastičkih mapa.

Druga linija istraživanja se tiče *switching* dinamike indukovane interakcijom šuma i razdvajanja vremenskih skala u malim sistemima lokalno eksitabilnih jedinica. Sprovevši analizu na dva paradigmatska modela, pokazali smo da koefekti šuma i velikog, ali konačnog razdvajanja vremenskih skala dovode do dve vrste alternirajuće dinamike: sporih stohastičkih fluktuacija i stohastičkog burstovanja. U prvom slučaju, razmatranom na motivu koji se sastoji od dve adaptivno spregnute stohastičke jedinice sa eksitabilnom lokalnom dinamikom, pokazali smo da forma sporih fluktuacija kvalitativno zavisi od razdvajanja skala. U jednom od scenarija, šum uvodi dve nove vremenske skale, izazivajući *switching* između dve mode oscilacija izazvanih šumom. U drugom slučaju, uvevši model stohastičke eksitabilne jedinice sa sporo adaptirajućom povratnom spregom (*feedback*), pokazali smo da se *switching* između metastabilnih stanja izvedenih iz determinističkih atraktora manifestuje kao režim burstovanja, čije granice stabilnosti smo izračunali koristeći novi metod stohastičkog usrednjavanja, proširivši teoriju singularnih perturbacija na stohastičke sisteme sa *multiscale* dinamikom.

U sklopu treće linije istraživanja, proučavali smo rezonantne fenomene u spregnutim sistemima sa lokalnom dinamikom blizu bifurkacionog praga. Razmatrajući uticaj šuma na paradigmatski model dve jedinice sa eksitabilnom ili oscilatornom lokalnom dinamikom, identifikovali smo dva generička scenarija za pojavu inverzne stohastičke rezonance: jedan zasnovan na neuravnoteženom *switching*-u, a drugi povezan sa stabilizacijom deterministički nestabilne fiksne tačke šumom. Pored toga, uveli smo novi metod kontrole rezonance koherencije, pokazavši kako se rezonantni efekat može pojačati ili suzbiti prilagođavanjem jačine sporo adaptirajuće povratne sprege.

Ključne reči: eksitabilnost, šum, dinamika na višestrukim vremenskim skalama, makroskopska eksitabilnost, switching dinamika, rezonantni fenomeni
Naučna oblast: Fizika
Uža naučna oblast: Statistička fizika
UDK broj: 536

Contents

List of Figures

Chapter 1

Introduction

The spontaneous emergence of increased organization in a system led only by its own dynamics, referred to as **self-organization**, is a fundamental feature of our world [1, 2, 3, 4]. Many forms of fascinating self-organized behavior are encountered across all scales, including the formation of planetary systems and galaxies [5], crystal growth [6], sand dunes [7], flocking behavior in birds and fish [8], the development of living organisms [9], traffic flow [10], the stock market [11], the Internet [12], and the evolution of language [13]. Brain functionality also heavily relies on self-organizing processes [14] [15], and even consciousness can be considered a result of self-organization [16] [17]. In physics, self-organization is often related to phase transitions and spontaneous symmetry breaking, typically manifested as the formation of complex spatio-temporal patterns, with examples ranging from the synchronization transition in coupled oscillators, crystal growth, and spontaneous magnetization in classical physics to superconductivity, lasers, and Bose-Einstein condensation in quantum physics [18].

The idea of order spontaneously appearing from disorder has sparked human curiosity for centuries and millennia [19]. The oldest known reference to this notion reaches back to ancient Greek philosophers, when thinkers belonging to the atomist intellectual tradition, such as Lucretius and Democritus, speculated that, given enough matter, space and time, order emerges on its own without divine intervention [20]. Centuries later, several classical philosophers including René Descartes [21], Immanuel Kant [22], and Friedrich Wilhelm Joseph von Schelling [19] also pondered over this concept. In his *Critique of Judgment* from 1787, Kant was the first to propose the term self-organization, recognizing the possibility of an organization at the systemic level which cannot be explained by reducing the behavior of the system as a whole to the behavior of its constituents. For Schelling, self-organization was essential in considerations of the philosophy of nature.

As far as contemporary science is concerned, in 1947 the cyberneticist W. Ross Ashby introduced the concept to general systems theory by applying the term "self-organizing" to describe self-induced changes in organization in determinate systems [23]. Indeed, the main contributions in the initial stages of theoretical developments came from general systems theory and cybernetics, lead by prominent theorists such as Heinz von Förster, Gordon

Pask, and Norbert Wiener [24, 25, 26, 27, 28]. During the following decades, the idea was embraced by physicists and chemists within research on phase transitions. Eventually, physical chemist Ilya Prigogine bridged the gap between general systems theory and thermodynamics with his pioneering work on self-organization in chemical systems [29], for which he was awarded the Nobel Prize in 1977 [30].

Another major contribution was provided by Hermann Haken, founder of the interdisciplinary field of "synergetics", dedicated to self-organization and pattern formation in open systems far from equilibrium [1, 2]. Alongside the development of synergetics, a new interdisciplinary field of research emerged, termed "complexity science" [3, 4]. The focal point of this discipline is the investigation of **complexity** – collective behavior which arises as a result of local interactions between constituents of a complex system, as well as the interactions of the system and its environment. Complexity characterizes diverse phenomena relevant to a wide variety of both natural and social sciences, from the climate to transportation systems to the human body. While an intuitive grasp on the notion of complexity seems quite straightforward, it is rather difficult, if not impossible, to construct an universal definition. Indeed, the definition of complexity has been the subject of many debates [31].

Despite disagreements about the precise formulation of a universal definition of complexity, there are several general features that are generally agreed upon to be common characteristics of complex systems, such as that they all consist of *interacting components* [32]. Another intrinsic feature of complex systems is **emergence**, which refers to system traits that arise exclusively due to interactions of the constituents of the system, and which cannot be inferred by considering those parts in isolation [33]. Although emergence and self-organization are closely related concepts, the following distinction should be emphasized: while emergence refers to the appearance of a novel property on a global level arising from local interactions, self-organization concerns the increase in order resulting from internal dynamics in the absence of external influences [34].

Ever since it was established that complexity is a crucial feature of systems capable of exhibiting self-organizing behavior, research on self-organization and complex systems has become deeply interwoven [4]. Since these studies typically concern systems with many degrees of freedom which are impossible to treat mathematically, the analysis often consists of a qualitative approach, significantly relying on computer simulations [35]. In the early 2000s, empirical studies of real-world complex systems motivated a convenient representation of complex systems within the framework of **networks** in which the interactions between the constituents are described by links between nodes [36, 37, 38], providing an intuitive depiction of any system consisting of related components.

The mathematical field of *nonlinear dynamics*, devoted to the qualitative behavior of nonlinear dynamical systems [39], has turned out to be essential to the study of self-organization and, in general, the dynamics of complex systems. Within nonlinear dynamics, one aims to qualitatively understand the long-term behavior of systems, classifying the stable solutions for a given set of parameters (attractors). Dynamical systems which exhibit the coexistence

of several attractors are referred to as **multistable** systems [40]. If a multistable system is exposed to a sufficiently strong perturbation and/or rapid parameter change, it may **switch** between different attractors [41]. Under the action of noise, the attractors of a multistable system become **metastable states**. Sufficiently strong noise may induce large fluctuations due to which the system exhibits continuous switching between different metastable states [42].

The dynamical structure of complex systems often involves multiple characteristic timescales, whereby such **multiscale dynamics** may arise from the local dynamics of the system's constituents and/or may appear due to the dynamics of the interactions (coupling dynamics). Coupling dynamics may involve mechanisms such as feedback or adaptivity in which the system's structure adaptively reorganizes itself in response to the dynamics [43, 44, 45, 46]. Systems whose dynamics involves a strong separation of characteristic timescales are referred to as slow-fast systems within the mathematical framework of *singular perturbation theory* [47, 48, 49, 50, 51].

Let us now establish a link between the fields of nonlinear dynamics and *statistical physics*, associated with critical transitions. Critical transitions occur at so-called tipping points, where the system suddenly shifts from one stable state to another qualitatively different stable regime [41, 52, 53, 54]. While critical transitions may, on one hand, result in undesired catastrophic outcomes, on the other hand, being in the vicinity of a tipping point may also have favorable consequences. For instance, in the brain, the transition from normal to epileptic brain activity is undesired [55], while transitions which contribute to switching between mutually exclusive motor programs are desired [56].

Deeper insight into critical transitions has been provided within the theory of nonlinear dynamics by considering stochastic multiscale (slow-fast) models [57]. Within this approach, a critical transition corresponds to a bifurcation – a qualitative change in the dynamics due to a small smooth variation of system parameter(s) [39] – such that the tipping point coincides with the bifurcation condition. In the vicinity of critical transitions, complex systems are extremely sensitive to perturbations, and may, depending on the dynamical character of the transition, exhibit two qualitatively different types of fluctuations [54]. In particular, they may either exhibit slow (critical) fluctuations, featuring a slow recovery to a stable state after a perturbation, or multistable fluctuations, manifested as stochastic switching (flickering) between metastable states [52]. The two types yield qualitatively different statistics: critical fluctuations are characterized by a scale-free power-law distribution, while multistable fluctuations follow an exponential distribution akin to a Poisson process. If we invoke an analogy with statistical physics, critical fluctuations mathematically correspond to a second-order (continuous) phase transition, whereas metastable fluctuations coincide with a first-order (discontinuous) one.

One of the key examples of self-organizing phenomena in complex systems is provided by the **synchronization transition** in coupled oscillators. The synchronization transition is typically described using the Kuramoto paradigmatic minimal model [58], which has been

applied to analyze problems from a wide range of disciplines, including physics [59], engineering [60], chemistry [61], and biology [62]. The Kuramoto model consists of globally coupled oscillators described by their phases, each with its intrinsic natural frequency given by a common distribution. Under the variation of the coupling strength, the model displays a second-order (continuous) transition from an unsynchronized state of phase turbulence to partial synchrony [63], corresponding to a Hopf bifurcation of the complex order parameter. From the standpoint of statistical physics, synchronization is a non-equilibrium phase transition, since the dynamics settles to non-equilibrium stationary states [64].

Having provided a general introduction to the notion of self-organization in complex systems, describing central concepts such as emergence, multiscale dynamics, multistability and switching, as well as explaining the crucial role of stochastic effects in complex dynamics, a few words should be said about emergence and self-organization in **coupled excitable systems** to which this thesis is devoted to. In general, coupled excitable systems exhibit a variety of self-organized behaviors, including oscillations, pulses and (rotating, spiral, and scroll) waves, as well as localized and propagative spatio-temporal patterns such as localized spots and periodic or chaotic patterns [65, 66]. However, the governing principles of self-organization in coupled excitable systems are different from those in coupled oscillators because in the absence of input, an excitable unit settles into a stationary state.

In conceptual terms, the excitable behavior of single units influenced by different types of noise is well understood. However, much remains to be understood about the *excitable behavior of coupled systems*, where open questions concern the details of the nonlinear threshold-like behavior, the characteristic non-monotonous response to noise (resonant phenomena), as well as noise-induced switching dynamics. In particular, in the case of populations of excitable units, an interesting problem involves the scenario in which a whole population of coupled excitable units becomes an excitable system itself, a feature relevant to both theory and applications. We will refer to this emergent phenomenon as *macroscopic excitability*. Nonetheless, an equally interesting open issue concerns the interplay of noise and adaptivity-induced multiple timescale dynamics in small motifs consisting of locally excitable units. Moreover, although it is well-known that noise plays a constructive role in a variety of applications [67], including stochastic facilitation in neural systems [68, 69, 70] which mainly involves resonant phenomena, phenomena such as coherence resonance and inverse stochastic resonance have mostly been considered in the case of single units.

Studies of these effects in coupled systems are still lacking, despite their relevance in the context of neural networks [71, 72]. Indeed, our motivation for considering coupled stochastic multiscale excitable systems arises primarily from studies of neuronal systems, such as small network motifs and neural networks, whose activity is shaped by the interaction of multiple timescale dynamics, facilitated e.g. by synaptic plasticity, and diverse sources of intrinsic or external noise. The particular **types of self-organized dynamics explored within this thesis** include:

- the excitability of coupled systems,

- synchronization of noise-induced oscillations, namely the ordering transition accounting for the onset of a collective mode via a stochastic bifurcation,

- noise-induced multistability,

- noise-enhanced stabilization of deterministically unstable structures,

- noise-induced switching, and

- resonant phenomena,

whereby the **main conceptual novelties** include

- the introduction of the notion of macroscopic excitability, and

- the discovery of generic mechanisms of inverse stochastic resonance.

From a methodological standpoint, this study relies on standard methods from nonlinear dynamics and statistical physics, including the following **analytical and numerical techniques**:

- stability and bifurcation analysis,

- multiple timescale analysis for deterministic systems,

- numerical modeling of systems of deterministic and stochastic differential equations,

- calculation of phase response curves for coupled systems, and

- the Fokker-Planck method,

as well as **newly introduced analytical methods**, such as

- the application of mean-field theory to coupled time-discrete systems, and

- stochastic averaging for the analysis of stochastic multiscale systems.

The analysis of the above-mentioned phenomena will be carried out on several models with stochastic multiple timescale dynamics. In fact, each phenomenon will be studied with reference to more than one model in order to demonstrate its generality. To this end, the following **paradigmatic models** will be taken into consideration:

- an assembly of coupled stochastic map neurons,

- a stochastic slow-fast system of two adaptively coupled units,

- a stochastic excitable unit with a slowly adapting feedback, and

- the Morris-Lecar neuron model.

The remainder of this chapter contains an overview of the fundamental concepts underlying the present thesis, whereby section 1.1 concerns *multiple timescale dynamics*, including an introduction to geometric and asymptotic singular perturbation theory. Section 1.2 concerns the *concept of excitability*, including the phenomenology and dynamical features of excitable behavior. Furthermore, *the effect of noise on excitable systems* is discussed in section 1.3. Finally, section 1.4 contains an outline of the thesis.

1.1 *Multiple timescale dynamics*

In many complex systems, the components evolve on different characteristic timescales, giving rise to various forms of multiple timescale dynamics. For instance, in neural networks, the interplay of biochemical synaptic mechanisms and electrical spiking activity gives rise to complex phenomena which involve more than one timescale [73]. Considering single neurons, the membrane potential typically changes faster than the recovery variables [74]. Similarly, the optical and electrical components of optoelectronic devices operate on different timescales [75, 76]. Additional examples of multi-timescale systems include chemical reactors [77, 78], mechanical systems [79, 80], and ecological systems [81, 82].

Generally speaking, the multiplicity of timescales may appear (*i*) as a feature of the *local dynamics* of a single unit, and/or (*ii*) due to the *coupling dynamics* of interacting units. In the latter case, the interactions between the constituents of a system are time-dependent, whereby the system's structure responds to its dynamics by adaptively reorganizing itself [43, 44, 45, 46]. The interactions typically evolve slower than the state of the system, naturally invoking a distinction between the fast local dynamics and the slow dynamics of the couplings. Nevertheless, the evolution of such systems involves a feedback mechanism in which the couplings adapt to the dynamical processes at the units, but the changes in couplings in turn influence the evolution of the units itself. This interplay, illustrated in Fig. 1.1, is referred to as *adaptivity* or adaptation.

In neuronal systems, the concept of adaptivity is embodied in *synaptic plasticity*, a biological mechanism accounting for the changes in the strength of neural connections [83]. Depending on relative spike times of presynaptic and postsynaptic neurons, synaptic strengths may increase or decrease over time, resulting in short- or long-term potentiation or depression of synapses. Synaptic plasticity makes self-organization in neuronal systems a multi-timescale process: short-term spiking activity unfolds on a quasi-static coupling configuration, while the slow adjustment of couplings depends on the time-averaged evolution of units. In the interplay of neuronal activity and synaptic dynamics, the spiking pattern influences the synaptic connections, which results in new spiking patterns. In this context, plasticity has been modeled by different rules, such as Hebbian learning and spike-time-dependent plasticity (STDP) [84, 85, 86].

Dynamical systems involving a strong separation of timescales are referred to as *slow-fast systems* and are treated within the mathematical framework of *singular perturbation theory*
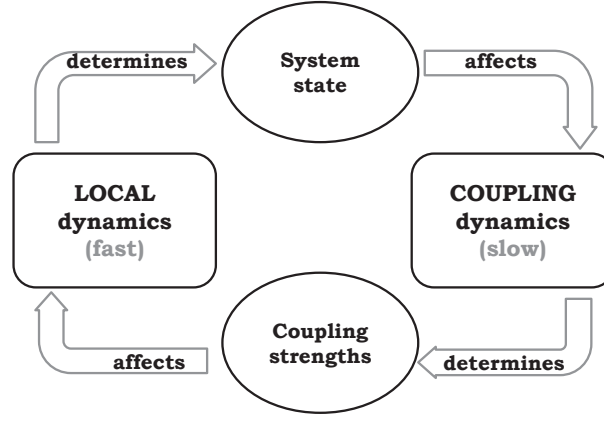
Figure 1.1: Schematic representation of adaptivity. The interplay between the local dynamics, occurring on the fast timescale, and the coupling dynamics, evolving on a slower timescale, gives rise to a feedback loop whereby the local dynamics determines the state of the system, which affects the coupling dynamics. The subsequent slow changes in coupling strengths in turn influence the system state.

[47, 48, 49, 50, 51].

1.1.1 Singular perturbation theory and slow-fast analysis

For simplicity, let us consider dynamical systems involving only two characteristic timescales, the fast and the slow one. Ordinary differential equations in which one set of variables has derivatives of a much larger magnitude than the remaining variables may be written in the following general form [47]:

$$\varepsilon \frac{d\overrightarrow{x}}{d\tau} = \varepsilon \dot{\overrightarrow{x}} = f(\overrightarrow{x}, \overrightarrow{y}, \varepsilon)$$
$$\frac{d\overrightarrow{y}}{d\tau} = \dot{\overrightarrow{y}} = g(\overrightarrow{x}, \overrightarrow{y}, \varepsilon),$$
(1.1)

where $f : \mathbb{R}^m \times \mathbb{R}^n \to \mathbb{R}^m$, $g : \mathbb{R}^m \times \mathbb{R}^n \to \mathbb{R}^n$. The timescale separation is defined by the small positive parameter $0 < \varepsilon \ll 1$, implying that the $\overrightarrow{x}$ variables are the **fast variables**, while the $\overrightarrow{y}$ variables are the **slow variables**. By rescaling time as $t = \tau/\varepsilon$, we obtain the following equivalent formulation:

$$\frac{d\overrightarrow{x}}{dt} = \overrightarrow{x}' = f(\overrightarrow{x}, \overrightarrow{y}, \varepsilon)$$
$$\frac{d\overrightarrow{y}}{dt} = \overrightarrow{y}' = \varepsilon g(\overrightarrow{x}, \overrightarrow{y}, \varepsilon),$$
(1.2)

such that t corresponds to the **fast timescale** while τ refers to the **slow timescale**. Both (1.1) and (1.2) are referred to as the **full system**.

It is important to emphasize that the dynamics of slow-fast systems cannot be analyzed within the framework of regular perturbation theory, where the small parameter ε would be simply approximated with zero. Rather, slow-fast systems belong to the class of singularly perturbed problems, i. e. those involving a qualitative difference between the solutions of

the problem at a limiting value of the parameter and limit of the solutions of the general problem. In this case, **the singular limit** $\varepsilon = 0$ corresponds to an infinite timescale separation. Nevertheless, a natural first step in the analysis of such systems is to consider the singular limit such that the full system reduces to the fast and slow subsystems evolving on separate timescales t and τ.

1.1.1.1 Geometric singular perturbation theory

GSPT provides a framework for a mathematically rigorous treatment of solutions of singularly perturbed systems. In the singular limit, the dynamics of the full system reduces to lower-dimensional problems on the fast or the slow timescale, which are used to predict the behavior of the full system for small, but finite scale separation ε.

In particular, by setting $\varepsilon = 0$ in (1.2), we obtain the **layer problem** or **fast subsystem**, a *parametrized system of ordinary differential equations* defined on the fast timescale:

$$
\begin{aligned}
\vec{x}' &= f(\vec{x}, \vec{y}, 0) \\
\vec{y}' &= 0,
\end{aligned}
\tag{1.3}
$$

whose vector flow is called the **fast flow**. The dynamics of the fast subsystem is obtained by treating the slow variables y as parameters, whereby each fixed value of y describes one "layer" of the fast subsystem.

Conversely, setting $\varepsilon = 0$ in (1.1) yields the **reduced problem** or **slow subsystem**, a *differential-algebraic equation* defined on the slow timescale:

$$
\begin{aligned}
0 &= f(\vec{x}, \vec{y}, 0) \\
\dot{\vec{y}} &= g(\vec{x}, \vec{y}, 0),
\end{aligned}
\tag{1.4}
$$

such that the corresponding vector flow is the **slow flow**. A natural way to analyze the orbits of the full system for finite $0 < \varepsilon \ll 1$ is to divide them into singular limit segments, such that, depending on the region of phase space, the dynamics of the full system converges to either the solution of the layer problem or the reduced one. Determining the dynamics of the slow flow involves time-averaging over the stable regimes of the fast flow of the layer problem. If the fast flow exhibits several attractors, multiple stable sheets of the slow flow emerge from the averaged dynamics of the different attractors of the fast flow. The initial conditions $\{\vec{x}(0), \vec{y}(0)\} = \{\vec{x_0}, \vec{y_0}\}$ must satisfy the constraint $0 = f(\vec{x}, \vec{y}, 0)$ in order to ensure the existence of the solution.

In the vicinity of the set described by the algebraic equation $f(\vec{x}, \vec{y}, 0) = 0$, referred to as the *critical set $C_0 = \{(\vec{x}, \vec{y}) \in \mathbb{R}^m \times \mathbb{R}^n : f(\vec{x}, \vec{y}, 0) = 0\}$*, a trajectory of the full system is approximately described by the solutions of the slow flow. On the other hand, sufficiently far from C_0, approximate trajectories of the full system are given by the fast flow. If C_0 is a submanifold of $\mathbb{R}^m \times \mathbb{R}^n$, C_0 is called the **critical manifold**. The proximity to C_0 determines which subsystem provides an appropriate approximation of the full system, whereas combining such singular limit segments should result in an approximated trajectory of the full

system. Moreover, C_0 *is equivalent to the set of equilibria of the fast flow.* Trajectories of the layer problem approach C_0 along the **fast fibres**, such that C_0 comprises the set of base points of the fast fibres, connecting the fast and slow flow.

The structure of slow-fast systems typically involves segments where the fast dynamics unfolding orthogonal to the critical manifold dominates the slow dynamics tangential to the critical manifold. **Normal hyperbolicity** refers to the general feature of manifolds where the linearized dynamics in the orthogonal direction prevails over that in the tangential direction. In other words, perturbations applied in the direction orthogonal to the manifold grow exponentially with a larger rate than that of the exponential growth of tangential perturbations.

Considering that C_0 consists of equilibria, a subset $S \subset C_0$ is normally hyperbolic if and only if all points $p \in S$ are hyperbolic equilibria of the fast subsystem, i. e. none of the eigenvalues of the associated Jacobian matrix $D_x f(p, \varepsilon = 0)$ have zero real parts. A normally hyperbolic subset $S \subset C_0$ is **attracting** if all points $p \in S$ are *stable* equilibria of the fast subsystem (all eigenvalues have negative real parts), **repelling** if all $p \in S$ are *unstable* equilibria (all eigenvalues have positive real parts), and of **saddle type** otherwise. The slow and fast dynamics are tangent at local extrema of C_0, meaning that there is locally no separation of timescales. Although classic GSPT falls apart in such points, there are methods for desingularizing nonhyperbolic equilibrium points, such as the blow-up method [87].

Fenichel's theorem [88] establishes a correspondence between invariant manifolds obtained for $\varepsilon = 0$ and analogous invariant slow manifolds obtained for $\varepsilon > 0$. In particular, if $S \in C_0$ is normally hyperbolic, then S perturbs to $\mathcal{O}(\varepsilon)$-nearby invariant **slow manifolds** S_ε of the singularly perturbed system, whereas the flow on S_ε converges to the slow flow on S as $\varepsilon \to 0$. Note that S_ε is not unique; rather, it is a family of curves that lie within an $\mathcal{O}(e^{-\frac{K}{\varepsilon}}), K \in \mathbb{R}$ distance from each other.

Bifurcations of the layer problem result in the *loss of normal hyperbolicity* of the critical manifold since the eigenvalues of the Jacobian $D_x f(p, \varepsilon = 0)$ change sign in a bifurcation. Under certain circumstances, this results in the appearance of a special class of solutions of singularly perturbed systems. Generally, the loss of normal hyperbolicity of invariant critical manifolds often accounts for the generation of complex patterns in slow-fast systems, especially those which involve *folded critical manifolds* [89]. The fold point of a critical manifold is a **folded singularity** if it is a nondegenerate fold and an equilibrium (singular point) of the full system. Moreover, the folded singularity is **generic** if the g-nullcline (i) intersects C_0 transversally and (ii) passes through the folded singularity at nonzero speed.

The simplest example in $\mathbb{R}^2$ is provided by a parabolic critical manifold comprised of an attractive branch C^a and a repelling one C^r, separated by a fold point L in which normal hyperbolicity is lost (the layer problem undergoes a saddle-node bifurcation), i. e. $C_0 = C^a \cup L \cup C^r$. For finite ε, the corresponding slow manifolds are C^a_ε and C^r_ε. A **maximal canard** is a trajectory which lies at the intersections of the slow manifolds $C^a_\varepsilon \cap C^r_\varepsilon$ in the vicinity of

a non-hyperbolic point $p \in L$. Such trajectories consist of motion along an attracting slow manifold followed by motion along a repelling slow manifold after passing near a folded singularity. In general, a **canard** is a trajectory which remains within $\mathcal{O}(\varepsilon)$ distance to a repelling slow manifold for an $\mathcal{O}(1)$ amount of time on the slow timescale $\tau = \varepsilon t$. In the singular limit, the maximal canard is unique and corresponds to a canard which stays in the vicinity of C^r for as long as it exists. However, for finite ε, the maximal canard consists of an exponentially thin layer of trajectories. Under the variation of a bifurcation parameter, the maximal canard is path-followed by tracing the solution which has the longest period. In practice, it is not easy to detect such solutions, since they appear in exponentially small regions of the parameter space. It should also be noted that *canards constitute separatrices for trajectories of the slow subsystem*, separating different forms of dynamical behavior.

Finally, let us consider one scenario of global dynamics involving canards in a planar system. Assume that a fast-slow system of the form

$$\varepsilon \dot{x} = f(x, y, \lambda)$$
$$\dot{y} = g(x, y, \lambda), \lambda \in \mathbb{R},$$

undergoes a singular Hopf bifurcation at $\lambda = \lambda_H$ (eigenvalues are singular as $\varepsilon \to 0$) and that the following holds:

(1) the critical manifold $C_0 = \{(x, y) \in \mathbb{R}^2 : f(x, y) = 0, y = h(x)\}$ is a smooth S-shaped curve comprised of normally hyperbolic attracting $C_0^{a\pm}$ and repelling C_0^r subsets connected by two generic fold points $p_\pm = (x_\pm, y_\pm)$, namely $C_0 = C_0^{a-} \cup \{p_-\} \cup C_0^r \cup \{p_+\} \cup C_0^{a+}$;

(2) p_- (p_+) is a local maximum (minimum) of h. At $\lambda = \lambda_c$, p_+ (p_-) is a generic folded singularity (generic fold point), namely

$$\frac{\partial f}{\partial x}(p_\pm, \lambda) = 0, \frac{\partial f}{\partial y}(p_\pm, \lambda) \neq 0$$
$$\frac{\partial^2 f}{\partial x^2}(p_-, \lambda) > 0, \frac{\partial^2 f}{\partial x^2}(p_+, \lambda) < 0$$
$$\frac{\partial g}{\partial x}(p_-, \lambda_c) \neq 0, \frac{\partial g}{\partial \lambda}(p_-, \lambda_c) \neq 0$$
$$g(p_+, \lambda_c) = 0, g(p_-, \lambda) \neq 0;$$

(3) at $\lambda = \lambda_c$, the slow flow fulfills $\dot{x} < 0$ ($\dot{x} > 0$) on $C_0^{a+} \cup C_0^r$ (C_0^{a-}).

The singular Hopf bifurcation at $\lambda = \lambda_H$ creates small-amplitude limit cycles of order $\mathcal{O}(\varepsilon)$, typically referred to as **subthreshold oscillations**. However, under assumptions (1)–(3), with varying λ the amplitude of the limit cycle rapidly increases at the maximal canard value $\lambda = \lambda_C$. Moreover, further variation of λ results in large-amplitude $\mathcal{O}(1)$ order **relaxation oscillations**. A relaxation oscillation converges to a singular trajectory comprised of continuous concatenations of alternating slow and fast segments forming a closed loop in the singular limit. For finite ε, limit cycles of intermediate size, between subthreshold and relaxation oscillations, are perturbations of **singular canard cycles** found for $\varepsilon = 0$. This scenario, accounting for the transition between small- and large-amplitude limit cy-

cles, occurs within an exponentially small parameter range and is called a **canard explosion** [87, 90, 91, 92].

1.1.1.2 Asymptotic singular perturbation theory

Analytical approximations of singularly perturbed problems are derived within *asymptotic analysis*, where the goal is to obtain an asymptotic expansion of a function, describing its limiting behavior in terms of a sequence of gauge functions. A *gauge function* $\delta(\varepsilon)$ is a positive, monotonically decreasing function (as $\varepsilon \to 0$), continuously differentiable in the neighborhood of $\varepsilon = 0$. For instance, $\delta(\varepsilon) = \varepsilon^n, n \in \mathbb{N}$ is a standard choice for a gauge function. Moreover, if $\delta_{n+1}(\varepsilon) = o(\delta_n(\varepsilon))$ for all n as $\varepsilon \to 0$, then the sequence of gauge functions $\{\delta_n(\varepsilon)\}_{n=0}^{\infty}$ is called an *asymptotic sequence*. The **asymptotic expansion** of the function $v(x, \varepsilon)$ at x_0 up to order $\delta_N(\varepsilon)$ as $\varepsilon \to 0$ is given by

$$v(x_0, \varepsilon) = \sum_{n=0}^{N} a_n(x_0)\delta_n(\varepsilon) + b_N(x_0) \cdot o(\delta_N(\varepsilon)), \tag{1.5}$$

where the functions $b_N(x)$ and $\{a_n(x)\}_{n=0}^{N}$ are finite in x_0. Moreover, if (1.5) holds for all x_0 and $b_N(x)$ is a uniformly bounded function, then the uniformly valid asymptotic expansion of v up to order $\delta_N(\varepsilon)$ is given by:

$$v(x, \varepsilon) = \sum_{n=0}^{N} a_n(x)\delta_n(\varepsilon) + o(\delta_N(\varepsilon)). \tag{1.6}$$

If (1.6) holds for all $n \in \mathbb{N}$, then we have the **asymptotic series** of v:

$$v(x, \varepsilon) \sim \sum_{n=0}^{\infty} a_n(x)\delta_n(\varepsilon).$$

In general, asymptotic series are not convergent and the accuracy of the approximation is the highest only near a certain value of x_0 and for small ε. It is not possible to *a priori* determine the optimal number of terms for approximating a function with its asymptotic series.

———————————— 1.2 *The concept of excitability* ————————————

1.2.1 Phenomenology

The concept of excitability refers to a system with a rest state that, when perturbed, displays **nonlinear threshold-like behavior** [74, 67].

Historically, the notion of excitability was first introduced by Norbert Wiener and Arturo Rosenblueth in 1946 within research on propagating contractions in the cardiac muscle. Without making any reference to the theory of nonlinear dynamical systems, they proposed a simple phenomenological paradigm by which all excitable systems have three characteristic states: **rest** (excitable), **excitatory**, and **refractory** [93]. Although the rest state classically

refers to a stable equilibrium, it can also be a stable periodic orbit [94]. In the absence of external stimuli, an excitable system remains in the rest state. However, when perturbed, it may exhibit two qualitatively different types of behavior, whereby the introduced perturbation evokes either a small- or a large-amplitude deviation before the system relaxes to the rest state. This threshold-like response naturally invokes the following distinction:

- **subthreshold perturbations** cause a small-amplitude *linear* response after which the system rapidly relaxes back to the rest state;

- **superthreshold perturbations** evoke a large-amplitude *nonlinear* response, referred to as an excitation, whereby the system performs a large excursion in the phase space before returning to the rest state, followed by a refractory period during which the system cannot be excited again. If the rest state is a stable equilibrium, the excitation is pulse-like and referred to as a "spike".

Therefore, marginally different perturbations within a narrow range of stimuli magnitudes near the threshold may result in qualitatively different responses of the system. The concept of excitability is best understood in analogy to neuronal dynamics, as shown by the example of the membrane potential's response to external stimulus in Fig. 1.2. In the case of a subthreshold perturbation, the membrane potential exhibits a small-amplitude linear response in the form of a subthreshold (small graded) postsynaptic potential, whereas a suprathreshold perturbation elicits an order of magnitude larger, nonlinear response, generating a spike or action potential.

Since it was originally believed that the phenomenon of excitability is exclusive to biological systems, initial studies concerned the excitable behavior of biophysical systems such as nervous tissue [95], the myocardium [96], and the response of the human eye to a light stimulus [97, 98]. Nevertheless, research carried out during the following decades revealed that excitability is encountered in a much wider variety of systems. Nowadays, the concept of excitability provides a universal framework for explaining the behavior of a whole class of systems. Apart from biological systems such as neuronal networks, cardiac tissue, pancreatic beta cells, and gene regulatory networks [73, 99, 100, 101, 102], examples of excitable systems include lasers [103], semiconductors [104], models of chemical kinetics [105], social interactions [106, 107], climate dynamics [108], and earthquake faults [109].

1.2.2 Dynamical features of excitable systems

Historically, following the phenomenological paradigm of Wiener and Rosenblueth, another significant contribution to understanding excitable behavior was provided by the physiologist and biophysicist Alan Hodgkin, who proposed a *classification of excitability* in 1948 [110]. Based on purely experimental observations of the excitable response of crustacean nerves to external stimuli, Hodgkin had classified excitable behavior into distinct classes or types. This classification, relevant to this day, recognizes that the transition from small- to large-amplitude responses may be abrupt or continuous [73, 74].
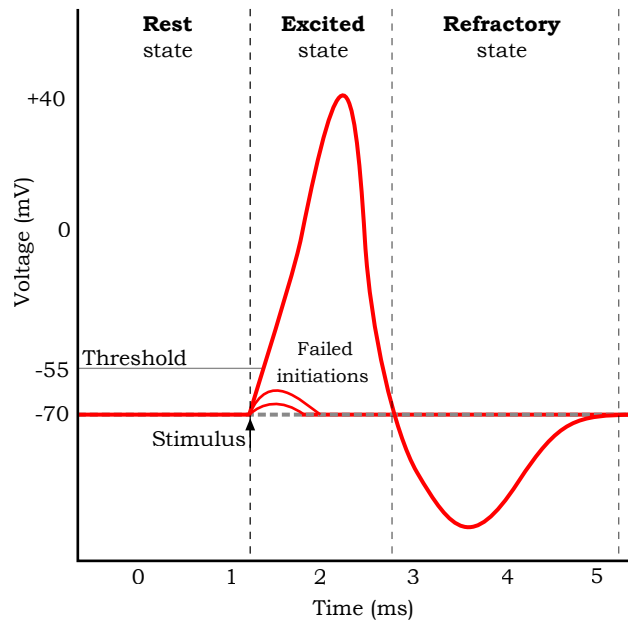
Figure 1.2: Excitable behavior illustrated by the example of neuronal dynamics. The plot shows a qualitative scheme of the membrane potential's response to stimulus, depicting three characteristic states of an excitable system: rest, excited, and refractory. Depending on whether the applied stimulus is below or above the threshold, the membrane potential displays either a linear response corresponding to subthreshold (small graded) postsynaptic potentials, or undergoes a nonlinear response in the form of an action potential or spike, followed by a refractory period during which no further spikes can be elicited.

The next milestone in the development of the theory of excitability emerged as a result of the collaborative research between Alan Hodgkin and fellow physiologist and biophysicist, Andrew Huxley, on the propagation of nerve impulses in the squid giant axon. In their legendary paper from 1952 [111], the duo provided *the first description of excitability within the framework of nonlinear dynamical systems*, having derived a mathematical model consisting of four nonlinear differential equations in order to describe the ionic mechanism of generating action potentials. For this discovery, today referred to as the Hodgkin-Huxley model, they were jointly awarded the 1963 Nobel Prize in Physiology or Medicine [112].

Several decades later, mathematicians John Rinzel and Bard Ermentrout explained Hodgkin's classification in mathematical terms by establishing a *correspondence between the different forms of experimentally observed behavior and bifurcations occurring in two-dimensional systems* [74, 113]. In general, the notion of bifurcation refers to a qualitative change in the dynamics of a system resulting from a small smooth change made to one or multiple system parameters [39]. In scenarios relevant to this thesis, the change in dynamics occurs as a result of a change in the number and stability of fixed points and limit cycles (isolated periodic solutions) in the phase space. In particular,

1. at the **saddle-node infinite period (SNIPER) bifurcation** (Fig. 1.3a), a saddle point and stable node collide and annihilate on an invariant circle, giving rise to an infinite-period limit cycle which appears as a homoclinic orbit. The SNIPER bifurcation is also

(a) **S**addle-**N**ode **I**nfinite **Per**iod bifurcation

(b) Type I excitability

(c) Hopf bifurcation (supercritical)

(d) Type II excitability
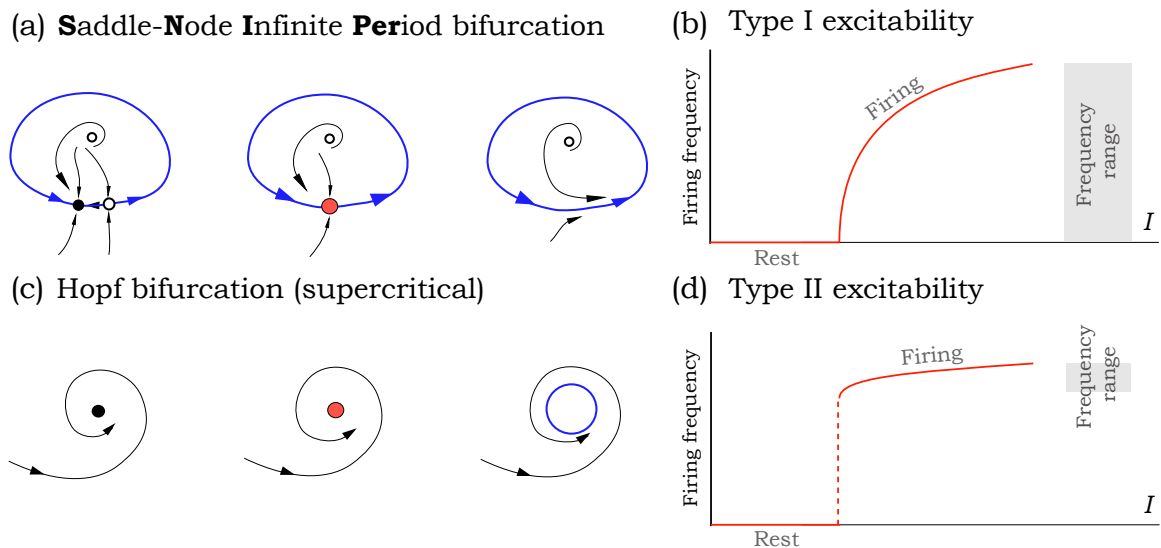
Figure 1.3: In the (a) SNIPER bifurcation scenario, two fixed points collide and annihilate on the invariant circle, giving rise to (b) Type I excitable behavior, characterized by a continuous change in firing frequencies within a wide range. On the other hand, in the (c) supercritical Hopf scenario, a small-amplitude limit cycle is born from a fixed point which loses its stability, leading to (d) Type II excitable behavior, in which the emerging limit cycle has a finite frequency assuming values from a narrow range. The figure is adapted from [73].

referred to as the saddle-node on invariant circle bifurcation.

2. in the **Hopf bifurcation** scenario (Fig. 1.3b), a fixed point changes its stability via a pair of imaginary eigenvalues as a small-amplitude limit cycle is born. Depending on the stability of the emerging limit cycle, we distinguish between the subcritical (unstable) and the supercritical (stable) Hopf bifurcation. In the former case, the stable equilibrium coexists with an unstable limit cycle, losing its stability as the unstable limit cycle engulfs it, while in the latter case, the stable equilibrium loses its stability in the bifurcation as a stable limit cycle is born.

Rinzel and Ermentrout primarily determined that the **necessary condition for observing excitable behavior in a dynamical system is that it lies near a bifurcation from the rest state to sustained oscillatory motion**. Moreover, they demonstrated that different types of bifurcations mediating the transition between stationary and oscillatory dynamics give rise to different types of excitable behavior. Based on Hodgkin's findings enriched by the mathematical characterization, we distinguish between two classes or types of excitability of a stable equilibrium, namely:

1. **Type I excitability**, which involves systems that lie close to the *SNIPER bifurcation* (Fig. 1.3a-b); and

2. **Type II excitability** (Fig. 1.3c-d), which refers to systems whose local dynamics is near the *Hopf bifurcation*.

These two mechanisms result in different dependencies of the spiking frequency on the stimulation amplitude in the vicinity of the bifurcation point, explaining Hodgkin's observations. Specifically, in Type I excitable systems, as the period of the limit cycle approaches infinity, the frequency of the oscillations becomes arbitrarily low, tending to zero. This is not the case for Type II excitable systems, in which the oscillation frequency always remains finite near the bifurcation point. Moreover, **the threshold separating small- and large-amplitude responses is more apparent in Type I than in Type II excitable systems** [74, 114]. From a mathematical point of view, thresholds are not points, but rather manifolds, whereby the mechanism of the threshold-like behavior depends on the geometric structure of the phase space of the system as follows:

1. Type I excitability involves a *separatrix* associated with *stable manifolds of saddle structures*, such as those found in the saddle-node or subcritical Hopf bifurcations. Such a structure accounts for a sharp distinction between small- and large-amplitude responses ("all-or-none" spiking), and the shape of the spike is completely independent of the stimulation properties.

2. Type II excitability, found in systems with a timescale separation, involves a *threshold manifold* or *ghost separatrix* related to the existence of *canard separatrices* [73, 74, 89, 114, 115]. Although such a structure results in a smooth crossover between the two types of responses within a narrow range of stimuli amplitudes, the system may still display a high sensitivity to perturbations given a sufficiently large timescale separation.

The details regarding the first point will be presented in section 1.2.3.1, whereas the notion of the threshold manifold will be explained within the framework of singular perturbation theory in section 1.2.3.2.

The concept of excitability has recently been extended to a relaxation limit cycle attractor [94]. In this case, the system's response to perturbations is *phase-sensitive*, i. e. non-uniform along the periodic orbit: the maximal canard provides the threshold, and the nonlinear response occurs only if superthreshold perturbations are applied to a certain part of the periodic orbit and in the appropriate direction.

Finally, regardless of the excitability type, all excitable systems share the following two **generic features**:

1. a nonlinear threshold-like response to external perturbation;

2. a non-monotonous dependence of the system's response to continuous random perturbations (*noise*).

The details concerning the second point will be elaborated in section 1.3. Here we just mention that noise may, in general, change the deterministic behavior of systems in two ways, one of which involves the crossing of thresholds or separatrices.

1.2.3 Minimal models of excitability

The generic features of excitability arise from the fact that excitable systems lie close to a bifurcation threshold. Although the specific processes accounting for the excitability of the wide variety of systems from the end of section 1.2.1 are diverse, their features are essentially alike on a fundamental level: they are all either Type I or Type II excitable.

Therefore, the significance of the classification of excitability from section 1.2.2 lies in the convenience of representing the behavior of a wider class of systems by a limited number of minimal models. Indeed, the nonlinear dynamical mechanisms responsible for *all* excitable behavior can be reduced to either the SNIPER bifurcation or the singular Hopf bifurcation, rendering it sufficient to consider only two classes of models in order to describe the entirety of excitable phenomena. This is mathematically formulated though the notion of the *normal form* of a bifurcation, i. e. the minimal dynamical system to which all other systems exhibiting this type of bifurcation are locally topologically equivalent [39].

Since the focus of this thesis concerns the mathematical properties of excitability regardless of the particular details of a system, I will consider two paradigmatic minimal models of excitability, corresponding to each excitability type.

1.2.3.1 Type I Excitability: The active rotator model

The active rotator is a simple one-dimensional model canonical for Type-I excitability. It was originally suggested by physicists Shigeru Shinomoto and Yoshiki Kuramoto in the context of the development of a statistical description of the synchronization process of a large population of oscillatory or excitable units [116]. Despite its simplicity, the active rotator model is capable of describing the behavior of an assortment of systems, including phase-locked loops in electronics, the flashing rhythms of fireflies, the mechanics of an overdamped pendulum driven by a constant torque, Josephson junctions, and lasers, to name but a few [39]. Moreover, as a one-dimensional model exhibiting the SNIPER bifurcation, it is equivalent to the biologically plausible theta model of neuronal dynamics, also known as the Ermentrout–Kopell canonical model. Although it was initially developed to describe the propagation of action potentials in the neurons of *Aplysia* sea slugs [117], it has since been applied to computational neuroscience [118, 119] as well as artificial intelligence [120].

Mathematically, the active rotator model is given by the following differential equation:

$$\frac{d\varphi}{dt} \equiv \dot{\varphi} = I - \sin\varphi \tag{1.7}$$

in which the phase state variable $\varphi \in S^1 \equiv \frac{\mathbb{R}}{2\pi\mathbb{Z}}$ is 2π-periodic, while the bifurcation parameter $I \in \mathbb{R}$ governs the local dynamics. In the context of neuroscience, φ qualitatively describes the oscillations of the neuronal membrane potential and I corresponds to the external bias current. The active rotator exhibits rather simple behavior (cf. Fig. 1.4) [73].
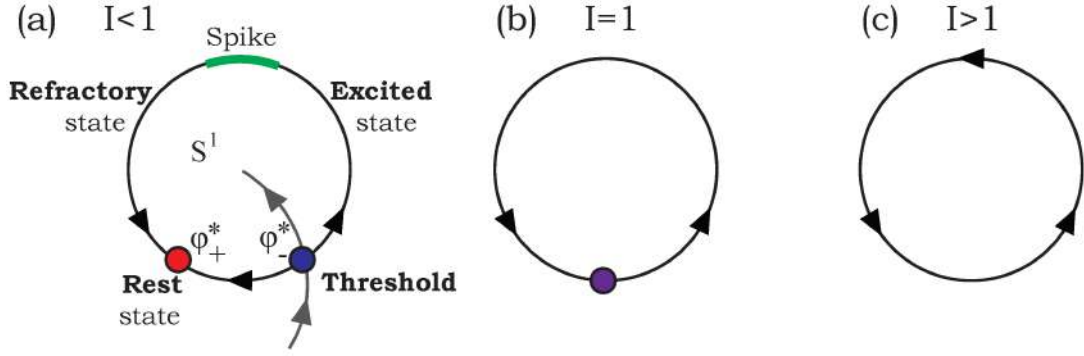
Figure 1.4: Dynamical regimes of the active rotator model (1.7) with respect to the bifurcation parameter I. The model is (a) excitable for $I < 1$, with a stable node φ_+^* corresponding to the rest state (red) and a threshold determined by the stable manifold (grey) of the saddle point (blue) φ_-^*. If φ_-^* is crossed, the system enters the excited state and emits a spike, followed by the refractory state before returning to the rest state. At (b) $I = 1$ the fixed points collide in the SNIPER bifurcation, whereas for (c) $I > 1$ the model exhibits oscillations.

Excitable regime for $I < 1$. In this regime, the system has two equilibria, a stable node φ_+^* and a saddle point φ_-^*:

$$\varphi_+^* = \arcsin I$$
$$\varphi_-^* = \pi - \varphi_+$$

corresponding to the rest state and the threshold, respectively. Small perturbations around the rest state that do not cause φ to cross the threshold value φ_-^* vanish exponentially. However, sufficiently large perturbations that lead φ beyond the stable manifold of the saddle induce a spike, whereby φ is driven to a large-amplitude excursion before returning to φ_+^*.

SNIPER bifurcation at $I = 1$. As $I \to 1^-$, the fixed points φ_+^* and φ_-^* approach each other on the invariant circle. The qualitative behavior of the system changes exactly at the bifurcation point in which the fixed points coalesce and the limit cycle becomes a homoclinic orbit to a saddle-node.

Oscillatory regime for $I > 1$. In this case, the system is a nonlinear oscillator with a unique limit cycle attractor. The oscillation period T can be obtained analytically by applying the substitution $u = tg\frac{\varphi}{2}$ to equation (1.7) as follows [39] :

$$T = \int dt = \int_0^{2\pi} \frac{dt}{d\varphi} d\varphi = \int_0^{2\pi} \frac{d\varphi}{I - \sin\varphi} = 2 \int_{-\infty}^{+\infty} \frac{du}{I + u^2 - 2u} = \frac{2\pi}{\sqrt{I^2 - 1}}, \quad (1.8)$$

from which we see that the period T diverges as a square-root $(I - 1)^{-1/2}$ as $I \to 1^+$, a scaling law which characterizes all systems near a saddle-node bifurcation.

The analysis presented above clarifies the origin of the well-defined threshold behavior found in Type I excitable systems: the perturbation must be strong enough to drive the

system beyond the stable manifold of the saddle point; otherwise it remains in the resting state. This sharp threshold accounts for the all-or-nothing spiking response described in section 1.2.2 and explains why all realized spikes have the same shape and amplitude regardless of the form of the applied perturbation.

1.2.3.2 Type II Excitability: The FitzHugh-Nagumo model

The FitzHugh–Nagumo (FHN) model is a mathematical model of neuronal excitability. Derived by FitzHugh in 1961, the model was obtained by simplifying the Hodgkin–Huxley model to a two-dimensional system [121]. The following year, Jin-Ichi Nagumo, Suguru Arimoto, and Shuji Yoshizawa created an equivalent tunnel diode circuit [122]. Although the FHN model was initially derived in order to analyze the mathematical properties of neuronal excitability, subsequent research revealed that it can be applied to a variety of other phenomena, including excitability in Belousov–Zhabotinsky chemical reactions [123, 124, 125], cardiac arrhythmias [126], flutter and fibrillation of the myocardium [127], as well as cortisol secretion [128].

The significance of the FHN model, canonical for Type II excitability, lies in the fact that it is analytically tractable. It consists of (i) an *activator* variable x whose dynamics involves a cubic nonlinearity, and (ii) a *recovery* variable y with linear dynamics unfolding on a slower timescale, evolving according to

$$\frac{dx}{d\tau} \equiv x' = x - \frac{x^3}{3} - y \tag{1.9}$$
$$\frac{dy}{d\tau} \equiv y' = \varepsilon(x + b).$$

The separation of timescales between the fast variable x and slow variable y is mediated by the small parameter $0 < \varepsilon \ll 1$, whereas the excitability of the system is controlled by the parameter b. In the context of neuroscience, the activator variable represents the membrane potential, while the recovery variable corresponds to the coarse-grained action of the potassium ion gating channels.

System (1.9) is defined on the fast timescale, whereas rescaling time as $\tau = t/\varepsilon$ yields the equivalent slow timescale formulation of the system,

$$\varepsilon\frac{dx}{dt} \equiv \varepsilon\dot{x} = x - \frac{x^3}{3} - y \equiv \varepsilon f(x, y, \varepsilon, b) \tag{1.10}$$
$$\frac{dy}{dt} \equiv \dot{y} = x + b \equiv g(x, y, \varepsilon, b).$$

The system's unique fixed point FP, corresponding to the neuron's rest membrane potential

$$FP \equiv \{-b, -b + \frac{b^3}{3}\}, \tag{1.11}$$

lies at the intersection of the nullclines, curves which divide the phase plane into regions where $\dot{x}$ and $\dot{y}$ have opposing signs, namely

$$\dot{x} = 0 \Rightarrow y = x - x^3/3 \tag{1.12}$$
$$\dot{y} = 0 \Rightarrow x = -b,$$

whereby the former is referred to as the *cubic* or fast nullcline, whereas the latter is the *linear* or slow nullcline. Moreover, FP is characterized by the following eigenvalues

$$\lambda_{\pm} = \frac{b^2 - 1 \pm \sqrt{(b^2 - 1)^2 - 4\varepsilon}}{2\varepsilon},$$

which reveal that it is stable for $|b| > 1$ and unstable for $|b| < 1$. It is sufficient to consider $b > 0$ due to the invariance of Eq. (1.9) under $(x, y, b) \rightarrow (-x, -y, -b)$. Given that $\lambda_{\pm}$ become singular when $\varepsilon = 0$, the bifurcation occurring at $b_H = 1$ has a *singular* nature. In particular, the system undergoes a singular supercritical Hopf bifurcation that gives rise to a small-amplitude stable limit cycle. Nevertheless, the system's multiscale structure gives rise to a *canard explosion* at $b_C < b_H$ in which these subthreshold harmonic oscillations exhibit a rapid transition to large-amplitude relaxation oscillations. Therefore, in order to elucidate the effect of b on the dynamical features of the FHN system, it is essential to analyze it within the framework of **geometric singular perturbation theory** [47, 89, 115, 129]. Indeed, without taking the singular nature of the FHN system into account, one can neither explain the absence of all-or-none spikes nor, consequentially, the absence of a well-defined firing threshold.

Recall from section 1.1.1 that, in the singular limit, a trajectory is comprised of continuously concatenated slow and fast segments, such that during fast motion, the trajectories of the full system converge to the solutions of the *layer (fast) problem*, obtained by setting $\varepsilon = 0$ in (1.9)

$$\dot{x} = x - \frac{x^3}{3} - y \tag{1.13}$$
$$\dot{y} = 0,$$

whereas substituting $\varepsilon = 0$ into (1.10) yields the *reduced (slow) problem*, to whose solutions trajectories of the full system converge during slow motion:

$$0 = x - \frac{x^3}{3} - y \tag{1.14}$$
$$y' = x + b.$$

Moreover, the set of equilibria of (1.13) define the critical manifold,

$$C = \{(x, y) \in \mathbb{R} \times \mathbb{R} | x - \frac{x^3}{3} - y = 0\}.$$

The cubic-shaped manifold C, shown on Fig 1.5, consists of two stable (attracting) outer branches, namely the *refractory* C_R and *spiking* C_S branch, separated by an unstable (repelling) middle branch C_U. The branches are connected via two local extrema, fold points $F^{\pm}$ in which normal hyperbolicity is lost,

$$C = C_R \cup F^- \cup C_U \cup F^+ \cup C_S. \tag{1.15}$$

Trajectories of the layer problem (1.13) approach C along horizontal *fast fibres*. Note that C coincides with the cubic nullcline (1.12). The stability properties of C as a set of equilibria of (1.13) confirm that C_R and C_S are normally hyperbolic, given that

$$\frac{\partial f}{\partial x}(x,y,0,b) = 1 - x^2 < 0 \quad \text{for} \quad (x,y) \in \{C_R, C_S\} \Leftrightarrow |x| > 1, \tag{1.16}$$

$$\frac{\partial f}{\partial x}(x,y,0,b) = 1 - x^2 > 0 \quad \text{for} \quad (x,y) \in C_U \Leftrightarrow |x| < 1,$$

while the layer problem undergoes saddle-node bifurcations at $F^{\pm} = (x^{\pm}, y^{\pm}) = (\pm 1, \pm\frac{2}{3})$, where the flow changes direction, such that

$$\frac{\partial f}{\partial x}(x^+, y^+, 0, b) = 1 - x^2 = 0, \quad \frac{\partial^2 f}{\partial x^2}(x^+, y^+, 0, b) = -2x^+ = -2 < 0 \tag{1.17}$$

$$\frac{\partial f}{\partial x}(x^-, y^-, 0, b) = 1 - x^2 = 0, \quad \frac{\partial^2 f}{\partial x^2}(x^-, y^-, 0, b) = -2x^- = 2 > 0,$$

whereby the fold point F^- coincides with FP (1.11) for $b = 1$. Moreover,

$$\frac{\partial g}{\partial x}(x^+, y^+, 0, b_C) = 1 \neq 0, \tag{1.18}$$

$$\frac{\partial g}{\partial b}(x^+, y^+, 0, b_C) = 1 \neq 0,$$

$$g(x^-, y^-, 0, b_C) = x^- + b_C = -1 + b_C = 0,$$

$$g(x^+, y^+, 0, b) = x^+ + b = 1 + b \neq 0,$$

from which we derive the condition $b_C = 1$. The slow flow is restricted to motion along C, i. e. $y = x - \frac{x^3}{3} \equiv \Phi(x)$. Considering

$$y = \Phi(x) \implies \dot{y} = \dot{x}\Phi_x'(x) = g(x, \Phi(x), b, 0) \implies \dot{x} = \frac{g(x, \Phi(x), b, 0)}{\Phi_x'(x)},$$

the following holds for the slow flow at $b = b_C = 1$:

$$\dot{x}|_{b=b_C} = \frac{1+x}{1-x^2} = \frac{1}{1-x} \implies \begin{cases} \dot{x} < 0 & \text{for} \quad x > 1 \Leftrightarrow (x,y) \in C_S \\ \dot{x} > 0 & \text{for} \quad x < 1 \Leftrightarrow (x,y) \in C_R \cup C_U, \end{cases}$$

implying that the slow flow changes direction in F^+.

Eqs. (1.15), (1.16), (1.17), (1.18), (1.19) fully determine the geometry of the phase space. Furthermore, the FHN model satisfies the conditions for the existence of a *canard solution* as well as those for a *canard explosion* at $b = b_C$, both of which crucially influence the dynamics of the non-singular FHN system: in the excitable regime, a canard-like trajectory accounts for the system's threshold-like response to perturbation, while in the oscillatory regime, the canard explosion gives rise to large-amplitude relaxation oscillations.

Let us now consider the dynamical regimes of the FHN system in detail [129, 130], see Fig. 1.5.
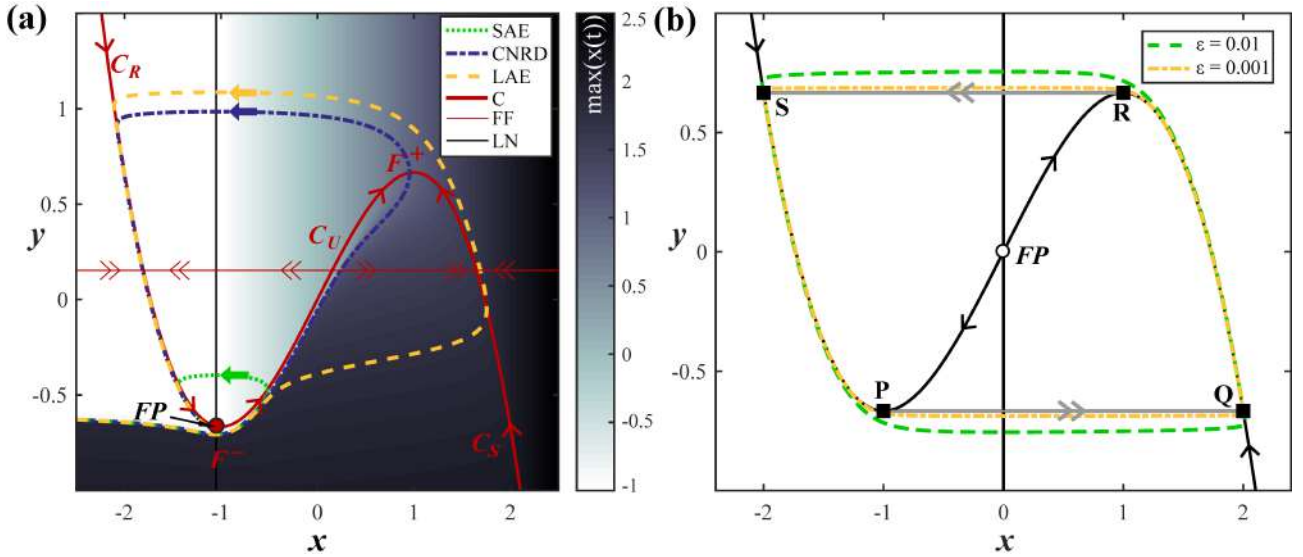
Figure 1.5: Phase portraits and trajectories of the FHN model in the (a) excitable and (b) oscillatory regime. The background of subplot (a) shows the model's response in terms of $max(x)$ depending on the initial conditions $\{x(0), y(0)\}$, demonstrating the absence of all-or-none spikes (obtained for $\varepsilon = 0.05, b = 1.05$). The trajectories are obtained by varying $y(0) \in \{-0.6204, -0.620482000763042, -0.6206\}$ with fixed $x(0) = -3$, for SAE, LAE and $CNRD$ (small-, large-amplitude responses, and a canard-like trajectory accounting for the threshold, respectively). Slow motion occurs along the critical manifold C, comprised of the stable refractory C_R, unstable C_U, and stable spiking C_S branches, connected by fold points $F^{\pm} = (\pm 1, \pm \frac{2}{3})$, whereas fast motion occurs along the horizontal fast fibres FF. Arrows indicate the direction of motion. The linear nullcline LN intersects the cubic nullcline (which coincides with C) at the fixed point $FP = (-b, -b + \frac{b^3}{3})$. Subplot (b) shows the phase portrait for $b = 0$ with two relaxation oscillation trajectories, obtained for $\varepsilon \in \{0.001, 0.01\}$. The unstable FP lies at the intersection of the nullclines. Between the turning points P and Q, as well as R and S, the system rapidly jumps between the branches along the fast fibres in the direction indicated by the arrows, while motion along the branches is much slower.

Excitable regime for $b > 1$. The stable focus FP (1.11), as the sole attractor, is the rest state. When perturbed, the system typically displays either a small-amplitude excitation (SAE, green curve on Fig 1.5a)) or large-amplitude excitation or spike (LAE, yellow curve), whereby the threshold separating the SAE and LAE is not as clearly defined as it is in Type I excitability. Indeed, the Hopf bifurcation does not provide an object which could account for a well-defined boundary, such as the stable manifold of the saddle in the previously considered class of models.

Nevertheless, the details of the threshold-like response can be explained by considering the singular limit where global trajectories consist of continuously concatenated solutions of the layer and reduced and problems, cf. Fig 1.5a). Starting from initial conditions away from FP, any trajectory will first rapidly approach an attracting segment of C along a fast fibre (layer problem), forming a new initial condition for the slow dynamics on C (reduced problem). For $\varepsilon = 0$, the threshold separating SAE and LAE is a canard trajectory which follows C_U and separates nearby trajectories into those that sharply diverge to the left or
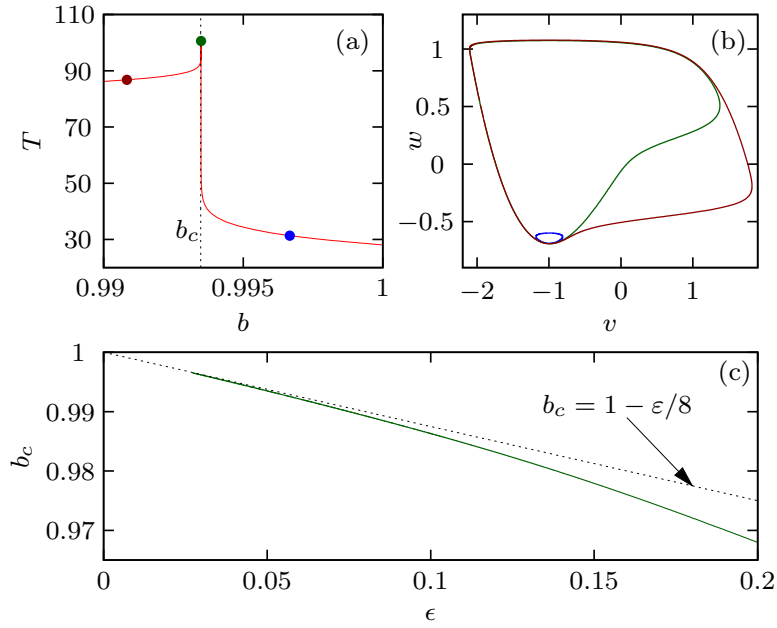
Figure 1.6: Canard explosion in the FHN system, adopted from [131]. Subplot (a) shows the dependence of the period T on b for fixed $\varepsilon = 0.05$, (b) contains the phase portraits of a subthreshold oscillation ($b_C < b < b_H$, blue), the canard trajectory ($b = b_C$, green), and a relaxation oscillation ($b > b_C$, red), whereas (c) shows a comparison of the $b_C(\varepsilon)$ dependence obtained by path-following of the canard solution (green solid) and the asymptotic formula Eq. (1.19) (black dashed). Symbols in (a) denote chosen b values for (b).

right of the canard, reaching either the refractory C_R or spiking C_S branch. In other words, the canard is a separatrix for solutions of the reduced problem, such that, depending on the position of the base point of the fast fibre relative to the singular canard trajectory, the system exhibits

- either a **SAE**, in which the trajectory returns to FP before reaching the spiking branch C_S, such that a singular global trajectory consists of motion along C_U, followed by a rapid jump via a fast fibre to C_R, along which it approaches FP;

- or a **LAE (spike)**, whereby the trajectory involves partial motion along C_S before returning to FP, such that it consists of motion along C_U, followed by a jump via a fast fibre to C_S, along which it slowly moves to F^+, from where it jumps along a fast fibre back to C_R, from where it reaches FP.

When the timescale separation is finite $0 < \varepsilon \ll 1$, the system inherits a so-called "ghost separatrix" structure from the singular limit [114], comprised of an exponentially thin layer of trajectories around C_U. Such canard-like trajectories ($CNRD$, blue curve in Fig 1.5a)) follow C_U and separate (a) trajectories which jump along the fast fibres to the left to C_S and produce a spike or LAE from (b) those that jump along the fast fibres to the right to C_R, resulting in a SAE. Given a sufficient separation of timescales, the system still displays a high sensitivity to perturbations, allowing the approximation of the ghost separatrix by a threshold in the conventional sense. Therefore, canards and repelling slow manifolds approximate

the spiking threshold [74], explaining the absence of a well-defined spiking threshold in the FHN model. Although the crossover between these two types of responses is continuous, intermediate-amplitude responses of the system are rather difficult to detect. FitzHugh himself had observed this behavior, calling it the "quasi-threshold" [132], whereas he named the region of the phase plane which contains trajectories starting in the vicinity of the quasi-threshold "No Man's Land".

Let us now consider the absence of an all-or-none spiking response. The background of Fig. 1.5a) shows the peak value of the activator variable x depending on the initial conditions $\{x(0), y(0)\}$, such that dark regions indicate a LAE whereas white regions indicate a SAE, clearly indicating that the model exhibits a continuous but rapid blow-up of $max(x(t))$ in a small region near C_U, corresponding to intermediate-amplitude responses. See [133] for an overview of such behavior in other neuronal models.

Supercritical *singular* Hopf bifurcation at $b = b_H = 1$. As FP loses its stability, $FP = F^-$, and a small-amplitude harmonic limit cycle characterized by an ε-dependent period and amplitude of orders $\mathcal{O}(1/\sqrt{\varepsilon})$ and $\mathcal{O}(\varepsilon)$, respectively, emerges around FP.

Oscillatory regime for $b < 1$. The now unstable focus FP has crossed F^-, moving from C_R to C_U, whereas the stable limit cycle accounts for self-sustained oscillatory motion, derived from the local features of the unstable focus. Nevertheless, such a limit cycle persists only for a narrow range of values $b < b_H$, whereas further reducing b leads to a blow-up of the oscillation amplitude to the order $\mathcal{O}(1)$, accompanied by a change in the order of the period from $\mathcal{O}(1/\sqrt{\varepsilon})$ to $\mathcal{O}(1/\varepsilon)$. Specifically, considering (a) a cubic shaped critical manifold $C = C_R \cup F^- \cup C_U \cup F^+ \cup C_S$ such that C_R, C_S (C_U) are normally hyperbolic attracting (repelling), whereby (b) $F-$ ($F+$) is a folded singularity (generic fold point), and that (c) at $b = b_c$ the slow flow on C changes direction in $F+$ such that $\dot{x} < 0$ for $(x, y) \in C_S$ and $\dot{x} > 0$ for $(x, y) \in C_R \cup C_U$, the system fulfills the conditions for a *canard explosion* at $b = b_C$ (recall section 1.1.1 and conditions given by Eqs. (1.15), (1.16), (1.17), (1.18), (1.19)). In the singular limit, $b_C = b_H = 1$, but for $0 < \varepsilon \ll 1$, $b_C < b_H$, accounting for an abrupt increase in the amplitude of the limit cycle born in the Hopf bifurcation [134, 135, 136], see Fig. 1.6(a)-(b). The first-order asymptotic approximation for $b_C(\varepsilon)$ is given by [137, 138],

$$b_C \approx 1 - \frac{\varepsilon}{8}. \tag{1.19}$$

whereas Fig. 1.6(c) shows a comparison of analytically calculated and numerically obtained results. Nevertheless, periodic solutions of intermediate amplitude (canard cycles) are hard to detect because they occur only for a narrow range of values. Neuroscientifically, the canard explosion accounts for a transition route from rest to spiking through subthreshold oscillations.

The large-amplitude limit cycle, as a relaxation oscillation, consists of segments of slow and fast motion. In contrast to the local nature of harmonic oscillations born in the supercritical Hopf bifurcation, relaxation oscillations arise from the global structure of the phase

space. In the singular limit, see Fig. 1.5 b), the relaxation trajectory involves turning points of the trajectory, namely $\{P, Q, R, S\} = \{(-1, -\frac{2}{3}), (2, -\frac{2}{3}), (1, \frac{2}{3}), (-2, \frac{2}{3})\}$, such that slow motion is confined to the slow manifold ($Q \to R$ and $S \to P$), whereas fast motion consists of the trajectory jumping along the fast fibres between different parts of the slow manifold ($P \to Q$ and $R \to S$) in the direction indicated by the gray arrows. With increasing ε, the fast segments of the trajectory deviate from those obtained in the singular limit, and the system "overshoots" the horizontal straight line in the vicinity of the turning points, extending the oscillation period T (cf. trajectories in Fig. 1.5 b) for different ε). Nevertheless, the $T(b)$ dependence may be approximated by neglecting the fast transitions and including only the motion along the slow manifold, cf. Eq. (1.14), namely

$$y = x - \frac{x^3}{3} \Rightarrow \dot{y} = \dot{x}(1 - x^2) = x + b \Rightarrow \dot{x} = \frac{x+b}{1-x^2}.$$

The system spends T_S and T_R amounts of time on the spiking branch and refractory branch, respectively,

$$T_S = \int_2^1 dx \frac{x+b}{1-x^2} = (b^2-1)\ln\frac{b+2}{b+1} - b + \frac{3}{2}$$
$$T_R = \int_{-2}^{-1} dx \frac{x+b}{1-x^2} = (b^2-1)\ln\frac{b-2}{b-1} + b + \frac{3}{2},$$

yielding the following estimation for the period of oscillations:

$$T = T_S + T_R = (b^2-1)\ln\frac{b^2-4}{b^2-1} + 3.$$

Although with increasing ε this formula predicts a shorter period compared to that obtained from numerical simulations, it turns out that the additional time has a similar dependence on b, allowing one to rescale the period with a constant parameter $e \in \mathbb{R}$ as follows [129]

$$T = \left((b^2-1)\ln\frac{b^2-4}{b^2-1} + 3\right)(1+e).$$

1.3 Effects of noise in excitable systems

The dynamics of far-from-equilibrium systems inherently involves fluctuations or noise, which may originate from the embedding environment (external sources) or describe the system's inherent fluctuations (intrinsic sources) [67]. Moreover, noise may derive from coarse-graining over the degrees of freedom associated with small spatial and temporal scales. In excitable systems, instances of internal fluctuations include the quasi-random release of neurotransmitters by the synapses in neurons, quantum fluctuations in lasers [139], and finite-size effects in chemical reactions [140]. On the other hand, an example of external noise is provided by synaptic bombardment in which each neuron is impacted by a large number of uncorrelated presynaptic inputs [141].

The deterministic behavior of excitable systems is rather well understood. However, given that noise may substantially modify their nonlinear threshold-like behavior, many issues concerning the effects of noise on such systems still remain open. Since noisy signals consist of successive sub- and super-threshold perturbations occurring in an unpredictable fashion, excitable systems are considerably sensitive to the influence of noise. Indeed, noise-induced fluctuations may give rise to a variety of dynamical behaviors, essentially influencing systems by [67]:

1. either *modulating the deterministic behavior* by acting non-uniformly on different states of the system thus amplifying or suppressing some of its features; or

2. *giving rise to completely novel forms of behavior*, typically based on crossing the thresholds or separatrices, or involving an enhanced stability of deterministically unstable structures.

In particular, the key effects of noise in excitable systems include:

1. the onset of **noise-induced oscillations** [142, 143, 144, 145, 146, 147, 148]; and

2. different types of **resonant phenomena**, manifested as a characteristic non-monotonous dependence on the noise level, associated with noise introducing a new characteristic timescale to the dynamics.

Under certain circumstances, noise may increase the coherence or regularity of the system's dynamics [149]. For instance, in excitable systems exhibiting *noise-induced oscillations*, a notable example is *coherence resonance* (CR), in which the regularity of noise-induced oscillations becomes maximal at an optimal noise intensity [149, 150, 151, 152, 153, 154, 155, 156]. The prevalence of CR is well established for the case of single excitable units, coupled stochastic units [157], as well as at the level of collective variables in coupled systems [158]. CR has been found in a variety of neural models, laser models, excitable biomembrane models and climate models, and has been experimentally observed in systems as diverse as electronic circuits, laser diodes, excitable chemical reactions, and the cat's cortical dynamics [108, 159, 160, 161, 162, 163, 164, 165, 166, 167, 168, 169, 170]. The mechanism of the effect relies on a particular balance between the noise-dependent variabilities of the (*i*) activation process, which describes the escape from the vicinity of the stable equilibrium, and the (*ii*) relaxation process, which corresponds to the return to the fixed point [67]. CR is observed when the noise intensity is simultaneously large enough to ensure a short activation time and small enough to maintain the deterministic nature of the relaxation process.

Another resonant phenomenon appearing in noisy dynamics of a single excitable unit is *self-induced stochastic resonance* (SISR) [171]. While both CR and SISR lead to increased coherence in the system, the underlying mechanisms are different, due to the fact that noise perturbs the deterministic slow-fast structure of the underlying system in a different way.

A more recent development concerns the observation of resonant phenomena in oscillating units near the bifurcation threshold. In contrast to the previously considered excitable

regime in which such phenomena involve noise-induced oscillations, in this scenario, resonant effects are related to *noise-perturbed oscillations*. A curious example of such behavior is *inverse stochastic resonance* (ISR), where the frequency of noise-perturbed oscillations becomes minimal at an optimal noise intensity [94, 68, 172, 173, 174, 175, 176, 177, 178]. In ISR, the effect of noise is inhibitory: it may either induce bursting-like behavior in which oscillations are interrupted with quiescent episodes, or completely quench the oscillations. Such an inhibitory effect of noise has recently been explicitly corroborated for cerebellar Purkinje cells [178, 179, 42, 180]. Moreover, ISR has been indicated to play important functional roles in neuronal systems, including the reduction of spiking frequency in the absence of neuromodulators, suppression of pathologically long short-term memories, triggering of on-off tonic spiking activity, and even optimization of information transfer along the signal propagation pathways [68, 174, 176, 178].

1.4 *This thesis*

Having introduced the fundamental concepts underlying this thesis, we shall now provide an outline of its contents. The complementary directions of research which the thesis is comprised of concern **three groups of emergent phenomena**, namely:

1. the excitability of coupled systems,

2. switching dynamics induced by the interplay of adaptivity and noise, and

3. resonant phenomena in coupled systems with local dynamics near the bifurcation threshold.

The remainder of the thesis consists of three chapters, each devoted to one group of considered emergent phenomena, followed by a final concluding chapter. Since different aspects of the same models are relevant to phenomena explored in particular chapters, there is a partial overlap between the chapters in the sense that certain analyses rely on previously presented results. The outline of the thesis is as follows.

Chapter 2 addresses the problem of extending the notion of excitability to coupled systems by considering the following issues:

- the excitable dynamics of an adaptively coupled motif of two locally excitable units, and

- the *macroscopic excitability* feature in a population of stochastic map neurons,

where the fundamental question is how interactions modify the local excitability feature. In the former case, our analysis concerns deterministic excitable regimes of two adaptively coupled active rotators [181, 182, 183, 184], whereby our goal is to classify the modalities of the system's response to external perturbation and explain them in terms of bifurcation analysis. These results have been published in [181].

Concerning macroscopic excitability, we have derived a mean-field approach in order to systematically analyze the emergent behavior, underlying bifurcations, and the stimulus-response relationship of a population of stochastic map neurons, whereby the derivation of the effective model relies on a cumulant approach complemented by the Gaussian closure hypothesis [67, 185, 186, 187, 188, 189, 190]. Our goal here will be to demonstrate that the reduced model captures the qualitative and quantitative features of the spontaneous and induced collective dynamics of the exact system. These results have been published in [191].

Chapter 3 presents a systematic analysis of stochastic switching arising due to the interplay of multiple timescale dynamics and noise. To this end, we investigate two simplified yet paradigmatic models that incorporate three basic ingredients of neurodynamics, namely, excitability, plasticity, and noise. The considered systems include:

- two adaptively coupled stochastic active rotators; and

- a self-coupled stochastic active rotator with slowly adapting feedback.

In the case of two coupled rotators, our central discovery is the appearance of slow stochastic fluctuations, whereby their form qualitatively depends on the scale separation between the fast and the slow variables. These results have been published in [181]. The analysis of the deterministic structure of the system, as well as our methods for obtaining a qualitative insight into the mechanisms guiding the switching dynamics, rely on geometric singular perturbation theory.

In the case of the self-coupled stochastic active rotator with adaptation, our main finding is that the system is capable of displaying stochastic bursting due to noise-induced switching. We have explained the mechanism behind the stochastic bursting regime, its stability boundaries, and the means of controlling its features by introducing a novel method of stochastic averaging. These results have been published in [192].

Chapter 4 is devoted to the investigation of resonant phenomena in small motifs of units whose local dynamics is set close to the bifurcation threshold. Essentially, the goal of this chapter is to extend previous research of non-monotonous responses to noise in single units presented in section 1.3. In particular, we investigate:

- new generic scenarios for *inverse stochastic resonance* (ISR) in two adaptively coupled stochastic active rotators; and

- *coherence resonance* (CR) in a stochastic active rotator with slowly adapting feedback.

Concerning ISR, we have discovered two generic mechanisms of the effect, whereby one is based on biased switching between metastable states associated with coexisting attractors of the corresponding deterministic system, whereas the other is due to noise-enhanced stabilization of a deterministically unstable fixed point. Moreover, by showing that the same phenomena can be found in a single Morris-Lecar unit, we have established that the effects are independent on the excitability class. These results have been published in [193, 194].

As far as the latter point is concerned, we have introduced a novel method of control of CR in excitable systems via a slowly adapting feedback. The control mechanism has been explained by extending the methods of multiscale analysis to stochastic systems. These results have been published in [192].

Finally, **Chapter 5** concludes the thesis by summarizing the main conceptual and methodological advances of the presented results and providing an outlook for future research.

Chapter 2

The Excitability of Coupled Systems

One method of exciting an excitable unit is by coupling it to other units. Systems comprised of interacting excitable elements – widely encountered in physics, chemistry, and biology – are capable of exhibiting a rich variety of self-organizing phenomena in which novel features emerge at the collective level [195]. Spatially coupled excitable units comprise excitable media, capable of supporting localized or propagative patterns. In general, coupling in networks or arrays (spatially distributed systems) may give rise to oscillations, manifested either as the onset of collective mode or cluster states; pulses; wavefronts and circular, spiral, and scroll waves; as well as patterns such as localized spots, periodic and chaotic spatio-temporal patterns [65, 66]. Another interesting discovery concerns chimera states, characterized by coexisting domains of spatially coherent and incoherent dynamics, recently found in nonlocally coupled excitable systems [196]. Given the prevalence of coupled excitable systems, investigating their collective behavior is relevant to a broad range of fields, whereby understanding the emergent features of such systems requires going far beyond the analysis of constituent elements. The fundamental question to which this chapter is devoted to is how interactions modify the local excitability feature.

In neuroscience, for instance, gaining a comprehensive understanding of the emergent dynamics of neuronal populations and their interactions is a topical issue [71, 72]. According to contemporary neuroscientific paradigms, the key functional unit of the mammalian CNS is comprised of distributed ensembles of neurons rather than single neurons [197]. Indeed, the brain is a complex system characterized by a nontrivial hierarchical organization over multiple temporal and spatial scales, whereby neurobiological research indicates that processes occurring at different organizational levels are distributed across anatomically segregated, but functionally integrated moduli [14, 198, 199].

Nevertheless, although excitability is well-understood at the level of individual units, the excitable behavior of interacting systems remains an open problem. In this context, the present chapter concerns the following fundamental questions:

1. Can excitability be found at the level of coupled systems, i.e. does macroscopic excitability exist? If yes, how does it relate to local excitability features? In particular, how do interactions modify local excitability and what are the differences between

macroscopic and microscopic excitability?

2. What determines the nonlinear threshold-like behavior of coupled systems?

3. What are the stability boundaries of such an excitable state and which bifurcations account for the transitions to other states? Can one derive a reduced model to identify the conditions giving rise to collective excitability?

As a first step, it seems reasonable to study the influence of coupling on the excitable behavior of a small network *motif*. Motifs are basic building blocks of complex networks, consisting of a small number of coupled elements [14, 200]. In neurobiology, for instance, a single structural motif can support multiple functional motifs [201, 202, 203, 204], each characterized by a particular weight configuration and direction of information flow. Bridging the gap between research on individual excitable units and our understanding of the excitability of coupled systems, this chapter concerns

1. the **excitability of an adaptively coupled motif** of two locally excitable units [181]; and

2. the **macroscopic excitability** feature in a population of locally excitable elements [191].

The main motivation for studying problem (1) comes from neuroscience, where network motifs of just a few neurons involve synaptic connections whose strength is slowly modified by synaptic plasticity, dependent on the averaged dynamics of pre- and postsynaptic neurons. Although our setup is simple, it is also paradigmatic: the active rotator model is canonical for Type I excitability, whereas the chosen phase-dependent adaptivity rule mimics the typical properties of synaptic plasticity [182, 205, 206, 207]. The considered system can be interpreted as a binary neuron motif.

Our aim regarding problem (1) is to (*i*) determine which plasticity rules facilitate the excitability of the coupled system, as well as (*ii*) understand the details of the associated threshold-like behavior. Our results indicate that the threshold-like behavior is determined by the manifolds of the saddle structures of the coupled system. It turns out the system is capable of displaying several distinct types of responses to external perturbation, characterized by different patterns with respect to the spiking of individual units. We explain the modalities of the system's response to external perturbation in terms of the interplay of the thresholds of individual units and asymmetry in the coupling.

A detailed analysis of this issue is provided in section 2.1, which is organized as follows. The details of the model are introduced in section 2.1.1, whereas section 2.1.2 contains a detailed analysis of deterministic dynamics, focusing on the stationary states which may exhibit excitable behavior. The final section 2.1.3 provides a classification of the different excitable regimes displayed by the binary motif.

Problem (2), considering a population of excitable neurons, concerns a population of coupled stochastic maps, which may be considered as a model of a mesoscopic neuronal population. At the level of collective dynamics, an important open issue relevant to both

theoretical and experimental considerations involves the macroscopic excitability scenario in which a whole population of excitable units acts as an excitable element itself. The idea of macroscopic excitability is analogous to an often-invoked paradigm in nonlinear dynamics by which a population of coupled oscillators displaying a collective mode is treated as a macroscopic oscillator [208]. Within this approach, the goal is to describe the collective mode by developing a reduced and analytically tractable description of the population's behavior based on different forms of mean-field (*MF*) approximations. This is typically done by applying a bottom-up strategy [209], starting from a high-dimensional system of (stochastic) differential equations which describes local neuronal dynamics.

The *MF* approach and its generalization to spatially extended systems have become a standard tool for analyzing diverse problems in neuroscience and other fields [210, 211, 212, 213, 214, 215, 216]. Nevertheless, it has thus far been applied only to systems described by coupled ordinary or delay differential equations, while effective models for assemblies of coupled maps have been lacking. In particular, although the collective motion of spiking or bursting neurons influenced by noise has been extensively studied in different models of coupled discrete systems, such as Rulkov [202, 217, 218, 219, 220, 221, 222, 204] or Izhikevich neuron maps [223, 224], this has not been complemented by an appropriate *MF* theory, most likely because the Fokker-Planck formalism cannot be applied to discrete-time systems. Our analysis is the first *MF* theory obtained for a population of coupled stochastic neuronal maps. The derivation relies on the cumulant approach complemented by the Gaussian closure hypothesis [67, 185, 186, 187, 188, 189, 190]. Our immediate goal is to establish the regime of macroscopic excitability, as a new form of emergent behavior, study its stability boundaries and bifurcations to other regimes, as well as to examine the related stimulus-response relationship of the population.

Section 2.2 of this chapter is devoted to this corpus of problems. In particular, section 2.2.1 contains an overview of the local map dynamics and introduces the population model, whereas section 2.2.2 outlines the derivation of the *MF* model. Then, in section 2.2.3, we provide proof of the the qualitative and quantitative agreement between the dynamics of the exact and the *MF* model, in terms of appropriate bifurcation diagrams as well as a comparison of the characteristic features of the associated regimes. Section 2.2.4 concerns the assembly's stimulus-response relationship, where we first investigate the analogy between the respective phase-response curves (*PRCs*) of the exact system and the effective model in spiking and bursting regimes and then consider the extent to which the *MF* model reproduces the population's response to perturbations of finite amplitude and duration.

A summary and discussion of our results concerning the excitability of the adaptively coupled motif, as well as the neuronal population are provided in the concluding section 2.3 of this chapter.

—— 2.1 *Excitability of a motif of two adaptively coupled units* ——

In this section, we classify the excitable regimes of a motif consisting of two active rotators interacting by phase-dependent adaptive couplings. The active rotator model is canonical for Type I local excitability, whereas the slower dynamics of the coupling strengths plays the role of plasticity in neuronal systems. Our first goal is to identify conditions that give rise to excitable behavior at the level of the motif. To this end, we perform stability and bifurcation analysis and find that the considered plasticity rule supports a parameter regime admitting two excitable equilibria. In terms of coupling strengths, these fixed points effectively correspond to master-slave configurations, characterized by an asymmetry in the influence the units have on each other. Our findings reveal that the system is capable of generating several distinct threshold-like responses to external perturbation, whereby these modalities can be explained in terms of the threshold behavior of individual units and the disparity of the coupling strengths.

2.1.1 Model

In our model, the dynamics of the phases $\{\varphi_1(t), \varphi_2(t)\}$ and the couplings $\{\kappa_1(t), \kappa_2(t)\}$ is described by the following system of ordinary differential equations:

$$\dot{\varphi}_1 = I_0 - \sin \varphi_1 + \kappa_1 \sin (\varphi_2 - \varphi_1)$$
$$\dot{\varphi}_2 = I_0 - \sin \varphi_2 + \kappa_2 \sin (\varphi_1 - \varphi_2)$$
$$\dot{\kappa}_1 = \varepsilon(-\kappa_1 + \sin(\varphi_2 - \varphi_1 + \beta))$$
$$\dot{\kappa}_2 = \varepsilon(-\kappa_2 + \sin(\varphi_1 - \varphi_2 + \beta)), \tag{2.1}$$

where $\varphi_1, \varphi_2 \in S^1$ and $\kappa_1, \kappa_2 \in \mathbb{R}$. The rotators are assumed to be identical, with the local dynamics governed by the excitability parameter I_0. In particular, isolated units undergo the SNIPER bifurcation at the critical value $I_0 = 1$, separating the excitable ($I_0 < 1$) and oscillatory ($I_0 > 1$) regimes. Since this section concerns excitable local dynamics, $I_0 = 0.95$ will be kept fixed for simplicity. In the excitable regime, the uncoupled system always converges to a steady state, whereas the interactions may induce emergent oscillations in the coupled system. The parameter $0 < \varepsilon \ll 1$ defines the timescale separation between the fast dynamics of the phases and the slow dynamics of adaptation. In the context of neuroscience, I_0 can be interpreted as an external bias current. The system has $\mathbb{Z}_2$ symmetry since the equations are invariant to the exchange of indices $1 \leftrightarrow 2$.

The plasticity rule is controlled by the phase shift parameter β, which describes the modality of the plasticity rule with respect to the phase difference $\Delta\varphi = \varphi_2 - \varphi_1$, allowing one to interpolate between different adaptation modalities. The analogy between the adaptivity dynamics in classical neuronal systems and the systems of coupled phase oscillators has been addressed in [205, 206, 207], whereas a deeper analysis of the correspondence between the phase-dependent plasticity rules and the STDP has been provided in [182]. From

these studies, it follows that the scenario found for $\beta = 3\pi/2$, where the stationary weights increase for smaller phase differences and decrease for larger ones ("like-and-like" form of behavior), qualitatively resembles the Hebbian learning rule [206, 207]. Nevertheless, in the case $\beta = \pi$, the two couplings always change in opposite directions, which may be interpreted as promoting an STDP-like plasticity rule. This is shown in Fig. 2.1. Our interest lies in the β interval between these two limit cases, since it admits two coexisting excitable fixed points.

2.1.2   Deterministic dynamics: stationary states

We will now consider the system's fixed points in order to understand the excitable behavior of the motif. Note that due to $\mathbb{Z}_2$, fixed points always appear in pairs which share the same stability features.

In line with a standard slow-fast approach (singular perturbation theory), we may consider the *layer problem (fast subsystem) fast subsystem*, defined on the fast timescale:

$$\dot{\varphi}_1 = I_0 - \sin\varphi_1 + \kappa_1 \sin(\varphi_2 - \varphi_1)$$
$$\dot{\varphi}_2 = I_0 - \sin\varphi_2 + \kappa_2 \sin(\varphi_1 - \varphi_2), \tag{2.2}$$

in which κ_1 and κ_2 are treated as fixed parameters; as well as the associated *reduced problem (slow subsystem)*, defined on the slow timescale, whose dynamics is given by:

$$\dot{\kappa}_1 = -\kappa_1 + \sin(\varphi_2 - \varphi_1 + \beta)$$
$$\dot{\kappa}_2 = -\kappa_2 + \sin(\varphi_1 - \varphi_2 + \beta), \tag{2.3}$$

In general, the fixed points $(\varphi_1^*, \varphi_2^*, \kappa_1^*, \kappa_2^*)$ of the full system (2.1) are given by the solutions of the following set of equations:

$$\sin\varphi_1^* - \sin(\varphi_2^* - \varphi_1^* + \beta)\sin(\varphi_2^* - \varphi_1^*) = I_0,$$
$$\sin\varphi_2^* - \sin(\varphi_1^* - \varphi_2^* + \beta)\sin(\varphi_1^* - \varphi_2^*) = I_0, \tag{2.4}$$

with

$$\kappa_1^* = \sin(\varphi_2^* - \varphi_1^* + \beta),$$
$$\kappa_2^* = \sin(\varphi_1^* - \varphi_2^* + \beta). \tag{2.5}$$

Equations (2.4) can be numerically solved for any fixed parameter set, while numerical path-following allows one to study the dependence of the coordinates of the fixed points on the parameters. The fast flow is useful because it allows for analytical tractability, whereas the exchange symmetry can be taken into account by considering the solutions on and off the synchronization manifold of the fast subsystem ($\varphi_1 = \varphi_2$).

The following subsections contain a brief analysis of the stability of the fixed points on the synchronization manifold of the fast subsystem for four paradigmatic values of β which reduce the dimension of the full system (2.1), as well as a more rigorous analysis on the

fast flow which explicitly considers the β-dependence of the number and stability of fixed points. The explicit study of the points on and off the synchronization manifold is motivated by the system's $\mathbb{Z}_2$ exchange symmetry.

2.1.2.1 Stability of fixed points on the synchronization manifold

The fixed points on the synchronization manifold can be obtained from the equations for the fast flow by setting $\varphi_1 = \varphi_2$ in the fast subsystem (2.2). The following holds for $i \in \{1, 2\}$:

$$\dot{\varphi}_i = I_0 - \sin \varphi_i = 0 \Rightarrow \sin \varphi_i = I_0 \Longleftrightarrow \varphi_i = (-1)^n \arcsin I_0 + \pi n, n \in \mathbb{Z}$$

implying that the *fast subspace always contains fixed points on the synchronization manifold for $I_0 \in (0, 1)$*. Indeed, the fast flow has two fixed points on the synchronization manifold, both independent of the stationary values of the couplings:

$$P1 \equiv \{\varphi_1, \varphi_2\} = \{\arcsin I_0, \arcsin I_0\} \tag{2.6}$$
$$P2 \equiv \{\varphi_1, \varphi_2\} = \{\pi - \arcsin I_0, \pi - \arcsin I_0\}.$$

The stability of these fixed points along the transversal $\lambda_\perp$ and longitudinal $\lambda_\parallel$ directions follows from the eigenvalues of the Jacobian. In particular, the corresponding eigenvalues of $P1$ are given by:

$$\lambda_\perp = -\sqrt{1 - I_0^2} - \kappa_1^* - \kappa_2^*$$
$$\lambda_\parallel = -\sqrt{1 - I_0^2} < 0,$$

whereas those of $P2$ read:

$$\lambda_\perp = \sqrt{1 - I_0^2} - \kappa_1^* - \kappa_2^*$$
$$\lambda_\parallel = \sqrt{1 - I_0^2} > 0,$$

revealing that both $P1$ and $P2$ change transversal stability depending on the stationary values of the couplings, whereas $P1$ ($P2$) is always longitudinally stable (unstable) for $I_0 < 1$. Thus, the synchronization manifold contains one fixed point ($P1$) which always remains longitudinally stable, whereas its transversal stability depends on the coupling.

Since β determines the stationary values of the weights (2.5), the plasticity rule has a nontrivial impact on the dynamics of the full system. Let us first consider four paradigmatic values $\beta \in \{0, \pi/2, \pi, 3\pi/2\}$ which give rise to symmetrical behavior of the coupling strengths ($\kappa_1 = \pm\kappa_2$), reducing the dimension of the full system by one. By analyzing the impact of the global stability of the longitudinally stable fixed point on the synchronization manifold $P1$ (2.6), as well as the impact of β on the stationary couplings, we arrive to the following conclusions, see also Fig. 2.1.

1. $\beta = \frac{\pi}{2} :\Rightarrow \kappa_1^* = \kappa_2^* = +1$:
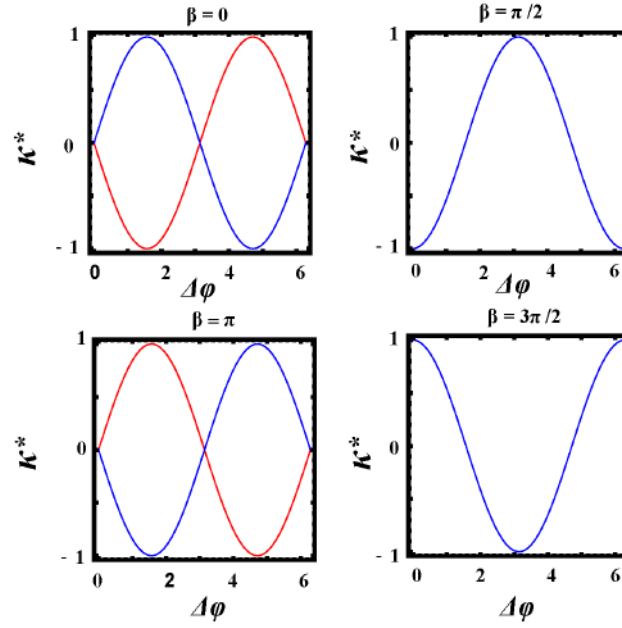
Figure 2.1: The stationary values of the coupling strengths (2.5) as a function of $\Delta\varphi = \varphi_2 - \varphi_1$ for several paradigmatic β values: $\beta \in \{0, \pi/2, \pi, 3\pi/2\}$. According to [206], the scenario for $\beta = 3\pi/2$, where the stationary weight increases for smaller phase differences and decreases for larger ones ("like-and-like" form of behavior), qualitatively corresponds to the well-known Hebbian learning rule. By the same token, the case $\beta = \pi/2$ qualitatively corresponds to the anti-Hebbian learning rule, whereas the $\kappa^*(\Delta\varphi)$ profiles for $\beta \in \{0, \pi\}$ may be interpreted as STDP-like plasticity rules.

- Attractive coupling.
- $P1$ is a transversally stable node.
- The full system converges to the completely synchronized state
  $(\varphi_1^*, \varphi_2^*, \kappa_1^*, \kappa_2^*) = (\arcsin I_0, \arcsin I_0, +1, +1)$.
- No emergent oscillations.
- Anti-Hebbian learning rule.

2. $\beta \in \{0, \pi\} :\Rightarrow \kappa_1^* = -\kappa_2^* = 0$:

- Decoupled state.
- $P1$ is a transversally stable node.
- No emergent oscillations.
- STDP-like learning rules.

3. $\beta = \frac{3\pi}{2} \Rightarrow \kappa_1^* = \kappa_2^* = -1$:

- Repulsive coupling.
- $P1$ is a transversally unstable node.
- The system exhibits emergent oscillations.
- Hebbian learning rule.

2.1.2.2 β-dependence of the number and stability of fixed points

Let us rewrite the equations of the fast flow (2.2) by applying the following transformation of coordinates $(\varphi_1, \varphi_2) \mapsto (\delta\varphi, \Phi)$:

$$\delta\varphi = \frac{1}{2}(\varphi_1 - \varphi_2)$$
$$\Phi = \frac{1}{2}(\varphi_1 + \varphi_2).$$

The dynamics of the fast flow in terms of the new variables is then given by

$$\dot{\delta\varphi} = -\sin\delta\varphi(\cos\Phi + (\kappa_1 + \kappa_2)\cos\delta\varphi)$$
$$\dot{\Phi} = I_0 - \cos\delta\varphi(\sin\Phi + (\kappa_1 - \kappa_2)\sin\delta\varphi),$$

where κ_1 and κ_2 are fixed parameters. The dependence of the number of fixed points of the fast flow, as well as their stability in terms of β, can be analyzed by substituting the stationary weight values into the equations of fast flow. In particular, the slow flow (2.5) in terms of $(\delta\varphi, \Phi)$ reads

$$\dot{\kappa_\pm} = \varepsilon(-\kappa + \sin(\pm\delta\varphi + \beta))$$
$$= \varepsilon(-\kappa + \sin\beta\cos\delta\varphi \pm \cos\beta\sin\delta\varphi)$$

meaning that the stationary weights are given by

$$\kappa_1^* = \cos\beta\sin\delta\varphi + \sin\beta\cos\delta\varphi \tag{2.7}$$
$$\kappa_2^* = \cos\beta\sin\delta\varphi - \sin\beta\cos\delta\varphi.$$

Finally, by substituting (2.7) into (2.2), the fast subsystem becomes

$$\dot{\varphi}_1 = I_0 - \sin\varphi_1 + \cos\beta(\sin\delta\varphi)^2 + \sin\beta\cos\delta\varphi\sin\delta\varphi \tag{2.8}$$
$$\dot{\varphi}_2 = I_0 - \sin\varphi_2 + \cos\beta(\sin\delta\varphi)^2 - \sin\beta\cos\delta\varphi\sin\delta\varphi.$$

Note that the synchronization manifold is once again invariant due to (2.8) being symmetrical with respect to the exchange of indices $1 \leftrightarrow 2$. Due to this symmetry, all fixed points outside of the synchronization manifold appear in pairs within which members share stability features.

We have verified that the number and stability of the fixed points of the full system (2.1) matches those of the fast subsystem (2.8). The complete bifurcation diagram showing the fixed points of (2.1) as a function of β, obtained in the described way, is provided in Fig. 2.2. With respect to the number of fixed points, the system admits seven distinct regimes:

1. $\beta \in (0, 0.156)$: **4 fixed points**, one stable on the synchronization manifold, one unstable, two saddles;

2. $\beta \in (0.156, 1.787)$: **2 fixed points**, one stable and one saddle on the synchronization manifold;

(a)

(b)
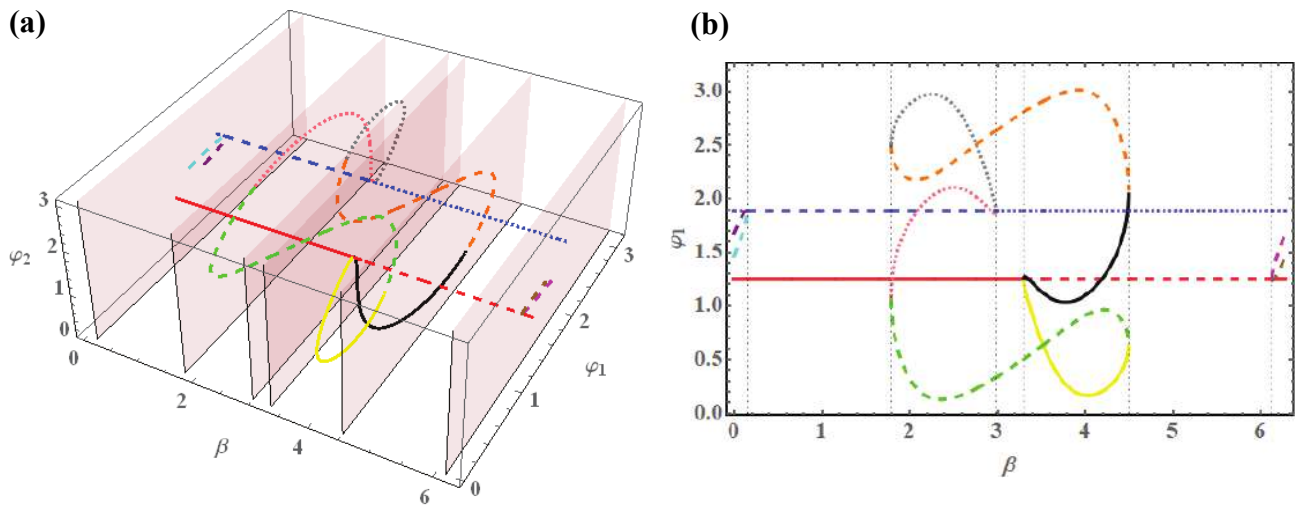
Figure 2.2: Subplot (a) shows the bifurcation diagram for the fixed points of the fast flow in the $(\beta, \varphi_1, \varphi_2)$ space, whereas (b) shows projection of the bifurcation diagram to (β, φ_1) plane. The two fixed points independent on β belong to the synchronization manifold: the red (blue) one is always longitudinally stable (unstable). The solid lines denote stable fixed points, whereas the dashed and dotted lines denote saddles of unstable dimension 1 and 2, respectively.

3. $\beta \in (1.787, 2.984)$: **6 fixed points**, one stable on the synchronization manifold, two unstable points and three saddles;

4. $\beta \in (2.984, 3.298)$: **4 fixed points**, one stable on the synchronization manifold, one unstable, two saddles;

5. $\beta \in (3.298, 4.495)$: **6 fixed points**, two stable outside of synchronization manifold, one unstable point and three saddles;

6. $\beta \in (4.495, 6.126)$: **2 fixed points**, one unstable and one saddle on the synchronization manifold;

7. $\beta \in (6.126, 2\pi)$: **4 fixed points**, one stable on the synchronization manifold, one unstable, two saddles.

Under increasing β, the associated bifurcations are as follows:

1. $\beta = 0.156$: **inverse supercritical pitchfork bifurcation** in which the longitudinally unstable fixed point on the synchronization manifold gains transversal stability;

2. $\beta = 1.787$: **two fold bifurcations** giving rise to two pairs of symmetry-related fixed points, each comprised of a saddle point and an unstable point;

3. $\beta = 2.984$: **subcritical pitchfork bifurcation** in which the longitudinally unstable fixed point on the synchronization manifold is destabilized in the transversal direction;
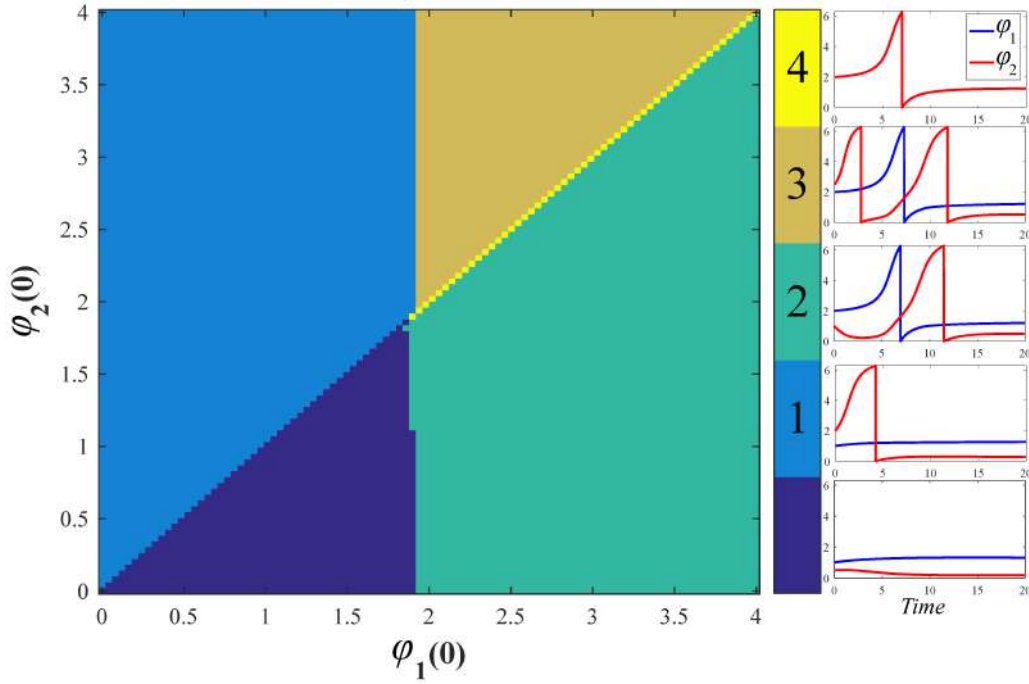
Figure 2.3: Modalities of the response to external perturbation for system (2.1). The system parameters are fixed to $I_0 = 0.95$, $\varepsilon = 0.01$ and $\beta = 4.212$, whereas the initial conditions for the couplings are set to $\kappa_1(0) = -0.0078$, $\kappa_2(0) = -0.8456$. Depending on the initial phases $(\varphi_1(0), \varphi_2(0))$, one may observe the following regimes: (0) no spikes; (1) the unit with larger $\varphi(0)$ emits one spike and the other does not; (2) both units emit a single spike, with the unit with larger $\varphi(0)$ firing first; (3) the unit with larger $\varphi(0)$ emits two spikes and the other unit emits one; (4) both units spike synchronously.

4. $\beta = 3.298$: **supercritical symmetry-breaking pitchfork bifurcation** in which two stable fixed points are created off the synchronization manifold;

5. $\beta = 4.495$: **two symmetrical inverse saddle node bifurcations** in which pairs consisting of a stable and an unstable fixed point off the synchronization manifold are destroyed;

6. $\beta = 6.126$: **inverse subcritical pitchfork bifurcation** which stabilizes the longitudinally stable fixed point on the synchronization manifold in the transversal direction.

2.1.3 Stimulus-response relationship and threshold-like behavior

Since our study concerns plasticity rules which support excitable fixed points, we have confined our analysis to interval (5) $\beta \in (3.298, 4.495)$, where the system has two stable fixed points off the synchronization manifold (i. e. $\varphi_1 \neq \varphi_2$), which are excitable, as well as four unstable fixed points. In further considerations, we shall fix β to a particular value within the relevant interval. For instance, for $\beta = 4.212$, the symmetry-related pair of stable foci is given by

$$(\varphi_1^*, \varphi_2^*, \kappa_1^*, \kappa_2^*) = (1.2757, 0.2127, -0.0078, -0.8456) \tag{2.9}$$
$$(\varphi_1^*, \varphi_2^*, \kappa_1^*, \kappa_2^*) = (0.2127, 1.2757, -0.8456, -0.0078)$$

These asymmetric coupling strengths support effective *master-slave configurations* in which one unit exerts a much stronger influence on the other unit than vice versa.

The excitability of the two stable asymmetric foci (2.9) manifests itself as several different types of responses to external perturbations of the coupled system, as shown in the classification provided in Fig. 2.3 and the corresponding phase portraits 2.4. The perturbation is introduced by the setting of different initial conditions $\{\varphi_1(0), \varphi_2(0)\}$ with fixed $\kappa_1(0) = -0.0078, \kappa_2(0) = -0.8456$ to values from 2.9.

By analyzing the subsequent relaxation of the phases to the rest state, we observe that the excitability of the coupled system involves **well-defined threshold-like behavior**. The threshold set is partially determined by the unstable manifold of the saddle point on the synchronization manifold whose coordinates are given by:

$$(\varphi_1^*, \varphi_2^*, \kappa_1^*, \kappa_2^*) = (\pi - \arcsin I_0, \pi - \arcsin I_0, \sin \beta, -\sin \beta),$$

which means that the excitation threshold for individual units is given by the value $\varphi_{thr} = \pi - \arcsin I_0$. If the perturbation excites either φ_1 or φ_2 to values larger than φ_{thr}, the corresponding unit will emit a spike.

Moreover, the response of the coupled system is asymmetric due to the disparity of coupling strengths and phases of the two steady states (2.9). Namely, if the initial conditions are set to $\varphi_2(0) > \varphi_1(0)$, the steady state will be achieved only after a large excursion in the phase space (compare (0) and (1) from Fig. 2.3). The phase portraits shown in Fig. 2.4) clearly demonstrate that trajectories cannot directly cross the synchronization manifold $\varphi_1 = \varphi_2$ (dashed line) during relaxation; rather, a spike must occur before the system settles back to the rest state.

When both units are perturbed below threshold, neither unit fires (regime 0). In order to observe spiking behavior, at least one of the units must be perturbed at or above the threshold (regimes 1–4). This may be achieved either by crossing the unstable manifold of the saddle point on the synchronization manifold ($\varphi_1(0) > \varphi_{thr}$ or $\varphi_2(0) > \varphi_{thr}$) or by setting the initial conditions to $\varphi_2(0) > \varphi_1(0)$. Depending on the perturbation, the system emits between one and three spikes in total. In general, in scenarios in which both units respond with a spike, the order of firing is such that the unit with larger initial phase fires first (regimes 2–3). Nonetheless, if both units are set exactly onto the synchronization manifold by the perturbation with $\varphi_1(0) = \varphi_2(0) > \varphi_{thr}$, they will both emit a single spike synchronously (regime 4).

$-$ 2.2 *Macroscopic excitability: assembly of coupled neuronal maps* $-$

In this section, we establish the concept of macroscopic excitability based on the idea of synchronized local activity, examine the stability boundaries of this regime and bifurcations to other regimes, as well as examine the population's stimulus-response relationship. To
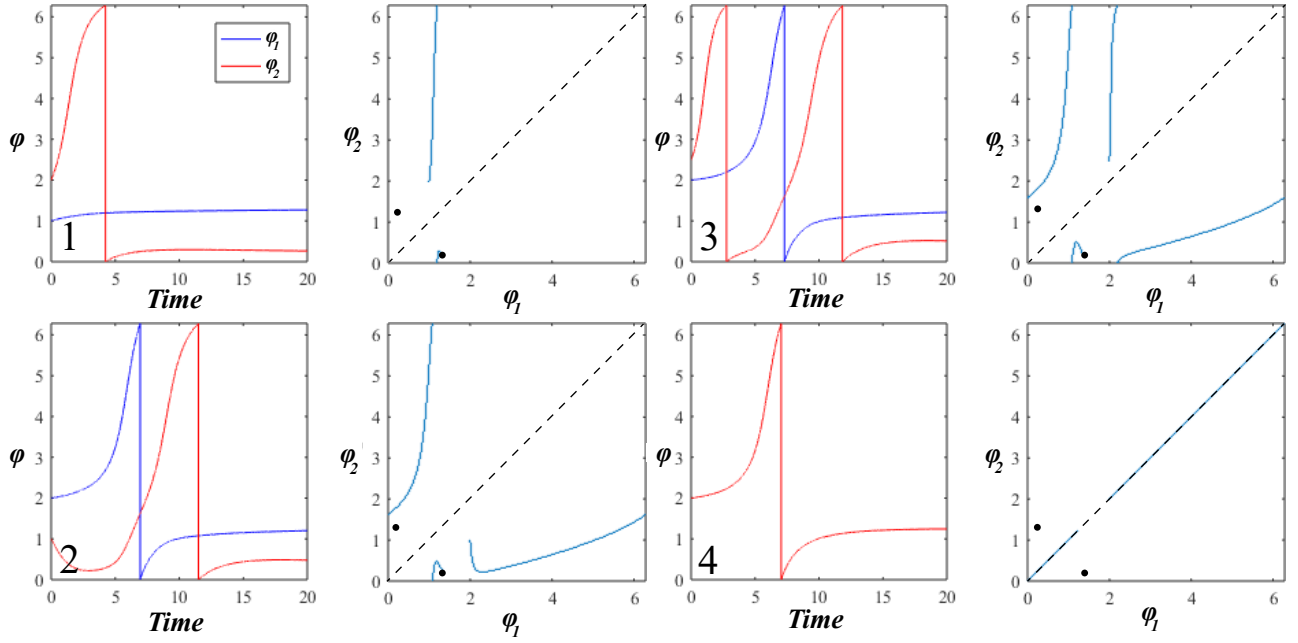
Figure 2.4: Time series $\{\varphi_1(t), \varphi_2(t)\}$ (blue and red, respectively) and trajectories in the (φ_1, φ_2) plane (light blue) corresponding to the spiking responses 1–4 from Fig. 2.3 for system (2.1). The system parameters are fixed to $I_0 = 0.95$, $\varepsilon = 0.01$ and $\beta = 4.212$, whereas the initial conditions for the couplings are set to $\kappa_1(0) = -0.0078$, $\kappa_2(0) = -0.8456$. Depending on the initial conditions, the system exhibits different modalities of relaxing to one of the excitable equilibria (black dots), emiting between one and three spikes in total. The black dashed line denotes the synchronization manifold ($\varphi_1 = \varphi_2$).

address these issues, we derive a reduced effective (mean field) model based on a cumulant approach complemented by the Gaussian closure hypothesis [191].

2.2.1 Local map dynamics and the population model

The local dynamics is represented by the map model:

$$x_{n+1} = x_n + G(x_n) - \beta H(x_n - d) - y_n, \tag{2.10}$$
$$y_{n+1} = y_n + \varepsilon(x_n - J),$$

where n denotes the iteration step. The variable x_n qualitatively accounts for the membrane potential, whereas the recovery variable y_n, whose rate of change is set by the small parameter $\varepsilon = 0.01$, mimics the behavior of ion-gating channels. The parameters a, β and d modify the oscillation profile, while J crucially influences the neural excitability, viz. the transitions from silence to active regimes. The model be considered as a discrete version of the FHN neuron model, and has first been introduced in [225, 226]. The local dynamics may exhibit a variety of regimes found in real neurons, including excitability, subthreshold oscillations, regular and chaotic spiking or bursting, as well as mixed spiking-bursting oscillations [227, 228, 229, 230].
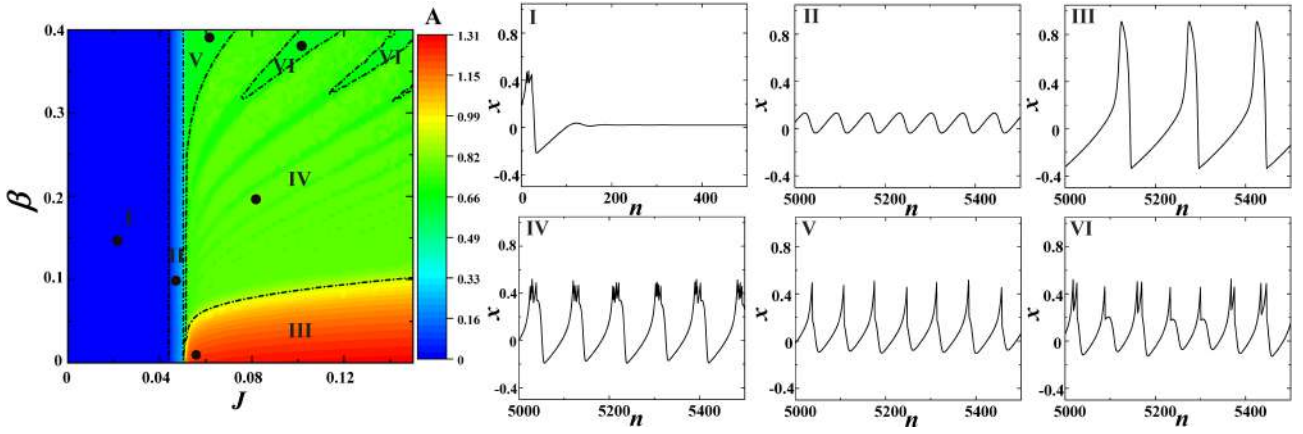
Figure 2.5: Dynamical regimes of the neuron map model (2.10). The heat map shows the variation of the amplitude of oscillations A of the x time series in the $J - \beta$ plane. The waveforms shown in subfigures $I - VI$ illustrate different generic forms of neuronal behavior, including excitability (I), subthreshold oscillations (II), regular spiking (III), chaotic bursting (IV), chaotic spiking (V), as well as mixed spike-burst activity (VI). The dots in the heat map indicate the particular (J, β) values for which the representative waveforms were obtained.

The evolution of x_n features two nonlinear terms: (i) a FitzHugh-Nagumo-like cubic nonlinearity $G(x_n) = x_n(x_n - a)(1 - x_n)$, which is complemented by (ii) a discontinuity term $-\beta H(x_n - d)$, where H stands for the Heaviside step function. The parameters $a = 0.1$ and $d = 0.45$ are kept fixed throughout the chapter. The discontinuity makes the fast subsystem (Eq. (2.10) with $\varepsilon = 0$) a Lorenz-type map within certain parameter domains [226, 231], due to which the model may exhibit chaotic spiking or bursting oscillations, typically absent in Fitzhugh-Nagumo type of systems.

Under the variation of J and β, the considered map (2.10) is capable of reproducing a rich repertoire of generic regimes displayed by real neurons, as demonstrated in Fig. 2.5. In particular, the main frame shows the amplitudes of the corresponding x time series as a function of (J, β), while the remaining subfigures illustrate characteristic waveforms corresponding to the excitable regime (region I), subthreshold oscillations (II), regular (III) or chaotic spiking (IV), chaotic bursting (V), as well as mixed chaotic spike-burst activity (VI). Some of the indicated boundaries, such as those involving domains IV, V and VI should be understood as tentative since the associated transitions are smooth and therefore difficult to discern.

A detailed phase plane analysis concerning the relevant unstable invariant curves and the mechanisms underlying the transitions between the different dynamical regimes can be found in [232]. Here we briefly mention that under increasing J, the equilibrium loses stability via the Neimarck-Sacker bifurcation which gives rise to subthreshold oscillations. These subthreshold oscillations may be considered excitable in the sense that a sufficiently strong perturbation elicits a spike, but the system relaxes to a closed invariant curve instead of a steady state.
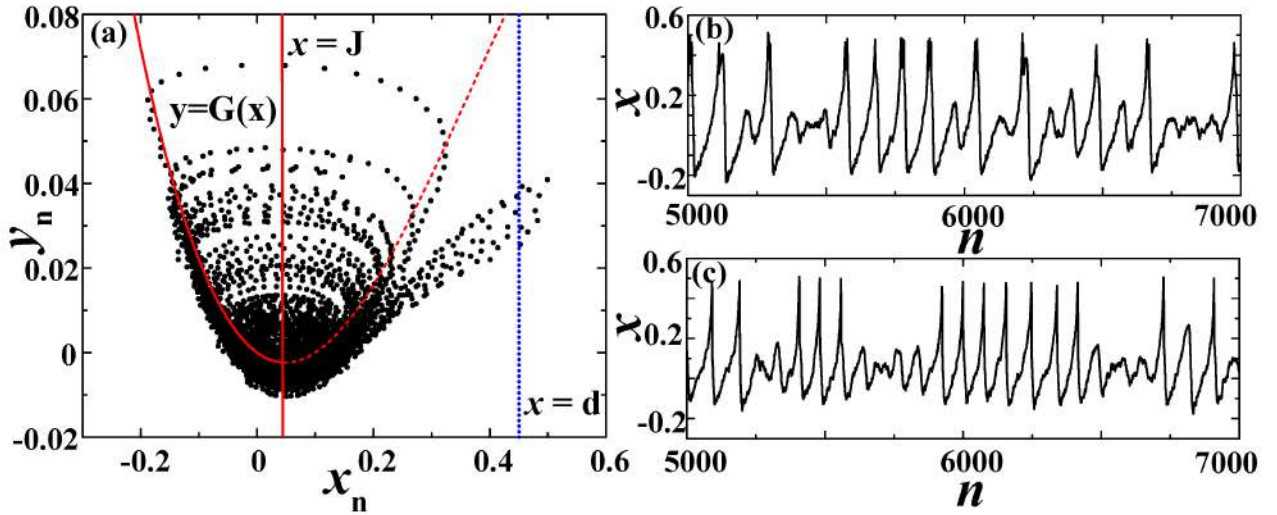
Figure 2.6: Impact of noise on a single map neuron in the excitable regime. (a) indicates the mechanism behind noise-induced spiking. The data are obtained for $J = 0.046, \beta = 0.4, \sigma = 0.005$. The equilibrium is deterministically stable given that the line $x = J$ intersects the invariant curve $y = G(x)$ below the curve's minimum. (b) shows the x_n series corresponding to noise-induced bursting ($J = 0.042, \beta = 0.2, \sigma = 0.008$), whereas (c) demonstrates stochastic spiking superimposed on subthreshold oscillations ($J = 0.048, \beta = 0.4, \sigma = 0.008$).

We are now interested in the behavior of an assembly of N globally electrically (diffusively) coupled stochastic neurons whose local dynamics conforms to (2.10). Each neuron receives input from all other units within the assembly through electrical synapses and is further influenced by synaptic noise, representing uncorrelated input from the embedding environment. Note that in multiscale neuron models, the term "synaptic noise" typically refers to external sources of noise acting on the fast (activator) variables, while the stochastic terms included in the slow (recovery) variables are interpreted as mimicking the influence of intrinsic (ion-channel) neuronal noise [69, 233]. The population activity is described by the following system:

$$x_{i,n+1} = x_{i,n} + G(x_{i,n}) - \beta H(x_{i,n} - d) - y_{i,n} + I_{i,n}^{syn}, \tag{2.11}$$

$$y_{i,n+1} = y_{i,n} + \varepsilon(x_{i,n} - J),$$

$$I_{i,n}^{syn} = I_{i,n}^{coup} + I_{i,n}^{rand} = \frac{c}{N} \sum_{j=1,j\neq i}^{N} (x_{j,n} - x_{i,n}) + \sigma\xi_{i,n},$$

where i specifies the particular neuron. The synaptic currents $I_{i,n}^{syn}$ consist of two terms: (i) *diffusive couplings* $I_{i,n}^{coup}$ characterized by strength c, assumed to be uniform over the network and set to $c = 1$ in the remainder of the chapter; and (ii) *random inputs* $I_{i,n}^{rand}$ which involve uncorrelated white noise ($E[\xi_{i,n}] = 0, E[\xi_{i,n}\xi_{j,n'}] = \delta_{ij}\delta(n - n')$) of intensity σ.

Confined to a single unit, the stochastic component influences the dynamics either by perturbing the deterministic oscillatory regimes or by inducing oscillations in the excitable regime, cf. Fig. 2.6(b). The onset of noise-induced spiking or bursting within domain I in Fig. 2.5, where the fixed point is deterministically stable, corresponds to a *stochastic bifur-*

cation [189, 234, 235, 236, 237]. Stochastic bifurcations are noise-induced transitions. The present scenario is an instance of a *P* (phenomenological) stochastic bifurcation, characterized by a qualitative change in a time-averaged quantity (such as the asymptotic probability distributions of relevant variables or the associated power spectra) under the variation of noise intensity. Unlike deterministic bifurcations that occur at a clearly defined critical value of the control parameter, stochastic bifurcations involve a gradual change in the system's behavior [189]. Within region II, noise may perturb the regime of subthreshold oscillations by eliciting the dynamics similar to mixed-mode oscillations, with interspersed relaxation and subthreshold oscillations, cf. Fig. 2.6(c).

So far, models similar to (2.11) have been applied to address a number of problems associated with collective phenomena in networks of coupled neurons, including synchronization of electrically coupled units with spike-burst activity [238, 239], pattern formation in complex networks with modular architecture [227, 228, 240], transient cluster activity in evolving dynamical networks [230], as well as the basin stability of synchronization regimes in small-world networks [229]. In our analysis, the collective motion will be described in terms of the global variables $X_n = \frac{1}{N} \sum_{i=1}^{N} x_{i,n}$ and $Y_n = \frac{1}{N} \sum_{i=1}^{N} y_{i,n}$.

2.2.2 Derivation of the mean-field model

Considering a *MF* approximation, our main goal is to derive a reduced low-dimensional deterministic set of nonlinear difference equations whose dynamics is qualitatively analogous to the collective motion of the original system (2.11) comprised of $2N$ coupled stochastic maps. In particular, the *MF* model should should reproduce the qualitative and quantitative features of all the regimes displayed by the exact system, further allowing one to determine the respective stability domains and bifurcations outlining their boundaries. Regarding the explicit effects of noise, the *MF* model is expected to account for the onset or suppression of different types of collective modes associated with macroscopic spiking or bursting activity, which are mediated by synchronization or desynchronization of the dynamics of individual neurons, respectively. The synchronization processes may be influenced by noise in a variety of ways, including scenarios in which noise acts as a perturbation to mainly deterministic (and chaotic) local oscillations, as well as those in which noise plays a facilitatory role, in the sense that the collective mode emerges through the synchronization of noise-induced local dynamics.

Given that (2.11) is a system of discrete-time equations, the standard approach to deriving *MF* models which relies on the Fokker-Planck formalism cannot be applied [190]. Nevertheless, an analytically tractable *MF* model may still be built by considering the evolution of cumulants [67, 185, 186, 189], whereby the full density of states is factorized into a series of marginal densities. This approach allows us to truncate the underlying cumulant series by introducing simplifying approximations in a controlled fashion. Such approximations, stated in the form of a *closure hypothesis* [67], are required due to the nonlinearity of the original system causing the dynamics of cumulants of a given order to be coupled to those

of the higher order.

In our case, the derivation of the effective model incorporates an explicit *Gaussian closure hypothesis* [67, 185, 186, 189], according to which all cumulants above second order are assumed to vanish. The collective dynamics is then described by a set of five variables (the first- and second-order cumulants), including

(i) the **means**, given by $m_{x,n} = \lim\limits_{N\to\infty} \frac{1}{N} \sum_{i=1}^{N} x_{i,n} \equiv \langle x_{i,n} \rangle$, $m_{y,n} = \lim\limits_{N\to\infty} \frac{1}{N} \sum_{i=1}^{N} y_{i,n} \equiv \langle y_{i,n} \rangle$;

(ii) the **variances**, defined as $S_{x,n} = \langle x_{i,n}^2 \rangle - \langle x_{i,n} \rangle^2 = \langle x_{i,n}^2 \rangle - m_{x,n}^2$ and $S_{y,n} = \langle y_{i,n}^2 \rangle - \langle y_{i,n} \rangle^2 = \langle y_{i,n}^2 \rangle - m_{y,n}^2$;

(iii) the **covariance** $U_n = \langle x_{i,n} y_{i,n} \rangle - m_{x,n} m_{y,n}$.

The expressions for higher order moments $\langle x_{i,n}^k \rangle$ in terms of the first- and second-order cumulants [241], such as

$$\langle x_i^3 \rangle = m_x^3 + 3 m_x S_x \tag{2.12}$$
$$\langle x_i^4 \rangle = m_x^4 + 6 m_x^2 S_x + 3 S_x^2$$
$$\langle x_i^2 y_i \rangle = m_y S_x + m_y m_x^2 + 2 m_x U$$
$$\langle x_i^3 y_i \rangle = 3 S_x U + 3 S_x m_x m_y + 3 m_x^2 U + m_y m_x^3$$
$$\langle x_i^5 \rangle = m_x^5 + 15 m_x S_x^2 + 10 m_x^3 S_x$$
$$\langle x_i^6 \rangle = m_x^6 + 15 S_x^3 + 15 m_x^4 S_x + 45 m_x^2 S_x^2,$$

can be derived using the closure hypothesis.

The Gaussian approximation effectively amounts to an assumption that the relation

$$\lim_{N\to\infty} \frac{1}{N} \sum_{i=1}^{N} x_{i,n}^k \approx E[x_{i,n}^k],$$

holds, whereby E refers to the expectation value obtained by averaging over an ensemble of different stochastic realizations. In other words, we suppose that the local variables are independent and are drawn from the normal distribution $\mathcal{N}(m_x, S_x)$. However, we cannot know *a priori* whether such an assumption is fulfilled or not. Rather, we may judge its validity by verifying whether the predictions on the population dynamics provided by the *MF* model are correct.

Since the effective model concerns the dynamics of the assembly in the thermodynamic limit $N \to \infty$, we can neglect the stochastic terms, as it can be shown that they contribute to finite size effects which scale as $1/N$. This means that the influence of noise in our *MF* model is felt only via the noise intensity, which assumes the role of an additional bifurcation parameter.

Let us illustrate the main technical points required for the derivation of the *MF* model. We begin by considering the dynamics of m_x, which is given by

$$m_{x,n+1} = m_{x,n} - m_{y,n} + \langle G(x_{i,n}) \rangle - \beta \langle H(x_{j,n} - d) \rangle \tag{2.13}$$

It is easy to see that there is no contribution from the coupling term. As far as the third term on the r.h.s. of Eq. (2.13) is concerned, using Eq. (2.12), one arrives at

$$\langle G(x_i) \rangle = \langle -x_i^3 + (1+a)x_i^2 - ax_i \rangle = G(m_x) + S_x(1 + a - 3m_x). \tag{2.14}$$

In the last expression, we have dropped the time index for simplicity and have introduced the shorthand notation $G(m_x) \equiv -m_x^3 + (1+a)(m_x^2 + S_x)$.

The key problem is how to treat the final term in the r.h.s. of Eq. (2.13). Our approach consists in replacing the assembly average by the expectation value ($\langle H(x_i - d) \rangle \approx E[H(x_i - d)]$), obtained by assuming that the local variables at an arbitrary moment of time are normally distributed according to $P(x_i) \sim \mathcal{N}(m_x, S_x)$. The expectation may then be evaluated as

$$E[-\beta\langle H(x_i - d)\rangle] = \int dx_1 \int dx_2 ... \int dx_N (-\frac{\beta}{N}\sum_i H(x_i - d))p(x_1, x_2, ..., x_N) =$$

$$-\beta\int_{-\infty}^{\infty} dx_1 H(x_1 - d)p(x_1) = -\beta\int_{d}^{\infty} \frac{1}{\sqrt{2\pi S_x}}e^{-\frac{(x_1 - m_x)^2}{2S_x}} = -\frac{\beta}{2}(1 - Erf\left[\frac{d - m_x}{\sqrt{2S_x}}\right]),$$

with the error function $Erf(x) = \frac{2}{\sqrt{\pi}}\int_0^x e^{-t^2}dt$. In the above calculation, we have explicitly used the assumption on the independence of distributions of local variables at any given moment of time.

In a similar fashion, one may consider the S_x dynamics, which constitutes the most demanding part of the derivation. In particular, proceeding from the S_x definition, we obtain

$$S_{x,n+1} = \langle x_{i,n+1}^2 \rangle - \langle x_{i,n+1} \rangle^2 = \tag{2.15}$$
$$= \langle [(1 - c)x_{i,n} + G(x_{i,n}) - \beta H(x_{i,n} - d) - y_{i,n} + \xi_{i,n} + cm_{x,n}]^2 \rangle$$
$$- (m_{x,n} - m_{y,n} + G(m_{x,n}) + S_{x,n}(1 + a - 3m_{x,n}) - \beta\langle H(x_{i,n} - d)\rangle)^2.$$

As an illustration, let us evaluate one of the terms containing an average over the threshold function:

$$-2\beta E\left[\langle G(x_i)H(x_i - d)\rangle - \langle G(x_i)\rangle\langle H(x_i - d)\rangle\right] =$$
$$-2\beta\left[\int dx_1 G(x_1)H(x_1 - d)p(x_1) - \int dx_1 H(x_1 - d)p(x_1)\left[G(m_x) + S_x(1 + a - 3m_x)\right]\right]$$
$$\approx -2\beta\left[\int dx_1 (G(m_x) + G'(m_x)(x_1 - m_x) + \frac{1}{2}G''(m_x) \times (x_1 - m_x)^2)H(x_1 - d)p(x_1) -\right.$$
$$\int dx_1 H(x_1 - d)p(x_1) \times \left[G(m_x) + S_x(1 + a - 3m_x)\right]] = ... =$$
$$-2\beta\left[(1 + a)(m_x + d) - a - 3m_xd\right]\sqrt{\frac{S_x}{2\pi}}\exp\left[-\frac{(d - m_x)^2}{2S_x}\right].$$

Again, the time indices have been suppressed to simplify the notation.

Following some algebra, Eq. (2.15) can be transformed to

$$S_{x,n+1} = (1-c)^2 S_{x,n} + S_{y,n} + \sigma^2 - 2(1-c)U_n + \underbrace{(\langle G(x_{i,n})^2\rangle - \langle G(x_{i,n})\rangle^2)}_{Var(G(x_{i,n}))}$$

$$+ 2(1-c)(\langle x_{i,n}G(x_{i,n})\rangle - m_{x,n}\langle G(x_{i,n})\rangle) - 2(\langle y_{i,n}G(x_{i,n})\rangle - m_{y,n}\langle G(x_{i,n})\rangle)$$

$$- 2\beta(1-c)\left[\langle x_{i,n}H(x_{i,n}-d)\rangle - m_{x,n}\langle H(x_{i,n}-d)\rangle\right]$$

$$- 2\beta(\langle G(x_{i,n})H(x_{i,n}-d)\rangle - \langle G(x_{i,n})\rangle\langle H(x_{i,n}-d)\rangle)$$

$$+ \beta^2 \underbrace{(\langle H(x_{i,n}-d)^2\rangle - \langle H(x_{i,n}-d)\rangle^2)}_{Var(H(x_{i,n}-d)))}.$$

The partial results required for completing the calculation are given by

$$\langle x_i G(x_i)\rangle - m_x\langle G(x_i)\rangle = G'(m_x)S_x - 3S_x^2$$

$$\langle y_i G(x_i)\rangle - m_y\langle G(x_i)\rangle = -3S_x U_{xy} - 3m_x^2 U_{xy} + 2(1+a)m_x U_{xy},$$

where $G'(m_x) \equiv -3m_x^2 + 2(1+a)m_x - a$. Note that the time indexes have been omitted for simplicity. After some straightforward calculations, it may also be shown that the expression for variance $Var(G(x_i))$ reads

$$Var(G(x_i)) = G'^2(m_x)S_x + S_x^2\left[36m_x^2 - 24(1+a)m_x + 2(1+a)^2 + 6a\right] + 15S_x^3.$$

Let us now explicitly calculate the terms containing the threshold function. First we have

$$- 2\beta(1-c)\left[\langle x_i H(x_i-d)\rangle - \langle x_i\rangle\langle H(x_i-d)\rangle\right] =$$

$$- 2\beta(1-c)\left[\int dx_1 dx_2...dx_N \frac{1}{N}\sum_i x_i H(x_i-d)p(x_1,...,x_N)\right.$$

$$\left. -m_x\int dx_1 dx_2...dx_N \frac{1}{N}\sum_i H(x_i-d)p(x_1,...,x_N)\right] =$$

$$... = -2\beta(1-c)\left[\int dx_1(x_1-m_x)H(x_1-d)p(x_1)\right] = -2\beta(1-c)\sqrt{\frac{S_x}{2\pi}}\exp\left[-\frac{(d-m_x)^2}{2S_x}\right].$$

Finally, let us address the term $\beta^2 Var(H(x_i-d))$, which can be estimated by considering the associated expectation $\beta^2 Var(H(x_i-d)) \approx \beta^2\left[\langle H(x_i-d)^2\rangle - \langle H(x_i-d)\rangle^2\right]$. By applying the introduced technique, we obtain

$$E[\beta^2 H(x_i-d)^2] = \beta^2\int dx_1\int dx_2...\int dx_N(\frac{1}{N^2}\sum_i\sum_j H(x_i-d)H(x_j-d))p(x_1,x_2,...,x_N)$$

$$= \underbrace{\frac{\beta^2}{N^2}N\int dx_1 H(x_1-d)p(x_1)}_{N \text{ cases where } i=j} + \underbrace{\frac{\beta^2}{N^2}N(N-1)\int dx_1\int dx_2 H(x_1-d)H(x_2-d)p(x_1)p(x_2)}_{N(N-1) \text{ cases where } i\neq j}$$

$$= \frac{\beta^2}{2N}[1-Erf[\frac{d-m_x}{\sqrt{2S_x}}]] + \frac{\beta^2}{4N^2}N(N-1)[1-Erf[\frac{d-m_x}{\sqrt{2S_x}}]]^2.$$

Given that $\beta^2 \langle H(x_i - d) \rangle^2 = \frac{\beta^2}{4} \left[1 - Erf[\frac{d-m_x}{\sqrt{2S_x}}] \right]^2$, one arrives at

$$\beta^2 Var(H(x_i - d)) = \frac{\beta^2}{4N}(1 - Erf[\frac{d - m_x}{\sqrt{2S_x}}])([1 + Erf[\frac{d - m_x}{\sqrt{2S_x}}]).$$

This shows that the variance of the threshold function ultimately contributes to a finite-size effect which can be neglected in the thermodynamic limit.

Ultimately, by combining all these elements, one arrives at the final equations of the *MF* model in the thermodynamic limit:

$$
\begin{aligned}
m_{x,n+1} =& m_{x,n} - m_{y,n} + G(m_{x,n}) + S_{x,n}(1 + a - 3m_{x,n}) - \frac{\beta}{2}\left(1 - Erf\left[\frac{d - m_{x,n}}{\sqrt{2S_{x,n}}}\right]\right) \quad (2.16)
\end{aligned}
$$

$$
\begin{aligned}
m_{y,n+1} =& m_{y,n} + \varepsilon(m_{x,n} - J) \\
S_{x,n+1} =& (1 - c)^2 S_{x,n} + S_{y,n} + \sigma^2 - 2(1 - c)U_n + S_{x,n}(-3m_{x,n}^2 + 2(1 + a)m_{x,n} - a)^2 \\
& - 2(1 - c)(3m_{x,n}^2 S_{x,n} + 3S_{x,n}^2 - 2(1 + a)m_{x,n}S_{x,n} + aS_{x,n}) \\
& + 2(3S_{x,n}U_n + 3m_{x,n}^2 U_n - 2(1 + a)m_{x,n}U_n) \\
& - 2\beta\left[(1 + a)(m_{x,n} + d) - a - 3dm_{x,n}\right]\sqrt{\frac{S_{x,n}}{2\pi}}\exp\left[-\frac{(d - m_{x,n})^2}{2S_{x,n}}\right] \\
& - 2\beta(1 - c)\sqrt{\frac{S_{x,n}}{2\pi}}\exp\left[-\frac{(d - m_{x,n})^2}{2S_{x,n}}\right] \\
& + S_{x,n}^2\left[36m_{x,n}^2 - 24(1 + a)\ m_{x,n} + 2(1 + a)^2 + 6a\right] + 15S_{x,n}^3 \\
S_{y,n+1} =& S_{y,n} + \varepsilon^2 S_{x,n} + 2\varepsilon U_n \\
U_{n+1} =& U_n - (a + c + \varepsilon)U_n + \varepsilon(1 - c - a)S_{x,n} - S_{y,n} \\
& - (U_n + \varepsilon S_{x,n})(3S_{x,n} + 3m_{x,n}^2 - 2(1 + a)m_{x,n}) - \beta\varepsilon\sqrt{\frac{S_{x,n}}{2\pi}}\exp\left[-\frac{(d - m_{x,n})^2}{2S_{x,n}}\right].
\end{aligned}
$$

2.2.3 Stability and bifurcation analysis for the macroscopic excitability state

This section focuses on the stability of the macroscopic excitability state and the bifurcations outlining the boundaries of its stability domain. To get a basic understanding of all the macroscopic regimes, we first examine the succession of macroscopic regimes in the $J - \beta$ parameter plane for σ fixed at an intermediate value $\sigma = 0.002$, see Fig. 2.7. As in the case of a single unit, J is relevant for the system's excitability, while β influences the waveforms of the active states (spiking, bursting, or mixed spike-bursting activity). The assembly is found to exhibit collective modes that qualitatively correspond to the dynamics of a single unit illustrated in plates $III - VI$ of Fig. 2.5. The heat maps in the left column of Fig. 2.7 provide a comparison between the oscillation amplitudes A of the global variable X (top row) and the *MF* variable m_x (bottom row) for the given (J, β). The right column indicates how well the average interspike interval (or the average bursting cycle) T of the exact system matches with the corresponding characteristics of the dynamics of the *MF* model (2.16).
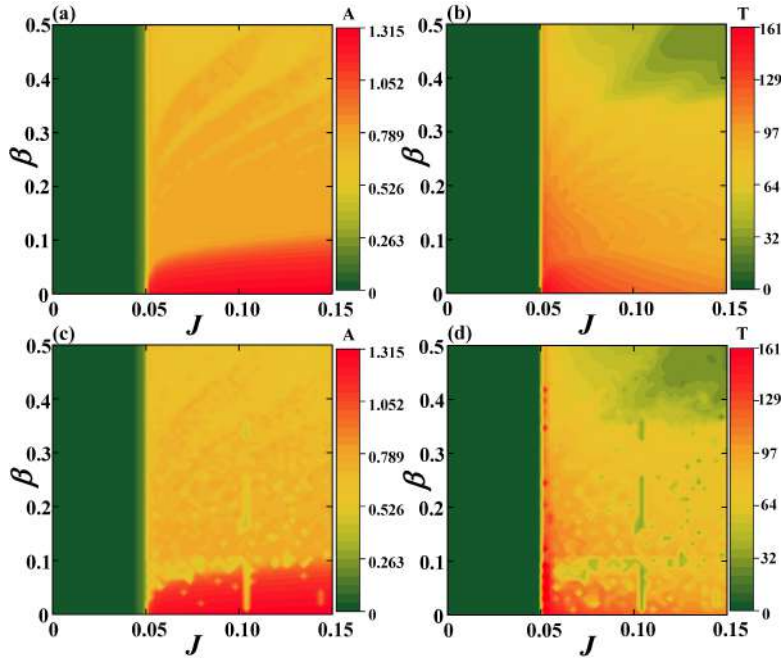
Figure 2.7: The heat maps in (a) and (b) show the dependencies of the oscillation amplitudes $A(J, \beta)$ and average interspike intervals $T(J, \beta)$ obtained by stochastic averaging for a network of $N = 100$ neurons, respectively. (c) and (d) illustrate the analogous results for the *MF* model. The noise intensity in all instances is $\sigma = 0.001$.

In our numerical experiments, the exact system is an assembly consisting of $N = 100$ units. We have obtained A by averaging over sufficiently long time series, whereas T is determined by averaging over an ensemble of 20 different stochastic realizations. To calculate T, we have selected the threshold value $X = \theta = 0.2$ ($m_X = \theta = 0.2$) for the exact system (MF model), since it is convenient for clearly detecting individual spikes, as well as unambiguously discerning the initiation stage of bursts, required for calculating the length of the bursting cycle.

In order to examine the phenomenon of macroscopic excitability, we focus on the domain of J values where the exact system exhibits a stochastically stable equilibrium, while the *MF* model has a stable stationary state. Stochastic stability physically implies that fluctuations around the deterministic fixed point are typically of the order of noise, though some rare spikes may still be evoked. For J sufficiently close to the region which admits subthreshold oscillations, the population manifests macroscopic excitability. The term "macroscopic" here refers to a form of emergent assembly behavior, rather than a characteristic spatial scale. To properly illustrate this feature, we have analyzed the assembly dynamics in the limit $\sigma = 0$, cf. Fig. 2.8. In particular, figures 2.8(a) and 2.8(b) show the maximum X and m_x values reached in the corresponding time series obtained for sets of different initial conditions (X_0, Y_0) and $(m_{x,0}, m_{y,0})$, respectively. A comparison of the two plots corroborates that the boundary defining the domain of the spiking response is appropriately anticipated by the *MF* model. An important remark is that for a particular value of J, the assembly may exhibit different forms of macroscopic excitability, generating a single spike or a burst of
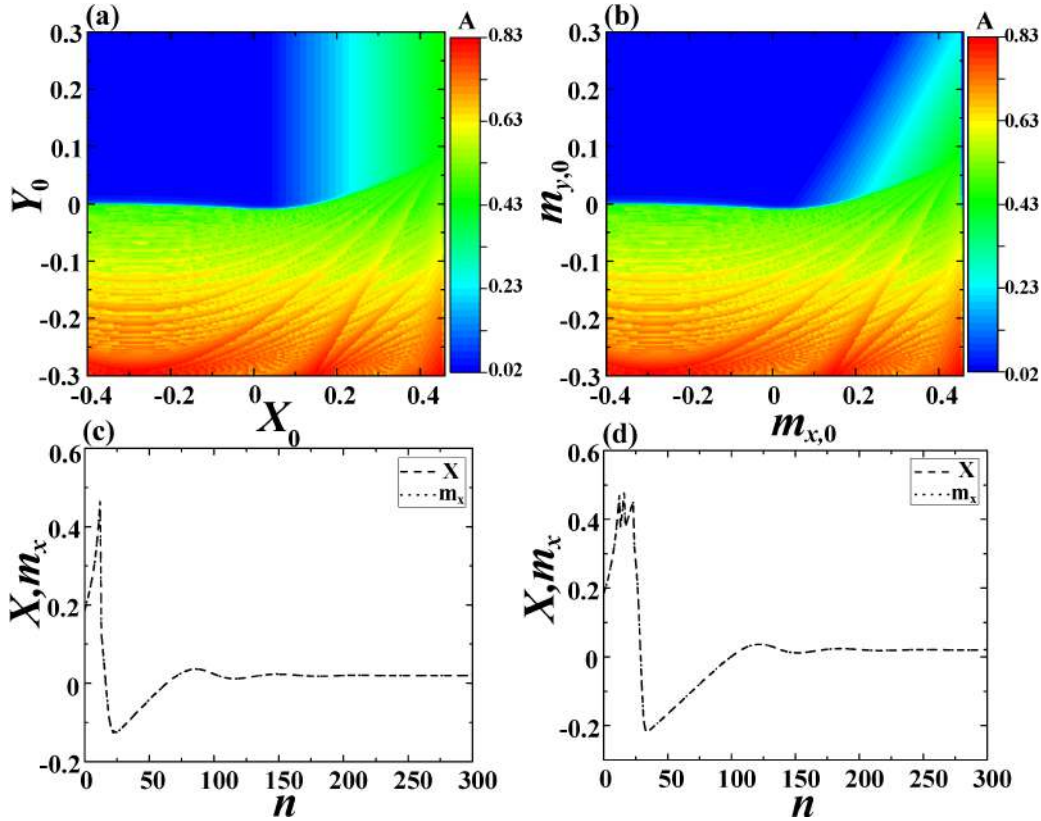
Figure 2.8: The macroscopic excitability feature. The heatmaps in (a) and (b) show the maximum values of X and m_x reached by the exact and the *MF* system, starting from analogous initial conditions (X_0, Y_0) and $(m_{x,0}, m_{y,0})$, respectively. The parameters are $J = 0.02, \beta = 0.4$. (c) illustrates the case where a strong enough perturbation elicits a single-spike response $(J = 0.02, \beta = 0.4)$, whereas (d) corresponds to a bursting response made up of three spikes $(J = 0.02, \beta = 0.15)$. In both instances, the time series of the *MF* model (dotted line) is indistinguishable from that of the exact system (dashed line).
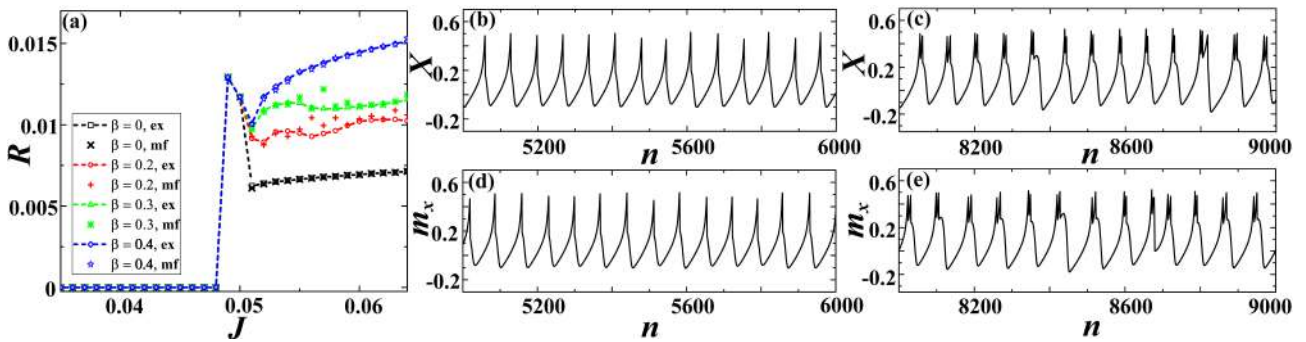
Figure 2.9: (a) shows a family of $R(J)$ curves for different β for a network of size $N = 100$ under fixed $\sigma = 0.001$ with the results for the *MF* model superimposed on the plot, whereby the symbols $\times, +, *, \star$ correspond to $\beta = 0, 0.2, 0.3$ and 0.4, respectively. (b) and (c) illustrate the time series of X associated with the spiking and the bursting collective modes. The considered network is made up of $N = 100$ neurons, with the parameters set to $J = 0.06, \beta = 0.4, \sigma = 0.001$ in (b), and $J = 0.08, \beta = 0.2, \sigma = 0.001$ in (c). (d) and (e) show the m_x series obtained for the parameters from (b) and (c).

spikes, depending on the value of β. This is demonstrated by the time series in figures 2.8(c) and 2.8(d). The former refers to a one-spike response in the case of $\beta = 0.4$. For smaller β, one observes responses comprising two or more closely packed spikes, with Fig. 2.8(d) illustrating a three-spike burst encountered for $\beta = 0.25$. Note that the time series of the full system and the *MF* model exactly coincide in the limit $\sigma = 0$.

The next relevant issue concerns noise-influenced transitions from quiescent to active regimes observed under increasing J. These transitions define the stability boundaries of the macroscopic excitability state, corresponding to gradual stochastic bifurcations in the exact system and proper bifurcations in the MF system. In particular, Fig. 2.9(a) shows how the firing (spiking or bursting) frequency R changes for an assembly consisting of $N = 100$. The average frequency is determined by considering an ensemble of 20 different stochastic realizations, having σ fixed to the moderate value $\sigma = 0.001$. The results from simulations of the full system (2.11) are compared against the data obtained for the *MF* model. In this context, two points should be stressed: (*i*) for moderate σ, the firing frequencies of the *MF* model lie in close agreement to those of the exact system; and (*ii*) one finds that the quantitative agreement also holds for different types of transitions from silent to active regimes. As already indicated, the waveforms of the active states depend on β and the associated transitions are mediated by distinct synchronization processes. For instance, synchronization at $\beta = 0$ involves time series of single units that conform to spiking activity of type *III* from Figure 2.5, which is quite resilient to the impact of noise. On the other hand, for $\beta = 0.3$ or $\beta = 0.4$, individual units exhibit chaotic bursting or spiking activity, respectively, such that the underlying synchronization process is more susceptible to stochastic effects. Typical time series of X for different collective modes are compared to the corresponding m_x series in figures 2.9(b)-(e). The top (bottom) row concerns the data for the exact system (*MF* model).

For a deeper understanding of the influence of noise for J in the vicinity of the transition from silence to active regimes, we examine how the profiles of $R(J)$ curves change under increasing σ. The results for a population comprised of $N = 100$ neurons with $\beta = 0.2$ are shown in Fig. 2.10. As expected, the transition is quite sharp for moderate noise ($\sigma = 0.001$), but is considerably flattened for larger σ (e. g. $\sigma = 0.05$). The crosses indicate the firing frequencies predicted by the *MF* model for $\sigma = 0.001$. For larger σ, the *MF* model fails to reproduce the behavior of the exact system in the vicinity of the threshold, in the sense that it overestimates the maximal value of R, as well as the actual critical J corresponding to the transition. Viewed from another angle, one may infer that for sufficiently large σ and J below the threshold given by the *MF* model, the *MF* model fails to capture the impact of synchronization processes taking place between the noise-induced oscillations of individual units. This especially refers to the J interval within which spikes or bursts (depending on β) are superimposed on the background of subthreshold oscillations. An example of such a discrepancy between the behavior of the exact and the effective system is provided in Fig. 2.11, cf. Fig. 2.11(a) and Fig. 2.11(c). Also, for strong σ and J values above the transition, the
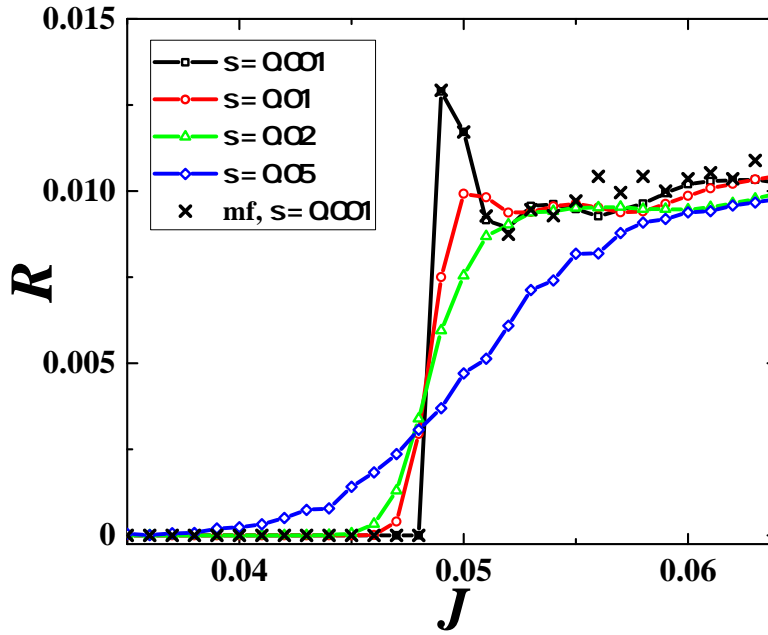
Figure 2.10: Family of $R(J)$ curves over σ for a network of $N = 100$ neurons under fixed $\beta = 0.2$. The different symbols correspond to cases $\sigma = 0.001$ (squares), $\sigma = 0.01$ (circles), $\sigma = 0.02$ (triangles) and $\sigma = 0.05$ (diamonds). The crosses connected by the dashed line highlight the $R(J)$ curve for the MF model at $\sigma = 0.001$.

firing frequencies anticipated by the effective model are typically higher than those of the exact system (not shown). Within this region, the stochastic effects suppress synchronization between the chaotic oscillations of single neurons, thereby reducing the corresponding R value. This is not accounted for with sufficient accuracy by the MF system. Note that such suppression of synchronization is reflected in the corresponding X series by the spike (burst) "skipping" mechanism, where the large-amplitude oscillations are occasionally replaced with subthreshold oscillations. For the associated J and σ values, such a phenomenon is absent in the dynamics of the effective model, cf. Fig. 2.11(b) and Fig. 2.11(d). In both scenarios illustrated in Fig. 2.11, the MF model fails because the Gaussian approximation breaks down due to large stochastic fluctuations.

In order to elucidate how the validity of the effective model's predictions deteriorates with increasing σ, we consider the $A(J,\sigma)$ and $T(J,\sigma)$ dependencies for the exact and the approximate system at fixed $\beta = 0.4$ and $N = 100$, see Fig. 2.12. A comparison between the respective A (left column) and T plots (right column) suggests that the range of σ values where the MF approximation applies is contingent on J. For instance, in the J region below the deterministic threshold, one may estimate this range by noting that the effective bifurcation diagram in Fig. 2.12(a) indicates that noise-induced macroscopic oscillations emerge for $\sigma \approx 0.003$. Since this point is not adequately represented by the effective model, cf. Fig. 2.12(c), one may state that the Gaussian approximation breaks down around $\sigma \approx 0.003$ within the given J region. Nevertheless, for J above the deterministic threshold, the validity of the MF model appears to depend rather strongly on the particular value of J, such that the Gaussian approximation effectively fails for $\sigma \in (0.002, 0.006)$.
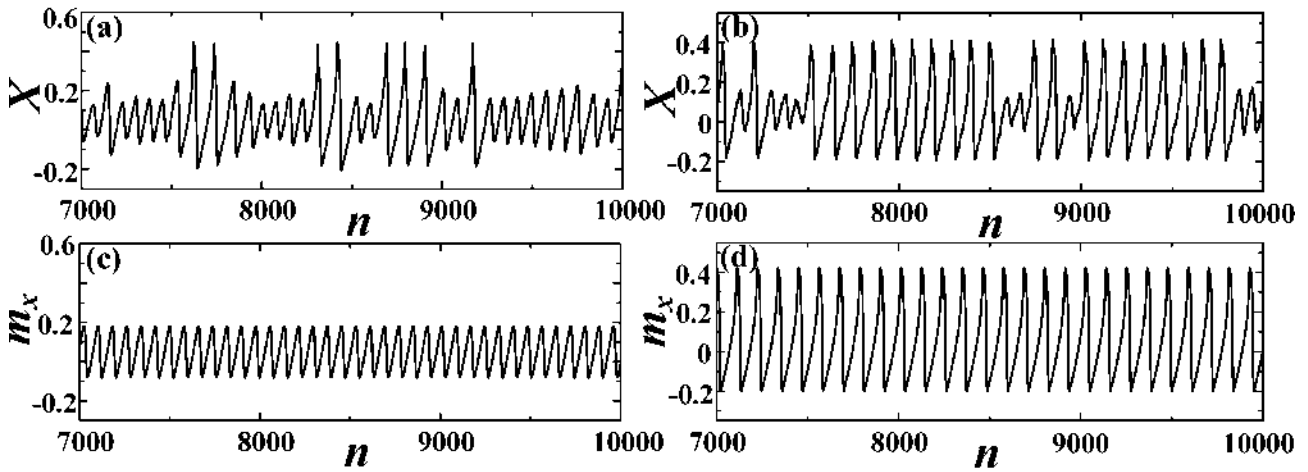
Figure 2.11: Noise-induced phenomena within the J interval in the vicinity of the deterministic threshold. X series in (a) show noise-induced spike-bursting activity on top of subthreshold oscillations ($J = 0.047, \beta = 0.2, \sigma = 0.02$). (b) illustrates the "skipping" phenomenon where the stochastic effects occasionally suppress the large-amplitude oscillations of the X variable ($J = 0.058, \beta = 0.2, \sigma = 0.01$). (c) and (d) show the m_x series corresponding to the parameter sets from (a) and (b), respectively.
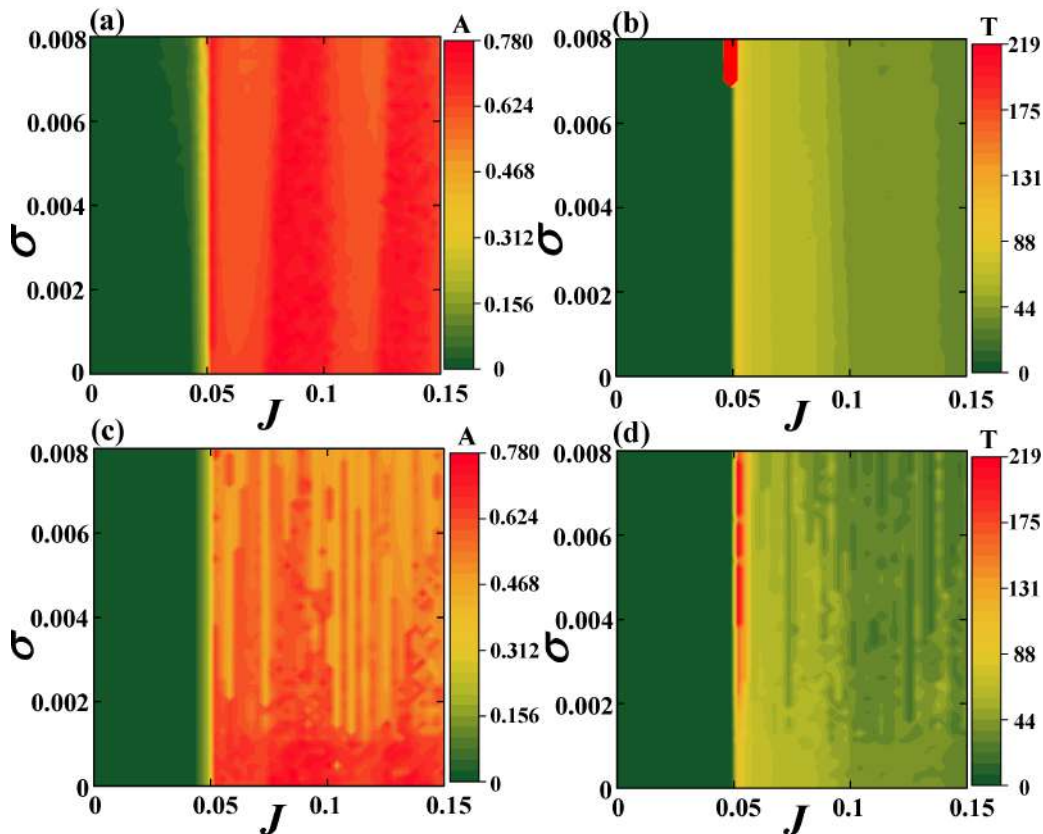
Figure 2.12: Subplots (a) and (b) respectively refer to the $A(J, \sigma)$ and $T(J, \sigma)$ dependencies for the network of $N = 100$ neurons at fixed $\beta = 0.4$. The results in (a) are obtained by averaging over sufficiently long time series, whereas data in (b) derive from averaging over an ensemble of 20 different stochastic realizations. The $A(J, \sigma)$ and $T(J, \sigma)$ dependencies determined by numerical simulations of the MF model are provided in (c) and (d).
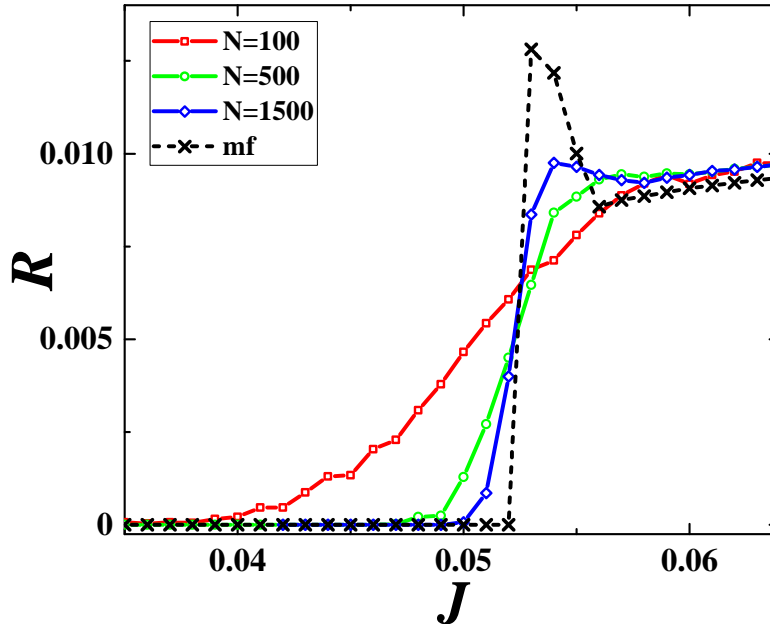
Figure 2.13: $R(J)$ dependencies for increasing N under fixed $(\beta, \sigma) = (0.2, 0.05)$. The squares, circles and diamonds correspond to cases $N = 100$, $N = 500$ and $N = 1500$, respectively. The results for the *MF* model, corresponding to the thermodynamic limit, are indicated by crosses connected with the dashed line.

So far, we have investigated the impact of noise by comparing the results for the network of size $N = 100$ to those obtained for the effective system. Nevertheless, it has already been emphasized in section 2.2.2 that the *MF* model, deterministic in character, refers to the system's behavior in the thermodynamic limit $N \to \infty$, whereas explicitly stochastic terms could only appear as finite-size effects. With this in mind, we have examined how the behavior of the exact system within the J domain around deterministic threshold changes for large and fixed σ under increasing N. Fig. 2.13 contains the $R(J)$ curves calculated for $N = 100$ (squares), $N = 500$ (circles) and $N = 1500$ (diamonds) at fixed $\beta = 0.2, \sigma = 0.05$. The curve for $N = 100$ indicates that the chosen σ value is quite large in the sense that it is sufficient to induce collective oscillations within the excitable regime. Alongside the dependencies for the full system, we also show the $R(J)$ curve associated with the *MF* model (dashed line with crosses). An interesting point regarding the latter is that the J threshold for the emergence of the collective mode is shifted toward a larger value compared to the case $\sigma \approx 0.01$. While the transition itself appears quite sharp, the curves corresponding to the exact system approach it with increasing N, both in terms of the J threshold and the R values above the transition, corroborating that the (J, σ) domain in which the Gaussian approximation fails expectedly reduces with system size.

2.2.4 Response to external stimuli

Within this section, we demonstrate that the *MF* model can be used to predict the stimulus-response relationship of an assembly exhibiting different macroscopic regimes, including the macroscopic excitability state as well as the spiking and bursting collective modes. Let
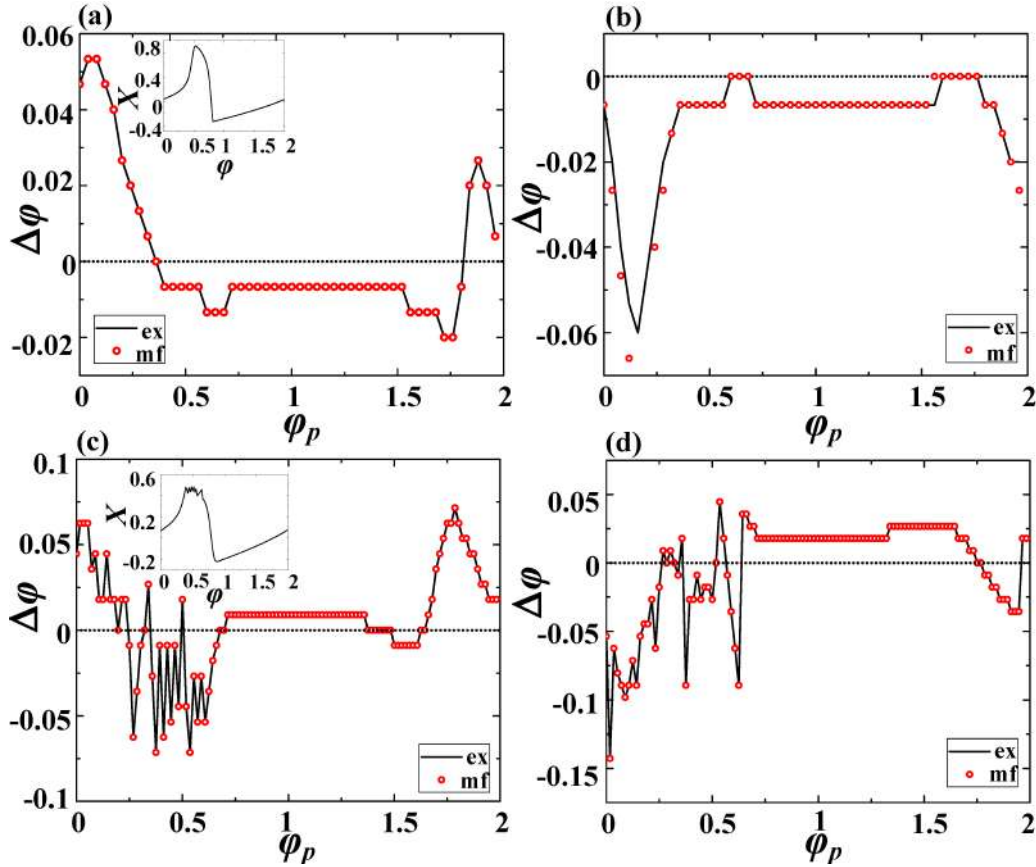
Figure 2.14: Assembly phase resetting. (a) and (b) show the *PRCs* for a population in spiking regime ($J = 0.055, \beta = 0$) under excitatory ($a = 0.008$) and inhibitory stimulation ($a = -0.008$), respectively. Results for the exact system ($N = 500$) are indicated by the solid line, whereas the data for the *MF* model are denoted by circles. The bottom row illustrates the *PRCs* for an assembly exhibiting macroscopic bursting ($J = 0.06, \beta = 0.1$), whereby (c) describes the effect of an excitatory ($a = 0.01$), and (d) of an inhibitory pulse perturbation ($a = -0.01$). The insets in (a) and (c) demonstrate how the phases are assigned to the points within the spiking and bursting cycles, respectively. The phase is expressed in units of π.

us first focus on the two latter instances and examine the sensitivity of a population to an external pulse perturbation within the framework of phase resetting theory [242, 243, 74, 244]. To compare the behavior of the exact system and the effective model, we determine the corresponding phase resetting curves (*PRCs*), which describe the phase shift $\Delta\varphi$, induced by the perturbation, in terms of the phase φ_p when the perturbation is applied. The considered stimulus has a form of a short pulse current $I_p = a_p H(n - n_i) H(n - n_f)$, whose magnitude a_p and width $\Delta = n_i - n_f$ are small compared to the amplitude and duration of the spiking (or bursting) cycle T_0, respectively. In the case of the exact system, the same pulse current is delivered to each neuron i, adding the term I_p to x_i dynamics, whereas, in the effective model, the stimulation is administered via the m_x variable. The phase φ_p is defined in reference to T_0 by $\varphi_p = n_p/T_0$. The associated phase difference following the reset is calculated as $\Delta\varphi = 1 - T_1/T_0$, where T_1 denotes the duration of the perturbed spiking or bursting cycle.

The *PRCs* characterizing the assembly response in the spiking regime are provided in
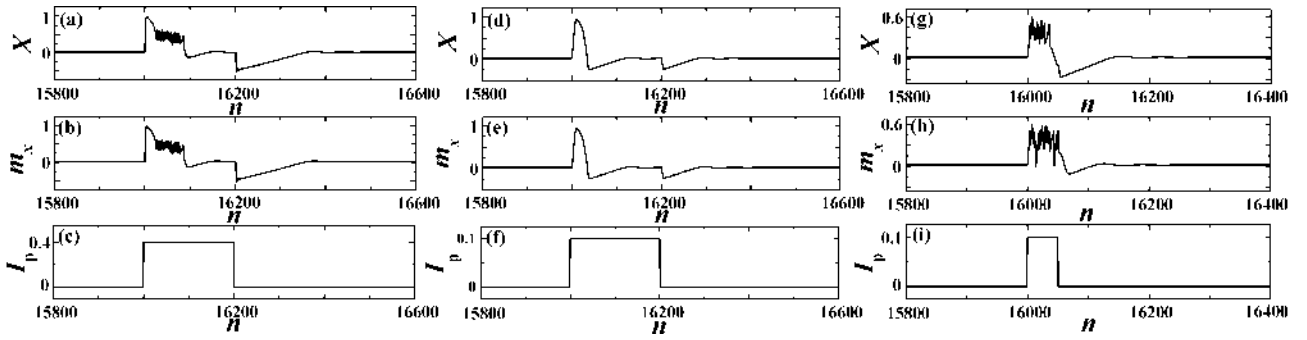
Figure 2.15: Stimulus-response relationship in the excitable regime ($J = 0.02$). The top (middle) row refers to the response of the full system (*MF* model), whereas the bottom row shows the profile of the external stimulation. In the panels (a)-(c), the system parameters are $\beta = 0.4, \sigma = 0$, while the perturbation is characterized by $a_p = 0.4, \Delta = 200$. Panels (d)-(f) concern the response of an assembly ($\beta = 0.1, \sigma = 0.001$) subjected to a rectangular pulse $a_p = 0.4, \Delta = 200$. Panels (g)-(i) illustrate the response of a population ($\beta = 0.4, \sigma = 0.001$) influenced by the external stimulation $a_p = 0.1, \Delta = 50$. The considered network is of size $N = 500$.

Fig. 2.14(a) and Fig. 2.14(b), whereby the former is obtained under the action of an excitatory ($a_p > 0$), and the latter under the influence of an inhibitory stimulation ($a_p < 0$). We stress that in both instances, the results derived from the effective model, denoted by circles, show excellent agreement with the data for the exact system (solid lines). In qualitative terms, one observes that excitatory stimulation may advance the phase of the spiking cycle if it arrives sufficiently close to the spike, but still before the sharp rising stage. However, an excitatory perturbation acting during the spike or within the effective refractory period has a suppression effect where the next spike is delayed. In contrast to excitatory stimulation, the inhibitory pulse postpones the next firing time if it is introduced within the interval close to the rising stage of the spike.

The *PRCs* determined for an assembly exhibiting collective bursting show qualitatively analogous effects to those described so far, see Fig. 2.14(c) and Fig. 2.14(d). This especially refers to the impact of perturbation delivered sufficiently close to a moment of burst initiation. An apparent difference compared to Fig. 2.14(a) and Fig. 2.14(b) emerges during the bursting stage itself, where the associated *PRCs* expectedly exhibit strong fluctuations. Apart from that, one finds an interesting effect: both the excitatory and the inhibitory stimulation have a facilitatory role, i. e. cause phase advancement during the relaxation stage of the bursting cycle.

For a population in the macroscopic excitability state, we consider scenarios in which the system is perturbed by a rectangular pulse of finite magnitude and duration, where finite means that it is comparable to corresponding features of typical spiking or bursting cycles. Note that the selected J value $J = 0.02$ lies sufficiently far from the interval admitting subthreshold oscillations. To determine whether the *MF* model correctly anticipates the response of the exact system, now in the presence of small to moderate noise, we have

provided several illustrative examples of the stimulus-response relationship under finite perturbation in Fig. 2.15. The top and middle row refer to the X and corresponding m_x time series, respectively, while the bottom row shows the profile of the applied stimulus. We find that in the absence of noise or for sufficiently small σ, the effective model reproduces the induced dynamics of the full system quite accurately. This also refers to some highly complex forms of responses, as corroborated in Fig. 2.15(a)-(c), which concern relatively large a_p and Δ. Under increasing σ, the ability of the MF model to predict the dynamics of the exact system gradually reduces in a way which depends nontrivially on β. In particular, for smaller $\beta \approx 0.1$, which would facilitate the macroscopic spiking mode for supercritical J, it turns out that the dynamics of the MF model lies in close agreement to that of the exact system even for moderate noise $\sigma = 0.001$, cf. Fig. 2.15(d)-(f). However, for larger β, such an analogy between the responses of the exact and the MF system is lost, see Fig. 2.15(g)-(i). Naturally, the validity of the predictions given by the MF model deteriorates if the stimulation amplitude a_p and the duration Δ are large, especially in the presence of non-negligible noise.

—————————— 2.3 *Chapter summary and discussion* ——————————

In the present chapter, we have extended the notion of excitability to coupled multiscale systems by studying two paradigmatic examples, namely a motif of adaptively coupled active rotators and a network of globally coupled map neurons.

In section 2.1, we have

- **identified the excitable equilibria** of a binary motif,

- determined the features of the associated **threshold-like behavior**, and

- examined its **stimulus-response relationship**.

Concerning the last point, we have determined four different types of excitable responses to external perturbation. Our findings indicate that the system exhibits *well-defined threshold behavior*, characteristic for Type I excitability, whereby the threshold set partially corresponds to the stable manifold of the saddle point on the synchronization manifold.

Moreover, in section 2.2, we have extended the notion of excitability, showing that an assembly of coupled excitable elements can act as a macroscopic excitable element. We have derived an effective mean field (MF) model to address

- the **stability domains and (noise-induced) bifurcations** associated with the macroscopic excitability regime, and

- the **stimulus-response relationship** of the population.

Our reduced low-dimensional model has been derived within the framework of Gaussian approximation, formally introduced in the form of a closure hypothesis. In physical terms, this approximation suggests that the local variables are independent and conform to a normal distribution centered about the assembly mean and characterized by the associated assembly variance. Although the validity of this approximation cannot be established *a priori*, it has been systematically verified by numerically corroborating that the *MF* model reproduces the behavior of the exact system with sufficient accuracy.

Nevertheless, the accuracy of the model has certain limitations, namely

- for too **large noise**, the collective variables of the exact system manifest large fluctuations, explicitly violating the Gaussian approximation, and

- in the vicinity of stochastic bifurcations, where the neglected **finite-size effects** are most prominent, the Gaussian approximation breaks down.

Finally, we have also verified that the *MF* model is capable of capturing the stimulus-response features of the exact system. In the macroscopic excitable regime, for scenarios where the assembly is stimulated by rectangular pulse perturbations of finite amplitude and duration, we have observed substantial analogies between the *PRC*s of the exact and reduced system. For short pulse-like perturbations, it has been found that the approximate system reproduces the *PRC*s of the exact system for both the spiking and bursting regimes of collective activity with high accuracy.

The *MF* model has enabled us to examine the stability and bifurcations of the emergent macroscopic regimes, most notably macroscopic excitability, in a *homogeneous* network of *globally* coupled stochastic maps, as well as to analyze the related stimulus-response relationship. Nevertheless, the remaining open questions are how the macroscopic excitability state is affected by the diversity (parameter heterogeneity) of units, as well as complex network topologies [227, 229].

Chapter 3

Switching Dynamics Induced by the Interplay of Adaptivity and Noise

The present chapter comprises a study of noise-induced switching dynamics in excitable systems with a multiple timescale structure, whereby we will consider the conditions that give rise to the phenomenon, as well as the mechanisms underlying it. Within this study, we will combine classical multiple timescale analysis for deterministic systems with standard concepts from stochastic systems, such as metastable states, escape processes, and noise-induced switching.

A feature common to many nonlinear dynamical systems is the coexistence of several stable states (attractors) for a given set of parameters, referred to as *multistability* [40]. Multistability may emerge due to a variety of mechanisms, including coupling or delayed feedback [41]. In such systems, each attractor has a corresponding basin of attraction, i. e. the set of external initial conditions from which the system's dynamics converges to that particular attractor. Due to a sufficiently strong perturbation and/or rapid change of a parameter, a multistable system may *switch* from one stable state to another [41]. Switching may also be induced by *noise*, in which case it connects metastable states derived from the attractors of the deterministic system. The process of noise-induced switching is characterized by an additional timescale introduced by noise.

The dynamics of many complex systems involves a multiple timescale structure, which may be inherent to local dynamics of the units and/or may be associated with the coupling dynamics. An example of the former is provided by classical neuronal models where the evolution of the recovery or gating variables is typically much slower than the changes in the membrane potential [74, 245], while the latter involves mechanisms such as feedback or adaptivity. Adaptivity refers to the feature of complex systems where the interactions between the constituents are affected by the constituents' states [43, 44, 45, 46]. Such self-organized dynamics involves complex feedback mechanisms where the structure of the couplings adapts to the dynamics of the constituent units, which in turn influences their evolution. The modeling of such systems is based on the paradigm of adaptive networks, where self-organization unfolds both at the level of the interactions and the con-

stituents' collective dynamics. Typically, the dynamics of adaptive networks features multiple characteristic timescales, differing in orders of magnitude, whereby the faster/slower timescale is associated with the dynamics of the units/couplings. Such a separation of timescales implies that the short-term evolution of the units occurs on a quasi-static network, whereas the slow changes in couplings depend on the time-averaged dynamics of the units. For instance, at the level of neural networks, certain mechanisms of synaptic adaptation, such as spike-timing-dependent plasticity (STDP) [84, 85, 86, 246, 247, 248], are slower than the spiking dynamics of individual neurons. Investigating the dynamics of such multiple timescale systems has lead to the development of a number of useful asymptotic and geometric methods [47, 48, 49, 50, 51]. Subjecting an excitable system to additional feedback or coupling it to other such systems may give rise to the emergence of different forms of oscillations, patterns, propagating waves, and other self-organizing phenomena [67, 94, 130, 149, 181, 249, 250, 251, 252, 253].

Another essential feature of complex systems is stochasticity or randomness. In modeling, noise may describe the intrinsic randomness of the system, account for the fluctuations in the embedding environment, or derive from coarse-graining over the degrees of freedom associated with small spatial or temporal scales [2, 67]. Neural dynamics, for instance, is influenced by intrinsic sources of noise, such as the random opening of ion channels, as well as by external sources, like synaptic noise [69]. Recent years have witnessed a rapid expansion of stochastic models for a wide variety of important physical and biological phenomena, from sub-cellular processes and tissue dynamics, over large-scale population dynamics and genetic switching to optical devices, Josephson junctions, fluid mechanics, and climatology. These studies have demonstrated that the effects of noise manifest themselves on a broad range of scales, nevertheless displaying certain universal features. From a physical standpoint, noise either modifies the deterministic features of the system or induces qualitatively novel types of behavior [67], such as noise-induced switching.

To study the impact of noise on excitable systems with a multiple timescale structure, we have constructed the following two simplified models:

A. **two identical adaptively coupled stochastic active rotators with excitable local dynamics** [181, 193, 254], whereby adaptivity is modeled by phase-dependent plasticity [205, 206, 207];

B. **a stochastic excitable active rotator with a slowly adapting feedback**.

Both models incorporate the basic ingredients of neurodynamics such as excitability, plasticity, and noise. The active rotator model, common to both systems, is paradigmatic for Type I excitability, whereas the stochasticity, modeled by Gaussian white noise, accounts for synaptic noise. Model A may be interpreted as a binary neuron motif, while model B may describe a neuron with a slow recovery variable, a model of population dynamics influenced by a slowly varying environment, or, more generally, an excitable system under the influence of a nonlinear control mechanism. As far as adaptivity is concerned, the setup in

model *A* allows for continuous interpolation between different plasticity rules such as those analogous to Hebbian learning or STDP, whereas the one considered in model *B* provides positive feedback for spiking behavior. In the following, we will provide a preview of the main results and methods applied.

Within our study on model *A*, we have discovered two qualitatively different types of slow stochastic fluctuations depending on the scale separation, or rather adaptivity rate. For slow adaptation, noise induces two characteristic timescales, one related to two modes of noise-induced oscillations, and the other giving rise to slow stochastic fluctuations between them. For faster adaptation, noise gives rise to bursting-like behavior, based on stochastic switching between the metastable states derived from coexisting attractors of the deterministic system.

Within our research on model *B*, we have found that the interplay of slowly adapting feedback and noise may give rise to three dynamical regimes, namely *noise-induced spiking, noise-perturbed oscillations, and stochastic busting*. The last is a new type of emergent behavior based on switching dynamics due to which the system alternates between episodes of spiking and relative quiescence. Moreover, we demonstrate that adjusting the feedback strength influences the form of the switching dynamics, providing a mechanism for the control of the statistical features of stochastic bursting.

In terms of theoretical methods, the main significance of the research on model B lies in the development of a novel approach which provides an extension of the classical singular perturbation theory to stochastic multiscale systems. In particular, we have first analyzed the noise-free system, employing a combination of two standard multiscale methods – *adiabatic elimination* in the regime where the fast subsystem has a stable equilibrium, and *averaging* when the fast subsystem is oscillatory. A bifurcation analysis of the resulting reduced slow system reveals that the two attractors of the fast flow give rise to bistable dynamics within the slow flow for a sufficiently strong feedback. Moreover, to perform a multiscale analysis of the system's noisy dynamics, we have applied the method of *stochastic averaging* [181, 182, 255, 256, 257] in which the dynamics of the slow flow is determined using the distribution density for the fast variable obtained from a stationary Fokker-Plank equation. This has allowed us to obtain averaged slow dynamics for which we have performed a complete numerical bifurcation analysis with respect to noise intensity and the control gain or feedback strength parameter, obtaining a bifurcation diagram with a characteristic bistability region of the slow flow, as well as the stability boundaries of the three dynamical regimes. In the case of finite scale separation, stochastic bursting is found to emerge due to noise-induced switching of Kramers type.

The chapter is organized as follows. Section 3.1 is devoted to the analysis of switching dynamics in model *A*. The model is presented in section 3.1.1 along with its deterministic dynamics, while section 3.1.2 contains the results of the corresponding slow-fast analysis. Finally, section 3.1.3 concerns the stochastic behavior of model *A*, whereby the features of the two generic types of switching behavior are considered within a multiscale framework.

Section 3.2 addresses the switching dynamics exhibited by model *B*. In particular, the details of the model are introduced in section 3.2.1, whereas section 3.2.2 contains an analysis of its deterministic dynamics within the framework of singular perturbation theory. Sections 3.2.3 and 3.2.4 address the influence of noise in model B, whereby the former concerns the extension of singular perturbation theory to stochastic systems by employing the method of stochastic averaging, while the latter provides an analysis of switching dynamics in the case of finite timescale separation. The concluding section 3.3 contains a summary and discussion of the presented results.

– 3.1 *Switching in a motif of two adaptively coupled excitable units* –

In this section, we will show that the interplay of noise and plasticity gives rise to slow stochastic fluctuations in a system of two coupled active rotators with excitable local dynamics. Depending on the scale separation (adaptation rate), we observe two qualitatively different types of switching behavior. For slower adaptation, one finds alternation between two modes of noise-induced oscillations, whereby the modes are distinguished by a different order of spiking between the units. In the case of faster adaptation, the system switches between four metastable states derived from coexisting attractors of the corresponding deterministic system, whereby the phases exhibit bursting-like behavior. The qualitative features of the switching dynamics are analyzed within the framework of slow-fast analysis [181].

3.1.1 Model and deterministic dynamics of the full system

The model considered in this section is a stochastic version of system (2.1) from the previous chapter. In particular, the dynamics of the phases $\{\varphi_1(t), \varphi_2(t)\}$ and the couplings $\{\kappa_1(t), \kappa_2(t)\}$ now reads

$$
\begin{aligned}
\dot{\varphi}_1 &= I_0 - \sin \varphi_1 + \kappa_1 \sin (\varphi_2 - \varphi_1) + \sqrt{D}\xi_1 \\
\dot{\varphi}_2 &= I_0 - \sin \varphi_2 + \kappa_2 \sin (\varphi_1 - \varphi_2) + \sqrt{D}\xi_2 \\
\dot{\kappa}_1 &= \varepsilon(-\kappa_1 + \sin(\varphi_2 - \varphi_1 + \beta)) \\
\dot{\kappa}_2 &= \varepsilon(-\kappa_2 + \sin(\varphi_1 - \varphi_2 + \beta)),
\end{aligned}
\tag{3.1}
$$

where $\varphi_1, \varphi_2 \in S^1$, while $\kappa_1, \kappa_2 \in \mathbb{R}$, and $0 < \varepsilon \ll 1$ is the timescale separation parameter. Once again, the analysis will be confined to excitable local dynamics ($I_0 < 1$) with $I_0 = 0.95$ fixed, as well as the β interval which admits excitable fixed points, interpolating between the Hebbian learning rule $\beta = 3\pi/2$ [206, 207] and the STDP-like plasticity rule $\beta = \pi$. White noise of variance D acts only within the subspace of fast variables, whereby the terms $\xi_1(t)$ and $\xi_2(t)$ are independent ($\langle\xi_i(t)\xi_j(t')\rangle = \delta_{ij}\delta(t - t')$ for $i, j \in \{1, 2\}$). Recall that system (3.1) with $D = 0$ is invariant to exchange of units' indices ($\mathbb{Z}_2$ symmetry).

The noiseless uncoupled system always converges to a steady state, whereas oscillations may emerge due to interactions and/or noise. Let us first consider the impact of interactions by analyzing the deterministic dynamics of (3.1). To this end, we will evoke the previously obtained results on the stationary states and the associated excitability feature, see section 2.1, after which we will analyze the onset and waveform of emergent oscillations.

3.1.1.1 Stationary states

Recall that the fixed points $(\varphi_1^*, \varphi_2^*, \kappa_1^*, \kappa_2^*)$ of the full system (3.1) with $D = 0$ are given by the solutions of the following set of equations:

$$\sin \varphi_1^* - \sin(\varphi_2^* - \varphi_1^* + \beta) \sin(\varphi_2^* - \varphi_1^*) = I_0,$$
$$\sin \varphi_2^* - \sin(\varphi_1^* - \varphi_2^* + \beta) \sin(\varphi_1^* - \varphi_2^*) = I_0,$$

having used

$$\kappa_1^* = \sin(\varphi_2^* - \varphi_1^* + \beta),$$
$$\kappa_2^* = \sin(\varphi_1^* - \varphi_2^* + \beta).$$

Depending on β, there may be two, four or six fixed points, see Fig. 2.2. Nevertheless, our analysis concerns the interval $\beta \in (3.298, 4.495)$ in which the system has *two stable* fixed points lying off the synchronization manifold $\varphi_1 = \varphi_2$ as well as four unstable fixed points. The bifurcations associated with the boundaries of the given β interval are as follows: at $\beta = 3.298$ the system undergoes a supercritical symmetry-breaking pitchfork bifurcation where a symmetry-related pair of two stable fixed points off the synchronization manifold is created, whereas at $\beta = 4.495$, this pair meets a pair of unstable fixed points off the synchronization manifold, getting annihilated in symmetry-related inverse saddle-node bifurcations.

The two stable fixed points in the interval $\beta \in (3.298, 4.495)$ are *excitable foci*. Recall that the system may exhibit several different types of response to external perturbations as illustrated in Fig. 2.3. Once again, we will set the plasticity parameter to $\beta = 4.212$ for which the fixed points are given by

$$(\varphi_1^*, \varphi_2^*, \kappa_1^*, \kappa_2^*) = (1.2757, 0.2127, -0.0078, -0.8456)$$
$$(\varphi_1^*, \varphi_2^*, \kappa_1^*, \kappa_2^*) = (0.2127, 1.2757, -0.8456, -0.0078).$$

Note that these weight levels support effective master-slave configurations in which one unit exerts a much stronger influence on the other unit than vice versa.

3.1.1.2 The onset of oscillations

The onset of emergent oscillations in the full system (3.1) with $D = 0$ depends on the interplay between the plasticity rule, specified by β, and the adaptation rate, characterized by ε. We have determined the maximal stability region of the periodic solution in the (β, ε) parameter plane by numerical continuation, in which the final state reached for a certain set of (β, ε)
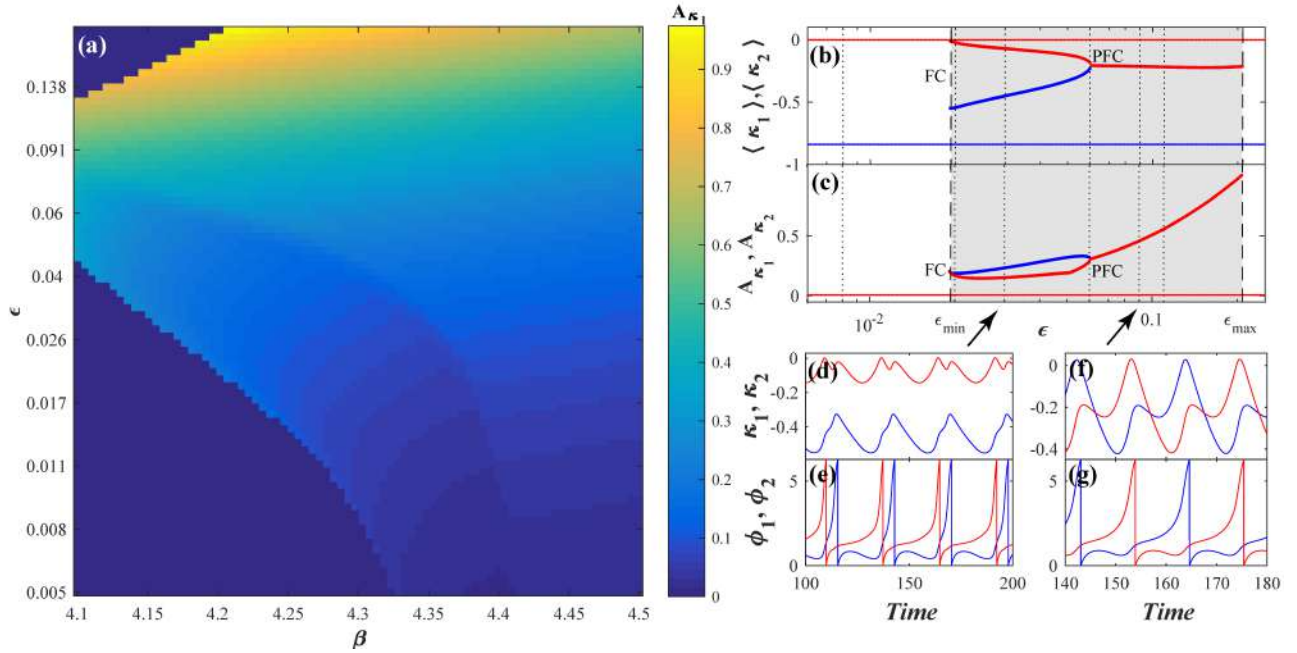
Figure 3.1: Emergence of oscillations in system (3.1) with $D = 0$ for $I_0 = 0.95$. The maximal stability region of the periodic solutions is indicated in panel (a), which shows how the variation A_{κ_1} of the coupling weight κ_1 changes in the (β, ε) plane. Panel (b) shows the dependencies $\langle \kappa_1 \rangle(\varepsilon)$ and $\langle \kappa_2 \rangle(\varepsilon)$, whereas panel (c) contains $A_{\kappa_1}(\varepsilon)$ and $A_{\kappa_2}(\varepsilon)$, both under fixed $\beta = 4.212$. In (b) and (c), the red and blue thick (thin) solid lines in correspond to the oscillatory (stationary) state, black dotted lines indicate ε values corresponding to the time traces in Fig. 3.5, gray shading designates the ε region supporting multistability of two symmetry-related equilibria and two limit cycles, while FC and PFC denote the fold of limit cycles and pitchfork of limit cycles bifurcations, respectively. Panels (d)-(g) show the waveforms before and after PFC, obtained for $\varepsilon = 0.03$ and $\varepsilon = 0.09$, respectively (indicated by the arrows).

values provides the initial conditions for the simulation of the system at incremented parameter values. A parameter scan indicating the variation of κ_1, $A_{\kappa_1} = \max(\kappa_1(t)) - \min(\kappa_1(t))$, in terms of (β, ε) is shown in Fig. 3.1(a). Positive values $A_{\kappa_1} > 0$ correspond to oscillations, whereas the steady states are characterized by $A_{\kappa_1} = 0$.

For fixed β within the relevant range, we find an interval of timescale separation values $\varepsilon \in (\varepsilon_{min}, \varepsilon_{max})$ admitting stable periodic solutions which appear as symmetry-related twins. The onset of oscillations at $\varepsilon = \varepsilon_{min}(\beta)$ corresponds to the appearance of *two* stable periodic solutions related via the exchange symmetry of the indices. These solutions are born via two symmetrical fold-cycle bifurcations, indicated by FC in Fig. 3.1(b). Under increasing ε, the two branches of oscillatory solutions eventually merge at $\varepsilon \approx 0.06$, where the system undergoes an inverse (symmetry-gaining) pitchfork bifurcation of limit cycles (PFC). The oscillations coexist with two symmetry-related stable stationary states, cf. Fig. 3.1(b)-(c). Moreover, under increasing β, the maximal stability region of oscillations changes such that the lower boundary value $\varepsilon_{min}(\beta)$ reduces, whereas the upper boundary value $\varepsilon_{max}(\beta)$ grows.

Below the PFC bifurcation, the phases $\varphi_1(t)$ and $\varphi_2(t)$ maintain a small phase-shift, while $\kappa_1(t)$ and $\kappa_2(t)$ have different oscillation profiles, see Fig. 3.1(d) and Fig. 3.1(e), respectively. Above the bifurcation, the system gains anti-phase space-time symmetry,

$$\varphi_1(t) = \varphi_2(t + T/2)$$
$$\kappa_1(t) = \kappa_2(t + T/2),$$

where T denotes the oscillation period, cf. the associated waveforms in Fig. 3.1(g) and Fig. 3.1(f).

3.1.2 Slow-fast analysis of deterministic dynamics

The deterministic dynamics in case of sharp timescale separation between the fast and slow variables, which conforms to slow adaptation, may be analyzed within the framework of singular perturbation theory. This involves complementary treatments of the layer problem, defined on the fast timescale, and the reduced problem, which concerns the slow timescale. Within the layer problem, our aim is to determine the fast flow dynamics $(\varphi_1(t; \kappa_1, \kappa_2), \varphi_2(t; \kappa_1, \kappa_2))$ by treating the slow variables κ_1 and κ_2 as additional system parameters. The goal of the reduced problem is to determine the dynamics of the slow flow $(\kappa_1(t), \kappa_2(t))$ by assuming that the fast flow of the layer problem is either at a stable equilibrium or at the averaged value of a stable periodic solution. Note that multistability of the fast flow gives rise to multiple stable sheets of the slow flow.

3.1.2.1 Dynamics of the fast flow: the layer problem

Within the layer problem, we study the fast subsystem

$$\dot{\varphi}_1 = I_0 - \sin \varphi_1 + \kappa_1 \sin (\varphi_2 - \varphi_1)$$
$$\dot{\varphi}_2 = I_0 - \sin \varphi_2 + \kappa_2 \sin (\varphi_1 - \varphi_2), \tag{3.2}$$

where $\kappa_1, \kappa_2 \in [-1, 1]$ are considered as additional system parameters. Formally, system (3.2) is obtained by setting $\varepsilon = 0$ in (3.1) for $D = 0$.

The numerically obtained bifurcation diagram shown in Fig. 3.2(a) indicates that the fast flow is monostable for the majority of (κ_1, κ_2) values, exhibiting either a fixed point or a limit cycle attractor. The stability boundary of the periodic solution (red curves) has been obtained by numerical continuation of the stable periodic solution, using the final state reached for the given (κ_1, κ_2) set as initial conditions for the system dynamics at the next iteration step. The coexistence between a stable fixed point, lying on the synchronization manifold $\varphi_1 = \varphi_2$, and a limit cycle is found within a small region near the diagonal, shown white in Fig. 3.2(a). Let us now classify the fixed points of the fast flow and then examine the scenarios that give rise to oscillations.

Fixed points — It can be shown that the fast flow admits either two or four fixed points, with the associated (κ_1, κ_2) regions indicated in Fig. 3.2(b). In particular, there are two fixed
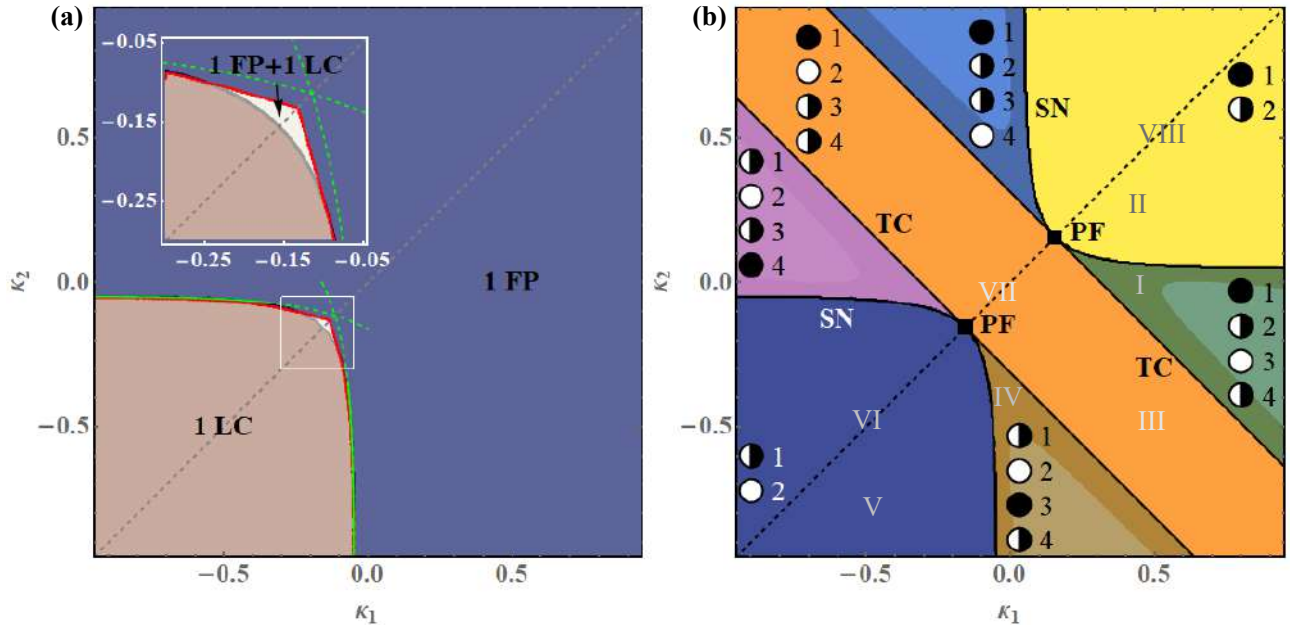
Figure 3.2: (a) Attractors of the fast flow (3.2) in terms of κ_1 and κ_2, now considered as parameters. The fast flow is typically monostable, supporting either a stable fixed point (FP) or a stable limit cycle (LC), apart from a small region near the main diagonal, indicated in white, where it exhibits bistable behavior. The green curves indicate approximations of two branches of SNIPER bifurcations obtained by the method described in the text. The red lines correspond to the numerically determined stability boundaries of the oscillatory solution. (b) Classification of the fixed points of the fast flow (3.2). The labels of the fixed points correspond to those referenced in the main text, with their stability indicated as follows: full circles denote stable fixed points, semi-full circles represent saddle points and white circles correspond to doubly unstable fixed points. Within the four light-shaded triangular-shaped regions, the node which lies off the synchronization manifold becomes a focus without changing stability. The notation I-VIII refers to parameter values corresponding to the phase portraits in Fig. 3.3.

points on the synchronization manifold, whose coordinates are independent of κ_1 and κ_2:

$$FP1 \equiv (\varphi_1^*, \varphi_2^*) = (\arcsin I_0, \arcsin I_0)$$
$$FP2 \equiv (\varphi_1^*, \varphi_2^*) = (\pi - \arcsin I_0, \pi - \arcsin I_0)$$

Moreover, the fast flow may contain two additional fixed points off the synchronization manifold, referred to as $FP3$ and $FP4$ in Fig. 3.2(b). The bifurcations affecting the number and stability of the fixed points, starting from the lower left region of the (κ_1, κ_2) plane, can be summarized as follows. Along the main diagonal $\kappa_1 = \kappa_2$, we find two points of *supercritical pitchfork bifurcations* (PF) in which the saddles $FP3$ and $FP4$ appear and disappear from symmetric fixed points. Off the main diagonal $\kappa_1 \neq \kappa_2$, the pitchforks unfold into curves of *saddle-node* (SN) and *transcritical bifurcations* (TC), as shown in Fig. 3.2(b).

Within regions of the phase plane where either $FP3$ or $FP4$ is a node, we find subregions where their character changes while retaining the stability features. In particular, in region IV from Fig. 3.2(b), the stable node $FP3$ becomes a stable focus, whereas in region I the

unstable node *FP3* becomes an unstable focus. Analogous scenarios concerning *FP4* hold for the two regions symmetrical with respect to the main diagonal (purple and light blue).

Periodic solutions — The (κ_1, κ_2) region featuring stable oscillations almost exactly matches the lower left domain admitting two unstable fixed points. Within this region, each periodic solution obtained for (κ_1, κ_2) above the main diagonal $\kappa_1 = \kappa_2$ has a symmetry-related counterpart in the domain below the main diagonal. Depending on κ_1 and κ_2, we find three distinct scenarios by which the two periodic solutions emerge.

In particular, sufficiently far from the main diagonal $\kappa_1 = \kappa_2$, the oscillations emerge via two branches of *SNIPER bifurcations*, where either κ_1 or κ_2 remain nearly constant and close to zero. In either scenario, *FP3* and *FP4* collide and disappear as the limit cycle is born. Near the main diagonal, in the small (κ_1, κ_2) region admitting coexistence between fixed point and limit cycle attractors, the onset of oscillations cannot conform to the SNIPER bifurcation scenario, because the total number of fixed points remains unchanged. Instead, the oscillations there emerge via a *heteroclinic bifurcation* in which an orbit connects the two saddles *FP3* and *FP4* lying off the synchronization manifold. The orbit of the limit cycle follows the unstable manifold of the saddle point *FP2* on the synchronization manifold. Slightly away from the main diagonal, one finds that Z_2 symmetry-related limit cycles are born from *homoclinic bifurcations* in which a saddle point, either *FP3* or *FP4*, emerging as a homoclinic orbit to the saddle FP3 or FP4.

Schematic phase portraits indicating the fixed points along with their stability manifolds, as well as the representative limit cycle, for each of the characteristic regimes of the fast flow denoted by I-VIII in Fig. 3.2(b) are illustrated in Fig. 3.3.

The two branches of SNIPER bifurcations may readily be approximated for small values of κ_1 and κ_2 by a simple scheme which amounts to reducing the fast flow to the normal form of the saddle-node bifurcation. Let us first suppose that $\kappa_1 \ll 1$ and $I_0 - 1 \ll 1$. More specifically, let $\xi \ll 1$ be a small parameter such that $I_0 - 1 = \xi$, and $\kappa_1 = \gamma \xi$, where γ is a rescaling parameter of κ_1, allowing for a zoom in the neighborhood of zero. Then, the steady states are given by the system

$$1 + \xi - \sin \varphi_1 + \xi \gamma \sin(\varphi_2 - \varphi_1) = 0,$$
$$1 + \xi - \sin \varphi_2 + \kappa_2 \sin(\varphi_1 - \varphi_2) = 0. \tag{3.3}$$

In the zeroth order approximation, the first equation yields $\varphi_1 = \pi/2$. Using the perturbation technique, we obtain that the coordinates $(\varphi_1^*, \varphi_2^*)$ of the steady states satisfy

$$\varphi_1^* = \frac{\pi}{2} + \sqrt{\xi}\Psi_1 + \cdots,$$
$$\varphi_2^* = \Psi_2 + \cdots, \tag{3.4}$$

where the $\sqrt{\xi}$ scaling follows from the Taylor expansion of the function $\sin \varphi_1$ at $\pi/2$. By inserting (3.4) into (3.3), we arrive at the following system of equations for Ψ_1 and Ψ_2

$$1 + \frac{1}{2}\Psi_1^2 - \gamma \cos \Psi_2 = 0,$$
$$1 - \sin \Psi_2 + \kappa_2 \cos \Psi_2 = 0.$$
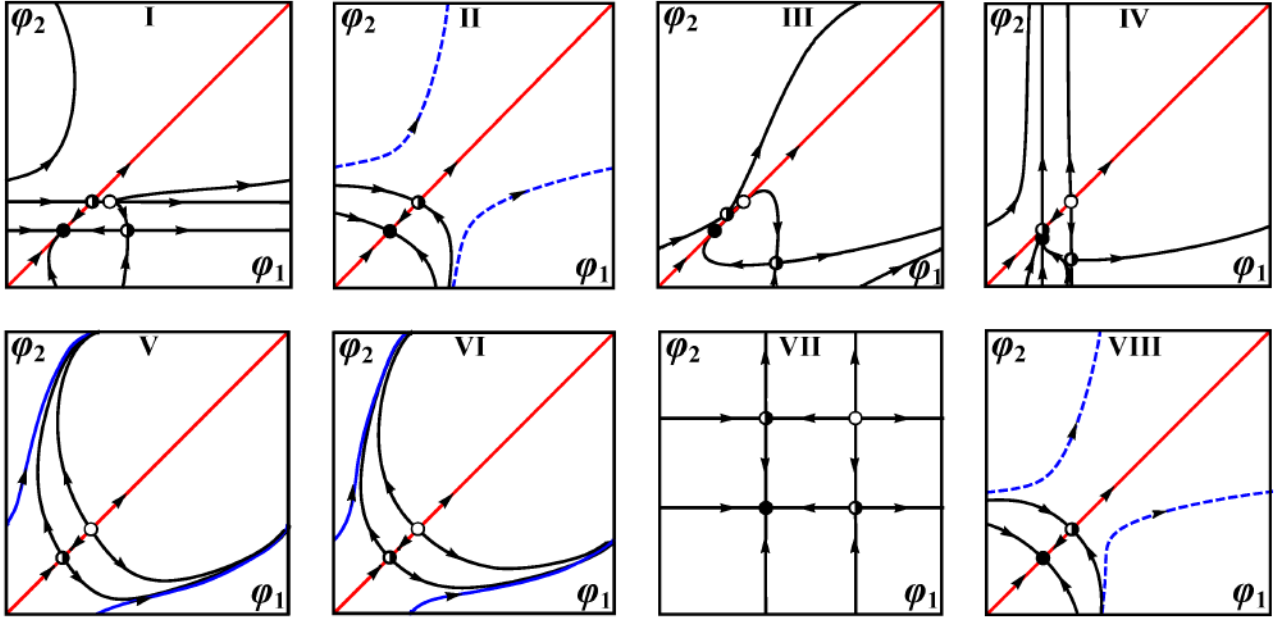
Figure 3.3: Schematic phase portraits corresponding to the characteristic regimes of the fast flow. The panels I-VIII refer to representative parameter values indicated in Fig. 3.2(b). Also, the stability of fixed points is presented the same way as in Fig. 3.2(b). The invariant synchronization manifold is denoted by the red color, whereas the orbit of a stable/unstable limit cycle is indicated by the solid/dashed blue lines.

The saddle-node bifurcation occurs if $\Psi_1 = 0$, i. e. when the condition $1 - \gamma \cos \Psi_2 = 0$ is satisfied. This leads to the following parametric representation of the saddle-node curve for small κ_1 values

$$\kappa_1 = \tilde{\xi}\gamma = \frac{I_0 - 1}{\cos \Psi_2},$$
$$\kappa_2 = \frac{\sin \Psi_2 - 1}{\cos \Psi_2},$$

where Ψ_2 plays the role of the parameter along the curve. An analogous approach may be used to capture the second branch of saddle-node bifurcations, cf. the green dashed lines in Fig. 3.2(a).

3.1.2.2 Dynamics of the slow flow: the reduced problem

We have numerically obtained the dynamics of the slow flow by applying the following two-step approach.

1. Determine the time-averaged dynamics of the fast flow (3.2), $\langle \varphi_2 - \varphi_1 \rangle_t = f(\kappa_1, \kappa_2)$ for fixed (κ_1, κ_2).

   The averaging $\langle \cdot \rangle_t$ must be performed over a sufficiently long time interval, having eliminated a transient. The resulting average depends on the type of attractor of the fast flow for given (κ_1, κ_2). In particular, if the fast flow has a stable fixed point, then
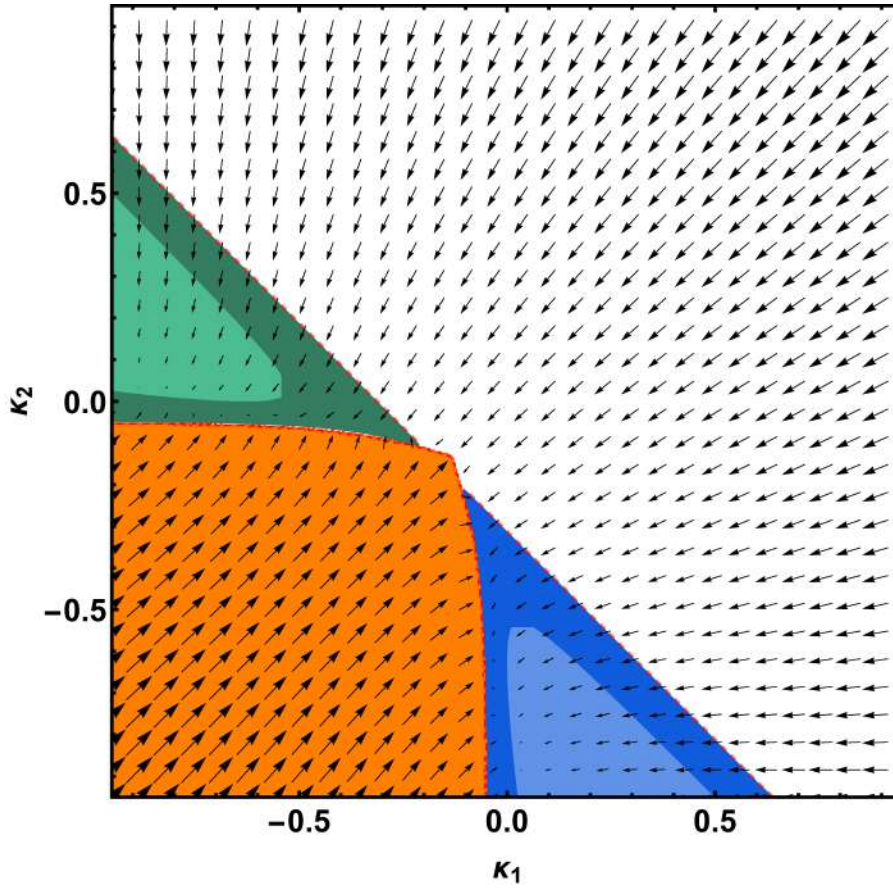
Figure 3.4: The vector field of the slow flow obtained by taking only the stable attractors of the fast flow into account. The color coding is as follows: orange color denotes the region associated with the stable limit cycle of the fast flow, white stands for the stable fixed point $FP1$ of the fast flow, whereas blue and green color correspond to the two stable fixed points $FP3$ and $FP4$. Within the lighter shaded regions, $FP3$ and $FP4$ are foci rather than nodes, cf. Fig. 3.2(b). The system parameters are $\beta = 4.212$, $I_0 = 0.95$.

$\langle \varphi_2 - \varphi_1 \rangle_t = \varphi_2^* - \varphi_1^*$, where $(\varphi_1^*, \varphi_2^*)$ is a solution of

$$I_0 - \sin \varphi_1^* + \kappa_1 \sin (\varphi_2^* - \varphi_1^*) = 0$$
$$I_0 - \sin \varphi_2^* + \kappa_2 \sin (\varphi_1^* - \varphi_2^*) = 0.$$

This procedure results in determining the slow critical manifold of the system. On the other hand, when the attractor of the fast flow is periodic, $\langle \varphi_2 - \varphi_1 \rangle_t$ presents the time average over the period. Approximating the the effect of the fast oscillations on the slow flow in this way constitutes a standard approach [182, 255], rather natural for describing the influence of oscillations in the fast flow on the dynamics of the slow flow.

2. Substitute the obtained time-averages into the coupling dynamics:

$$\dot{\kappa}_1 = \varepsilon[-\kappa_1 + \sin(f(\kappa_1, \kappa_2) + \beta)]$$
$$\dot{\kappa}_2 = \varepsilon[-\kappa_2 + \sin(-f(\kappa_1, \kappa_2) + \beta)]. \tag{3.5}$$

We have plotted the vector field of the slow flow (3.5) associated with each attractor of the fast flow within its respective stability region, thus obtaining the stable sheets of the slow flow over the (κ_1, κ_2) parameter plane, cf. Fig. 3.4. In the (κ_1, κ_2) region which admits coexisting stable solutions of the fast flow, namely a stable equilibrium and a stable limit cycle, the corresponding vector field of the slow flow is given by multiple overlapping sheets, since the value of the average $f(\kappa_1, \kappa_2)$ depends on the initial conditions.

Fig. 3.4 shows two important features of the slow flow: (*i*) it exhibits two symmetry-related fixed points within the green and blue regions, and (*ii*) the slow vector field is pointed in opposing directions near the boundary between the oscillatory regime (orange region) and the steady states of the fast flow (blue, green, and white regions). The latter implies that we can expect nontrivial effects near the border separating the oscillatory and steady state regime of the fast flow. In particular, adding noise causes fluctuations around this boundary, leading to switching between the quasi-stationary and the fast spiking dynamics. Such effects are studied in more detail within the next section.

3.1.3 Switching dynamics

In this section, we demonstrate how the interaction of plasticity and noise gives rise to slow stochastic fluctuations (switching dynamics) in a motif of two excitable active rotators. Depending on the adaptation rate, we find two qualitatively different scenarios, namely:

1. switching between two modes of noise-induced oscillations for *slower* adaptation (small $\varepsilon \sim 0.01$);

2. switching between multiple coexisting attractors of the deterministic dynamics for *faster* adaptation (intermediate $\varepsilon \simeq 0.05$).

In the first case, the impact of noise is twofold: on a short timescale, it gives rise to spiking dynamics, while on a long time scale, it induces random transitions between the two oscillatory modes. In the second case, the switching dynamics involves metastable states derived from two fixed points, as well as two limit cycles associated with the emergent oscillations of the corresponding deterministic system. The key difference between these two scenarios is that for slower adaptation, the system switches between oscillatory modes that do not exist as deterministic attractors. Moreover, the two generic types of switching are characterized by distinct phase dynamics. In particular, for slower adaptation, there is an alternation of noise-induced oscillation modes that involve a different order of spiking between the units. On the other hand, in the case of faster adaptation, the phases effectively exhibit bursting behavior, involving a succession of spiking episodes and relative quiescence.

Fig. 3.5 provides an overview of how the typical dynamics of couplings changes with ε for fixed β and noise intensity. Note that, for the deterministic system, the difference between the average couplings of the stable periodic solutions is much smaller than the typical distance between the levels corresponding to the stationary states, see Fig. 3.1(b). Concerning the influence of ε on the prevalence of metastable states, intermediate adaptation favors
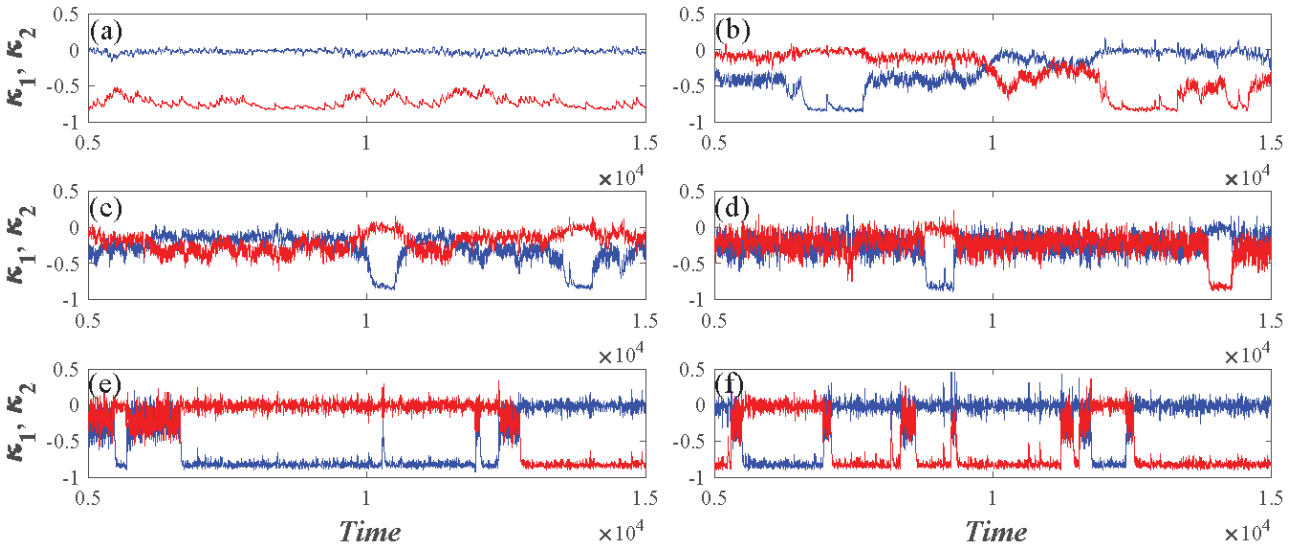
Figure 3.5: Switching dynamics under the variation of ε. The time traces $(\kappa_1(t), \kappa_2(t))$ are obtained for fixed $I_0 = 0.95$, $D = 0.006$, $\beta = 4.212$, whereas ε assumes the following values: (a) $\varepsilon = 0.008$, (b) $\varepsilon = 0.02$, (c) $\varepsilon = 0.03$, (d) $\varepsilon = 0.06$, (e) $\varepsilon = 0.09$, and (f) $\varepsilon = 0.11$.

oscillatory modes, whereas fast adaptation apparently promotes the two quasi-stationary states. The following subsections provide a deeper insight into the mechanisms underlying the switching dynamics.

3.1.3.1 Switching dynamics for slower adaptation

In this case, ε is sufficiently small, in the sense that it cannot facilitate emergent oscillations in the full system (3.1). Nevertheless, noise-induced oscillations may appear under appropriate noise levels for $\varepsilon \simeq 0.01$. These oscillations arise in a scenario that involves a multiple timescale stochastic bifurcation, whereby noise acts only within the fast subsystem of (3.1). The onset of oscillations under increasing D occurs in two stages. In the first stage, the phase dynamics gradually exhibits an increasing number of induced spikes, reflected in the fact that the stationary distributions of the phases eventually acquire a longer tail. Nevertheless, the stationary distributions of the couplings change considerably only at the second stage, reflecting the onset of oscillations of the couplings, which takes place for sufficiently large D. Note that the system (3.1) actually exhibits *two modes* of noise-induced oscillations, characterized by a different order of firing between the two units, as illustrated by the time traces of the phase dynamics and the associated evolution of the couplings in Fig. 3.6(a).

It is interesting to examine whether we can use the vector field of the slow flow, calculated in section 3.1.2.2 and shown on Fig. 3.4, to explain the slow stochastic fluctuations of the couplings. To this end, we have superimposed the $(\kappa_1(t), \kappa_2(t))$ orbits of the two noise-induced modes, as well as that of a switching episode, onto the vector field of the slow flow. Our first observation is that these orbits lie close to the boundary which outlines the transition between the two attractors of the fast flow, where the couplings are non-negligible. Moreover, the two modes are confined to small areas of the (κ_1, κ_2) plane symmetrical with
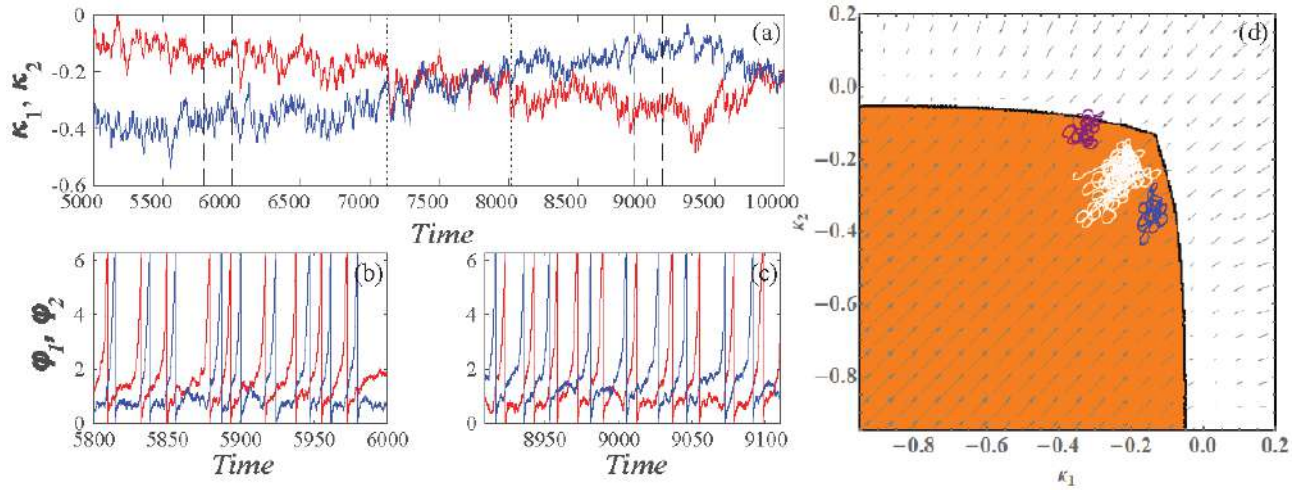
Figure 3.6: Switching dynamics between the two modes of noise-induced oscillations (slow adaptation) for $I_0 = 0.95, \beta = 4.212, \varepsilon = 0.01, D = 0.009$. Time traces of the weights are shown in panel (a), whereas panel (b) and (c) display the corresponding time traces of the phases during the intervals between the dashed lines in panel (a). Panel (d), we superimpose the $(\kappa_1(t), \kappa_2(t))$ projections of the orbits associated with each of the two modes (blue and purple), as well as the switching episode (white) onto the vector field of the slow flow from Fig. 3.4. The orange shaded area corresponds to the stable limit cycle.

respect to the main diagonal $\kappa_1 = \kappa_2$, whereas the switching episode virtually takes place on the diagonal. Apparently, the noise-induced modes occupy regions where the oscillations in the fast flow emerge via homoclinic bifurcations rather than by the SNIPER scenario. Nonetheless, the switching episode involves the domain featuring the coexistence of the two stable sheets of the slow vector field. Within these sheets, which correspond to the two attractors of the fast flow – a stable node and a stable limit cycle – the vector fields are oriented in opposing directions, thereby promoting the switching dynamics.

3.1.3.2 Switching dynamics for faster adaptation

The switching dynamics for faster adaptation involves four metastable states derived from the attractors of the deterministic system. Indeed, recall that for intermediate ε, deterministic multistability involves two symmetry-related stationary states and two symmetry-related limit cycles, cf. Fig. 3.1. While the two stable steady states exist for arbitrary small ε and are therefore visible in the slow flow in Fig. 3.4, the oscillatory solutions disappear for small ε and hence cannot be observed in the slow flow. The two oscillatory regimes are characterized by the same phase shift, however, the order of firing between the two units is reversed. Influenced by noise, the phases effectively engage in bursting behavior, manifesting slow stochastic fluctuations between episodes of intensive spiking activity and periods of relative quiescence, see Fig. 3.7(a). For a fixed noise level, the prevalence of metastable states changes with adaptation speed. In particular, for $\varepsilon \simeq 0.05$, the oscillatory dynamics is preferred, whereas the quasi-stationary states are dominant for $\varepsilon \simeq 0.1$.
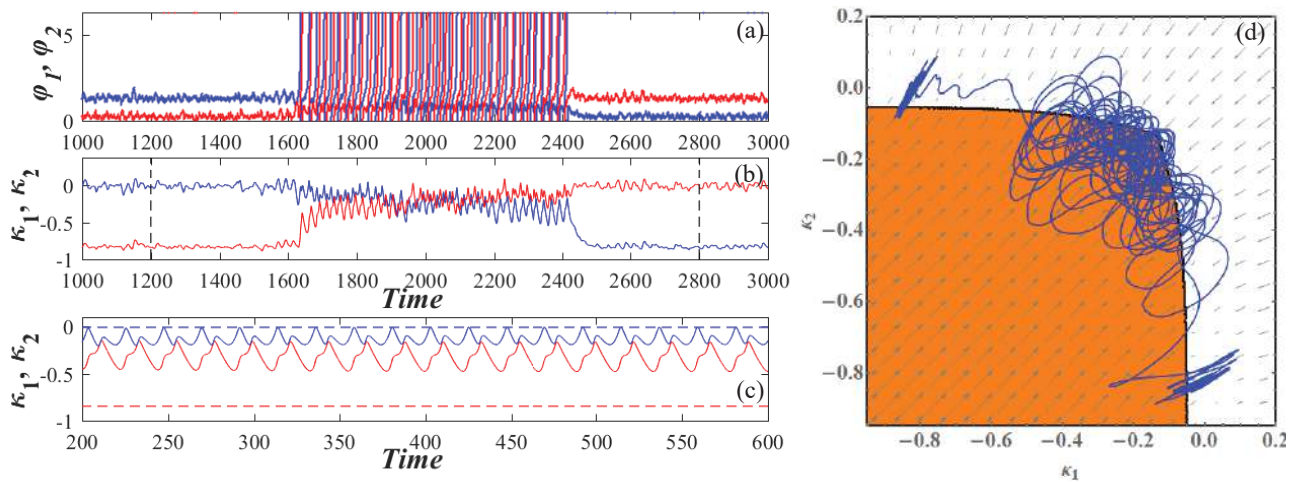
Figure 3.7: Time traces of the phases (a) and weights (b) associated with noise-induced switching between the coexisting attractors of the deterministic system (fast adaptation) for $I_0 = 0.95, \beta = 4.212, \varepsilon = 0.05, D = 0.004$. For comparison, panel (c) shows the deterministic dynamics of weights obtained for the same parameter values. In panel (d), the $(\kappa_1(t), \kappa_2(t))$ orbit corresponding to the interval between the dashed lines in (b) is superimposed onto the vector field of the slow flow, cf. Fig. 3.4.

Comparing the typical (κ_1, κ_2) orbits to the vector field of the slow flow from Fig. 3.4 reveals that the switching is again confined to the criticality region at the boundary between the stationary and oscillatory regimes of the fast flow, cf. Fig. 3.7. As far as the transitions between the different metastable states are concerned, it is clear from Fig. 3.7(b) that there can be no direct transitions between the two quasi-stationary states since the system must pass through the oscillatory states to reach the other stationary level. Moreover, the transition from oscillatory to quasi-stationary dynamics typically occurs once the couplings approach a "master-slave"-like configuration, where the coupling in one direction is much stronger than the other one. This scenario coincides with the SNIPER bifurcation of the fast flow described in section 3.1.2.1. The scenario accounting for transitions between the two metastable oscillatory states closely resembles the one occurring for slower adaptation.

- 3.2 *Switching in an excitable unit with a slowly adapting feedback* -

In this section, we study the model of an excitable system with a slowly adapting feedback to demonstrate how the interaction of noise and multiscale dynamics gives rise to a novel form of emergent behavior, *stochastic bursting*. By extending methods from multiscale analysis to stochastic systems, we have determined the existence domain of stochastic bursting regime, as well as the bifurcations underlying the transitions to other regimes. We also explain how the properties of the switching process, i. e. whether the switching is balanced or biased, influences the statistical features of stochastic bursting [192].

3.2.1 Model

In general, a stochastic excitable system influenced by a low-pass filtered feedback may be modeled as follows:

$$\dot{v} = f(v, \mu) + \sqrt{D}\xi(t), \tag{3.6}$$
$$\dot{\mu} = \varepsilon(-\mu + \eta g(v)),$$

where the small parameter $0 < \varepsilon \ll 1$ defines the timescale separation between the fast variable $v(t)$ and the slow feedback variable $\mu(t)$. The fast dynamics $\dot{v} = f(v, 0)$ is excitable, whereby the excitability feature is influenced by the slow feedback variable $\mu(t)$. Gaussian white noise $\xi(t)$ of variance D acts within the fast subsystem. The parameter η featured in the slow dynamics is the feedback strength, such that for $\eta = 0$ one recovers a classical noise-driven excitable system [67]. An important example of a system conforming to (3.6) for $\eta \neq 0$ is the Izhikevich neuron model [258], in which the stochastic input to the fast variable would describe the action of synaptic noise.

Our analysis will be carried out on a simple, yet paradigmatic model belonging to the class of systems given by (3.6). In particular, the excitable local dynamics is represented by the Type I excitable active rotator model while the slow adaptation is introduced as a positive periodic function $g(\varphi) = 1 - \sin \varphi$, such that the complete model reads

$$\dot{\varphi} = I_0 - \sin \varphi + \mu + \sqrt{D}\xi(t), \tag{3.7}$$
$$\dot{\mu} = \varepsilon\left(-\mu + \eta\left(1 - \sin \varphi\right)\right). \tag{3.8}$$

In the presence of feedback, the deterministic dynamics of the active rotator depends on the term $I_0 + \mu$ involving the control variable $\mu(t)$, which can induce switching between the excitable equilibrium ($|I_0 + \mu| < 1$) and the oscillatory regime ($|I_0 + \mu| > 1$). The chosen adaptation rule provides positive feedback for spiking behavior, since μ increases when $\varphi(t)$ exhibits noise-induced oscillations, effectively driving the system towards the oscillatory regime. On the other hand, in the vicinity of the equilibrium ($\sin \varphi \approx 1$), the feedback effectively vanishes. In the following sections, we will first perform an analysis of the deterministic dynamics within the framework of singular perturbation theory, after which we will extend the analysis to the stochastic dynamics in the limit of infinite timescale separation.

3.2.2 Slow-fast analysis of deterministic dynamics

In this section, we analyze system (3.7)–(3.8) in the absence of noise ($D = 0$)

$$\dot{\varphi}(t) = I_0 - \sin \varphi(t) + \mu(t), \tag{3.9}$$
$$\dot{\mu}(t) = \varepsilon\left(-\mu(t) + \eta\left(1 - \sin \varphi(t)\right)\right),$$

considering the limit $\varepsilon \to 0$ within the framework of singular perturbation theory. The dynamics on the fast timescale is described by the layer equation, formally obtained by
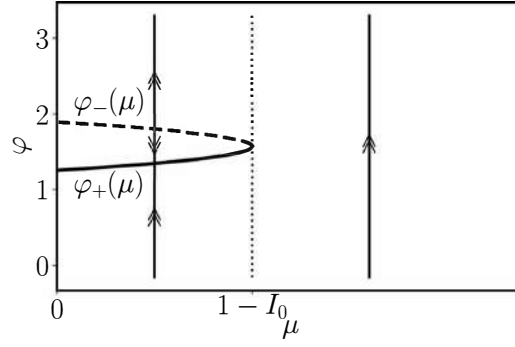
Figure 3.8: Dynamics of the fast flow (3.10). The critical manifold is comprised of the stable branch $\varphi_+(\mu)$, shown by the solid line, and the unstable branch $\varphi_-(\mu)$ (dashed line). For $\mu < 1 - I_0$, the fast dynamics converges to the stable branch of the critical manifold, while for $\mu > 1 - I_0$, it is oscillatory with periodic rotation of the phase φ. The bifurcation threshold $\mu = 1 - I_0$ is indicated by the dotted line.

setting $\varepsilon = 0$ in (3.9) and treating μ as an additional parameter:

$$\dot{\varphi}(t) = I_0 + \mu - \sin\varphi(t). \tag{3.10}$$

The subsequent analysis of the effects of the fast dynamics on the corresponding reduced problem will be based on a combination of two methods from multiple timescale analysis. In particular, depending on whether (3.10) exhibits a stable equilibrium or a limit cycle attractor, we will employ either adiabatic elimination or averaging over fast oscillations to obtain a reduced system capable of describing both regimes, as well as the transitions between them. A bifurcation analysis of the slow subsystem will show that, for sufficiently large η, the system exhibits bistability between the equilibrium and fast oscillations.

3.2.2.1 Stable equilibrium in the fast flow and the method of adiabatic elimination

In the case $\mu < 1 - I_0$, the layer equation (3.10) has two fixed points:

$$\varphi_+(\mu) = \arcsin(I_0 + \mu),$$
$$\varphi_-(\mu) = \pi - \varphi_+(\mu),$$

where φ_+ is stable and φ_- is unstable. As functions of the parameter μ, the two branches of equilibria, $\varphi_+(\mu)$ and $\varphi_-(\mu)$ merge in the fold point $\mu = 1 - I_0$, see Fig. 3.8. Equivalently, the set of equililbria of the fast subsystem

$$\{(\varphi, \mu) : \sin\varphi = I_0 + \mu\} \tag{3.11}$$

comprises the *critical manifold* of (3.9), with the stable part $\varphi_+(\mu)$ and the unstable part $\varphi_-(\mu)$.

For $\mu < 1 - I_0$, the fast dynamics is rapidly attracted to the stable branch of the critical manifold $\varphi_+(\mu)$, along which it slowly drifts for $\varepsilon \gtrsim 0$. In order to describe this slow

dynamics, we rescale time as $T = \varepsilon t$, obtaining

$$\varepsilon \varphi'(T) = I_0 + \mu(T) - \sin \varphi(T), \tag{3.12}$$

$$\mu'(T) = -\mu(T) + \eta(1 - \sin \varphi(T)), \tag{3.13}$$

where the prime denotes the derivative with respect to the slow time T. By setting $\varepsilon = 0$, we eliminate the $\sin \varphi = I_0 + \mu$ term and arrive at the equation for the slow dynamics on the critical manifold:

$$\mu'(T) = -\mu(T) + \eta(1 - I_0 - \mu(T)). \tag{3.14}$$

3.2.2.2 Stable periodic solution of the fast flow and averaging over fast oscillations

For $\mu > 1 - I_0$, the fast subsystem (3.10) has no fixed points, see Fig. 3.8. Instead, one finds periodic oscillations

$$\varphi_\mu(t) = 2 \arctan \frac{1 + \Omega(\mu) \tan \frac{t}{2}\Omega(\mu)}{I_0 + \mu} \tag{3.15}$$

with the μ-dependent oscillation frequency (recall eq. (1.8) from section 1.2.3.1)

$$\Omega(\mu) = \sqrt{(I_0 + \mu)^2 - 1}.$$

In this case, the fast oscillations $\varphi_\mu(t)$ should be averaged in order to approximate their influence on the dynamics of the slow variable $\mu(T)$. Let us first provide a simplified explanation of the averaging procedure. First, we substitute the fast-oscillating solution $\varphi = \varphi_\mu(t)$ of (3.10) into the equation for the slow variable (3.13):

$$\mu'(T) = -\mu(T) + \eta(1 - \sin \varphi_\mu(t)).$$

Since the term $\sin(\cdot)$ oscillates rapidly, the last equation can be averaged over the fast timescale t, which leads to

$$\mu'(T) = -\mu(T) + \eta \left(1 - \langle \sin \varphi_\mu(t) \rangle_t\right). \tag{3.16}$$

The average $\langle \sin \varphi_\mu(t) \rangle_t$ can be found by integrating (3.10) over the oscillation period

$$\langle \dot{\varphi}(t) \rangle_t = \Omega(\mu) = I_0 + \mu - \langle \sin \varphi_\mu(t) \rangle_t \Rightarrow \langle \sin \varphi_\mu(t) \rangle_t = I_0 + \mu(T) - \Omega(\mu(T)),$$

which we substitute into (3.16) to obtain the slow averaged dynamics:

$$\mu'(T) = -\mu(T) + \eta(1 - I_0 - \mu(T) + \Omega(\mu(T))). \tag{3.17}$$

Equation (3.17) for the dynamics of the slow flow ca formally be derived within the so-called *two-timing approach* [39], based on introducing a general multiscale Ansatz of the form:

$$\varphi = \bar{\varphi}(t, \varepsilon t) + \varepsilon \hat{\varphi}(t, \varepsilon t),$$

$$\mu = \bar{\mu}(t, \varepsilon t) + \varepsilon \hat{\mu}(t, \varepsilon t). \tag{3.18}$$

By substituting (3.18) into (3.9), we obtain up to the terms of the order ε

$$\partial_1\bar{\varphi} + \varepsilon\partial_2\bar{\varphi} + \varepsilon\partial_1\hat{\varphi} = I_0 - \sin\left(\bar{\varphi} + \varepsilon\hat{\varphi}\right) + \bar{\mu} + \varepsilon\hat{\mu},$$

$$\partial_1\bar{\mu} + \varepsilon\partial_2\bar{\mu} + \varepsilon\partial_1\hat{\mu} = \varepsilon\left(-\bar{\mu} - \varepsilon\hat{\mu} + \eta\left(1 - \sin\left(\bar{\varphi} + \varepsilon\hat{\varphi}\right)\right)\right),$$

where the subscripts 1 and 2 refer to partial derivatives with respect to t and εt, respectively.

The coefficients of each power of ε must vanish separately. Collecting the terms of order $\mathcal{O}(1)$ yields:

$$\partial_1\bar{\varphi} = I_0 - \sin\bar{\varphi} + \bar{\mu}, \tag{3.19}$$

$$\partial_1\bar{\mu} = 0. \tag{3.20}$$

The equation (3.20) implies that $\bar{\mu} = \bar{\mu}(\varepsilon t)$ depends only on the slow time and acts as a parameter in (3.19). For $\bar{\mu} > 1 - I_0$, equation (3.19) has the oscillating solution $\bar{\varphi} = \varphi_{\bar{\mu}}(t)$ given by (3.15). Note that the parameters of this solution can depend on the slow time.

In the next step, we consider the terms of order ε:

$$\partial_2\bar{\varphi} + \partial_1\hat{\varphi} = -\hat{\varphi}\cos\bar{\varphi} + \hat{\mu},$$

$$\partial_2\bar{\mu} + \partial_1\hat{\mu} = -\bar{\mu} + \eta\left(1 - \sin\bar{\varphi}\right), \tag{3.21}$$

whereby the second equation of (3.21) can be rewritten as

$$\partial_2\bar{\mu} + \bar{\mu} = -\partial_1\hat{\mu} + \eta\left(1 - \sin\bar{\varphi}\right), \tag{3.22}$$

where the left-hand side depends only on the slow time. Hence, the solvability condition for (3.22) is that its right-hand side is independent on the fast time t, i.e.

$$-\partial_1\hat{\mu} + \eta\left(1 - \sin\bar{\varphi}\right) = u(T) \tag{3.23}$$

with some function $u(T)$, where $T = \varepsilon t$ is the slow time. By integrating (3.23) with respect to the fast time, we obtain

$$\hat{\mu}(t) = \hat{\mu}(0) + \eta\left(t - \int_0^t \sin\bar{\varphi}dt\right) - tu(T) \tag{3.24}$$

The integral in (3.24) can be computed using the intergal form of (3.19), namely:

$$\int_0^t \sin\bar{\varphi}dt = tI_0 + t\bar{\mu} - \bar{\varphi}(t) + \bar{\varphi}(0),$$

so that

$$\hat{\mu}(t) = \hat{\mu}(0) + t\left[\eta\left(1 - I_0 - \bar{\mu} + \frac{\bar{\varphi}(t) - \bar{\varphi}(0)}{t}\right) - u(T)\right].$$

Taking into account that

$$\frac{\bar{\varphi}(t) - \bar{\varphi}(0)}{t} = \Omega(\bar{\mu}) + \mathcal{O}\left(\frac{1}{t}\right),$$

we obtain the expression for $\hat{\mu}$:

$$\hat{\mu}(t) = \hat{\mu}(0) + t\left[\eta\left(1 - I_0 - \bar{\mu} + \Omega(\bar{\mu})\right) - u(T)\right] + \mathcal{O}(1),$$
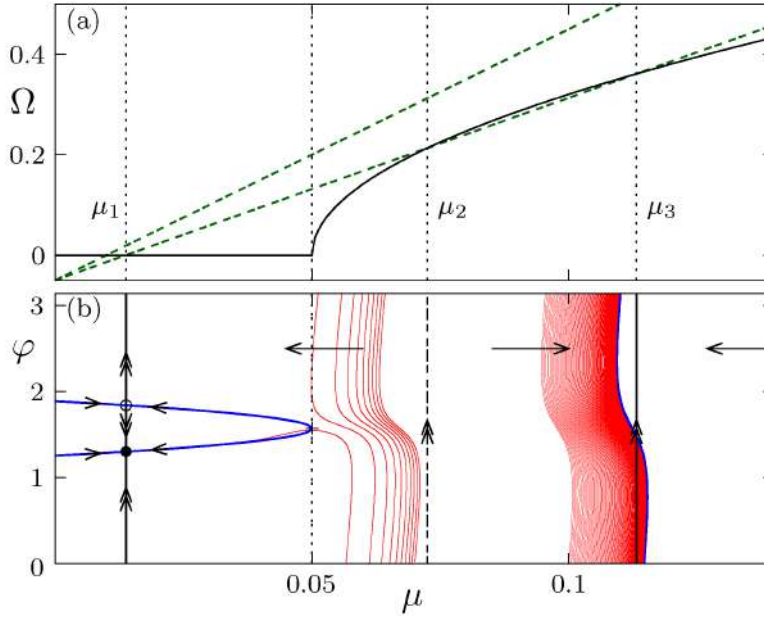
Figure 3.9: (a) Graphical solution of the fixed point equation (3.26): $\Omega(\mu)$ according to (3.25) (black solid line) and the right-hand side of (3.26) for two different choices of η (green dashed lines). Depending on η, the equation may have from one to three fixed points. (b) Scheme of the slow-fast dynamics of system (3.9) with parameters $I_0 = 0.95$ and $\eta = 0.38$ and the numerical sample trajectories for $\varepsilon = 0.005$ (red). For $\mu < 1 - I_0$, the trajectories are attracted to the stable branch of the slow manifold (blue curve) and subsequently slowly drift toward the stable fixed point $(\varphi_+(\mu_1), \mu_1)$ (black dot). For $\mu > 1 - I_0$, the sample trajectories show fast oscillations in φ with a slow average drift in μ in the direction indicated by the arrows.

where the linearly growing term must vanish for $\hat{\mu}(t)$ to be bounded. By setting this secular term to zero (even without computing explicitly $\hat{\mu}$), we have

$$u(T) = \eta \left(1 - I_0 - \bar{\mu} + \Omega(\bar{\mu}) \right).$$

Therefore, taking into account (3.22) and (3.23), the equation for the leading order approximation of the slow variable reads

$$\partial_2 \bar{\mu} + \bar{\mu} = \eta \left(1 - I_0 - \bar{\mu} + \Omega(\bar{\mu}) \right).$$

Since $\bar{\mu}$ is a function of the slow time only, we have $\partial_2 \bar{\mu} = \bar{\mu}'$, finally arriving at the equation for the slow dynamics given by (3.17),

$$\mu'(T) = -\mu(T) + \eta(1 - I_0 - \mu(T) + \Omega(\mu(T))).$$

3.2.2.3 Combined dynamics of the slow variable

Having obtained the dynamics of the slow variable for both $\mu < 1 - I_0$ and $\mu > 1 - I_0$ as given by equations (3.14) and (3.17), respectively, let us now combine these results into a single equation of the form (3.17) by extending the definition of the frequency $\Omega(\mu)$ to

$$\Omega(\mu) = \begin{cases} 0, & \mu < 1 - I_0 \\ \sqrt{(I_0 + \mu)^2 - 1}, & \mu > 1 - I_0 \end{cases}. \tag{3.25}$$

Since the slow dynamics is described by the scalar ordinary differential equation on the real line, the only possible attractors are fixed points, which are given by the zeros of the right-hand side of (3.17):

$$\Omega(\mu) = \frac{\eta+1}{\eta}\mu + I_0 - 1 \tag{3.26}$$

Geometrically, the fixed points correspond to the intersection points of the frequency profile $\Omega(\mu)$ and the line $\frac{\eta+1}{\eta}\mu + I_0 - 1$, as shown in Fig. 3.9(a). In particular, one fixed point always exists for $\Omega(\mu_1) = 0$, namely,

$$\mu_1 = \frac{\eta(1-I_0)}{1+\eta} < 1 - I_0, \tag{3.27}$$

corresponding to a pair of equilibria on the critical manifold (3.11). Since μ_1 is stable for the slow dynamics, the point $(\varphi_+(\mu_1), \mu_1)$ is also a stable equilibrium for the original system (3.9) with small ε. The other two fixed points of the slow equation

$$\mu_{2,3} = \frac{\eta\left(1+\eta - I_0 \mp \sqrt{(\eta+I_0)^2 - 1 - 2\eta}\right)}{1+2\eta}$$

with $\Omega(\mu_{2,3}) > 0$ appear in a saddle-node bifurcation at

$$\eta_{\mathrm{sn}} = 1 - I_0 + \sqrt{2(1-I_0)}, \tag{3.28}$$

and correspond to a pair of periodic orbits of the layer equation (3.10).

The results of our slow-fast analysis are schematically shown in Fig. 3.9(b) for $I_0 = 0.95$ and $\eta = 0.38$. The chosen parameter values admit two stable regimes, namely, the *fixed point* $(\varphi_+(\mu_1), \mu_1)$ and *fast oscillations* for which $\langle \mu(t) \rangle_t \approx \mu_3$ holds.

Finally, Fig. (3.10) presents the bifurcation diagram for the fixed points of the slow dynamics with respect to the feedback strength η. One observes that one branch of stable fixed points corresponding to the steady state always exists, while two stable fixed points corresponding to fast oscillations appear when $\eta > \eta_{\mathrm{sn}}$.

3.2.3 Slow-fast analysis of stochastic dynamics: stochastic averaging approach

This section contains details on how singular perturbation theory may be extended to the case where the fast flow dynamics is stochastically perturbed. In particular, to determine the dynamics of the slow flow, we will perform *stochastic averaging* over the stationary probability density of the fast variable obtained by solving the corresponding Fokker-Planck equation. This method allows us to numerically construct a bifurcation diagram in terms of D and η.

In analogy to the noise-free case, in the $\varepsilon \to 0$ limit we can consider the averaged fast dynamics

$$\langle \sin\varphi(t) \rangle_t = \lim_{t \to \infty} \frac{1}{t} \int_0^t \sin\varphi(t)\mathrm{d}t'$$
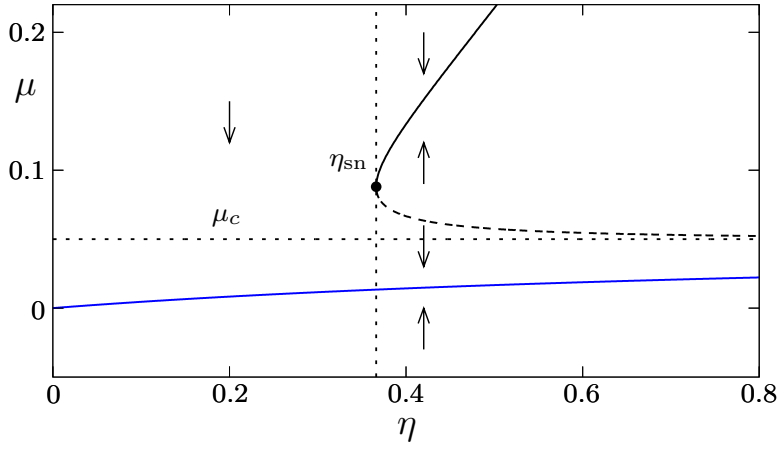
Figure 3.10: Fixed points of the slow dynamics (3.17) for varying feedback strength η. The values $\mu_{2,3}$ on the upper branch (black curve) correspond to periodic orbits of the layer equation (3.10), while μ_1 (blue curve) is the branch of fixed points (3.11). Solid and dashed lines indicate stable and unstable solutions, respectively. The direction of the motion in $\mu(T)$ is indicated by the arrows. The dotted lines indicate the onset of bistability for $\eta = \eta_{\text{sn}}$ (3.28) and the transition at $\mu_c = 1 - I_0$ from equilibria to periodic orbits.
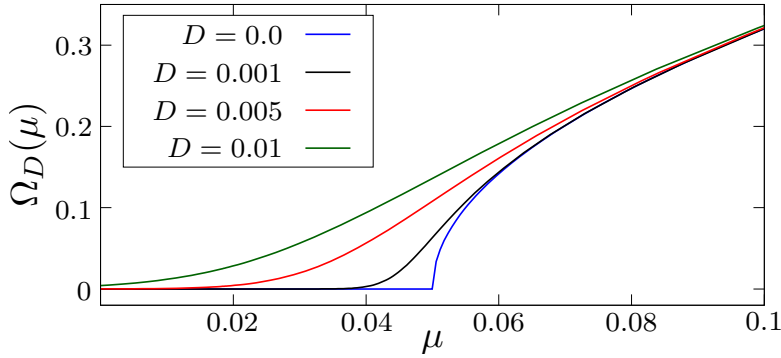
Figure 3.11: Average frequency of the fast dynamics (3.7) for $I_0 = 0.95$ given by (3.34)- (3.35) obtained by using numerical solutions of the stationary Fokker-Planck equation (3.31) in which μ acts as a time independent parameter.

for the stochastic layer dynamics

$$\dot{\varphi}(t) = I_0 + \mu - \sin \varphi(t) + \sqrt{D}\xi(t) \tag{3.29}$$

in order to approximate the slow flow (3.13) by

$$\mu'(T) = -\mu(T) + \eta(1 - \langle \sin \varphi(t) \rangle_t). \tag{3.30}$$

To calculate the average over stochastic fast dynamics, we use the *stationary probability density distribution* $\rho(\varphi; \mu, D)$, which is for fixed μ and noise intensity D given as a solution of the stationary Fokker-Planck equation

$$\frac{D}{2}\partial_{\varphi\varphi}\rho - \partial_\varphi \left[(I_0 + \mu - \sin \varphi)\rho \right] = 0, \tag{3.31}$$

complemented by the periodic boundary conditions

$$\rho(0) = \rho(2\pi) \tag{3.32}$$

as well as the normalization condition

$$\int_0^{2\pi} \rho(\varphi;\mu,D)\mathrm{d}\varphi = 1. \tag{3.33}$$

Then we can calculate the *stochastic average*

$$\langle \sin \varphi(t) \rangle_t = \int_0^{2\pi} \rho(\varphi;\mu,D)\sin \varphi \mathrm{d}\varphi \tag{3.34}$$

and obtain the mean frequency

$$\Omega_D(\mu) = I_0 + \mu - \langle \sin \varphi(t) \rangle_t, \tag{3.35}$$

which depends via (3.34) both on D and μ. Taking into account (3.30) and (3.35), the equation for the slow dynamics of $\mu(T)$ now reads

$$\mu'(T) = -\mu(T) + \eta(1 - I_0 - \mu + \Omega_D(\mu(T))), \tag{3.36}$$

i.e. it is of the same form as in the deterministic case (3.17). The corresponding fixed point equation for the stationary values of μ with respect to the slow dynamics is given by (3.26).

The stationary Fokker-Planck equation (3.31) can be solved directly by integral expressions. Integrating (3.31) once yields

$$\frac{D}{2}\partial_\varphi \rho - (I_0 + \mu - \sin \varphi)\rho = C \tag{3.37}$$

with the constant C to be determined. The solution of (3.37) with the normalization (3.33) and the boundary (3.32) conditions is given by

$$\rho(\varphi;\mu,D) = \frac{1}{g_\Lambda}\Lambda(\varphi), \text{where}$$
$$\Lambda(\varphi) = \int_0^{2\pi} \frac{\Psi(\varphi)}{\Psi(\varphi + \lambda)}d\lambda,$$
$$g_\Lambda = \int_0^{2\pi} \Lambda(\varphi)d\varphi,$$
$$\Psi(\varphi) = \exp\left\{\frac{2}{D}\left[(I_0 + \mu)\varphi + \cos \varphi - 1\right]\right\}. \tag{3.38}$$

For small non-vanishing D, the numerical evaluation of the integrals is difficult, so we have solved (3.31) as a first-order ODE boundary value problem with the software AUTO [259], which provides numerical solutions to boundary value problems by collocation methods together with continuation tools for numerical bifurcation analysis.

The numerically obtained effective frequencies $\Omega_D(\mu)$ for different noise levels D are shown in Fig. 3.11. Solving the stationary Fokker-Planck equation (3.31) together with the fixed point equation for $\mu(T)$ (3.26) yields branches of stationary solutions $(\mu^*, \rho(\varphi;\mu^*,D))$ for fixed values of D and varying feedback strength η, as shown in Fig. 3.12(a). For small noise intensities, these branches are folded, indicating the coexistence of up to three stationary solutions, similar to the noise-free case. Alternatively, we can also fix η and obtain
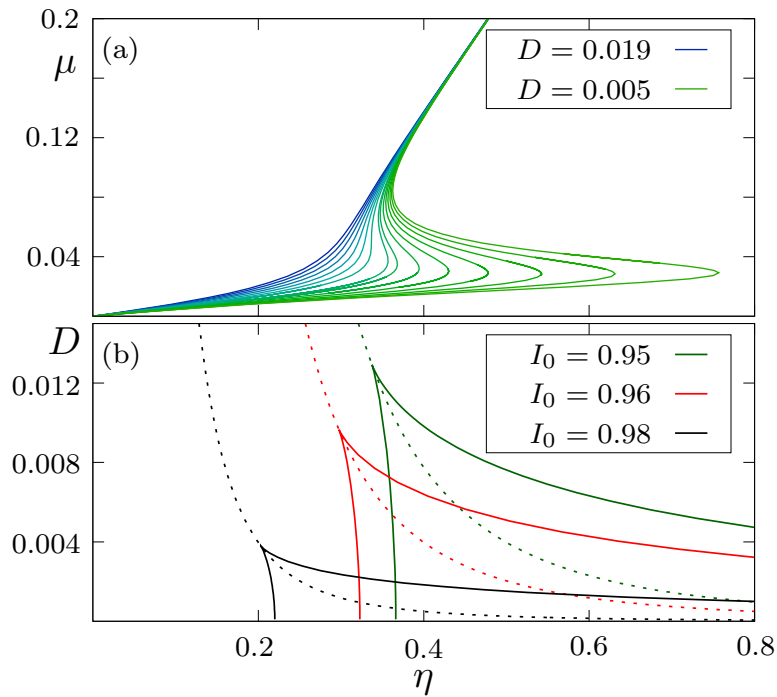
Figure 3.12: (a) Branches of fixed points $\mu^*(\eta)$ of the slow dynamics (3.36) for a set of noise values $D \in \{0.005, 0.006, \ldots, 0.019\}$ and $I_0 = 0.95$, calculated from (3.26) together with the stationary Fokker-Planck equation (3.31). (b) Two-dimensional bifurcation diagrams in terms of η and D for three different values of I_0 show the curves of fold bifurcations, which meet at the cusp point. The dashed curves indicate the case where $\mu = \mu_c = 1 - I_0$.
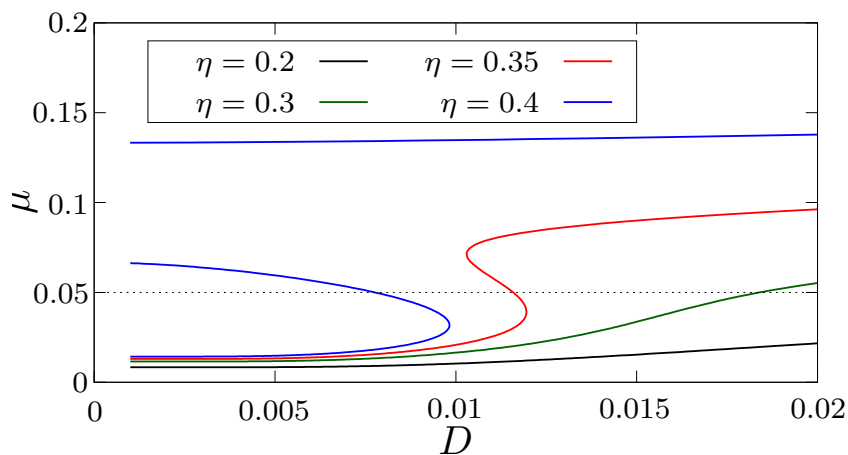

Figure 3.13: Branches of fixed points $\mu^*(D)$ of the slow dynamics (3.36) for a set of feedback strength values $\eta \in \{0.2, 0.3, 0.35, 0.4\}$ and fixed $I_0 = 0.95$, calculated from (3.26) together with the stationary Fokker-Planck equation (3.31).
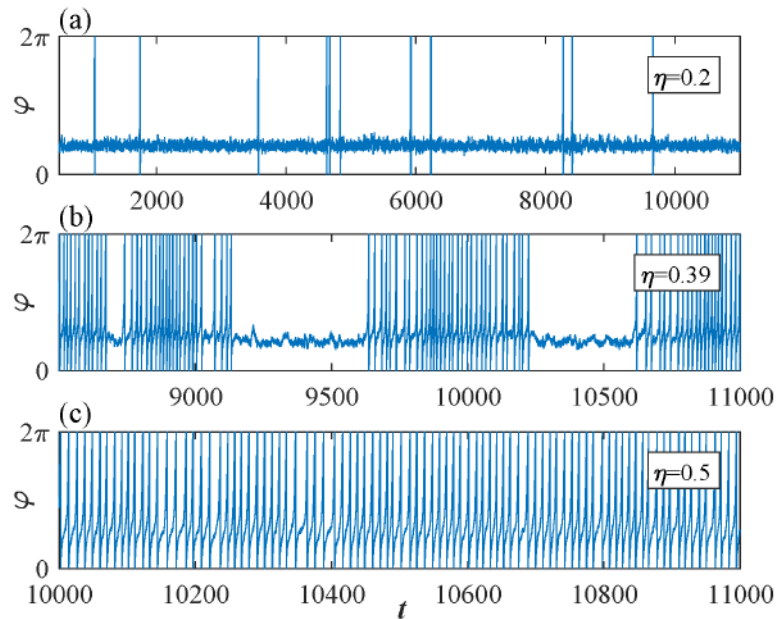
Figure 3.14: Different dynamical regimes in the stochastic excitable system subjected to a slowly adapting feedback (3.7)-(3.8) with $\varepsilon = 0.005$, $D = 0.008$, and different choices of the feedback strength η: noise-induced spiking (a), stochastic bursting (b), and noise-perturbed spiking (c).

branches for varying D, see Fig. 3.13. For small η they are monotonically increasing, while for larger η they are folded. For $\eta_{\mathrm{sn}} < \eta$ there are two separate branches, emanating from the three solutions of (3.26) at $D = 0$.

Continuation of the folds in the (η, D) parameter plane provides the curves which outline the boundaries of the bistability region. Fig. 3.12(b) shows that the two branches of folds meet at the cusp point $(\eta_{\mathrm{cu}}, D_{\mathrm{cu}})$. For $D \to 0$, one of the branches approaches the value $\eta = \eta_{\mathrm{sn}}$ calculated in (3.28), while the other one diverges to infinite values of η. When I_0 approaches the critical value $I_0 = 1$, the cusp point shifts to a smaller noise intensity D, decreasing the region of bistability. In terms of dynamical regimes, our study of stochastic dynamics reveals three characteristic (D, η) regions featuring noise-induced spiking, noise-perturbed spiking, and stochastic busting, see Figure 3.14.

For $D > 0$, all average frequencies satisfy $\Omega_D > 0$, so a clear distinction between the stationary and the oscillatory regime of the fast dynamics is no longer possible. However, one can compare the critical value of the deterministic fast dynamics

$$\mu_c = 1 - I_0$$

with the corresponding stationary value μ^* of the slow variable from (3.36) in order to distinguish between the regimes of noise-induced oscillations and oscillations originating from the deterministic component of the dynamics. If $\mu^* < \mu_c$, the oscillations are noise-induced and appear in the form of rare spikes, see Fig. 3.14(a), while for $\mu^* > \mu_c$ the deterministic oscillations are prevalent, see Fig. 3.14(c).

It turns out that the curves where the stationary values of μ satisfy the condition $\mu = \mu_c$,

shown by dashed lines in Fig. 3.12(b), pass exactly through the corresponding cusp point. Moreover, in the bistability region, these curves correspond to the unstable solutions given by the middle part of the S-shaped curves in Fig. 3.12(a). This leads us to conclude that varying the parameters across this line outside the bistability region results in a gradual transition between the regimes of noise-induced oscillations and the deterministic-driven oscillations. At the boundary of the bistability region, there is a hysteretic transition between the two stable regimes. Moreover, within the region of bistability, stochastic fluctuations may induce transitions between the two stable regimes when the timescale separation is finite.

3.2.4 Switching dynamics

In this section, we will examine how the interplay of the finite timescale separation and fluctuations gives rise to switching dynamics in the full system. In particular, we will consider how the region of bistability found in the singular limit $\varepsilon \to 0$ affects the dynamics of the full system for finite timescale separation $\varepsilon > 0$.

The two basic deterministic regimes of the fast dynamics – the excitable equilibrium and the oscillations – naturally induce two corresponding metastable states of the stochastic system with small $\varepsilon > 0$, namely

- **noise-induced spiking**, characterized by a Poissonian-like distribution of interspike intervals (ISIs), see Fig. 3.15(a); and

- **noisy oscillations**, involving a Gaussian-like distribution of the ISIs, centered around the deterministic oscillation period, see Fig. 3.15(b).

These states are found for sufficiently small or sufficiently large values of η, respectively, where only one corresponding branch of solutions of the deterministic system is available. Accordingly, the fluctuations of μ around its average value have no substantial impact on the dynamics. This is confirmed by in Fig. 3.15 which shows that the ISI distributions for the fast subsystem (3.30) complemented by the stationary solutions of (3.36) coincide with those of the full system (3.7)-(3.8). For sufficiently large noise levels above the cusp $D > D_{cu}$ and intermediate values of η, we observe a gradual transition between these two regimes. However, for smaller noise $D < D_{cu}$, in the limiting case $\varepsilon = 0$ the system lies in the region of bistability, cf. Fig. 3.12(b). In the case of finite scale separation, the two coexisting attractors from the singular limit, associated with a stable stationary and a periodic solution, become metastable states. Sufficiently strong noise may then induce large deviations from metastable states, giving rise to switching dynamics, illustrated by the time series in Fig. 3.14(b).

Based on the slow-fast analysis laid out above, the mechanism of noise-induced switching may be understood as follows. The noisy fluctuations of $\varphi(t)$ around its average distribution, given by the stationary Fokker-Planck equation (3.31), induce fluctuations of $\langle \sin \varphi(t) \rangle_t$, and hence also of μ, around the stationary average values we have calculated.
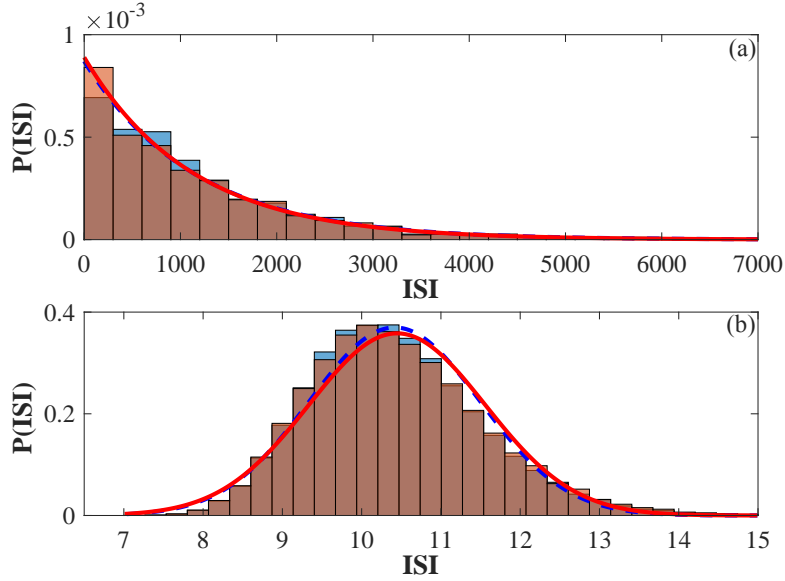
Figure 3.15: Histograms of interspike intervals (ISIs) of the phase variable for feedback strengths $\eta = 0.2$ (top panel) and $\eta = 0.5$ (bottom panel), obtained from numerical simulations of the full system (3.7)–(3.8) with $\varepsilon = 0.005$ (orange) and in the limit of infinite timescale separation (blue), using (3.29) with the stationary $\mu(T) \equiv \mu_D$ determined from the stationary Fokker-Planck equation (3.31). The solid red and dashed blue curves represent fits to (a) exponential decay and (b) Gaussian distributions for the ISI histograms of the full system and the limit of infinite scale separation, respectively.
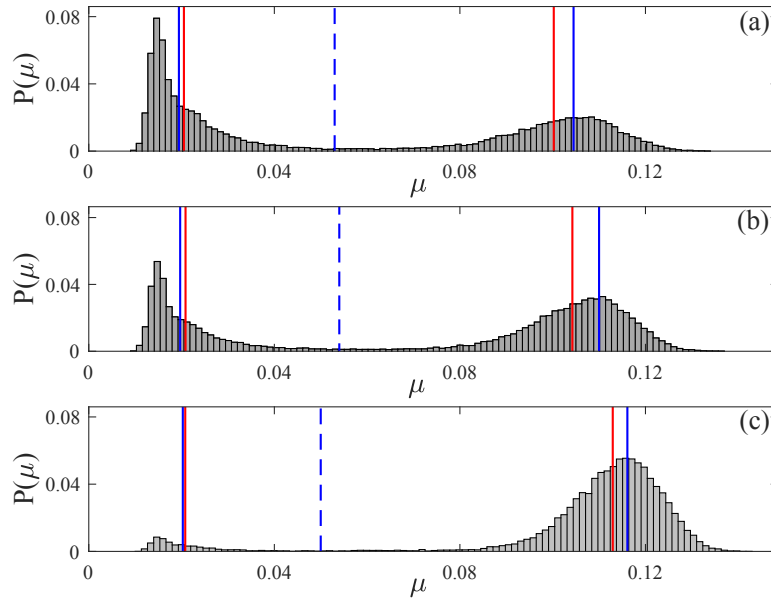
Figure 3.16: Stationary distributions $P(\mu)$, sampled from numerical simulations of the full system (3.7)–(3.8) with $\varepsilon = 0.005$. Parameters $\eta = 0.37$ in (a), $\eta = 0.373$ in (b) and $\eta = 0.38$ in (c) and fixed noise level $D = 0.009$ lie inside the bistability region from Fig. 3.12(b). Blue vertical lines indicate the fixed points of μ from the stationary Fokker-Planck equation (3.31) complemented with the fixed point equation (3.26) of the slow dynamics. Red vertical lines indicate the mean values of all μ in $P(\mu)$ below and of all μ above the unstable fixed point in the middle (dashed blue lines).
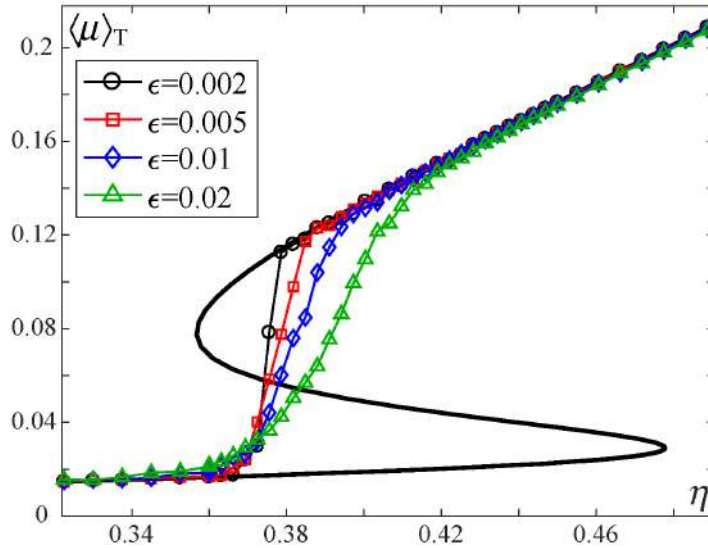
Figure 3.17: Long-time averages $\langle \mu \rangle_T$ obtained from numerical simulations of (3.7)–(3.8) with fixed noise intensity $D = 0.008$ and varying feedback strength η for different values of $\varepsilon \in \{0.002, 0.005, 0.01, 0.02\}$. The black curve represents the corresponding result for the infinite timescale separation, cf. Fig. 3.12(a).

For small ε, the corresponding distribution of μ consists of narrow peaks centered around the stable stationary values. However, with increasing ε, the nonlinear filtering induces a strong skewness of each peak in the distribution, and their overlapping indicates the possibility of noise-induced transitions between the two metastable states. Fig. 3.16 shows the distribution for $\varepsilon = 0.005$ and different values of the η within the bistability region. These transitions can be understood in analogy with the Eyring-Kramers process in a double-well potential [241, 256]: in the generic case of different energy levels corresponding to the two potential wells, transitions in one of the directions occur at a higher rate and the system prefers the state associated with the global minimum of the potential. Such **biased switching** behavior is very pronounced near the boundaries of the bistability region, where the transition to the state close to the fold is much less probable than the transition in the opposite direction.

To further investigate the properties of switching, we have numerically calculated the dependence of the time averages $\langle \mu(T) \rangle$ on the feedback strength η, shown in Fig. 3.17. For most values of η, the long time behavior is dominated by one of the two metastable states, indicating a biased switching process. Nevertheless, for intermediate values of η, the system exhibits **balanced switching** in which the transitions in both directions occur at an almost equal rate. An example of time series illustrating balanced switching is provided in Fig. 3.18. In the limit $\varepsilon \to 0$, the switching rate exponentially decreases to zero while the switching bias in the unbalanced regime increases. This results in the characteristic step-like behavior of the averages observed in Fig. 3.17 for smaller ε.

The noise-induced switching in Fig. 3.18 and Fig. 3.14(b) resembles the typical features of bursting dynamics found in neuronal systems. Here it emerges due to the interplay of slow adaptation and noise, whereby the bursts are triggered just by the stochastic fluctuations.
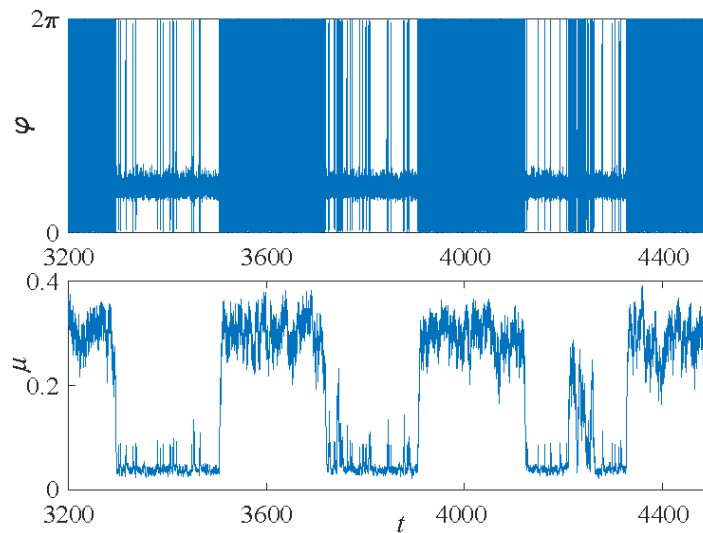
Figure 3.18: Time series $\varphi(t)$ (top panel) and $\mu(t)$ (bottom panel) illustrating the regime of balanced switching. The system parameters are $\eta = 0.38, D = 0.008, I_0 = 0.95, \varepsilon = 0.01$.

However, in the regime $\eta > \eta_{\mathrm{cu}}$, the system is also quite susceptible to external inputs, which could initiate the bursts even without any intrinsic noise.

─────────── 3.3 *Chapter summary and discussion* ───────────

In the present chapter, we have analyzed the switching dynamics in two paradigmatic stochastic multiscale systems with excitable fast dynamics.

First, we have analyzed a system consisting of locally excitable active rotators interacting by adaptive couplings, demonstrating that the interplay of plasticity and noise may give rise to slow stochastic fluctuations. In particular, we have identified two qualitatively different types of self-organized behavior depending on the adaptation rate. For slower adaptation, the switching dynamics features an alternation between two modes of noise-induced oscillations, associated with a preferred order of spiking between the two units. In this case, noise plays a twofold role: it gives rise to oscillations by perturbing the excitable local dynamics on a short timescale while causing alternation between the two oscillatory states on a long timescale. In the case of faster adaptation, the coupling elicits emergent oscillations in the deterministic system, which then exhibits complex multistable behavior involving two stationary and two oscillatory regimes. Under the influence of noise, the system undergoes switching between these four different metastable states, whose prevalence at a fixed noise level depends on the speed of adaptation. The deterministic attractors associated with metastable states are related by $\mathbb{Z}_2$ symmetry. Thus, a mismatch in excitability parameters would lead to symmetry-breaking, whereby a small mismatch would induce a bias in switching dynamics, whereas a larger mismatch, corresponding to the scenario involving one excitable and one oscillatory unit, would completely alter the observed dynamics.

Though the underlying phenomena are not found in the singular limit of infinite scale

separation, the fast-slow analysis we have applied still explains the qualitative features of both considered types of switching behavior. Studying the layer problem, and in particular, the vector field of the slow flow has enabled us to gain insight into the metastable states and the transitions between them. We have demonstrated that the coupling dynamics is always in a state of "criticality", being confined to the boundary between the stationary and oscillatory regimes of the fast flow.

Given that excitability, plasticity, and noise are inherent to neuronal systems, the obtained results can be interpreted in the context of neuroscience. It is well known that the backbone of neural networks is made up of binary and ternary neuron motifs, whereby a single structural motif typically supports multiple functional motifs, essentially characterized by a particular weight configuration and underlying direction of the information flow. With this in mind, the scenario of switching under slow adaptation may be important, because it implies that a binary motif can display slow alternation between two effectively unidirectional weight configurations, promoting opposite directions of information flow. For faster adaptation, we find multistability between unidirectional coupling and bidirectional coupling of moderate strength. Nonetheless, the underlying phase dynamics, if extended to networks, may be considered as a paradigm for UP-DOWN states, typical for cortical dynamics [180, 260].

Next, we have analyzed the multiscale dynamics of a stochastic excitable system with a slowly adapting nonlinear feedback, taken from a low pass filter of a function that provides positive feedback for oscillations by pushing the excitability parameter towards the oscillatory regime. Our paradigmatic model provides a novel perspective on how the interaction of a slowly adapting feedback and noise influences the dynamics of an excitable system, giving rise to three different dynamical regimes, including noise-induced spiking, noise-perturbed oscillations, and stochastic bursting. The latter is a novel form of emergent behavior in stochastic multiscale systems. A deep insight into the mechanism giving rise to stochastic bursting, as well as the means of controlling its statistical properties, has been gained by extending singular perturbation theory to the case of stochastic layer dynamics.

Employing the multiple timescale analysis in the limit of infinite timescale separation has allowed us to perform a numerical bifurcation analysis and determine the stability domains of different dynamical regimes. Within the domain where the limiting problem $\varepsilon = 0$ indicates bistability between an equilibrium and fast oscillations, the stochastic fluctuations at finite values of $\varepsilon > 0$ give rise to switching between the associated metastable states which accounts for the onset of stochastic bursting. However, our analysis shows that for sufficiently large noise intensity, this bistability vanishes, such that noise-induced and noise-perturbed oscillations can no longer be distinguished.

From the standpoint of multiscale systems theory, the deterministic part of the presented model provides one of the simplest examples involving a combination of a stable equilibrium regime and oscillations within the fast subsystem. A rigorous mathematical treatment of the dynamical transitions between the two regimes and corresponding reductions by the

standard adiabatic elimination method and the averaging technique is still missing. Also, our approach to the analysis of stochastic dynamics in multiscale systems based on introducing a stationary Fokker-Planck equation for the fast dynamics raises important questions concerning the limiting properties of the trajectories and the specific implications of the fluctuations. Nevertheless, we have only considered the case in which noise acts in the fast variable. An open problem is to study how noise in the slow variable influences the obtained results, where interesting new effects can be expected [261]. Since excitability, feedback, and noise are typical ingredients of neural systems, we believe that the application of our results to a specific neural model would be a next natural step, aiming to gain a deeper understanding of the onset of different dynamical regimes.

Chapter 4

Resonant Phenomena in Coupled Systems with Local Dynamics near the Bifurcation Threshold

Noise in excitable or bistable systems may induce two types of generic effects [67]. On one hand, it can modify the deterministic behavior by acting non-uniformly on different states of the system, thus amplifying or suppressing some of its features. For instance, noise may smoothen the threshold-like behavior, causing noise-induced linearization [262]. On the other hand, it may fundamentally change the deterministic dynamics by giving rise to qualitatively novel forms of behavior, typically based on crossing thresholds or separatrices or involving enhanced stability of deterministically unstable structures. In particular, the emergent dynamics may involve noise-induced oscillations and stochastic bursting [263, 264, 265], switching between metastable states [42, 181], or noise-enhanced stability of unstable and metastable states [266, 267, 268, 269, 270], to name but a few.

The constructive role of noise has been evinced in a wide range of real-world applications, from neural networks and chemical reactions to lasers and electronic circuits (see [67] and references therein). In neural systems, for instance, such phenomena are collectively referred to as *stochastic facilitation* [68, 69, 70]. The latter mainly refer to *resonant phenomena*, manifested as characteristic non-monotonous responses of the system to noise, whereby the most prominent examples include:

1. **coherence resonance** (CR) [149, 271, 272, 273, 274], where the regularity of *noise-induced oscillations* becomes maximal at an intermediate noise level;

2. **stochastic resonance** (SR) [70, 275], where the sensitivity of a system to a subthreshold periodic stimulation becomes maximal at a preferred noise level; and

3. **inverse stochastic resonance** (ISR) [94, 68, 172, 173, 174, 175, 176, 177, 178, 193], an inhibitory effect where the spiking frequency of *noise-perturbed oscillations* becomes minimal at a preferred noise level.

These effects are fundamentally related to the fact that noise induces an additional timescale compared to the deterministic system. For instance, in the case of ISR, noise introduces a timescale associated with the scale separation between the activation and relaxation processes.

In contrast to SR, the ISR effect concerns autonomous rather than periodically driven systems. ISR has recently been experimentally observed for cerebellar Purkinje cells [178], having explicitly demonstrated how the lifetimes of the spiking ("up") and the relative quiescence ("down") states [179, 42, 180] depend on the noise intensity. It has also been indicated that ISR plays a variety of important functional roles in neuronal systems, including the reduction of spiking frequency in the absence of neuromodulators, suppression of pathologically long short-term memories, triggering of on-off tonic spiking activity, and even optimization of information transfer along the signal propagation pathways [68, 174, 176, 178]. So far, the studies of ISR have described only one mechanism of the effect whereby a single neural oscillator exhibits bistable deterministic dynamics, featuring coexistence between a limit cycle and a stable equilibrium. Such bistability is typical for Type II neurons below the subcritical Hopf bifurcation, e.g. classical Hodgkin-Huxley and Morris-Lecar models [68, 173, 174, 175]. Influenced by noise, the deterministic attractors turn into metastable states between which the system then switches. The associated switching rates become strongly asymmetric at an intermediate noise level, favoring the quasi-stationary state rather than spiking activity. This is reflected in the characteristic non-monotone dependence of the spiking frequency on noise, a hallmark of ISR.

The issues unresolved prior to our research concern the mechanisms and robustness of the ISR effect. Is it dependent on the type of neuronal excitability? Can there be more than one mechanism of ISR? How does the effect depend on the form of couplings, e. g. can it be robust for adaptively changing couplings, typical for neuronal systems? Can the effect be observed in coupled excitable systems, in which noise influences *emergent* oscillations?

Having a longer history than ISR, both in terms of theoretical studies and experimental observations, CR has been explored in much more detail [108, 159, 160, 161, 162, 163, 164, 165, 166, 167, 168, 169, 170]. CR concerns noise-induced oscillations in (coupled) excitable or bistable systems. The resonant effect occurs when the noise intensity is simultaneously large enough to ensure a short activation time (escape from the vicinity of the stable equilibrium) and small enough to maintain the deterministic nature of the relaxation process (return to the fixed point), i. e. when the noise-dependent variabilities of the activation and relaxation processes are balanced in a certain way. A particularly relevant open issue concerns the mechanisms of enhancing (or in general, efficient *control* of) CR, whereby recent research has considered different mechanisms of control in networks of coupled oscillators, including time-delayed feedback [276, 277, 278, 279, 280, 281, 282], network topology [283, 284], and spatial heterogeneity of bifurcation parameters [285]. What we demonstrate is a novel efficient method of control of CR based on introducing a *slowly* adapting feedback to an excitable system, exploiting the multiscale dynamics to selectively enhance or suppress the

noise-induced spiking.

This chapter is devoted to understanding the characteristic non-monotonous response to noise arising in systems near a bifurcation between stationary and oscillatory states. In the light of the aforementioned open questions, the particular two problems that we will consider include

1. **generic scenarios for inverse stochastic resonance**; and

2. the **control of coherence resonance** by a slowly adapting feedback.

Our studies will be conducted on the two simplified, yet paradigmatic models from chapter 3 that combine the three typical ingredients of neuronal dynamics – excitability, noise and coupling plasticity – as well as an additional neuronal model, namely:

A. **two identical adaptively coupled stochastic active rotators** [181, 193, 254]; and

B. **a stochastic excitable active rotator with a slowly adapting (low-pass filtered) feedback**.

As far as problem (1) is concerned, we have investigated model *A* in both the excitable and the oscillatory regime. Within these studies, we have discovered two different generic scenarios accounting for the onset of ISR: one based on *biased switching*, and the other on the *noise-enhanced stability* of a deterministically unstable fixed point [266, 267, 268, 269, 270]. The former occurs due to noise-induced crossing over the separatrix between the stationary and oscillatory states, whereas the latter takes place due to "tunneling" through the bifurcation. We have confirmed that these two mechanisms can account for the onset of ISR in the classical neuronal model *B*, demonstrating the generality of our results.

Regarding problem (2), our research has shown that a slowly adapting feedback is capable of efficiently enhancing or suppressing CR, whereby the mechanism of control is not a simple additive effect where the system is effectively pushed towards or away from the bifurcation threshold.

The present chapter is organized as follows. Section 4.1 is devoted to ISR due to biased switching, arising in the system of two coupled rotators with excitable local dynamics. In particular, section 4.1.1 contains the details of the model and numerical bifurcation analysis of its deterministic dynamics, already addressed in section 3.1 of the previous chapter, while section 4.1.2 concerns our numerical results on ISR, where we quantify the effect in terms of the average frequency, corresponding stationary distributions, transition probabilities, and several other quantities. Then, 4.1.3 presents a slow-fast approach to understanding the role of plasticity in the resonant effect. Moreover, section 4.2 is dedicated to ISR due to noise-induced trapping in the vicinity of a deterministically unstable fixed point, arising in the system of two coupled active rotators with oscillatory local dynamics. Section 4.2.1 provides an overview of the model and its deterministic dynamics, section 4.2.2 concerns slow-fast analysis of the system, whereas section 4.2.3 refers to our numerical results on ISR. Furthermore, in section 4.3 we demonstrate that a single neuron model may display two

different scenarios for ISR, depending on the particular parameter values. Finally, section 4.4 concerns the control of CR by nonlinear adaptive feedback, whereby section 4.4.1 presents the model and its dynamics (from section 3.1 of the previous chapter), whereas section 4.4.2 shows how CR can be enhanced or suppressed by our scheme. In the concluding section 4.5, we overview the results and discuss their relevance.

───────────────── 4.1 *ISR due to biased switching* ─────────────────

In this section, we treat the problem of conditions giving rise to ISR in coupled excitable systems, where noise influences the emergent oscillations. Considering the example of emergent oscillations in two adaptively coupled active rotators with excitable local dynamics, we demonstrate a novel generic scenario for ISR in a multi-timescale system. The impact of plasticity is shown to be twofold. First, at the level of multiscale dynamics, one finds a range of intermediate adaptivity rates that give rise to the multistability of limit cycle attractors and stable equilibria, a condition necessary for the onset of the effect. Second, by applying slow-fast analysis, we show that the plasticity also plays a subtle facilitatory role by guiding the dynamics of the fast flow to parameter domains where its stable equilibria become foci rather than nodes, which effectively enhances the influence of noise. The described scenario persists for different plasticity rules, underlying its robustness in the light of potential applications to neuroscience and other types of cell dynamics. The following analysis strongly relies on our results on the slow stochastic fluctuations exhibited by this system presented in section 3.1 of the previous chapter.

4.1.1 Model and deterministic dynamics of the full system

As in section 2.1 of Chapter 2 and section 3.1 of Chapter 3, the considered model consists of two identical stochastic active rotators interacting by adaptive couplings [181, 182, 183, 184]

$$
\begin{aligned}
\dot{\varphi}_1 &= I_0 - \sin \varphi_1 + \kappa_1 \sin (\varphi_2 - \varphi_1) + \sqrt{D}\xi_1(t) \\
\dot{\varphi}_2 &= I_0 - \sin \varphi_2 + \kappa_2 \sin (\varphi_1 - \varphi_2) + \sqrt{D}\xi_2(t) \\
\dot{\kappa}_1 &= \varepsilon(-\kappa_1 + \sin(\varphi_2 - \varphi_1 + \beta)) \\
\dot{\kappa}_2 &= \varepsilon(-\kappa_2 + \sin(\varphi_1 - \varphi_2 + \beta)),
\end{aligned}
\tag{4.1}
$$

where the phases $\{\varphi_1, \varphi_2\} \in S^1$, while the couplings $\{\kappa_1, \kappa_2\} \in \mathbb{R}$. The uncoupled units undergo a SNIPER bifurcation at $I_0 = 1$, separating the excitable ($I_0 < 1$) and oscillatory ($I_0 > 1$) regimes. In the present section, we will keep $I_0 = 0.95$ fixed. The small parameter $0 < \varepsilon \ll 1$ defines the scale separation between the fast (phase) dynamics and the slow (adaptation) dynamics. Recall that due to $\mathbb{Z}_2$ symmetry of the noiseless version of (4.1), attractors always appear in pairs characterized by the same stability features. The fast variables are influenced by independent white noise of variance D such that $\xi_i(t)\xi_j(t') = \delta_{ij}\delta(t - t')$ for $i, j \in \{1, 2\}$, which embodies the action of synaptic noise in neuronal systems

[69]. The parameter β controls the modality of the plasticity rule, whereby we will once again focus on the β interval interpolating between the two limiting cases corresponding to the Hebbian learning rule ($\beta = 3\pi/2$) [287] and an STDP-like plasticity rule ($\beta = \pi$) [84, 85, 86, 182, 206, 207, 288, 289].

Recall from section 2.1.2 that depending on β, the system may have two, four or six fixed points, and that our analysis concerns the interval $\beta \in (3.298, 4.495)$, where the system has two stable fixed points lying off the synchronization manifold $\varphi_1 = \varphi_2$. These fixed points are excitable foci, born in a supercritical symmetry-breaking pitchfork bifurcation at $\beta = 3.298$ and annihilated in two symmetry-related inverse fold bifurcations at $\beta = 4.495$. In the present section, we shall mainly refer to the case $\beta = 4.2$, for which the two stable foci of (4.1) with $D = 0$ are given by

$$EQ1 \equiv (\varphi_1^*, \varphi_2^*, \kappa_1^*, \kappa_2^*) = (1.177, 0.175, 0.032, -0.92),$$
$$EQ2 \equiv (\varphi_1^*, \varphi_2^*, \kappa_1^*, \kappa_2^*) = (0.175, 1.177, -0.92, 0.032).$$

Let us now provide a brief reminder about the results on stable stationary states from section 2.1.2 and explain the onset of emergent oscillations in detail.

4.1.1.1 The onset of emergent oscillations

The onset of emergent oscillations for the deterministic version of (4.1) depends on the interplay of the plasticity rule, controlled by β, and the adaptation rate, characterized by ε. Due to the invariance of the system to exchange symmetry, the periodic solutions appear in pairs, sharing the same stability features. The maximal stability region of the periodic solutions is illustrated in Fig. 4.1(a), which shows the variation of the κ_1 variable, $\sigma_{\kappa_1} = \max(\kappa_1(t)) - \min(\kappa_1(t))$, in the (β, ε) parameter plane. This was obtained by numerical continuation starting from a stable periodic solution, such that the initial conditions for an incremented parameter value are given by the final state obtained for the previous iteration step. The scan reveals that for a given β, there exists an interval $\varepsilon \in (\varepsilon_{min}, \varepsilon_{max})$ of intermediate scale separation ratios supporting the oscillations, cf. the highlighted region in Fig. 4.1(b). At ε_{min}, two branches of stable periodic solutions emanate from fold of cycles bifurcations, denoted by FC in Fig. 4.1(b). Note that the associated threshold scale separation $\varepsilon_{min}(\beta)$ decreases with increasing β.

Recall from section 3.1.1.2 that the waveform of oscillations also changes as ε is increased under fixed β. In particular, for smaller ε, the waveforms corresponding to the two units are rather different. Nevertheless, the two branches of oscillatory solutions merge at $\varepsilon \approx 0.06$, where the system undergoes an inverse pitchfork bifurcation of limit cycles (PFC in Fig. 4.1(b)). This gives rise to anti-phase space-time symmetry $\varphi_1(t) = \varphi_2(t + T_{osc}/2), \kappa_1(t) = \kappa_2(t + T_{osc}/2)$ of the incipient stable limit cycle, with T_{osc} denoting the oscillation period.

Fig. 4.1(c) shows an example of the stability basins of the stationary and oscillatory solutions for $\varepsilon = 0.1$, obtained by fixing the initial values of the phases and varying the initial couplings within the range $\kappa_{i,ini} \in [-1, 1], i \in \{1, 2\}$. In the presence of noise, the coexist-
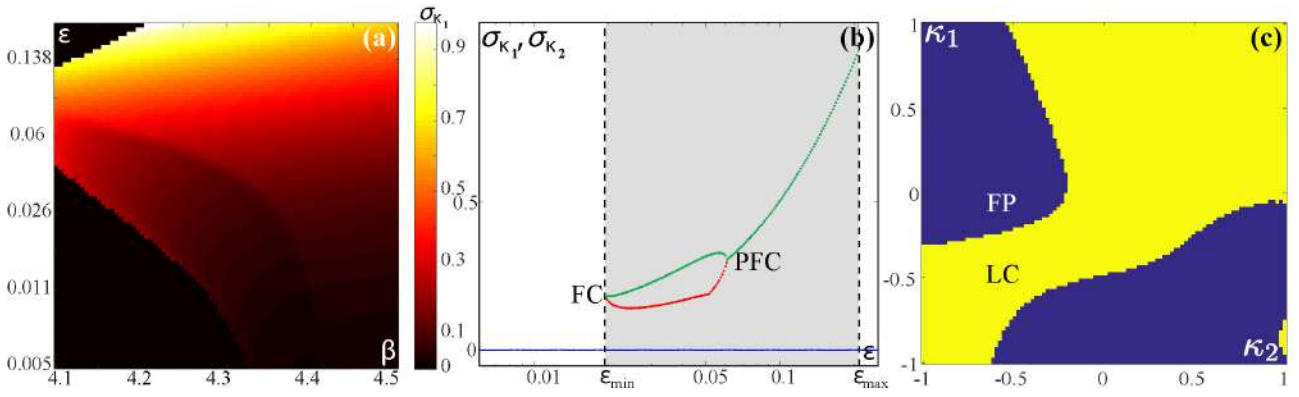
Figure 4.1: The onset of emergent oscillations in (4.1) for $I_0 = 0.95, D = 0$. (a) Variation $\sigma_{\kappa_1} = \max(\kappa_1(t)) - \min(\kappa_1(t))$ of the coupling weight κ_1 in the (β, ε) plane. (b) Dependencies $\sigma_{\kappa_i}(\varepsilon), i \in \{1, 2\}$ for the stationary (blue) and oscillatory solutions (red and green refer to the two units) for fixed $\beta = 4.2$. Shading indicates the interval $\varepsilon \in (\varepsilon_{min}, \varepsilon_{max})$ which supports the multistability of two symmetry-related stable equilibria and limit cycle(s), whereas FC and PFC denote the ε values where the fold of cycles and pitchfork of cycles occur. (c) Basins of stability of the stationary (FP, blue) and oscillatory solutions (LC, yellow) in the (κ_1, κ_2) plane, obtained by setting the initial phases to $(\varphi_1, \varphi_2) = (1.32, 0.58)$, with the remaining parameters fixed to $\beta = 4.2, \varepsilon = 0.1$.

ing attractors of the deterministic system give rise to metastable states, connected by noise-induced switching.

4.1.2 Numerical results on ISR

ISR occurs due to noise-mediated suppression of oscillations, whereby the frequency of noise-perturbed oscillations becomes minimal at a preferred noise level. For the considered motif of two adaptively coupled excitable active rotators (4.1), the characteristic non-monotone dependence on noise is generically found for intermediate adaptivity rates which support the multistability of stationary and oscillatory solutions. In the current section, we will quantify ISR in terms of the dependence of the average oscillation frequency on noise and analyze the corresponding stationary probability distributions, the noise dependence of the switching bias, as well as how the resonant effect changes with β and ε.

4.1.2.1 Characterization of ISR

A family of curves illustrating the dependence of the oscillation frequency on noise variance $\langle f \rangle(D)$ for several $\varepsilon \geq \varepsilon_{min}(\beta)$ values is shown in Fig. 4.2(a). The angular brackets $\langle \cdot \rangle$ refer to averaging over an ensemble of a 100 different stochastic realizations, having fixed a set of initial conditions within the basin of attraction of the limit cycle. Nonetheless, we have verified that qualitatively analogous results are obtained if for each realization of the stochastic process one randomly selects a new set of initial conditions from the same basin of attraction.
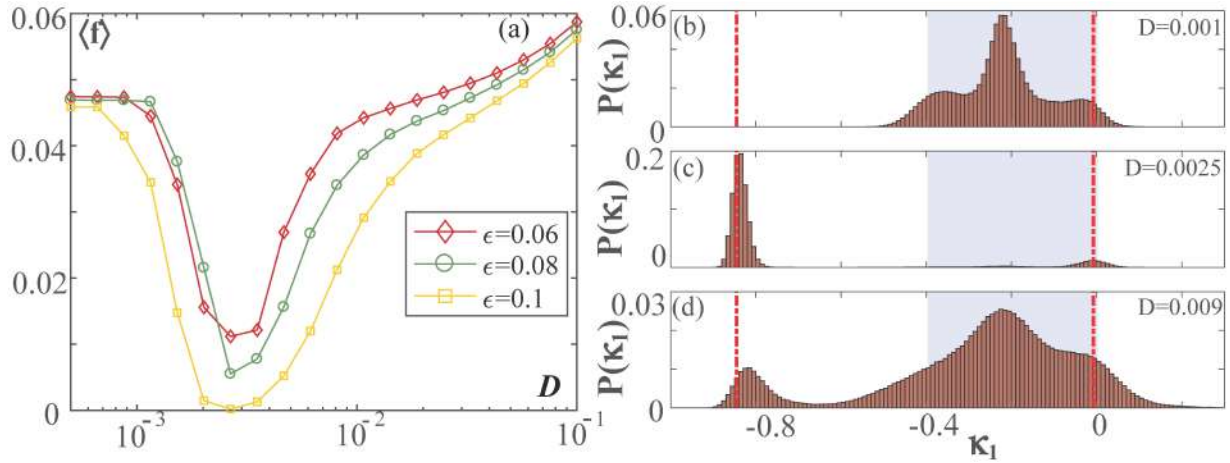
Figure 4.2: Inverse stochastic resonance in (4.1) with $I_0 = 0.95, \beta = 4.2$. (a) Dependencies of the mean oscillation frequency on noise $\langle f \rangle (D)$ for scale separation $\varepsilon \in \{0.06, 0.08, 0.01\}$. (b-d) show the stationary distributions $P(\kappa_1)$ for noise intensities below ($D = 0.001$), at ($D = 0.0025$), and above ($D = 0.009$) the resonant noise intensity for $\varepsilon = 0.1$. Dash-dotted red lines denote the κ_1 levels associated with the two stable equilibria, $\kappa_1^*(EQ1) = 0.032$ and $\kappa_1^*(EQ2) = -0.92$, while the blue shaded interval indicates the variation σ_{κ_1} of the unique stable periodic solution. For noise intensities near resonance, the system barely resides in the limit cycle metastable state.

In section 3.1.3.2, we have shown that noise-induced switching gives rise to bursting-like behavior. In particular, this occurs due to spiking being interrupted by quiescent episodes which correspond to the system residing in the vicinity of the quasi-stationary metastable states. These episodes are prevalent at noise levels around the minimum of $\langle f \rangle (D)$ from Fig. 4.2(a), essentially accounting for the appearance of inverse stochastic resonance in the system. For weaker noise $D \lesssim 10^{-3}$, the frequency of emergent oscillations remains close to the deterministic one, whereas for a much stronger noise, it increases above that of unperturbed oscillations. Moreover, the inhibitory effect of noise depends on the adaptivity rate, and is found to be more pronounced for faster adaptivity (cf. Fig. 3.5). Indeed, for smaller ε, $\varphi(t)$ series corresponding to the noise levels around the minimum of $\langle f \rangle (D)$ exhibit bursting-like behavior, whereas for larger ε, noise effectively quenches the oscillations, such that the minimal observed frequency approaches zero.

Let us now demonstrate how ISR is qualitatively reflected in the stationary distributions of the fast and the slow variables, considering their typical distributions below, at and above the resonant noise level. Using these distributions, which allow one to understand the features of the noise-induced switching process between the metastable states derived from coexisting attractors of the corresponding deterministic system, we will show that the mechanism of ISR is in fact based on biased switching between the oscillatory and quasi-stationary metastable states. Fig. 4.2(b)-(d) contains the stationary distributions $P(\kappa_1)$ for noise levels below, at and above the resonant level. For comparison with the noiseless system, we have indicated the weight levels associated with the two equilibria $\kappa_1^*(EQ1) = 0.032$ and $\kappa_1^*(EQ2) = -0.92$, as well as the variation σ_{κ_1} of the stable limit cycle. Note that the sta-
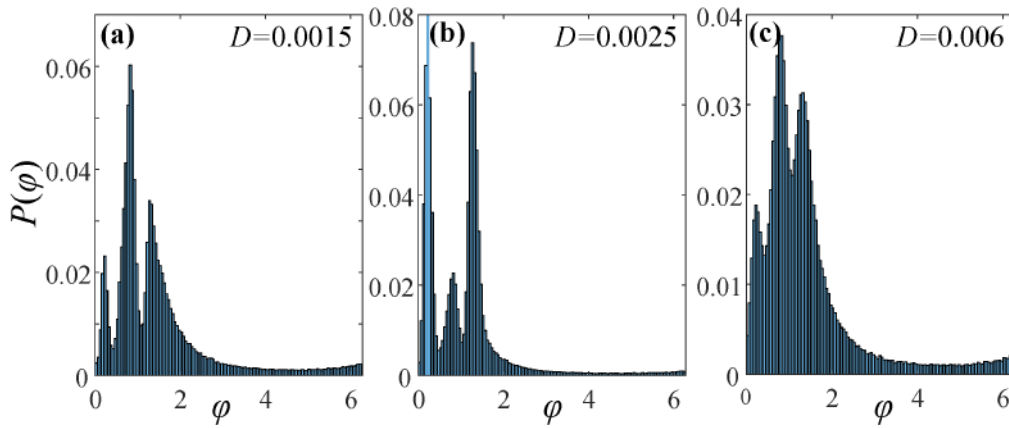
Figure 4.3: Stationary distribution $P(\varphi_1)$ for noise levels (a) below, (a) at, and (c) above the resonant value, with $I_0 = 0.95$, $\beta = 4.2$ and $\varepsilon = 0.06$. The middle peak, prevalent in (a) and (c), refers to the metastable state associated with the oscillatory mode of (4.1) for $D = 0$. The two lateral peaks, dominant in (b), correspond to quasi-stationary states derived from the stable equilibria.

ble periodic solution is unique for the considered timescale separation $\varepsilon = 0.1$ since the deterministic system lies above the pitchfork of cycles bifurcation, cf. PFC in Fig. 4.1(b). The stationary distribution $P(\kappa_1)$ at the resonant noise level expectedly shows a pronounced peak corresponding to one of the quasi-stationary states, while the distributions below and above the resonant noise level indicate a high occupancy of the oscillatory metastable state.

Fig. 4.3(a)-(c) shows the stationary distributions of one of the phase variables, $P(\varphi)$, for noise levels below, at and above the resonant value, with the remaining parameters set to $(\beta, \varepsilon) = (4.2, 0.06)$. The distribution $P(\varphi)$ is characterized by (i) two lateral peaks, corresponding to the two symmetry-related quasi-stationary states, and (ii) the area around the central peak, corresponding to the oscillatory mode. Expectedly, for small noise $D = 0.0015$, see Fig. 4.3(a), as well as very large noise $D = 0.006$, cf. Fig. 4.3(c), the central peak of $P(\varphi)$ is dominant. Nevertheless, the switching dynamics near the minimum of $\langle f \rangle(D)$ is fundamentally different. Indeed, the corresponding distribution $P(\varphi)$ for $D = 0.0025$ in Fig. 4.3(b) reveals that the system strongly prefers the quasi-stationary states to oscillations.

Note that the ISR effect is robust with respect to different modality rules. This is corroborated in Fig. 4.4, which illustrates how the average oscillation frequency changes with β and D for the fixed scale separation $\varepsilon = 0.09$. The nonlinear response to noise, conforming to a resonant effect with a minimum of oscillation frequency at an intermediate noise level, persists in a wide range of β, essentially interpolating between Hebbian-like and STDP-like adaptive dynamics.

4.1.2.2 Biased switching as a mechanism of ISR

To elucidate the mechanism behind ISR, we have calculated how the fraction of the total time spent in either of the oscillatory metastable states, T_{osc}/T_{tot}, changes with noise. Within our numerical experiments, the quasi-stationary and the oscillatory metastable states have
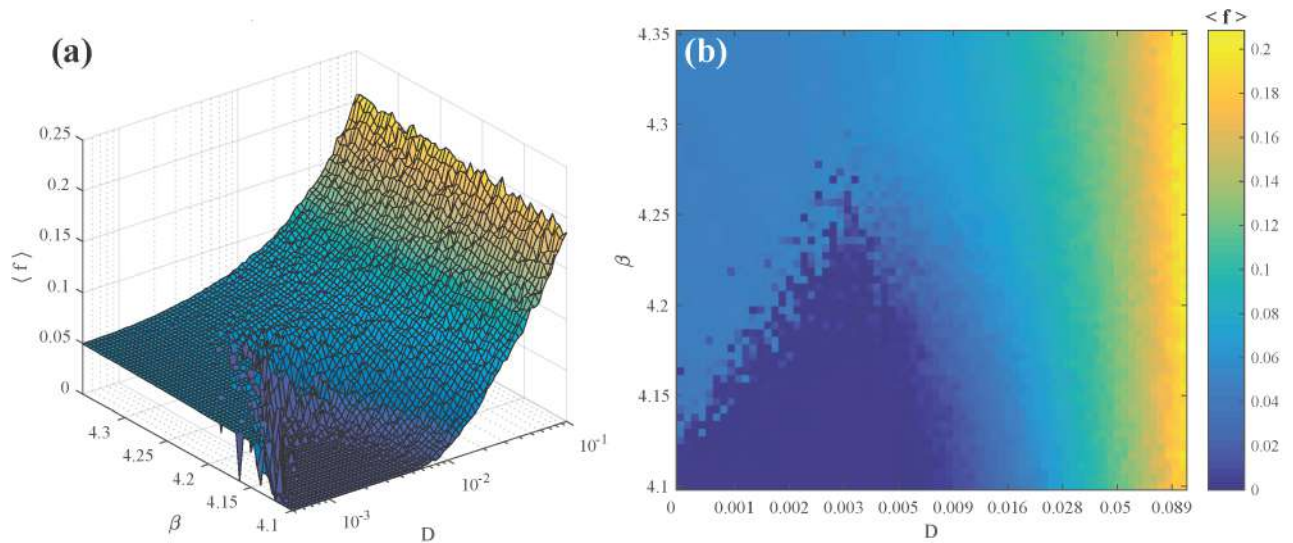
Figure 4.4: Mean spiking rate $\langle f \rangle$ as a function of β and D for fixed $\varepsilon = 0.09$, presented as (a) a 3D plot and (b) a heat map. The results corroborate the robustness of the effect with respect to different plasticity rules.
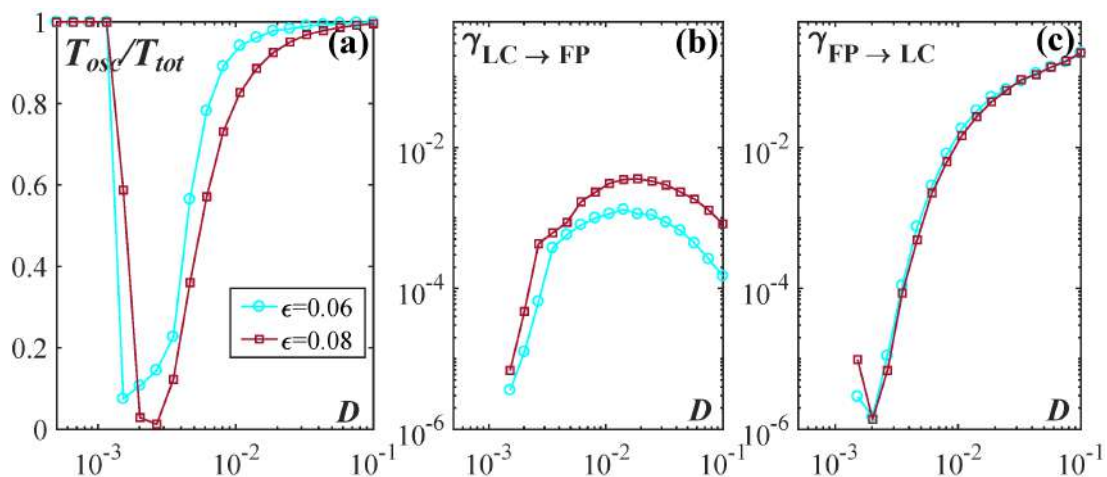
Figure 4.5: (a) Fraction of time spent in the oscillatory metastable state T_{osc}/T_{tot} as a function of noise for $\varepsilon \in \{0.06, 0.08\}$. (b) and (c) Numerically estimated transition rates from the oscillatory to the quasi-stationary metastable states, $\gamma_{LC \to FP}(D)$ and *vice versa*, $\gamma_{FP \to LC}(D)$. The remaining parameters are $I_0 = 0.95, \beta = 4.2$.

been distinguished by considering the corresponding coupling weight series. Specifically, as shown in Fig 3.7 (b), the difference $\Delta\kappa(t) = |\kappa_1(t) - \kappa_2(t)|$ is much larger for the quasi-stationary than for the oscillatory solutions. Thus, by setting the threshold to $\Delta\kappa_{thr} = 0.6$, we were able to identify the system's states and trace the associated transitions. Figure 4.5(a) indicates a non-monotone dependence of $T_{osc}/T_{tot}(D)$, implying that the switching process near the resonant noise level becomes strongly biased in favor of the quasi-stationary state, even more so for faster adaptivity. The biased switching process arises from the geometry of the phase space, whose structure is asymmetrical with respect to the separatrix between the coexisting attractors: the limit cycle lies much closer to the separatrix than the stationary states.

The nonlinear response to noise may be understood in terms of the competition between the transition processes from and to the limit cycle attractor. These processes are character-ized by the transition rates from the stability basin of the limit cycle attractor to that of the stationary states $\gamma_{LC\rightarrow FP}$ and *vice versa*, $\gamma_{FP\rightarrow LC}$. We have numerically estimated these quan-tities as the reciprocal values of the corresponding mean first-passage times [290]. Figures 4.5(b)-(c) corroborate that the dependencies $\gamma_{LC\rightarrow FP}(D)$ and $\gamma_{FP\rightarrow LC}(D)$ are qualitatively distinct: the former displays a maximum at the resonant noise level, whereas the latter just increases monotonously with noise. For small noise $D \lesssim 10^{-3}$, one observes virtually no switching to the quasi-stationary state, in accordance with the fact that the corresponding oscillation frequency is identical to the deterministic one. For increasing noise, the com-petition between the two processes is resolved such that for an intermediate (large) noise intensity, the impact of $\gamma_{LC\rightarrow FP}$ ($\gamma_{FP\rightarrow LC}$) becomes prevalent. The large values of $\gamma_{FP\rightarrow LC}$ found for quite strong noise $D \gtrsim 0.04$ reflect the fact that the system spends most of the time in the oscillatory metastable state, with only short excursions to the quasi-stationary state. Moreover, the fact that ISR is more pronounced for higher adaptivity rates is reflected in the curve $\gamma_{LC\rightarrow FP}(D)$ for $\varepsilon = 0.1$ lying substantially above that for $\varepsilon = 0.06$, as shown in Fig. 4.5(b). Large deviations from the oscillatory metastable state are quite rare.

4.1.2.3 Local stability of the limit cycle attractor: the impact of scale separation

To understand why the interplay of adaptivity rate and noise results in a stronger resonant effect for larger ε, we have investigated the susceptibility of the limit cycle attractor to exter-nal perturbation. The latter can be quantified by calculating the determinant of the Jacobian $det J = |\frac{\partial(\dot\varphi_1,\dot\varphi_2,\dot\kappa_1,\dot\kappa_2)}{\partial(\varphi_1,\varphi_2,\kappa_1,\kappa_2)}|$ for (4.1) with $D = 0$,

$$det J = \varepsilon^2 \cos(\kappa_1 - \kappa_2)(\kappa_1 \cos(\varphi_1 - 2\varphi_2) + \cos\varphi_1(\kappa_1 + 2\kappa_2 \cos(\varphi_1 - \varphi_2) + 2\cos\varphi_2)),$$

along the whole orbit of the limit cycle, whereby larger values indicate a more pronounced local instability.

Fig. 4.6 shows how the determinant of the Jacobian changes with the phase variable φ_1 for $\varepsilon = 0.06$ (blue line) and $\varepsilon = 0.1$ (orange line), respectively. For smaller ε, one may identify two particular points where the determinant of the Jacobian is the largest, i.e. where the
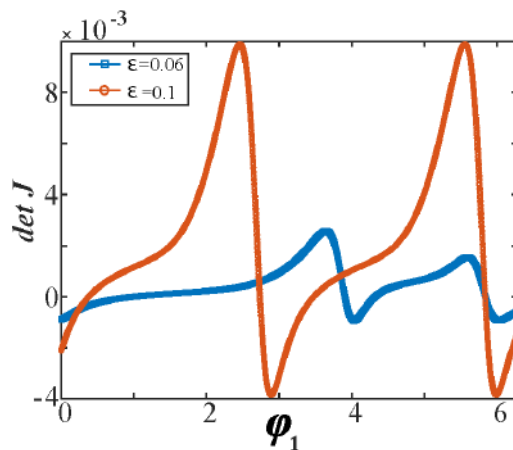
Figure 4.6: Determinant of the Jacobian calculated along the limit cycle orbit as a function of the phase variable for $\varepsilon \in \{0.06, 0.1\}$ with $I_0 = 0.95, \beta = 4.2$. This quantity indicates the sensitivity of certain sections of the orbit to external perturbation.

impact of external perturbation is felt the strongest. This implies that the perturbation is most likely to drive the system's trajectory away from the limit cycle attractor around these two sections of the orbit, which should lie closest to the boundary to the stability basins of the stationary states. Such a physical picture is maintained for larger ε, but one should stress that the sensitivity of limit cycle attractor to external perturbation substantially increases along the entire orbit, cf. Fig. 4.6. Translated to the stochastic system, this would imply that faster adaptivity enhances the impact of noise, contributing to a more pronounced ISR effect. This point will be addressed from another angle in the following subsection.

4.1.3 Facilitatory role of adaptivity in the resonant effect: slow-fast analysis

Though ISR is most pronounced for intermediate ε, it turns out that an additional subtlety in the mechanism of biased switching may be explained by employing the singular perturbation theory to the noiseless version of (4.1). In particular, by combining the critical manifold theory [47] and the averaging approach [255], we were able to explain the facilitatory role of plasticity in enhancing the resonant effect by showing that the adaptation drives the fast flow towards the parameter region where the stationary state is a focus rather than a node. It is well known that the response to noise in multi-timescale systems qualitatively depends on the character of stationary states. Indeed, using sample-paths approach and other advanced techniques, it has already been shown that such systems may exhibit fundamentally different scaling regimes with respect to the noise variance and the scale separation ratio [291, 292, 293]. Intuitively, one expects that the resonant effects are associated with the quasi-stationary states derived from foci rather than nodes [291], essentially because the local dynamics around the stationary state then involves an eigenfrequency.

Let us first briefly summarize the main results from section 3.1.2, concerning the layer and reduced problems for system (4.1) with $I_0 = 0.95, D = 0$. Within the layer problem, we

obtain the fast flow dynamics

$$\dot{\varphi}_1 = I_0 - \sin \varphi_1 + \kappa_1 \sin (\varphi_2 - \varphi_1)$$
$$\dot{\varphi}_2 = I_0 - \sin \varphi_2 + \kappa_2 \sin (\varphi_1 - \varphi_2), \qquad (4.2)$$

by treating the slow variables $\kappa_1, \kappa_2 \in [-1, 1]$ as additional system parameters. One may formally obtain (4.2) by setting $\varepsilon = 0$ in (4.1) with $D = 0$. Depending on κ_1 and κ_2, the fast flow dynamics is almost always monostable, exhibiting either a stable equilibrium or a limit cycle attractor, apart from a small region of bistability near the main diagonal where they coexist, as shown in Fig. 4.7(a). The maximal stability region of the oscillatory regime, encompassing both the domain where the oscillatory solution is monostable and where it coexists with a stable equilibrium, is indicated by the gray shading in Fig. 4.7(a). The latter has been determined by the method of numerical continuation, starting from a periodic solution. Note that each periodic solution above the main diagonal has a $\mathbb{Z}_2$ symmetry-related counterpart below the diagonal. The periodic solutions typically emanate from SNIPER bifurcations, which comprise two branches where either κ_1 or κ_2 are almost constant and close to zero.

By averaging over the different attractors of the fast flow dynamics, we have obtained multiple stable sheets of the slow flow [255]. The explicit procedure consists in determining the time average $\langle \varphi_2 - \varphi_1 \rangle_t = h(\kappa_1, \kappa_2)$ by iterating (4.2) for each fixed set (κ_1, κ_2) [181, 255], and then substituting these averages into the equations of the slow flow

$$\kappa_1' = [-\kappa_1 + \sin(h(\kappa_1, \kappa_2) + \beta)]$$
$$\kappa_2' = [-\kappa_2 + \sin(-h(\kappa_1, \kappa_2) + \beta)], \qquad (4.3)$$

where the prime refers to a derivative over the rescaled time variable $T := t/\varepsilon$. The arrows in Fig. 4.7(a) show the vector fields on the two stable sheets of the slow flow (4.3) associated with the stationary and the periodic attractors of the fast flow.

Fig. 4.7(b) shows the vector fields associated with each of the attractors (fixed point or limit cycle), presented within its respective (κ_1, κ_2) stability region. In the small region of the (κ_1, κ_2) plane supporting coexisting stable solutions of the fast flow, the corresponding vector field of the slow flow is consists of two overlapping sheets, since the value of the average $f(\kappa_1, \kappa_2)$ depends on the initial conditions.

Within the described slow-fast approach, the subtle influence of adaptivity on the mechanism behind the ISR may be explained as follows. Figure 4.7(b) shows a projection of a typical $(\kappa_1(t), \kappa_2(t))$ trajectory of the full system (4.1) corresponding to a switching episode between the metastable states associated with a limit cycle attractor and a stable equilibrium of the deterministic system, see the time traces in Fig. 4.7(c)-(d). One observes that for the oscillating regime, the coupling dynamics always remains close to the SNIPER bifurcation of the fast flow, cf. Fig. 4.7(a), which makes the oscillations quite susceptible to noise. Recall that the fast flow is typically monostable. Thus, switching events in the full system are associated with the fast flow undergoing the SNIPER bifurcation: either a direct one, leading
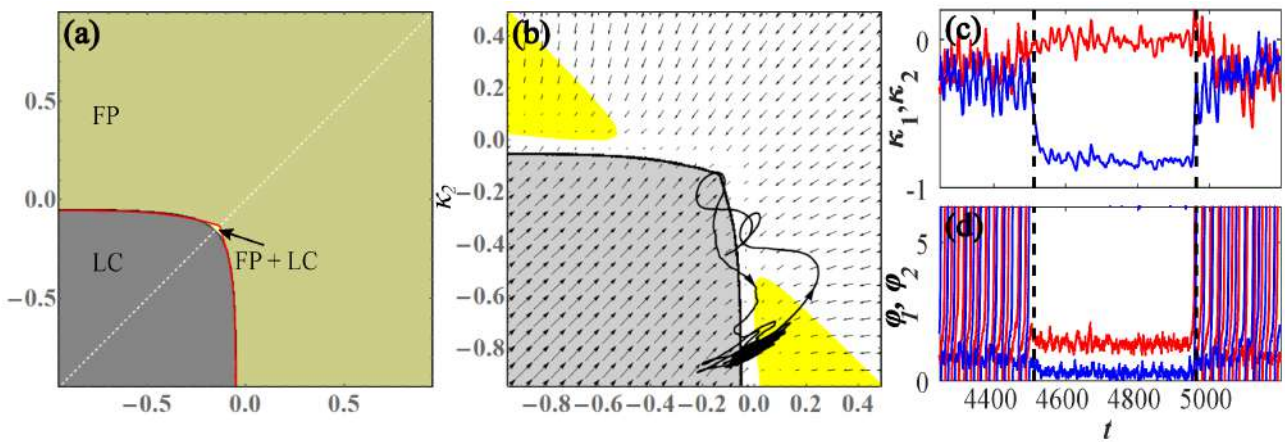
Figure 4.7: (a) Attractors of the fast flow (4.2) in terms of κ_1 and κ_2, now treated as system parameters. The fast flow is typically monostable, admitting either a stable fixed point (FP) or a stable limit cycle (LC), apart from a small region of bistability (FP+LC) around the main diagonal. (b) Vector field of the slow flow (4.3) determined by considering only the stable regimes of the fast flow for $\beta = 4.2$, $I_0 = 0.95$. Within the yellow-highlighted regions, stable fixed point of the fast flow is a focus rather than the node. The displayed orbit $(\kappa_1(t), \kappa_2(t))$ corresponds to a switching episode from the oscillatory state to the quasi-stationary state and back (evolution direction indicated by arrows). (c) and (d) show the time traces of phases and couplings during this switching episode.
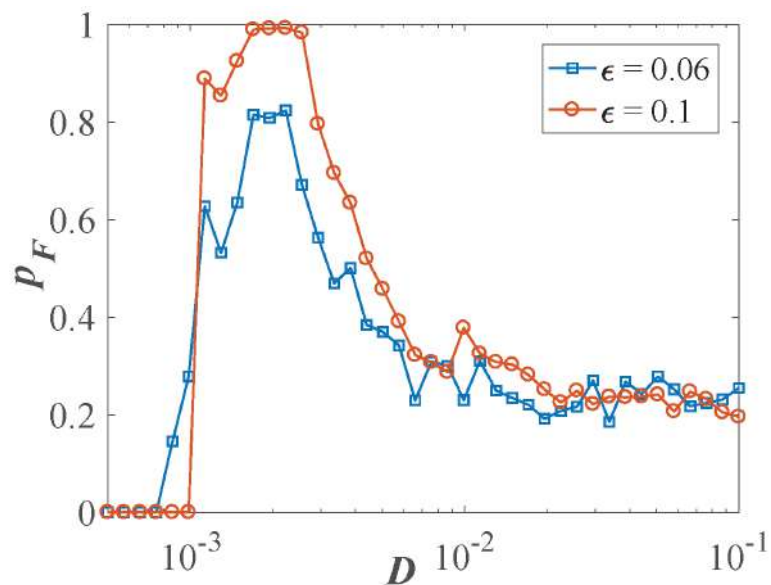

Figure 4.8: Conditional probability $p_F(D)$ for $\varepsilon = 0.06$ (blue squares) and $\varepsilon = 0.1$ (orange circles).

from the oscillatory to the stationary regime, or an inverse one, unfolding in the opposite direction.

For (κ_1, κ_2) values immediately after the SNIPER bifurcation toward the quiescent state, the stable equilibrium of the fast flow is a node. Nevertheless, for noise levels where ISR is most pronounced, we find that the coupling dynamics guides the system into the region where the equilibrium is a stable focus rather than a node, see the yellow highlighted region in Fig. 4.7(b). We have verified that this feature is a hallmark of the resonant effect by numerically calculating the conditional probability p_F that the events of crossing the SNIPER bifurcation are followed by the system's orbit visiting the (κ_1, κ_2) region where the stable equilibrium is a focus. The $p_F(D)$ dependencies for two characteristic ε values at fixed $\beta = 4.2$ plotted in Fig. 4.8 indeed show a maximum for the resonant noise levels, corresponding to the minima of the frequency dependencies in Fig. 4.2(a). From this we infer that the local dynamics near the focus causes a form of a *trapping* effect due to which the phase variables remain in the associated quasi-stationary states much longer than when the metastable states derive from the nodes of the fast flow. Small noise below the resonant values is insufficient to drive the system to the regions featuring focal equilibria, whereas for too strong noise, the stochastic fluctuations completely take over, washing out the quasi-stationary regime. The trapping effect is enhanced for the faster adaptivity rate, as evinced by the fact that the curve $p_F(D)$ for $\varepsilon = 0.1$ lies above the one for $\varepsilon = 0.06$, see Fig. 4.8.

4.2 *ISR due to noise-enhanced stabilization of an unstable fixed point*

By studying the paradigmatic example of two adaptively coupled stochastic active rotators with local dynamics in the oscillatory regime near the bifurcation threshold, we demonstrate a novel generic scenario for inverse stochastic resonance. In particular, the phenomenon arises due to a trapping effect associated with noise-enhanced stability of an unstable fixed point. To explain the details of the underlying mechanism, we perform a slow-fast analysis of the corresponding noiseless system, whereby we demonstrate that noise induces "tunneling" through the bifurcation threshold, temporarily stabilizing an unstable fixed point of the deterministic system.

4.2.1   Model and deterministic dynamics of the full system

In this section, we will consider the same model from the previous section (4.1), but with local dynamics in the *oscillatory* ($I_0 > 1$) rather than the excitable regime, keeping the parameter $I_0 = 1.05$ fixed near the bifurcation threshold. The plasticity parameter is set to $\beta = \pi$, such that the modality of the phase-dependent adaptivity rule resembles the spike-timing-dependent plasticity (STDP) in neuronal systems [84, 85, 86, 288, 289], whose typical form [182, 289] favors a causal relationship between the pre- and post-synaptic neuron firing times [206, 207]. For an illustration of the considered STDP-like rule, refer to Fig. 2.1 which

shows how the stationary values of the couplings depend on $\varphi_2 - \varphi_1$. The full model now reads:

$$\dot{\varphi}_1 = I_0 - \sin \varphi_1 + \kappa_1 \sin (\varphi_2 - \varphi_1) + \sqrt{D}\xi_1(t)$$
$$\dot{\varphi}_2 = I_0 - \sin \varphi_2 + \kappa_2 \sin (\varphi_1 - \varphi_2) + \sqrt{D}\xi_2(t)$$
$$\dot{\kappa}_1 = \varepsilon(-\kappa_1 - \sin(\varphi_2 - \varphi_1))$$
$$\dot{\kappa}_2 = \varepsilon(-\kappa_2 + \sin(\varphi_2 - \varphi_1)). \tag{4.4}$$

The following sections concern the noiseless ($D = 0$) dynamics of the system. We will first provide a numerical analysis of the multistability in the full system with finite scale separation, and then perform a slow-fast analysis considering the singular perturbation limit, which will allows us to gain a deeper understanding of the mechanism behind ISR.

4.2.1.1 Stationary states

The deterministic system of the full system is invariant to $\mathbb{Z}_2$ symmetry (exchange of indices), which implies that the solutions appear in pairs sharing the same stability properties. The specific feature of the plasticity rule $\beta = \pi$ is that it confines the dynamics of the couplings to a symmetry invariant subspace, namely, $\kappa_1(t) = -\kappa_2(t) \equiv \kappa(t)$, which is readily seen from adding the equations for the coupling dynamics. This reduces the deterministic version of the original system (4.1) to the following three-dimensional form

$$\dot{\varphi}_1 = I_0 - \sin \varphi_1 + \kappa \sin (\varphi_2 - \varphi_1)$$
$$\dot{\varphi}_2 = I_0 - \sin \varphi_2 + \kappa \sin (\varphi_2 - \varphi_1)$$
$$\dot{\kappa} = \varepsilon(-\kappa - \sin(\varphi_2 - \varphi_1)). \tag{4.5}$$

By numerically solving the corresponding eigenvalue problem, we have verified that (4.5) has no stable fixed points. Rather, the system possesses two pairs of $\mathbb{Z}_2$ symmetry-related fixed points: a pair of saddle nodes and a pair of saddle foci, whereby the following conditions hold for each of the fixed points:

$$\kappa_1^* = -\kappa_2^*$$
$$\varphi_1^* = \pi - \varphi_2^*. \tag{4.6}$$

The maximal real part of the eigenvalues of the foci displays a power-law dependence on the scale separation, tending to zero in the singular limit $\varepsilon \to 0$, cf. Fig 4.9. The stable manifolds of the saddle points determine the separatrices between the coexisting limit cycle attractors.

4.2.1.2 Multistability of oscillatory regimes in the full system

As far as oscillatory states are concerned, our numerical experiments show that (4.5) exhibits multistability of three periodic solutions which lie within the invariant subspace $\kappa_1(t) = -\kappa_2(t)$, namely
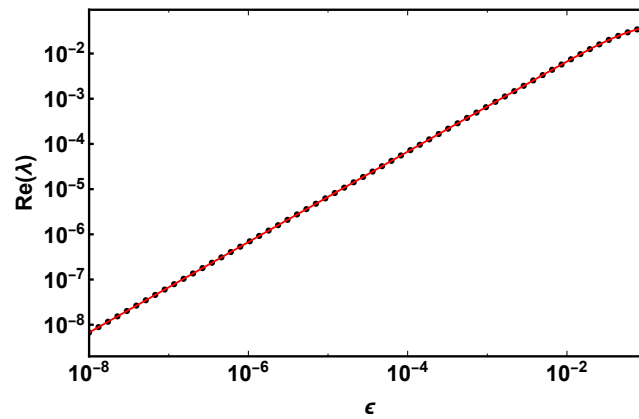
Figure 4.9: The dependence of the maximal real part of the eigenvalues of the two foci $\mathrm{Re}(\lambda)$ on timescale separation ε reveals that the values tend to zero as a power law in the singular limit ($\varepsilon \to 0$).

1. two non-zero coupling solutions with a constant phase shift **lying off the synchro-nization manifold**, related by the exchange symmetry of indices;

2. zero-coupling solutions with the fast variables synchronized in-phase, **lying on the synchronization manifold**.

These regimes are illustrated in Fig. 4.10, which shows the time traces of both variables, alongside the respective basins of attraction.

Nevertheless, the existence of these solutions critically depends on ε. In particular, for intermediate ε, the two periodic solutions off the synchronization manifold undergo a se-quence of period-doubling bifurcations, eventually vanishing in a homoclinic bifurcation, as they collide with the unstable manifold of the foci (which have two stable directions in the κ subspace). Fig. 4.11 shows the corresponding bifurcation diagram, constructed by the method of numerical continuation, such that the final state for the given ε value was taken as the initial state for the incremented ε value. The system is multistable until $\varepsilon \approx 0.382$, above which one lying on the synchronization manifold (effectively uncoupled units) remains the only attractor.

4.2.2 Slow-fast analysis

A deeper understanding of the ingredients relevant for gaining insight into the mechanism of inverse stochastic resonance can be gained within the framework of fast-slow analysis. In the present section, we will first study the layer problem by determining the stationary and periodic solutions of the fast flow, and then demonstrate that this particular value of β also gives rise to the invariance of the fast flow to time-reversal symmetry.
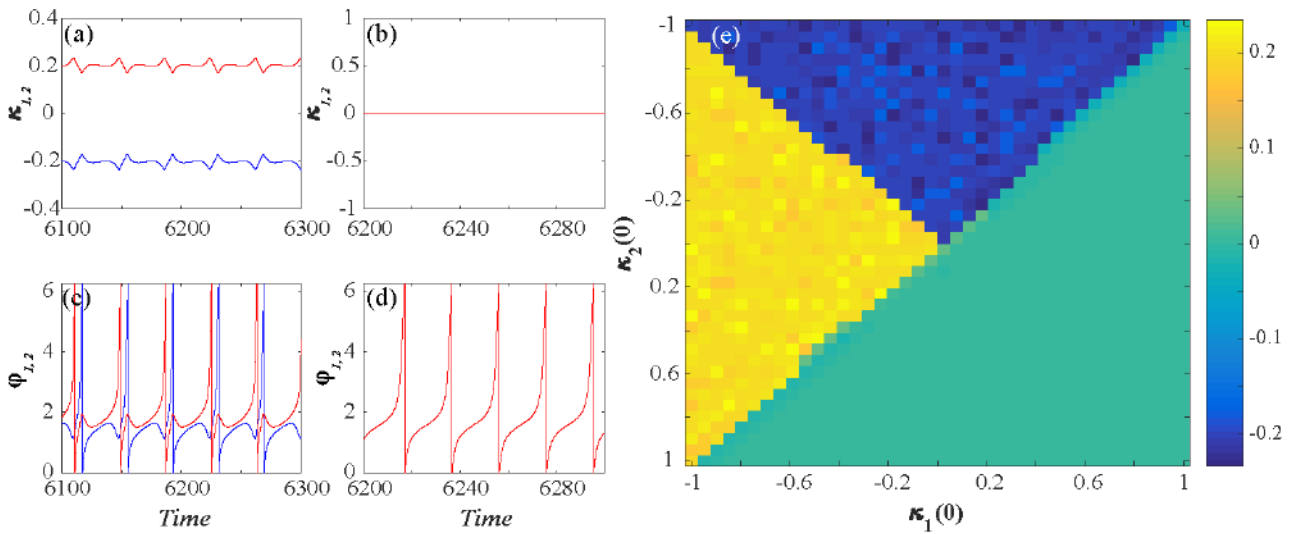
Figure 4.10: Multistability of the full system (4.5) for $I_0 = 1.05, \beta = \pi, \varepsilon = 0.01, D = 0$. (a)-(d) The left/middle column refers to the dynamics of the two periodic solutions off/on the synchronization manifold. The basins of attraction of all three regimes are shown in (e), whereby the yellow and the blue regions correspond to initial conditions leading to the two solutions off the synchronization manifold, whereas the green domain indicates those leading to the solution lying on the synchronization manifold.

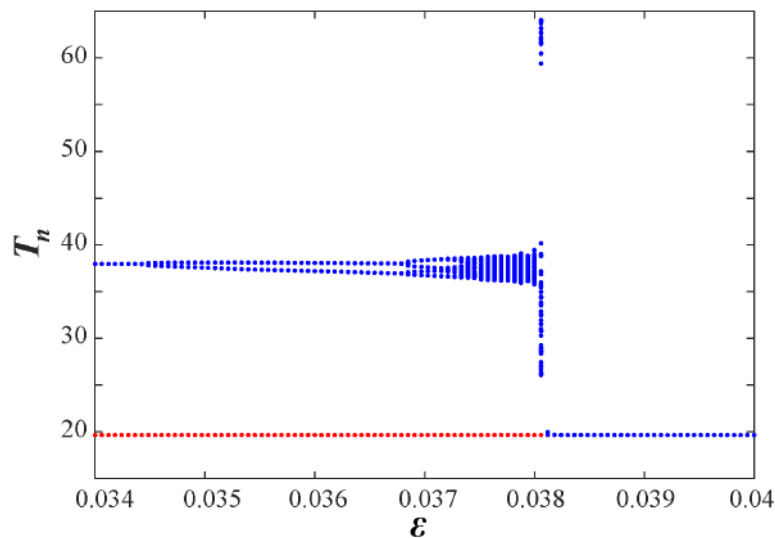Figure 4.11: Numerical bifurcation diagram obtained by determining the first return times T_n to the Poincare cross-section $\varphi_1 = 4.5$ for system (4.5) with $I_0 = 1.05, \beta = \pi, D = 0$, constructed by the method of numerical continuation. The blue dots refer to a representative periodic solution off the synchronization manifold, while the red dots correspond to the periodic solution on the synchronization manifold.

4.2.2.1 Layer problem: stationary states and periodic orbits of the fast flow

Let us now consider the layer problem, defined on the fast timescale, formally obtained by setting $\varepsilon = 0$ in the multiscale system (4.5),

$$\dot{\varphi}_1 = I_0 - \sin \varphi_1 + \kappa \sin (\varphi_2 - \varphi_1)$$
$$\dot{\varphi}_2 = I_0 - \sin \varphi_2 + \kappa \sin (\varphi_2 - \varphi_1), \tag{4.7}$$

where $\kappa \in [-1, 1]$ is treated as an additional system parameter.

To classify the stationary states of the fast flow, we will apply the coordinate transformation $(\varphi_1, \varphi_2) \mapsto (\Phi, \delta\varphi) = (\frac{\varphi_1 + \varphi_2}{2}, \frac{\varphi_1 - \varphi_2}{2})$, such that the fast flow (4.7) becomes

$$\delta\dot{\varphi} = -\sin \delta\varphi \cos \Phi$$
$$\dot{\Phi} = I_0 - \cos \delta\varphi (\sin \Phi + 2\kappa \sin \delta\varphi). \tag{4.8}$$

From the second equation in (4.8), one readily finds that the fast flow cannot possess any fixed points on the synchronization manifold for oscillatory local dynamics, since $\delta\varphi = 0$ cannot satisfy the system for $I_0 > 1$. Therefore, the stationary solutions $(\varphi_1^*, \varphi_2^*)$ may arise only from the condition $\cos \Phi = 0$, namely,

$$\cos \frac{\varphi_1^* + \varphi_2^*}{2} = 0 \Rightarrow \frac{\varphi_1^* + \varphi_2^*}{2} = \frac{\pi}{2} + n\pi, n \in \mathbb{Z} \Rightarrow \varphi_1^* + \varphi_2^* = \pi$$

A numerical bifurcation analysis reveals that the fast flow (4.7) exhibits either two fixed points or none at all, depending on κ and I_0, cf. Fig. 4.12 (a). The two fixed points are a saddle point $SP \equiv (\varphi_{1SP}, \varphi_{2SP})$ and a center $CP \equiv (\varphi_{1CP}, \varphi_{2CP})$ whose relative positions for fixed I_0 depend on the value of κ. The structure of the fast flow is organized around the **saddle-center bifurcation** which occurs at $\kappa = \kappa_{SC} \approx -0.1674$ for $I_0 = 1.05$. In this bifurcation scenario, the two fixed points get annihilated as a homoclinic orbit associated with the saddle collapses onto the center, as illustrated in Fig. 4.12 (b)-(c). Nevertheless, the two fixed points re-emerge at the symmetrical weight value $\kappa = -\kappa_{SC} \approx 0.1674$.

To gain a complete picture of the multistable dynamics of the fast flow, we have shown illustrative examples of the phase portraits and the associated vector fields for $\kappa < \kappa_{SC}$ and $\kappa > \kappa_{SC}$ in Figures 4.13(a) and 4.13(b), respectively. For $\kappa \in [-1, \kappa_{SC})$, the fast flow exhibits a limit cycle attractor, essentially derived from the local dynamics of the units, cf. the orbit indicated in orange in Fig. 4.13(a). Apart from the attracting periodic orbit, one observes two additional types of closed orbits, namely the homoclinic connections to the saddle point (SP), shown by blue and green, as well as periodic orbits around the center point (CP), an example of which is indicated in purple. On the other hand, for $\kappa > \kappa_{SC}$, the fast flow exhibits bistability of two oscillatory solutions, featuring the coexistence of a limit cycle inherited from the local dynamics of units and a limit cycle associated with the former homoclinic orbits, cf. Fig. 4.13(b).

The counterpart of the center point of the fast flow in the full system (4.5) is a weakly unstable focus. This difference originates from the fact that for finite scale separation, the
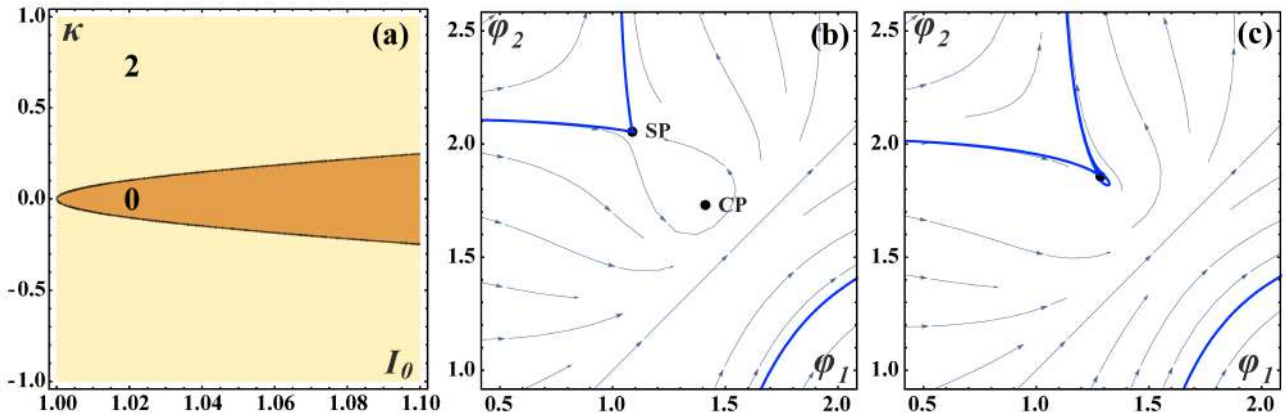
Figure 4.12: (a) The variation of the number of fixed points of the fast flow (4.7) in the (κ, I_0) plane, showing that it admits two or none fixed points. The saddle-center bifurcation scenario accounting for the change in the number of fixed points is shown in (b) and (c), obtained for $I_0 = 1.05$ with $\kappa = -0.2 < \kappa_{SC}$ in (b) and $\kappa = -0.1674 \approx \kappa_{SC}$ in (c). The homoclinic orbit of the saddle point SP, shown in blue, gradually engulfs the center point CP as the fixed points eventually collide and disappear at $\kappa = \kappa_{SC}$.
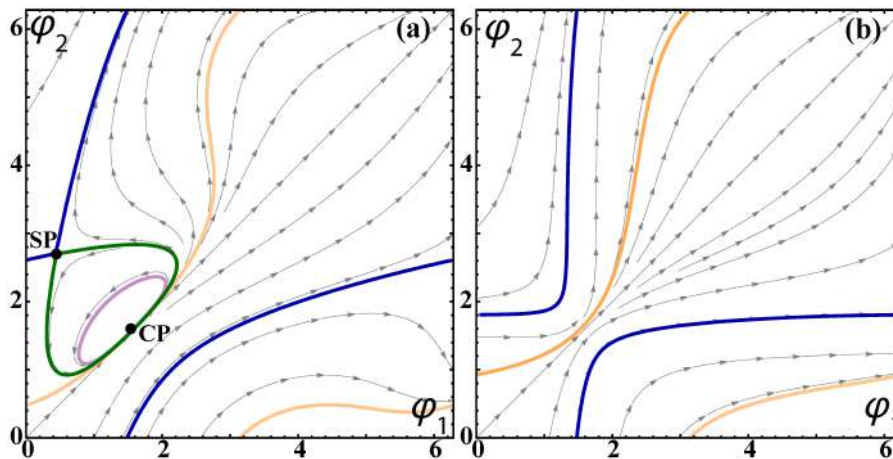
Figure 4.13: Multistable dynamics of the fast flow (4.7) for $I_0 = 1.05$ (a) below ($\kappa = -0.8$) and (b) above the saddle-center bifurcation ($\kappa = -0.08$). In (a), the system has two unstable fixed points, a saddle (SP) and a center (CP), and exhibits three types of closed orbits: a limit cycle attractor (orange) derived from the local dynamics of the units, homoclinic connections to SP (blue and green), and subthreshold oscillations around the center (purple). In (b), the system exhibits bistability between two oscillatory states, shown in orange and blue.

number and stability of fixed points depend on ε. In particular, the associated eigenvalues show that the fixed points of the full system are a pair of saddles (all eigenvalues real, one eigenvalue positive) and a pair of weakly unstable foci, rather than centers. The unstable foci are in fact saddle-foci, with two real negative eigenvalues and a pair of complex conjugate eigenvalues with positive real parts. However, as we have already shown in Fig. 4.9, it turns out that, as the singular limit $\varepsilon \to 0$ is approached, the maximal real part of the eigenvalues of the unstable foci tends to zero according to a power law dependency, corroborating the consistency of the slow-fast analysis with the dynamics of the full system in the singular limit.

4.2.2.2 Time-reversal symmetry of the fast flow

The appearance of the center point in the dynamics of the fast flow (4.7) is associated with its invariance to time-reversal symmetry. To show this explicitly, we will derive the symmetry-preserving map R, assuming that it has the form

$$
R = \begin{cases} \varphi_1 \to X - \varphi_2, \\ \varphi_2 \to X - \varphi_1, \\ t \to -t, \end{cases}
$$

where X has to be determined.

After applying R to (4.7), the indices in the l.h.s. of $\dot{\varphi}_1$ and $\dot{\varphi}_2$ are exchanged, while the coupling term remains unchanged:

$$
\dot{\varphi}_2 = I_0 - \sin(X - \varphi_2) + \kappa \sin(\varphi_2 - \varphi_1)
$$
$$
\dot{\varphi}_1 = I_0 - \sin(X - \varphi_1) + \kappa \sin(\varphi_2 - \varphi_1).
$$

Thus, X must satisfy the condition

$$
\sin(X - \varphi_i) = \sin \varphi_i, i = \{1, 2\} \iff X = (2k + 1)\pi, k \in \mathbb{Z},
$$

which leads to the symmetry-preserving map

$$
R = \begin{cases} \varphi_1 \to \pi - \varphi_2, \\ \varphi_2 \to \pi - \varphi_1, \\ t \to -t \end{cases} \tag{4.9}
$$

The invariance of (4.7) under R can readily be illustrated by superimposing the vector field plots of the system before and after applying the time-reversal transformation (4.9), cf. Fig. 4.14. Since the two vector fields coincide, one infers that the fast flow (4.7) is invariant to time-reversal symmetry.
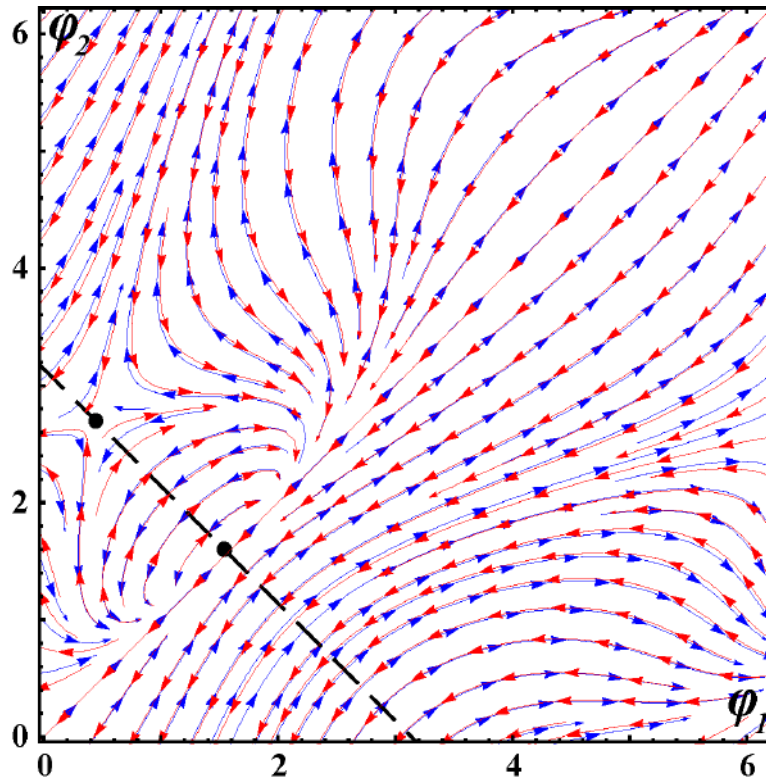
Figure 4.14: Time-reversal symmetry of the fast flow for $I_0 = 1.05, \kappa = -0.8$. The dashed line connects the saddle point and the center. Since the vector fields before (blue) and after (red) applying the time-reversal transformation 4.9 coincide, the fast flow is invariant under time-reversal.
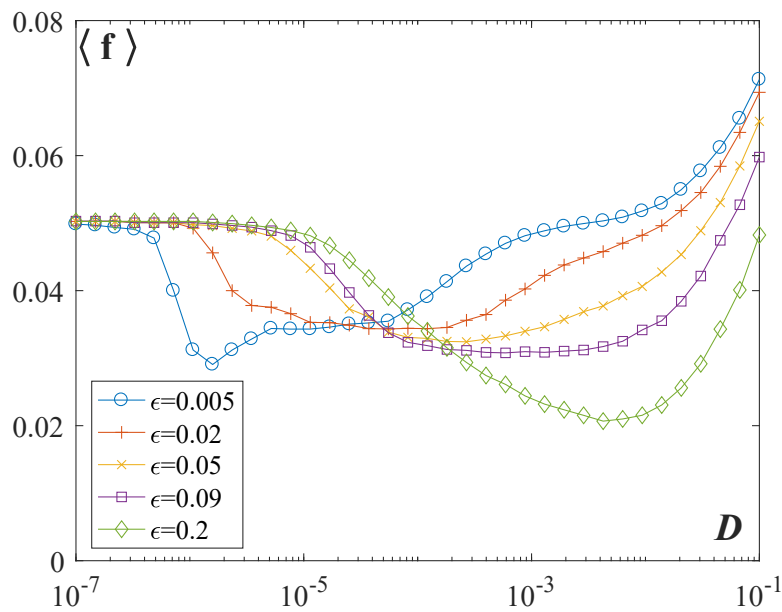
Figure 4.15: Observation of inverse stochastic resonance in system (4.4) with $I_0 = 1.05$. A family of dependencies $\langle f \rangle (D)$ for scale separations $\varepsilon \in \{0.005, 0.02, 0.05, 0.09, 0.2\}$.
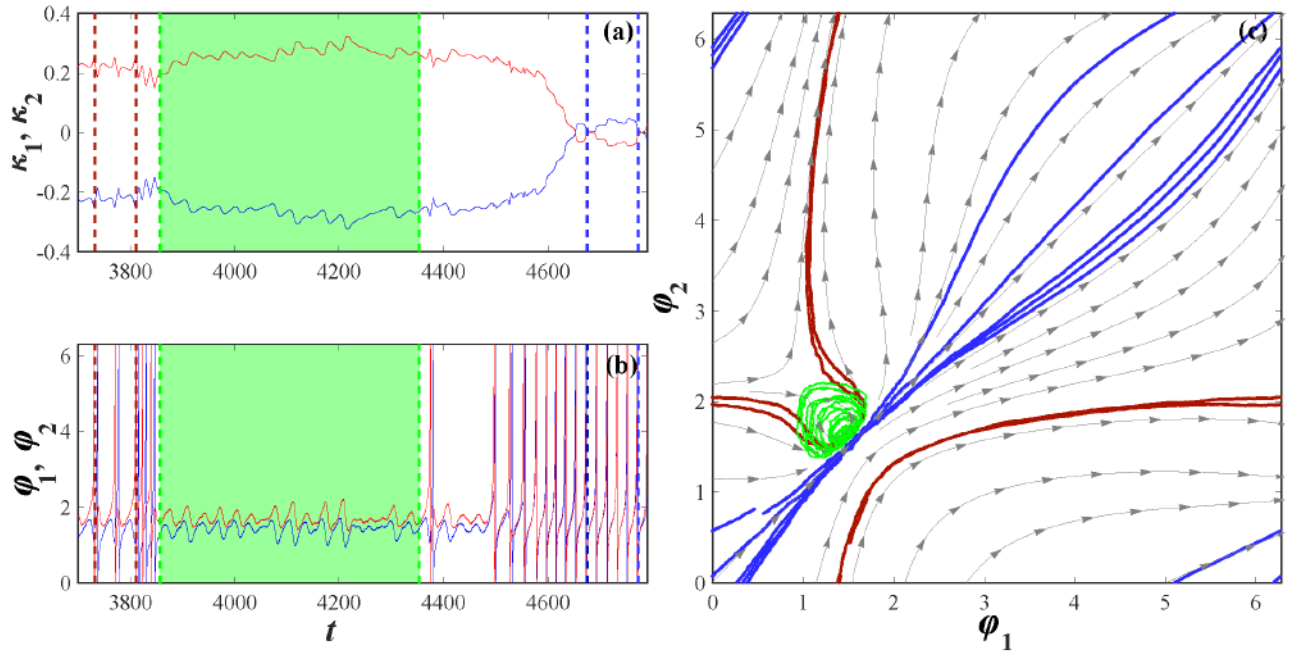
Figure 4.16: (a) and (b) show the time traces of $\kappa_i(t)$ and $\varphi_i(t), i \in \{1, 2\}$ respectively, with an episode during which the system remains in the vicinity of an unstable fixed point highlighted in green. The parameters are $I_0 = 1.05, \varepsilon = 0.035, \beta = \pi, D = 10^{-4}$. (c) The orbits conforming to the two metastable states characterized by large-amplitude oscillations of phases are shown in red and blue, whereas the subthreshold oscillations are indicated in green. Superimposed is the vector field of the fast flow, corresponding to the limit $\varepsilon \to 0$.

4.2.3 Numerical observation of ISR and the trapping effect

We find that system (4.5) exhibits the characteristic non-monotone response to noise in which the oscillation frequency of the phases $\langle f \rangle$ displays a minimum at an intermediate noise level, see Fig. 4.15. In contrast to the mechanism described in section 3.1, the onset of ISR here does not *qualitatively* depend on the adaptivity rate. Instead, the dependence of the system's nonlinear response to noise on ε is only *quantitative* whereby the resonant noise level shifts to larger values with increasing ε. Our exhaustive numerical simulations, in which we performed stochastic averaging over an ensemble of 100 different process realizations, indicate that the effect persists for slow adaptivity rates, cf. the example of the $\langle f(D) \rangle$ for $\varepsilon = 0.005$ in Fig. 4.15. Moreover, our slow-fast analysis also corroborates that all ingredients required for the ISR effect remain in the singular perturbation limit $\varepsilon \to 0$. The persistence of the ISR effect has also been numerically confirmed for faster adaptivity rates of the order $\varepsilon \sim 0.1$. In this case, we have observed that the minima of the $\langle f(D) \rangle$ curves become deeper with ε, suggesting that the effect becomes more pronounced for higher adaptivity rates.

Using the elements of singular perturbation theory, and in particular, the described layer dynamics, one may explain the mechanism behind ISR as follows. In the presence of noise, the described attractors of the fast flow (4.7) become metastable states. Nevertheless, in con-
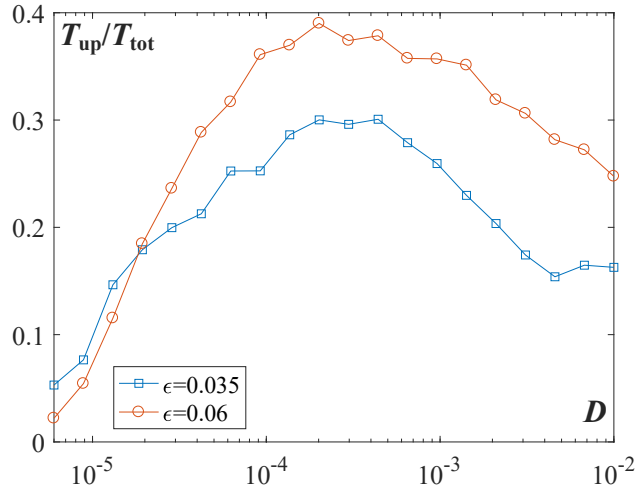
Figure 4.17: Numerically estimated fraction of time spent in the vicinity of the unstable fixed point T_{up}/T_{tot} as a function of noise for $\varepsilon = 0.035$ (squares) and $\varepsilon = 0.06$ (circles). Note that the positions of the maxima coincide with the corresponding resonant noise levels from Fig. 4.15. The remaining system parameters are set to $I_0 = 1.05, \beta = \pi$.

trast to the case of two adaptively coupled excitable units from section 3.1, slow stochastic fluctuations here involve not only switching between the metastable states, but also include *subthreshold oscillations* derived from periodic orbits around the center point. These subthreshold oscillations account for the trapping effect, which results in reducing the oscillation frequency. An example of time series $\kappa_i(t)$ and $\varphi_i(t), i \in \{1, 2\}$ obtained for an intermediate $\varepsilon = 0.035$, shown in Fig. 4.16(a)-(b), indeed involves three characteristic episodes, including visits to two distinct oscillatory metastable states and an extended stay in the vicinity of the center, cf. the stochastic orbits $(\varphi_1(t), \varphi_2(t))$ and the vector field of the fast flow in Fig. 4.16(c). In the case of finite scale separation, the trapping effect is manifested as the noise-enhanced stability of an unstable fixed point. The prevalence of subthreshold oscillations changes with noise in a non-monotone fashion, see the inset in Fig. 4.16(c), becoming maximal around the resonant noise level where the frequency dependence on noise exhibits a minimum, cf. Fig. 4.17 and Fig. 4.15. The fraction of time spent in the metastable state corresponding to subthreshold oscillations has been estimated by a threshold-based numerical procedure analogous to the one already described in section 4.1.

4.2.3.1 Degradation of ISR for different rules of adaptation

The present subsection concerns the robustness of ISR with respect to different plasticity rules, viz. its persistence as the plasticity parameter β is changed. For plasticity rules $\beta \lesssim \pi$, it has been found that the effect persists in a small interval below $\beta = \pi$. For instance, for fixed $\varepsilon = 0.05$, the effect is observed within the interval $\beta \in (\pi - 0.15, \pi)$. In this β range, the trapping efficiency of the phase space area around the weakly unstable focus is still sufficient to give rise to the nonlinear response to noise. The degradation of the resonant effect for decreasing β is illustrated in Fig. 4.18. Beyond the given β interval, the phase synchronized oscillations with constant bidirectional coupling remain the only stable
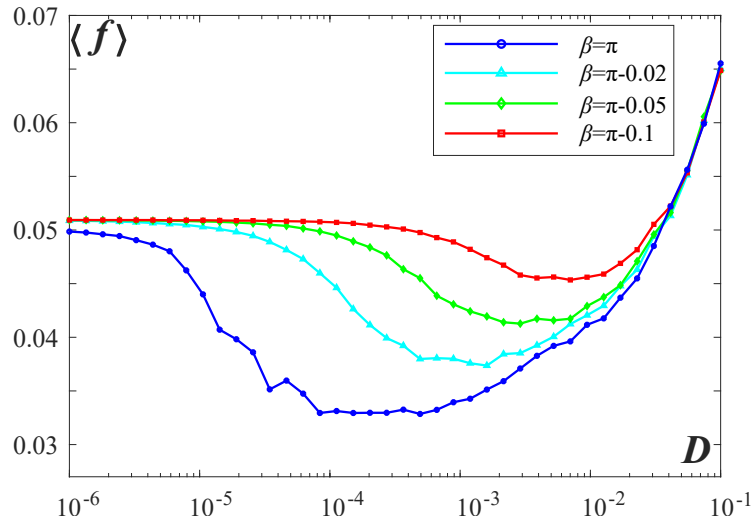
Figure 4.18: Family of $\langle \dot{f} \rangle(D)$ curves over $\beta \lesssim \pi$ for system (4.4) with $I_0 = 1.05$. The resonant effect is suppressed with reducing β.

solution of the deterministic system. This physical picture is only marginally perturbed by noise and there is no reduction of the oscillation frequency.

For plasticity rules $\pi < \beta < 4.391$, the dynamics is qualitatively different than the one for $\beta \lesssim \pi$ because the fast flow admits two coexisting stable fixed points (not shown). Note that the two stable fixed points are created as nodes at $\beta \approx 4.391$, but become foci as β decreases below $\beta \approx 4.1295$. Under the influence of noise, one finds switching between the two quasi-stationary metastable states, but no nonlinear response to noise is observed.

—— 4.3 *Two mechanisms of ISR in classical neuronal models* ——

So far, we have demonstrated two novel paradigmatic scenarios for ISR considering the examples of coupled Type I excitable oscillators, whose local dynamics is near a SNIPER bifurcation, either in the excitable or the oscillatory regime. Nevertheless, one may show that the onset of ISR and the underlying mechanisms do not depend on the excitability class of the local dynamics. In particular, it has recently been demonstrated that a single Type II Fitzhugh-Nagumo relaxation oscillator exhibits the qualitatively same form of non-monotone dependence on noise [94], with the mechanism involving noise-induced subthreshold oscillations that follow the maximal canard of an unstable focus. In that case, it has been established that the trapping effect and the related subthreshold oscillations are triggered due to the *phase-sensitive excitability* of a limit cycle.

Moreover, we have verified that the same model of neuronal dynamics, set to different parameter regimes, may exhibit the two generic scenarios of ISR we described. In particular,
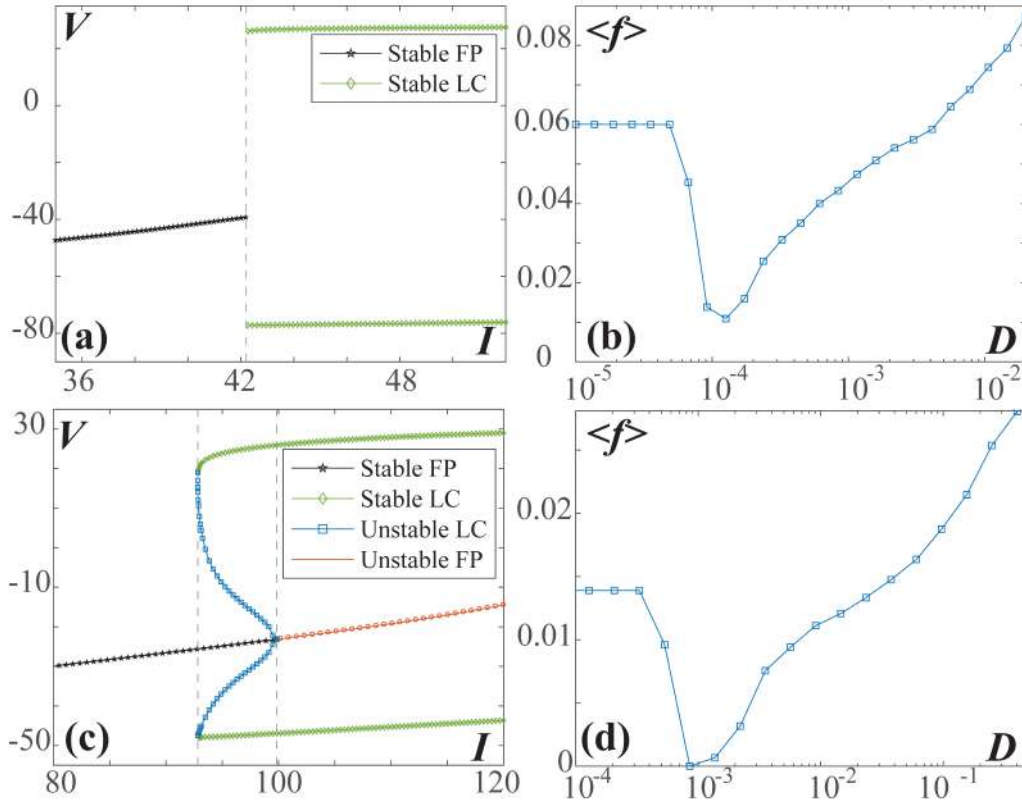
Figure 4.19: (a) The bifurcation diagram for the Morris-Lecar model in the vicinity of the *supercritical* Hopf bifurcation, showing the dependence of the membrane potential amplitudes V on the external bias current I. (b) illustrates the $\langle f \rangle (D)$ dependence for the Morris-Lecar neural oscillator at $I = 43$. (c) $V(I)$ bifurcation diagram for the Morris-Lecar model near the *subcritical* Hopf bifurcation. (d) The characteristic non-monotone dependence $\langle f \rangle (D)$ for the Morris-Lecar model from (c), with the bifurcation parameter $I = 95$ set to the bistable regime. The remaining parameters of the Morris-Lecar model for both cases are specified in the main text.

the Morris-Lecar neuron model is given by

$$C\frac{dv}{dt} = -g_{fast}m(v)(v - E_{Na}) - g_{slow}W(v - E_K) - g_{leak}(v - E_{leak}) + I$$
$$\frac{dv}{dt} = \phi\frac{W_\infty(v) - W}{\tau(v)}$$
$$m(v) = 0.5[1 + \tanh(\frac{v - \beta_m}{\gamma_m})]$$
$$W_\infty(v) = [1 + \tanh(\frac{v - \beta_w}{\gamma_w})]$$
$$\tau(v) = 1/\cosh(\frac{v - \beta_w}{2\gamma_w}),$$

where v and W denote the membrane potential and the slow recovery variable, respectively. The external bias current I is the bifurcation parameter. By an appropriate selection of the system parameters, the dynamics can be set to the vicinity of a supercritical or a subcritical Hopf bifurcation [294].

In the first case, obtained for $E_{Na} = 50\ mV, E_K = -100\ mV, E_{leak} = -70\ mV, g_{fast} =$

$20 \ mS/cm^2, g_{slow} = 20 \ mS/cm^2, g_{leak} = 2 \ mS/cm^2, \phi = 0.15, C = 2 \ \mu F/cm^2, \beta_m = -1.2 \ mV, \beta_w = -13 \ mV, \gamma_m = 18 \ mV, \gamma_w = 10 \ mV$, the model is monostable under the variation of I, and ISR is observed slightly above the Hopf bifurcation ($I = 43 \mu A/cm^2$) due to **noise-enhanced stability of an unstable fixed point**, cf. Fig. 4.19(a)-(b).

In the second case, conforming to the parameter set $E_{Na} = 120 \ mV, E_K = -84 \ mV, E_{leak} = -60 \ mV, g_{fast} = 4.4 \ mS/cm^2, g_{slow} = 8 \ mS/cm^2, g_{leak} = 2 \ mS/cm^2, \phi = 0.04, C = 20 \ \mu F/cm^2, \beta_m = -1.2 \ mV, \beta_w = 2 \ mV, \gamma_m = 18 \ mV, \gamma_w = 30 \ mV$, the model displays bistability between a limit cycle and a stable equilibrium in a range of I values just below the Hopf threshold. There, ISR emerges due to a mechanism based on **biased switching**, see the bifurcation diagram $V(I)$ in Fig. 4.19(c) as well as the dependence of the oscillation frequency on noise for $I = 95 \ \mu A/cm^2$ in Fig. 4.19(d).

—————— 4.4 *Controlling CR by nonlinear feedback* ——————

Coherence resonance is a phenomenon in which the regularity of noise-induced oscillations becomes maximal at an intermediate noise level [108, 159, 160, 161, 162, 163, 164, 165, 166, 167, 168, 169, 170]. A number of recent studies have addressed the *control* of the statistical features of noise-induced spiking in (coupled) excitable systems, i. e. mechanisms of enhancing or suppressing CR. In networks of coupled oscillators, efficient control mechanisms include time-delayed feedback [276, 277, 278, 279, 280, 281, 282], network topology [283], spatial heterogeneity of bifurcation parameters [285], as well as multiplexing it to another layer which exhibits SISR [284]. In the present section, we will study the control of CR due to an interaction between stochastic fluctuations and a slowly adapting feedback. Our main finding is that the filtered feedback employed in our model provides an efficient means of controlling this effect, whose prominence can be substantially enhanced or suppressed by a corresponding choice of the feedback gain. To explicitly demonstrate that our extension of singular perturbation theory to stochastic systems can be used to predict the statistical features of the noise-induced spiking, including its regularity, we will compare the regularity of oscillations arising in the original multiscale system to that of the limiting case of infinite time scale separation. Note that the present study strongly relies on the findings from section 3.2.

4.4.1 Paradigmatic model for the control of CR via a slowly adapting feedback

This study concerns a stochastic excitable system subjected to a slow control via a low-pass filtered feedback whose general form is

$$\dot{v} = f(v, \mu) + \sqrt{D}\xi(t) \tag{4.10}$$
$$\dot{\mu} = \varepsilon(-\mu + \eta g(v)),$$

where the small parameter $0 < \varepsilon \ll 1$ determines the timescale separation between the fast variable $v(t)$ and the slow feedback variable $\mu(t)$. The fast dynamics $\dot{v} = f(v, 0)$ is excitable and is influenced by Gaussian white noise $\xi(t)$ of variance D. Moreover, the slow feedback variable μ controls its excitability properties. The parameter η is the control gain or feedback strength, such that for $\eta = 0$ one recovers a classical noise-driven excitable system [67]. Systems like (4.10) conform both to spontaneous dynamics of classical neuronal models, such as the Izhikevich model [258], but may also be associated with dynamics of neuronal populations (where the collective dynamics is reduced to the evolution of the phase variable, such as the active rotator model) influenced by a slowly changing environment.

The simplest possible, yet paradigmatic choice of a model with excitable local dynamics is given by the active rotator. We have introduced the adaptation by considering a positive phase-dependent periodic function $g(\varphi) = 1 - \sin \varphi$, namely

$$\dot{\varphi} = I_0 - \sin \varphi + \mu + \sqrt{D}\xi(t), \qquad (4.11)$$
$$\dot{\mu} = \varepsilon \left(-\mu + \eta \left(1 - \sin \varphi \right) \right),$$

where the fast dynamics of the phase $\varphi \in S^1$ and the slow dynamics of the feedback variable $\mu \in \mathbb{R}$ involve a timescale separation defined by the small parameter $0 < \varepsilon \ll 1$. The excitability of the fast subsystem is controlled by the parameter I_0 and the slowly adapting feedback variable μ, characterized by the feedback strength parameter η which affects the fast dynamics via feedback. Moreover, the excitable fast dynamics is influenced by Gaussian white noise $\xi(t)$ of variance D.

In the absence of feedback and noise, i. e. for fixed $\mu = 0$ and $D = 0$, the fast subsystem undergoes a SNIPER bifurcation at $I_0 = 1$. Nevertheless, in the presence of feedback, the deterministic dynamics is governed by the term $I_0 + \mu(t)$ which can induce switching between the excitable equilibrium ($|I_0 + \mu| < 1$) and the oscillatory regime ($|I_0 + \mu| > 1$). This adaptation rule provides a positive feedback for the spikes and oscillations, since μ increases when $\varphi(t)$ is oscillating and drives the system towards the oscillatory regime, while in the vicinity of the equilibrium ($\sin \varphi \approx 1$) the control signal effectively vanishes.

The following subsections, we will provide the analysis of the deterministic dynamics of the system within the singular perturbation theory, and then extend the slow-fast approach to the noise-driven system.

4.4.1.1 Slow-fast analysis of the deterministic system

The layer problem, formally obtained by setting $\varepsilon = 0$ in (4.11), concerns the fast subsystem

$$\dot{\varphi} = I_0 + \mu - \sin \varphi, \qquad (4.12)$$

where μ is treated as an additional parameter. Depending on the value of μ, (4.12) with $D = 0$ may be either in the excitable ($\mu < 1 - I_0$) or in the oscillatory ($\mu > 1 - I_0$) regime. Conversely, in order to consider the reduced problem, defined on the slow timescale, we

rescale time as $T = \varepsilon t$ and set $\varepsilon = 0$ in the rescaled system, obtaining

$$\mu'(T) = -\mu(T) + \eta(1 - \sin\varphi(T)), \tag{4.13}$$

where the prime denotes the derivative with respect to the slow time T. Recall from section 3.2.2 that, by combining adiabatic elimination in the case of the stable equilibrium and averaging over fast oscillations in the case of oscillatory layer dynamics, we were able to derive a reduced slow system, which describes both the slow dynamics on the critical manifold, corresponding to the stable equilibrium of the fast flow, and the slow averaged dynamics corresponding to the oscillatory solution of the fast flow:

$$\mu'(T) = -\mu(T) + \eta(1 - I_0 - \mu(T) + \Omega(\mu(T))). \tag{4.14}$$

where the oscillation frequency $\Omega(\mu)$ is defined as follows

$$\Omega(\mu) = \begin{cases} 0, & \mu < 1 - I_0 \\ \sqrt{(I_0 + \mu)^2 - 1}, & \mu > 1 - I_0 \end{cases}.$$

4.4.1.2 Slow-fast analysis of the stochastic system

Let us now present a summary of our analysis of the stochastic dynamics of (4.11), using the method of stochastic averaging to extend the singular perturbation theory to stochastic systems. In particular, the goal is to derive the equation for the slow dynamics, analogous to (4.14), that would account for the averaged effect of noise in the layer dynamics

$$\mu'(T) = -\mu(T) + \eta(1 - \langle \sin\varphi(t)\rangle_t), \tag{4.15}$$

where $\langle \sin\varphi(t)\rangle_t$ is the stochastic average for solutions of the stochastic fast equation (4.12), calculated as follows

$$\langle \sin\varphi(t)\rangle_t = \lim_{t \to \infty} \frac{1}{t}\int_0^t \sin\varphi(t)\mathrm{d}t' = \int_0^{2\pi} \rho(\varphi;\mu,D)\sin\varphi\mathrm{d}\varphi. \tag{4.16}$$

The stationary probability density $\rho(\varphi;\mu,D)$ is the solution of the stationary Fokker-Planck equation for the stochastic layer dynamics. The mean frequency, obtained by time averaging of the layer dynamics (4.12), is given by

$$\Omega_D(\mu) = I_0 + \mu - \langle \sin\varphi(t)\rangle_t, \tag{4.17}$$

which depends on both D and μ via (4.16). After inserting (4.17) into (4.15), the equation for the slow dynamics of $\mu(T)$ reads

$$\mu'(T) = -\mu(T) + \eta(1 - I_0 - \mu + \Omega_D(\mu(T))), \tag{4.18}$$

i.e. it is of the same form as in the deterministic case (4.14).

The numerical bifurcation diagram with respect to D and η is obtained by simultaneously solving for the stationary solution of the Fokker-Planck equation for the layer dynamics (3.38) and the equation for the stationary solution of the slow subsystem. The diagram,
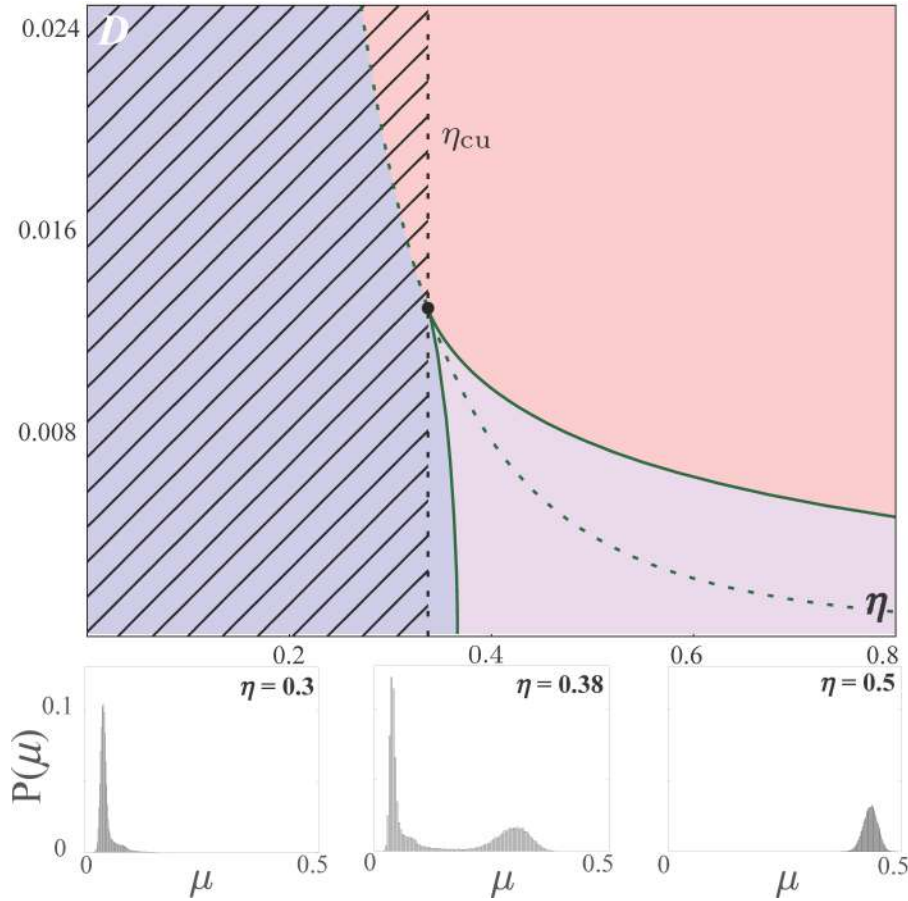
Figure 4.20: Comparison between the bifurcation diagram obtained within singular perturbation theory (upper panel) and numerical simulations for the full system with finite scale separation (lower panel). Upper panel: Stability domains for different dynamical regimes: noise-induced spiking (blue), noise-perturbed oscillations (red), and noise induced bursting (violet). The green dashed line refers to $\mu = \mu_c = 1 - I_0$. Enhanced coherence resonance can be found in the hatched region. Lower panels: Stationary distributions of $\mu(T)$, obtained from numerical simulations of the full system (4.11) with $\varepsilon = 0.005$, $D = 0.008$ and $\eta \in \{0.3, 0.38, 0.5\}$.

shown in Fig 4.20, reveals three characteristic (D, η) regions featuring noise-induced spiking, noise-perturbed spiking, and stochastic busting. For an illustration of the regimes, refer to Figure 3.14. Moreover, our numerical simulations for finite values of ε (lower panels in Fig. 4.20) show that the slowly varying control variable $\mu(T)$ is distributed around the stationary values from the limiting problem $\varepsilon = 0$, see also Figure 3.16. In the following, we will show that by varying the feedback strength within the region of noise-induced spiking, one can enhance or suppress coherence resonance.

4.4.2 Enhancing or suppressing CR by adjusting the feedback strength

The phenomenon of CR is well-known for noise-induced oscillations in excitable systems such as the classical model of the active rotator [161], given by the fast equation (4.12) without adaptation ($\eta = 0$ and therefore also $\mu = 0$), as well as in other phase models such as Adler's equation [155, 295] and the theta neuron [156]. In this section we demonstrate a

novel mechanism of control of CR, showing that the effect may be enhanced or suppressed by introducing a slowly adapting variable that, depending on the feedback strength, produces a positive or a negative feedback to noise-induced spikes, effectively driving the system in a self-adjusted way towards or away from the bifurcation threshold.

CR may be characterized by studying how the regularity of noise-induced oscillations changes with the noise intensity. As a measure of the variability of spike timing, one can use the so-called jitter, which represents the coefficient of variation of the interspike interval [149, 273]. In particular, for any 2π-periodic spiking variable φ, the spiking times t_k are defined as the first passage times $\varphi(t_k) = 2\pi k$, $k \in \mathbb{N}$. Then, the corresponding interspike intervals are given by $\tau_k = t_k - t_{k-1}$, such that the coefficient of variation of their distribution is defined as

$$R(D) = \frac{\sqrt{\langle \tau_k^2 \rangle - \langle \tau_k \rangle^2}}{\langle \tau_k \rangle}.$$

Since smaller values of the coefficient of variation indicate a higher regularity of noise-induced oscillations, the effect of CR is reflected in the curve $R(D)$ having a minimum at an intermediate noise level.

The control mechanism is based on coupling the excitable system to a slowly adapting variable, which gives rise to a multiscale system with a finite scale separation. Nevertheless, we show that the introduced extension of singular perturbation theory to stochastic systems may still be used to predict the impact of control on CR with sufficient accuracy. In particular, we were able to predict the statistical features of the response of the full system (4.11) to noise by considering a stochastic equation of the layer dynamics (4.12) where the control variable is replaced by its stationary value obtained from the corresponding reduced problem (4.13). This has allowed us to determine the $R(D)$ dependencies for the stochastic layer dynamics corresponding to different values of feedback strength, which show a good match to the $R(D)$ dependencies for the full system.

Let us now compare the $R(D)$ dependencies obtained for the *full* system (4.11) for a given η value and for the *fast* subsystem (4.12) with the corresponding stochastic averages $\mu^*(D; \eta)$ substituted into μ. In the former case, R can be determined from direct numerical simulations of (4.11), while in the latter case, $\mu^*(D; \eta)$ displays a strongly nonlinear dependence both on η and D, see also Figs. 3.12(a) and 3.13. In particular, for fixed η slightly below the cusp value η_{cu}, the strongly nonlinear dependence of μ^* on D has a substantial impact on the resonant behavior reflected in the form of $R(D)$.

Figure 4.21 displays the $R(D)$ dependence for different values of the feedback strength η, comparing the numerical results for the fast subsystem (4.12) with stationary values $\mu^*(D; \eta)$ substituted as fixed μ, to numerical simulations of the multiscale system (4.11) for $\varepsilon = 0.005$. While for $0 < \eta < \eta_{cu}$ one finds that CR can be substantially enhanced, cf. the $R(D)$ dependencies for $\eta = 0$ and $\eta = 0.3$. On the other hand, the resonant effect can be readily suppressed by introducing negative values of the feedback strength η, see the $R(D)$ curves for $\eta = -0.2$ in Fig. 4.21. This implies that the adaptive feedback we employ provides an

of Pyragas type [278, 279, 280], is that it involves only a single control parameter, namely the control gain. We suspect that such a control mechanism may even provide for a self-consistent control of spiking regularity in stochastic neuronal dynamics, e.g. in the Izhikevich neuron model.

Chapter 5

Conclusions

This thesis presents a systematic overview of assorted self-organizing phenomena in coupled excitable systems arising due the interplay of multiple timescale dynamics and noise. In particular, considering paradigmatic models, we have been able to demonstrate and analyze emergent phenomena such as **macroscopic excitability, slow stochastic fluctuations, stochastic bursting, inverse stochastic resonance**, and **coherence resonance**. These phenomena are based on mechanisms of self-organization, namely *synchronization of noise-induced oscillations, noise-induced switching, noise-enhanced stabilization of deterministically unstable structures*, and *noise-induced multistability*. Our results provide important advancements to contemporary studies in nonlinear dynamics, both in terms of the discovery of novel phenomena and their analysis, as well as from a methodological standpoint. Moreover, the present results may fundamentally increase our ability to characterize, predict and control biological systems, such as neuronal networks. Let us now summarize the scientific contributions of this thesis.

5.1 *Conceptual advancements*

1. Extension of the notion of excitability to coupled systems.

At variance with the classical notion of excitability which refers to the dynamics of individual units, this thesis extends the concept of excitability to *coupled* systems. In particular, we have analyzed the excitability of motifs consisting of two active rotators and assemblies of coupled neuronal maps. In the former case, we have classified different threshold-like responses of the coupled system to perturbation [181]. Concerning the latter, we were the first to introduce the concept of *macroscopic excitability* which refers to the scenario where a population of units acts like an excitable element [191].

2. Discovery of two generic mechanisms for inverse stochastic resonance.

We have identified two generic scenarios for inverse stochastic resonance (ISR), one based on biased switching and the other associated with noise-enhanced stabilization of

a deterministically unstable fixed point. The effect has been demonstrated both in the case of self-sustained oscillators near the bifurcation threshold and for emergent oscillations in coupled excitable systems. The particular type of slow dynamics, such as phase-dependent plasticity, have been shown to be capable of enhancing the resonant effect. The two mechanisms of ISR have been proven to be independent on the excitability class of local dynamics [193, 194].

So far, ISR has been observed for Type II excitable units with bistable local dynamics near the subcritical Hopf bifurcation [68, 173, 174, 175]. Our results support the idea that ISR may be a more widespread effect, observed in a wide range of systems. Since ISR has already been found in models of individual neurons [94, 173, 174, 176], motifs of units with neuron-like dynamics [172, 193], as well as neural networks [177], it is likely that ISR universal to neuronal dynamics, where it has already been suggested to play a number of important functional roles [68, 174, 176, 178, 180, 260].

3. Discovery of a new method of control of coherence resonance.

We have introduced a novel nonlinear control mechanism of coherence resonance, demonstrating how the resonant effect may be enhanced or suppressed by introducing a slowly adapting feedback to a stochastic excitable system. The adaptation rule provides a positive feedback for the noise-induced rare spikes and oscillations, while in the vicinity of the equilibrium the control signal effectively vanishes [192]. Compared with other types of control, like the one based on the Pyragas scheme of control via delayed feedback [278, 279, 280], the advantage of our method is that it features only one control parameter, namely the feedback strength.

4. Discovery of two types of slow fluctuations in stochastic excitable multiscale systems.

We have investigated switching dynamics in multiscale systems for small, but *finite* timescale separation, having found that it gives rise to two different effects, namely *slow stochastic fluctuations* and *stochastic bursting*. Considering a motif of two adaptively coupled stochastic excitable units, we have found that slow stochastic fluctuations qualitatively depend on the scale separation between the fast and slow variables, such that a larger separation gives rise to switching between two modes of noise-induced oscillations, whereas a smaller separation induces switching between metastable states derived from coexisting attractors of the deterministic dynamics [181]. For the paradigmatic system of a stochastic excitable unit with a slowly adapting feedback, we have demonstrated how the interaction of multiscale dynamics and noise may give rise to *stochastic bursting*, having explained it in terms of switching between metastable states derived from the deterministic version of the system by invoking an analogy with the Eyring-Kramers process in a double-well potential [192].

────────────── 5.2 *Methodological advancements* ──────────────

1. Extension of mean-field theory to coupled stochastic maps.

The mean-field method has so far been applied exclusively to the class of continuous-time systems, while effective models for discrete assemblies of coupled maps have been lacking due to the inability to implement the Fokker-Planck formalism to discrete-time systems. Using a cumulant approach complemented by the Gaussian closure hypothesis, we have derived the first effective model for the collective dynamics of coupled stochastic maps [191].

2. Extension of multiscale analysis methods to stochastic systems (stochastic averaging).

Within singular perturbation theory, one may consider two limiting problems corresponding to infinite timescale separation in a multiscale system, namely the layer problem, defined on the fast timescale, and the reduced problem, defined on the slow timescale. We have introduced a novel averaging approach for treating the reduced problem. The case of oscillatory layer dynamics in *deterministic* multiscale problems has typically been treated by performing the averaging over fast oscillations and inserting the obtained averages into the reduced problem dynamics. We have extended this idea to stochastic oscillatory layer dynamics, introducing the method of **stochastic averaging**. By this method, the noise-induced or noise-perturbed oscillations in layer dynamics are considered by solving for the stationary solution of the corresponding Fokker-Planck equation [192].

3. Extension of phase-response theory to coupled systems.

We have studied the stimulus-response relationship of an assembly of coupled neuronal maps, showing that the derived effective model is not only capable of successfully treating the asymptotic, but also the transient collective dynamics of an assembly of coupled stochastic maps. We have established that the effective model is capable of reproducing the phase response curves of the exact system and the assembly's response to external stimulation of finite amplitude and duration with sufficient accuracy [191].

────────────── 5.3 *Outlook* ──────────────

The presented results potentially have interdisciplinary applications. For instance, the newly-introduced concept of macroscopic excitability, which refers to the scenario in which a population of excitable elements acts like an excitable element itself, may be relevant to slow stochastic fluctuations unfolding on the intermediate (mesoscopic) scale of the brain's hierarchical organization [296], where assemblies are comprised of microcolumns or cortical columns [297, 298, 299]. Moreover, given that our motif model involves ingredients inherent to neuronal systems, such as excitability, plasticity and noise, the results on switching

dynamics can be interpreted in the context of neuroscience: the scenario of switching under slow adaptation implies that a binary neuron motif may display slow alternation between two effectively unidirectional weight configurations, promoting opposite direction of information flow, whereas the scenario found for faster adaptation, if extended to networks, may be considered as a paradigm for UP-DOWN states, typical for cortical dynamics [180, 260]. Concerning inverse stochastic resonance, it is already known that it plays a number of important functional roles in neuronal systems (triggering on-off tonic spiking activity, the suppression of pathologically long short-term memories [68, 174, 176, 178], and the formation of UP-DOWN states [180, 260]). Considering that models of individual neurons [94, 173, 174, 176], motifs of units with neuron-like dynamics [172, 181], and neural networks [177] have all been shown to exhibit the effect, it stands to reason that the phenomenon should be universal to neuronal dynamics. The scenarios for the onset of the effect presented in this thesis appear to be generic and should be expected in other biological systems comprised of units with local dynamics near a bifurcation threshold. Finally, our results on the new general method of control of coherence resonance via filtered feedback may have applications in neuroscience and engineering.

The novel averaging methods developed within our analysis have advanced the theoretical knowledge on multiscale stochastic systems on a fundamental level, shifting the paradigm from singular perturbation theory to understanding the effects of finite scale separation, primarily related to switching dynamics. Moreover, our mean-field model for coupled stochastic maps has set the stage for a more systematic exploration of spontaneous and induced collective dynamics of assemblies of map neurons by analytical means. We believe that the introduced techniques can be successfully applied for treating emergent behavior in a wide range of stochastic multiscale systems, allowing for an extension towards understanding critical transitions in systems with complex network topologies and interacting networks.

Bibliography

[1]   H. Haken, *Synergetics: An Introduction. Nonequilibrium Phase Transition and Self-Organization in Physics, Chemistry, and Biology, Third Revised and Enlarged Edition* (Springer-Verlag, Berlin, 1983).

[2]   H. Haken, *Synergetics, Introduction and Advanced Topics* (Springer, Berlin, 2004).

[3]   M. M. Waldrop, *Complexity: The Emerging Science at the Edge of Order and Chaos* (Viking, London, 1992).

[4]   Y. Bar-Yam, "General Features of Complex Systems" in *Encyclopedia of Life Support Systems* (EOLSS UNESCO Publishers, Oxford, 2002).

[5]   R. Cen, Astrophys. J. Lett. **785**, L21 (2014).

[6]   S. Jungblut and C. Dellago, Eur. J. Phys. E **39**, 77 (2016).

[7]   A. Baas, Geomorphology **48**, 309 (2002).

[8]   I. D. Couzin and J. Krause, Adv. Study. Behav. **32**, 1 (2003).

[9]   S. Camazine, J-L. Deneubourg, N. R. Franks, J. Sneyd, G. Theraulaz, and E. Bonabeau, *Self-Organization in Biological Systems* (Princeton University Press, Princeton, 2003).

[10] B. S. Kerner, Phys. Rev. Lett. **81**, 3797 (1998).

[11] P. Krugman, *The Self Organizing Economy* (Blackwell Publishers, Hoboken, 1995).

[12] C. Fuchs, Cybernetics and Human Knowing **12**, 37 (2005).

[13] B. de Boer, "Self-organization and language evolution" in *The Oxford Handbook of Language Evolution*, eds. K. R. Gibson, and M. Tallerman (Oxford University Press, Oxford, 2011).

[14] E. Bullmore and O. Sporns, Nat. Rev. Neurosci. **10**, 186 (2009).

[15] J. W. Krakauer, A. A. Ghazanfar, A. Gomez-Marin, M. A. MacIver, and D. Poeppel, Neuron **93**, 480 (2017).

[16] R. Ellis, Philos. Psychol. **13**, 173 (2000).

[17] P. Perruchet and A. Vinter, Behav. Brain Sci. **25**, 297 (2002).

[18] H. Haken, "Self-Organization in Physics", in *Nonlinear Dynamics of Transcritical Flows. Lecture Notes in Engineering, vol 13*, eds. H. L. Jordan, H. Oertel, and K. Robert (Springer, Berlin, Heidelberg, 1985).

[19] F. Paslack, *Urgeschichte der Selbstorganisation* (Vieweg, Braunschweig, 1991).

[20] A. Palmer, *Reading Lucretius in the Renaissance* (Harvard University Press, Cambridge, 2014).

[21] R. Descartes, *Discourse on Method and the Meditations* (Penguin, London, 1968).

[22] I. Kant, *Critique of Judgement* (Clarendon Press, Oxford, 2008).

[23] W. R. Ashby, J. Gen. Physchol. **37**, 125 (1947).

[24] P. Asaro, "Heinz von Foerster and the Bio-Computing Movements of the 1960s" in *An Unfinished Revolution? Heinz von Foerster and the Biological Computer Laboratory BCL 1958–1976*, eds. A. Müller, and K. H. Müller (Edition Echoraum, Vienna, 2007).

[25] H. von Foerster, "On self-organizing systems and their environments" in *Understanding Understanding: Essays on Cybernetics and Cognition* (Springer, New York, 2003).

[26] H. von Foerster and G. Pask, Cybernetica **3**, 258 (1961).

[27] H. von Foerster and G. Pask, Cybernetica **4**, 20 (1961).

[28] N. Wiener, *Cybernetics: or Control and Communication in the Animal and the Machine*, 2nd ed. (MIT Press, Cambridge, 1961).

[29] I. Prigogine, Bull. Cl. Sci. Acad. R. Belg. **31**, 600 (1945).

[30] `nobelprize.org/prizes/chemistry/1977/prigogine/lecture`

[31] L. Zuchowsky, Stud. Hist. Philos. M. P. **63**, 86 (2018).

[32] H. A. Simon, *The Sciences of the Artificial* (MIT Press, Cambridge, 1981).

[33] J. Goldstein, Emergence **1**, 49 (1999).

[34] T. de Wolf and T. Holvoet, "Emergence Versus Self-Organisation: Different Concepts but Promising When Combined" in *Engineering Self-Organising Systems*, eds. S. A. Brueckner, S. G. di Marzo, A. Karageorgos, and R. Nagpal (Springer, Berlin, Heidelberg, 2005).

[35] M. Benham-Hutchins, and T. Clancy, JONA **40**, 352 (2010).

[36] E. Estrada, *The Structure of Complex Networks: Theory and Applications* (Oxford University Press, Oxford, 2011).

[37] A.-L. Barabási, *Linked: How Everything Is Connected to Everything Else and What It Means for Business, Science, and Everyday Life* (Plume, New York, 2003).

[38] G. Caldarelli and M. Catanzaro, *Networks: A Very Short Introduction* (Oxford University Press, Oxford, 2012).

[39] S. Strogatz, *Nonlinear Dynamics and Chaos: with Applications to Physics, Biology, Chemistry, and Engineering* (Perseus Books Publishing, New York, 1994).

[40] U. Feudel, Int. J. Bifurcation Chaos **18**, 1607 (2008).

[41] U. Feudel, A. N. Pisarchik, and K. Showalter, Chaos **28**, 033501 (2018).

[42] I. Franović and V. Klinshov, Chaos **28**, 023111 (2018).

[43] F. Sorrentino and E. Ott, Phys. Rev. Lett. **100**, 114101 (2008).

[44] F. Vazquez, V. M. Eguiluz, and M. S. Miguel, Phys. Rev. Lett. **100**, 108702 (2008).

[45] N. Caporale and Y. Dan, Ann. Rev. Neurosci. **31**, 25 (2008).

[46] C. Furusawa and K. Kaneko, Phys. Rev. Lett. **90**, 088102 (2003).

[47] C. Kuehn, *Multiple Time Scale Dynamics* (Springer, Switzerland, 2015).

[48] M. Krupa, B. Sandstede, and P. Szmolyan, J. Differ. Equ. **133**, 49 (1997).

[49] M. Desroches, J. Guckenheimer, B. Krauskopf, C. Kuehn, H. M. Osinga, and M. Wechselberger, SIAM Rev. **54**, 211 (2012).

[50] M. Lichtner, M. Wolfrum, and S. Yanchuk, SIAM J. Math. Anal. **43**, 788 (2011).

[51] H. Jardon-Kojakhmetov and C. Kuehn (2019), `arxiv.org/abs/1901.01402`.

[52] M. Scheffer, et al., Nature **461**, 53 (2009).

[53] C. Meisel, A. Klaus, C. Kuehn, and D. Plenz, PloS Comput. Biol. **11**, e1004097 (2015).

[54] L. Cocchi, L. L. Gollo, A. Zalesky, and M. Breakspear, Prog. Neurobiol. **158**, 132 (2017).

[55] C. Meisel and C. Kuehn, PloS One **7**, e30371 (2012).

[56] G. Schöner and J. A. Kelso, Science **239**, 1513 (1988).

[57] C. Kuehn, Physica D **240**, 1020 (2011).

[58] Y. Kuramoto, in *International Symposium on Mathematical Problems in Theoretical Physics, Lecture Notes in Physics*, ed. H. Araki (Springer, New York, 1975).

[59] K. Wiesenfeld, P. Colet, and S. H. and Strogatz, Phys. Rev. Lett. **76**, 404 (1996).

[60] F. Dörfler, M. Chertkov, and F. Bullo, Proc. Natl. Acad. Sci. U.S.A. **110**, 2005 (2013).

[61] J. Aldridge, and E. K. Pye, Nature **259**, 670 (1976).

[62] D. C. Michaels, E. P. Matyas, and J. Jalife, Circ. Res. **61**, 704, (1987).

[63] M. Komarov, S. Gupta, and A. Pikovsky, EPL **106**, 40003 (2014).

[64] S. Gupta, A. Campa, and S. Ruffo, *Statistical Physics of Synchronization* (Springer, Cham, 2018).

[65] E. Meron, Phys. Rep. **218**, 1 (1992).

[66] T. Isele and E. Schöll, New J. Phys. **17**, 023058 (2015).

[67] B. Lindner, J. Garcia-Ojalvo, A. Neiman, and L. Schimansky-Geier, Phys. Rep. **392**, 321 (2004).

[68] B. A. Schmerl and M. D. McDonnell, Phys. Rev. E **88**, 052722 (2013).

[69] A. Destexhe and M. Rudolph-Lilith, *Neuronal Noise* (New York, Springer, 2012).

[70] M. D. McDonnell and L. M. Ward, Nat. Rev. Neurosci. **12**, 415 (2011).

[71] G. Buzsáki, *Rhythms of the Brain* (Oxford University Press, Oxford, 2009).

[72] A. Destexhe and D. Contreras, Science **314**, 85 (2006).

[73] E. M. Izhikevich, Int. J. Bifurc. **10**, 1171 (2000).

[74] E. M. Izhikevich, *The Dynamical Systems in Neuroscience: Geometry of Excitability and Bursting* (MIT Press, Cambridge, 2007)

[75] K. Ikeda, Opt. Commun. **30**, 257 (1979).

[76] D. Pieroux and T. Erneux, Phys. Rev. A **53**, 2765 (1996).

[77] R. J. Field and M. Burger, *Oscillations and Traveling Waves in Chemical Systems* (Wiley, New York, 1985).

[78] V. Petrov, S. K. Scott, and K. Showalter, J. Chem. Phys. **97**, 6191 (1992).

[79] I. T. Georgiou, A. K. Baja, and M. Corless, Int. J. Nonlin. Mech. **33**, 275 (1998).

[80] Z. H. Wang and H. Y. Hu, Nonlinear Dyn. **25**, 317 (2001).

[81] D. Ludwig, D. D. Jones, and C. S. Holling, J. Anima. Ecol. **47**, 315 (1978).

[82] S. Rinaldi and M. Scheffer, Ecosystems **3**, 507 (2000).

[83] L. F. Abbott and S. Nelson, Nat. Neurosci. **3**, 1178 (2000).

[84] H.-X. Wang, R. C. Gerkin, D. W. Nauen, and Bi G.-Q., Nat. Neurosci. **8**, 187 (2005).

[85] S. Song, K. D. Miller, and L. F. Abbott, Nat. Neurosci. **3**, 919 (2000).

[86] R. C. Froemke and Y. Dan, Nature **416**, 433 (2002).

[87] M. Krupa and P. Szmolyan, J. Differ. Equ. **174**, 312 (2001).

[88] N. Fenichel, J. Differ. Equ. **31**, 53 (1979).

[89] J. Mitry, M. McCarthy, N. Kopell, and M. Wechselberger, J. Math. Neurosci. **3**, 12 (2013).

[90] P. Szmolyan and M. Wechselberger, J. Differ. Equ. **177**, 419 (2001).

[91] M. Wechselberger, SIAM J. Appl. Dyn. Syst. **4**, 101 (2005).

[92] M. Wechselberger, Trans. Am. Math. Soc. **364**, 3289 (2012).

[93] N. Wiener and A. Rosenblueth, Arch. Inst. Cardiol. Mex. **16**, 205 (1946).

[94] I. Franović, O. E. Omel'chenko, and M. Wolfrum, Chaos **28**, 071105 (2018).

[95] K. Motokawa, Tohoku J. Exp. Med. **50**, 307 (1949).

[96] J. P. Green, N. J. Giarman, and W. T. Salte, Am. J. Physiol. **171**, 174 (1952).

[97] J. W. Gebhard, J. Exp. Psychol. **44**, 132 (1952).

[98] J. W. Gebhard, Psychol. Bull. **50**, 73 (1953).

[99] A. T. Winfree, *The Geometry of Biological Time* (Springer, New York, 1980).

[100] J. D. Murray, *Mathematical Biology* (Springer, Berlin–Heidelberg–New York, 1993).

[101] B. Hille, *Ionic Channels of Excitable Membranes* (Sinauer Associates, Sunderland, 2001).

[102] L. Glass, Nature **410**, 277 (2001).

[103] C. O. Weiss and R. Vilaseca, *Dynamics of Lasers* (VCH, Weinheim, 1991).

[104] A. M. Yacomotti, P. Monnier, F. Raineri, B. B. Bakir, C. Seassal, R. Raj, and J. A. Levenson, Phys. Rev. Lett. **97**, 143904 (2006).

[105] R. Kapral and K. Showalter (Eds.), *Chemical Waves and Patterns* (Kluwer Academic Publishers, Dordrecht, 1995).

[106] G. Bucchioni, A. Cavallo, D. Ippolito, G. Marton, and U. Castiello, Brain Cogn. **81**, 176 (2013).

[107] G. Dumas, G. C. de Guzman, E. Tognoli, and J. A. S. Kelso, PNAS **35**, E3726 (2014).

[108] A. Ganopolski and S. Rahmstorf, Phys. Rev. Lett. **88**, 038501 (2002).

[109] J. M. Carlson, J. S. Langer, and B. E. Shaw, Rev. Mod. Phys. **66**, 657 (1994).

[110] A. L. Hodgkin, J. Physiol. **107**, 165 (1948).

[111] A. L. Hodgkin and A. F. Huxley, J. Physiol. **117**, 500 (1952).

[112] `nobelprize.org/prizes/medicine/1963/summary`

[113] J. Rinzel and G. B. Ermentrout, "Analysis of neural excitability and oscillations" in *Methods in Neural Modeling*, eds. C. Koch and I. Segev (MIT Press, London, 1989).

[114] I. A. Khovanov, A. V. Polovinkin, D. G. Luchinsky, and P. V. E. McClintock, Phys. Rev. E **87**, 032116 (2013).

[115] P. de Maesschalck and M. Wechselberger, J. Math. Neurosci. **5**, 16 (2015).

[116] S. Shinomoto and Y. Kuramoto, Prog. Theor. Phys. **75**, 1105 (1986).

[117] G. B. Ermentrout and N. Kopell, SIAM J. Appl. Math, **46**, 233 (1986).

[118] C. Börger, S. Epstein, and N. Kopell, PNAS **105**, 18023 (2008).

[119] R. Osan, J. Rubin, and B. Ermentrout, SIAM J. Appl. Math. **62**, 1197 (2002).

[120] S. McKennoch, T. Voegtlin, and L. Bushnell, Neural Comput. **21**, 9 (2008).

[121] R. FitzHugh, Biophysical J. **1**, 445 (1961).

[122] J. Nagumo, S. Arimoto, and S. Yoshizawa, Proc. IRE **50**, 2061 (1962).

[123] A. M. Pertsov, E. A. Ermakova, and A. V. Panfilov, Physica D **14**, 117 (1984).

[124] V. S. Zykov, Biofizika **31**, 862 (1986).

[125] Y. Zhao, S. A. Billings, D. Coca, Y. Guo, R. I. Ristic, and L. DeMatos, Int. J. Bifurcat. Chaos. **21**, 3249 (2011).

[126] F. J. L. Capelle, and D. Durrer, Circ. Res. **47**, 454 (1980).

[127] J. J. Tyson and J. P. Keener, Physica D **29**, 215 (1987).

[128] R. T. Faghih, M. Sc. thesis. *The FitzHugh-Nagumo model dynamics with an application to the hypothalamic pituitary adrenal axis* (MIT, 2010).

[129] S. Brandstetter, M. A. Dahlem and E. Schöll, Philos. T. R. Soc. A **368**, 391 (2010).

[130] I. Franović, K. Todorović, M. Perc, N. Vasović, and N. Burić, Phys. Rev. E **92**, 062911 (2015).

[131] S. R. Eydam, I. Franović, and M. Wolfrum, Phys. Rev. E **99**, 042207 (2019).

[132] R. FitzHugh, Bull. Math. Biophys. **7**, 252 (1955).

[133] A. Tonnelier, Phys. Rev. E **90**, 022701 (2014).

[134] E. E. Benoit, J. L. Callot, F. Diener, and M. M. Diener, Collect. Math **32**, 37 (1981).

[135] M. Broens and K. Bar-Eli, J. Phys. Chem. **95**, 8706 (1991).

[136] B. Peng, V. Gaspar, and K. Showalter, Phil. Trans. R. Soc. Lond. A **337**, 275 (1991).

[137] S. M. Baer and T. Erneux, SIAM J. Appl. Math. **46**, 721 (1986).

[138] M. Krupa and P. Szmolyan, SIAM J. Math. Anal. **33**, 286 (2001).

[139] C. H. Henry and R. F. Kazarinov, Rev. Mod. Phys. **68**, 801 (1996).

[140] M. San Miguel and J. M. Sancho, Phys. Lett. A **90**, 455 (1982).

[141] N. Ho and A. Destexhe, J. Neurophysiol. **84**, 1488 (2000).

[142] H. Treutlein, K. Schulten, and Ber. Bunsenges, Phys. Chem. **89**, 710 (1985).

[143] W. Ebeling, H. Herzel, W. Richert, and L. Schimansky-Geier, Zeitschr. Angew. Mathem. Mechanik **66**, 161 (1986).

[144] D. Sigeti and W. Horsthemke, J. Stat. Phys. **54**, 1217 (1989).

[145] C. Kurrer and K. Schulten, Physica D **50**, 311 (1991).

[146] C. Kurrer,and K. Schulten, Int. J. Neural Systems **7**, 399 (1996).

[147] P. S. Landa, J. Commun. Techn. Electron. **47**, 1321 (2002).

[148] U. Hillenbrand, Phys. Rev. E **66**, 021909 (2002).

[149] A. Pikovsky and J. Kurths, Phys. Rev. Lett. **78**, 775 (1997).

[150] H. Gang, T. Ditzinger, C. Z. Ning, and H. Haken, Phys. Rev. Lett. **71**, 807 (1993).

[151] A. Longtin, Phys. Rev. E **55** 868 (1997).

[152] A. Neiman, P. I. Saparin, and L. Stone, Phys. Rev. E **56** 270 (1997).

[153] J. R. Pradines, G. V. Osipov, and J. J. Collins, Phys. Rev. E **60**, 6407 (1999).

[154] L. I and J.-M. Liu, Phys. Rev. Lett. **74**, 3161 (1995).

[155] M. Qian, M.-P. Qian, and X.-J. Zhang, Phys. Lett. A. **309**, 371 (2003).

[156] W. Lim, S.-Y. Kim, and S. Lee, J. Korean Phys. Soc. **50**, 219 (2007).

[157] Y. Wang, D. T. W. Chik, and Z. D. Wang, Phys. Rev. E **61**, 740 (2000).

[158] A. N. Pisarchik, V. A. Maksimenko, A. V. Andreev, et al., Sci Rep **9**, 18325 (2019).

[159] A. M. Lacasta, F. Sagués, and J. M. Sancho, Phys. Rev. E **66**, 045105 (2002).

[160] K. Pakdaman, S. Tanabe, and T. Shimokawa, Neural Networks **14**, 895 (2001).

[161] M. Qian, G.-X. Wang, and X.-J. Zhang, Phys. Rev. E **62**, 6469 (2000).

[162] S. Wu, W. Ren, K. He, and Z. Huang, Phys. Lett. A **279**, 347 (2001).

[163] P. L. Gong, J. X. Xu, and S.J. Hu, Chaos Soliton. Fract. **13**, 885 (2002).

[164] S.-G. Lee, A. Neiman, and S. Kim, Phys. Rev. E **57**, 3292 (1998).

[165] J. L. A. Dubbeldam, B. Krauskopf, and D. Lenstra, Phys. Rev. E **60**, 6580 (1999).

[166] S. Zhong and H. Xin, Chem. Phys. Lett. **321**, 309 (2000).

[167] D. E. Postnov, S. K. Han, T. G. Yim, and O. V. Sosnovtseva, Phys. Rev. E **59**, R3791 (1999).

[168] G. Giacomelli, M. Giudici, S. Balle, and J.R. Tredicce, Phys. Rev. Lett. **84**, 3289 (2000).

[169] Z. Hou and H. Xin, J. Phys. Chem. A **103**, 6181 (1999).

[170] E. Manjarrez, J. G. Rojas-Piloni, I. Méndez, L. Martínez, and D. Vélez D, Neurosci. Lett. **326**, 93 (2002).

[171] R. E. L. DeVille, E. Vanden-Eijnden, and C. B. Muratov, Phys. Rev. E **72**, 031105 (2005)

[172] B. S. Gutkin, J. Jost, and H. C. Tuckwell, EPL **81** 20005 (2008).

[173] H. C. Tuckwell, J. Jost, and B. S. Gutkin, Phys. Rev. E **80** 031907 (2009).

[174] M. Uzuntarla, J. R. Cressman, M. Ozer, and E. Barreto, Phys. Rev. E **88** 042712 (2013).

[175] M. Uzuntarla, Phys. Lett. A **377**, 2585 (2013).

[176] M. Uzuntarla, J. J. Torres, P. So., M. Ozer, and E. Barreto, Phys. Rev. E **95**, 012404 (2017).

[177] M. Uzuntarla, E. Barreto, and J. J. Torres, PLoS Comput. Biol. **13**, e1005646 (2017).

[178] A. Buchin, S. Rieubland, M. Häusser, B. S. Gutkin, and A. Roth, PLoS Comput. Biol. **12**, e1005000 (2016).

[179] I. Franović and V. Klinshov, EPL **116**, 48002 (2016).

[180] T. T. G. Hahn, J. M. McFarland, S. Berberich, B. Sakmann, and M. R. Mehta, Nat. Neurosci. **15**, 1531 (2012).

[181] I. Bačić, S. Yanchuk, M. Wolfrum, and I. Franović, EPJ ST **227**, 177 (2018).

[182] L. Lücken, O. V. Popovych, P. A Tass, and S. Yanchuk, Phys. Rev. E **93**, 032210 (2016).

[183] D. V. Kasatkin, and V. I. Nekorkin, Radiophys. Quantum Electron. **58**, 877 (2016).

[184] D. Kasatkin, S. Yanchuk, E. Schöll, and V. Nekorkin, Phys. Rev. E **96**, 062211 (2017).

[185] I. Franović, K. Todorović, N. Vasović, and N. Burić, Phys. Rev. E **89**, 022926 (2014).

[186] I. Franović, K. Todorović, N. Vasović, and N. Burić, Phys. Rev. E **87**, 012922 (2013).

[187] I. Franović, K. Todorović, N. Vasović, and N. Burić, Chaos **22**, 033147 (2012).

[188] V. Klinshov and I. Franović, Phys. Rev. E **92**, 062813 (2015).

[189] M. A. Zaks, X. Sailer, L. Schimansky-Geier, and A. B. Neiman, Chaos **15**, 026117 (2005).

[190] B. Sonnenschein, M. A. Zaks, A. B. Neiman, and L. Schimansky-Geier, EPJ ST **222**, 2517 (2013).

[191] I. Franović, O. V. Maslennikov, I. Bačić, and V. I. Nekorkin, Phys. Rev. E **96**, 012226 (2017).

[192] I. Franović, S. Yanchuk, S. Eydam, I. Bačić, and M. Wolfrum, Chaos **30**, 083109 (2020).

[193] I. Bačić, V. Klinshov, V. I. Nekorkin, M. Perc, and I. Franović, EPL **124** 40004 (2018).

[194] I. Bačić and I. Franović, Chaos **30**, 033123 (2020).

[195] V. S. Zykov and E. Bodenschatz, Annu. Rev. Condens. Matter Phys. **9**, 435 (2018).

[196] Q. Dai, M. Zhang, H. Cheng, et al., Nonlinear Dyn. **91**, 1723 (2018).

[197] M. A. L. Nicolelis and M. A. Lebedev, Nat. Rev. Neurosci., **10**, 530 (2009).

[198] C. Zhou, L. Zemanova, G. Zamora, C. Hilgetag, and J. Kurths, Phys. Rev. Lett. **97**, 238103 (2006).

[199] O. Sporns, D. Chialvo, M. Kaiser, and C. C. Hilgetag, Trends Cogn. Sci. **8**, 418 (2004).

[200] O. Sporns, *Networks of the Brain* (MIT Press, Cambridge, Massachusetts, 2011).

[201] O. Sporns and R. Kotter, PLoS Biol. **2**, e369 (2004).

[202] I. Franović and V. Miljković, Chaos Soliton. Fract. **44**, 122 (2011).

[203] I. Franović and V. Miljković, Chaos Soliton. Fract. **45**, 527 (2012).

[204] I. Franović and V. Miljković, EPL **92**, 68007 (2010).

[205] Y. L. Maistrenko, B. Lysyansky, C. Hauptmann, O. Burylko, and P. A. Tass, Phys. Rev. E **75**, 066207 (2007).

[206] T. Aoki and T. Aoyagi, Phys. Rev. Lett. **102**, 034101 (2009).

[207] T. Aoki and T. Aoyagi, Phys. Rev. E **84**, 066109 (2011).

[208] Y. Baibolatov, M. Rosenblum, Z. Z. Zhanabaev, M. Kyzgarina, and A. Pikovsky, Phys. Rev. E **80**, 046211 (2009).

[209] W. Gerstner, H. Sprekeler, and G. Deco, Science **338**, 60 (2012).

[210] S. E. Folias and P. C. Bressloff, Phys. Rev. Lett. **95**, 208107 (2005).

[211] S. E. Folias and P. C. Bressloff, SIAM J. Appl. Math. **65**, 2067 (2005).

[212] C. R. Laing, W. C. Troy, B. Gutkin, and G. B. Ermentrout, SIAM J. Appl. Math. **63**, 62 (2002).

[213] P. C. Bressloff, Phys. Rev. E **82**, 051903 (2010).

[214] M. A. Buice and J. D. Cowan, Phys. Rev. E **75**, 051919 (2007).

[215] N. Brunel and V. Hakim, Neural Comput. **11**, 1621 (1999).

[216] H. Hasegawa, Phys. Rev. E **67**, 041903 (2003).

[217] N. F. Rulkov, Phys. Rev. E **65**, 041922 (2002).

[218] N. F. Rulkov, I. Timofeev, and M. Bazhenov, J. Comput. Neurosci. **17**, 203 (2004).

[219] D. Q. Wei and X. S. Luo, Europhys. Lett. **77**, 68004 (2007).

[220] Q. Y. Wang, Z. Duan, M. Perc, and G. Chen, Europhys. Lett. **83**, 50008 (2008).

[221] C. A. S. Batista, A. M. Batista, J. A. C. de Pontes, R. L. Viana, and S. R. Lopes, Phys. Rev. E **76**, 016218 (2007).

[222] B. Ibarz, J. M. Casado, and M. A. F. Sanjuán, Phys. Rep. **501**, 1 (2011).

[223] E. M. Izhikevich, Neural Comput. **18**, 245 (2006).

[224] E. M. Izhikevich, and G. M. Edelman, Proc. Natl. Acad. Sci. USA **105**, 3593 (2008).

[225] V. I. Nekorkin, and L. V. Vdovin, Izv. Vyssh. Uchebn. Zaved. Prikladn. Nelinejn. Din **15**, 36 (2007).

[226] M. Courbage, V. I. Nekorkin, and L. V. Vdovin, Chaos **17**, 043109 (2007).

[227] O. V. Maslennikov and V. I. Nekorkin, Phys. Rev. E **90**, 012901 (2014).

[228] O. V. Maslennikov, D. V. Kasatkin, N. F. Rulkov, and V. I. Nekorkin, Phys. Rev. E **88**, 042907 (2013).

[229] O. V. Maslennikov, V. I. Nekorkin, and J. Kurths, Phys. Rev. E **92**, 042803 (2015).

[230] O. V. Maslennikov and V. I. Nekorkin, Commun. Nonlinear Sci. Numer. Simul. **23**, 10 (2015).

[231] O. V. Maslennikov and V. I. Nekorkin, Chaos **23**, 023129 (2013).

[232] O. V. Maslennikov and V. I. Nekorkin, "Map-Based Approach to Problems of Spiking Neural Network Dynamics" in *Nonlinear Dynamics and Complexity*, eds. V. Afraimovich, A. C. J. Luo, and X. Fu (Springer International Publishing, Switzerland, 2014).

[233] I. Franović, K. Todorović, M. Perc, N. Vasović, and N. Burić, Phys. Rev. E **92**, 062911 (2015).

[234] L. Arnold, *Random Dynamical Systems*, (SpringerVerlag, Berlin, 1999).

[235] J. A. Acebrón, A. R. Bulsara, and W.-J. Rappel, Phys. Rev. E **69**, 026202 (2004).

[236] M. Gaudreault, J. M. Berbert, and J. Viñals, Phys. Rev. E **83**, 011903 (2011).

[237] P. Kaluza, C. Strege, and H. Meyer-Ortmanns, Phys. Rev. E **82**, 036104 (2010).

[238] V. I. Nekorkin and O. V. Maslennikov, Radiophys. Quantum Electron. (Engl. Transl.) **54**, 56 (2011).

[239] M. Courbage, O. V. Maslennikov, and V. I. Nekorkin, Chaos Soliton. Fract. **45**, 645 (2012).

[240] O. V. Maslennikov and V. I. Nekorkin, Radiophys. Quantum Electron. (Engl. Transl.) **55**, 198 (2012).

[241] C. W. Gardiner, *Handbook of Stochastic Methods for Physics, Chemistry and the Natural Sciences*, 3rd ed. (Springer-Verlag, Berlin, 2004).

[242] N. W. Schultheiss, A. A. Prinz, and R. J. Butera (eds.) *Phase Response Curves in Neuroscience: Theory, Experiment, and Analysis* (Springer, New York, 2012).

[243] P. A. Tass, *Phase Resetting in Medicine and Biology: Stochastic Modeling and Data Analysis* (Springer, Berlin–Heidelberg, 2007).

[244] C. C. Canavier, Scholarpedia **1**, 1332 (2006).

[245] W. Gerstner, W. M. Kistler, R. Naud, and L. Paninski, *Neuronal Dynamics: From Single Neurons to Networks and Models of Cognition* (Cambridge University Press, Cambridge, 2014).

[246] L. F. Abbott and P. Dayan, *Theoretical Neuroscience* (The MIT Press, 2005).

[247] C. Clopath, L. Büsing, E. Vasilaki, and W. Gerstner, Nat. Neurosci. **13**, 344 (2010).

[248] O. Popovych, S. Yanchuk, and P. A. P. Tass, Sci. Rep. **3**, 2926 (2013).

[249] V.-C. Oriol, M. Ronny, R. Sten, and L. Schimansky-Geier, Phys. Rev. E **83**, 036209 (2011).

[250] G. B. Ermentrout and D. Kleinfeld, Neuron **29**, 33 (2001).

[251] L. Lücken, D. P. Rosin, V. M. Worlitzer, and S. Yanchuk, Chaos **27**, 13114 (2017).

[252] I. Franović, M. Perc, K. Todorović, S. Kostić, and N. Burić, Phys. Rev. E **92**, 062912 (2015).

[253] S. Yanchuk, S. Ruschel, J. Sieber, and M. Wolfrum, Phys. Rev. Lett. **123**, 053901 (2019).

[254] J. A. Kromer, R. D. Pinto, B. Lindner, and L. Schimansky-Geier, EPL **108**, 20007 (2014).

[255] A. Shilnikov, Int. J. Bifurcat. Chaos **18**, 2141 (2008).

[256] G. Pavliotis and A. Stuart, *Multiscale Methods: Averaging and Homogenization* (Springer, Berlin–Heidelberg, 2008).

[257] M. Galtier and G. Wainrib, Phys. Rev. E **2**, 13 (2012).

[258] E. M. Izhikevich, IEEE Trans. Neural Netw. **15**, 1063 (2004).

[259] E. J. Doedel, R. C. Paffenroth, A. R. Champneys, T. F. Fairgrieve, Y. A. Kuznetsov, B. Sandstede, and X. Wang, *AUTO-07p: Continuation and bifurcation software for ordinary differential equations* (Montreal, Canada, 2007), URL: indy.cs.concordia.ca/auto/

[260] V. V. Vyazovskiy and K. D. Harris, Nat. Rev. Neurosci. **14**, 443 (2013).

[261] P. H. Dannenberg, J. C. Neu, and S. W. Teitsworth, Phys. Rev. Lett. **113**, 020601 (2014).

[262] E. Hunsberger, M. Scott, and C. Eliasmith, Neural Comput. **26**, 1600 (2014).

[263] B. Neiman and D. F. Russell, Phys. Rev. Lett. **88**, 138103 (2002).

[264] L. Ryashko and E. Slepukhina, Phys. Rev. E **96**, 032212 (2017).

[265] C. Zheng and A. Pikovsky, Phys. Rev. E **98**, 042148 (2018).

[266] A. Fiasconaro, B. Spagnolo, and S. Boccaletti, Phys. Rev. E **72**, 061110 (2005).

[267] R. N. Mantegna and B. Spagnolo, Phys. Rev. Lett. **76**, 563 (1996).

[268] S. Ciuchi, F. de Pasquale, and B. Spagnolo, Phys. Rev. E **47**, 3915 (1993).

[269] N. V. Agudov, A. A. Dubkov, and B. Spagnolo, Physica A **325**, 144 (2003).

[270] G. Augello, D. Valentia, and B. Spagnolo, Eur. Phys. J. B **78**, 225 (2010).

[271] A. Zakharova, A. Feoktistov, T. Vadivasova and E. Schöll, EPJ ST **222**, 2481 (2013).

[272] N. Semenova, A. Zakharova, V. Anishchenko, and Eckehard Schöll, Phys. Rev. Lett. **117**, 014102 (2016).

[273] B. Lindner and L. Schimansky-Geier, Phys. Rev. E **60**, 7270 (1999).

[274] V. A. Makarov, V. I. Nekorkin, and M. G. Velarde, Phys. Rev. Lett. **86**, 3431 (2001).

[275] L. H. Gammaitoni, P. Hänggi, P. Jung, and F. Marchesoni, Rev. Mod. Phys. **70**, 223 (1998).

[276] J. Hizanidis and E. Schöll, Phys. Rev. E **78**, 066205 (2008).

[277] J. Hizanidis, A. Balanov, A. Amann, and E. Schöll, Phys. Rev. Lett. **96**, 244104 (2006).

[278] R. Aust, P. Hövel, J. Hizanidis, and E. Schöll, Eur. Phys. J. Spec. Top. **187**, 77 (2010).

[279] N. Kouvaris, L. Schimansky-Geier, and E. Schöll, Eur. Phys. J. Spec. Top. **191**, 29 (2010).

[280] N. B. Janson, A. Balanov, and E. Schöll, Phys. Rev. Lett. **93**, 010601 (2004).

[281] V. Semenov, A. Feoktistov, T. Vadivasova, E. Schöll, and A. Zakharova, Chaos **25**, 033111 (2015).

[282] B. Hauschildt, N. B. Janson, A. Balanov, and E. Schöll, Phys. Rev. E **74**, 051906 (2006).

[283] M. Masoliver, N. Malik, E. Schöll, and A. Zakharova, Chaos **27**, 101102 (2017).

[284] M. E. Yamakou and J. Jost, Phys. Rev. E **100**, 022313 (2019).

[285] C. Zhou, J. Kurths, and B. Hu, Phys. Rev. Lett. **87**, 098101 (2001).

[286] C. Morris and H. Lecar, Biophys. J. **35**, 193 (1981).

[287] D. O. Hebb, *The Organization of Behavior: A Neuropsychological Approach* (John Wiley & Sons, New York, 1949).

[288] O. V. Popovych, S. Yanchuk, and P. A. Tass, Sci. Rep. **3**, 2926 (2013).

[289] A. Morrison, M. Diesmann, and W. Gerstner, Biol. Cybern. **98**, 459 (2008).

[290] P. Hänggi, P. Talkner, and M. Borkovec, Rev. Mod. Phys. **62**, 251 (1990).

[291] N. Berglund and B. Gentz, *Noise-Induced Phenomena in Slow-Fast Dynamical Systems* (Springer, Berlin, 2006).

[292] C. Laing and G. J. Lord (eds.), *Stochastic Methods in Neuroscience* (Oxford University Press, London, 2009).

[293] J. Touboul and G. Wainrib, Physica D **307**, 42 (2015).

[294] H. Wang, L. Wang, L. Yu, and Y. Chen, Phys. Rev. E **83**, 021915 (2011).

[295] T. Ditzinger, C. Z. Ning, and G. Hu, Phys. Rev. E **50**, 3508 (1994).

[296] W. J. Freeman, *Neurodynamics: An Exploration in Mesoscopic Brain Dynamics* (Springer-Verlag, London, 2000).

[297] H. Liljenström, Scholarpedia **7**, 4601 (2012).

[298] G. Deco, V. K. Jirsa, P. A. Robinson, M. Breakspear, and K. Friston, PloS Comput. Biol. **4**, e1000092 (2008).

[299] J. L. P. Velazquez and R. Wennberg, *Coordinated Activity in the Brain: Measurements and Relevance to Brain Function and Behavior* (Springer, New York, 2009).

Curriculum Vitae

Born in Subotica, Republic of Serbia on June 12th, 1992, Iva Bačić completed elementary and secondary education in her hometown. As a student of the gymnasium "Svetozar Marković", she attended numerous seminars in Petnica Science Center. In 2010, she enrolled in the Bachelor of Science program Theoretical and Experimental physics at the Faculty of Physics, University of Belgrade. In 2014, after graduating with a GPA of 9.44/10, she continued her education, enrolling in the same program at the Master of Science level. Within research for her MSc thesis, she visited the SOLEIL synchrotron in France. Under the supervision of Dr. Aleksandar Milosavljević, an Associate Research Professor at the Institute of Physics Belgrade, she completed her MSc thesis entitled *Inner-Shell Action Spectroscopy of Trapped Substance P Peptide Ions and their Nanosolvated Complexes*. Following the defense of her thesis and graduation with a GPA of 9.67/10 in 2015, Iva started her doctoral studies at the Faculty of Physics, specializing in statistical physics and nonlinear dynamics. Under the supervision of Dr. Igor Franović, an Associate Research Professor from the Scientific Computing Laboratory of the National Center of Excellence for the Study of Complex Systems at the Institute of Physics Belgrade, Iva studies self-organizing dynamics in coupled systems.

Since March 2016, Iva has been employed at the Institute of Physics Belgrade as a Research Assistant, participating in the National Project ON171017 *Modeling and Numerical Simulations of Complex Many-Body Systems* funded by the Ministry of Education, Science and Technological Development of the Republic of Serbia. Alongside this, she was also a participant in the DAAD bilateral project *Emergent dynamics in systems of coupled excitable units* in 2017 and 2018, within which she paid three visits to the Weierstrass Institute in Berlin, Germany. During the past decade, Iva was also an assistant in the Petnica Science Center, where she delivered lectures on a variety of topics and supervised several projects.

As a doctoral student, Iva published five peer-reviewed research papers whose contents provide the basis for the present thesis (Phys. Rev. E **96**, 012226 (2017); EPJ ST **227**, 177 (2018); EPL **124** 40004 (2018); Chaos **30**, 033123 (2020); and Chaos **30**, 083109 (2020)), along with an additional publication unrelated to her thesis (EPL **120**, 68001 (2017)). The latter was chosen for EPL's *Highlights from the previous volumes*, while the main results were presented in Europhysics News **49** (3), 2018. Iva has presented her research at poster presentations and by giving contributed talks on several international conferences and workshops. She provided service to the scientific community by performing peer review for *Chaos: An Interdisciplinary Journal of Nonlinear Science*.

Изјава о ауторству

Име и презиме аутора – **Ива Бачић**

Број индекса – **2015/8018**

Изјављујем

да је докторска дисертација под насловом

Self-Organization in Coupled Excitable Systems: Interplay Between Multiple Timescale Dynamics and Noise

(Самоорганизација у спрегнутим екситабилним системима: садејство вишеструких временских скала и шума)

- резултат сопственог истраживачког рада;
- да дисертација у целини ни у деловима није била предложена за стицање друге дипломе према студијским програмима других високошколских установа;
- да су резултати коректно наведени и
- да нисам кршио/ла ауторска права и користио/ла интелектуалну својину других лица.

Потпис аутора

У Београду, 04. 09. 2020. год.

_____

Изјава о истоветности штампане и електронске верзије докторског рада

Име и презиме аутора – **Ива Бачић**

Број индекса – **2015/8018**

Студијски програм – **Физика**

Наслов рада – **Self-Organization in Coupled Excitable Systems: Interplay Between Multiple Timescale Dynamics and Noise (Самоорганизација у спрегнутим ексцитабилним системима: садејство вишеструких временских скала и шума)**
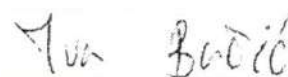
Ментор – **др Игор Франовић**

Изјављујем да је штампана верзија мог докторског рада истоветна електронској верзији коју сам предао/ла ради похрањивања у **Дигиталном репозиторијуму Универзитета у Београду.**

Дозвољавам да се објаве моји лични подаци везани за добијање академског назива доктора наука, као што су име и презиме, година и место рођења и датум одбране рада.

Ови лични подаци могу се објавити на мрежним страницама дигиталне библиотеке, у електронском каталогу и у публикацијама Универзитета у Београду.

Потпис аутора

У Београду, 04. 09. 2020. год.

Изјава о коришћењу

Овлашћујем Универзитетску библиотеку „Светозар Марковић" да у Дигитални репозиторијум Универзитета у Београду унесе моју докторску дисертацију под насловом:

Self-Organization in Coupled Excitable Systems: Interplay Between Multiple Timescale Dynamics and Noise (Самоорганизација у спрегнутим ексцитабилним системима: садејство вишеструких временских скала и шума)

која је моје ауторско дело.

Дисертацију са свим прилозима предао/ла сам у електронском формату погодном за трајно архивирање.

Моју докторску дисертацију похрањену у Дигиталном репозиторијуму Универзитета у Београду и доступну у отвореном приступу могу да користе сви који поштују одредбе садржане у одабраном типу лиценце Креативне заједнице (Creative Commons) за коју сам се одлучио/ла.

1. Ауторство (CC BY)

2. Ауторство – некомерцијално (CC BY-NC)

3. Ауторство – некомерцијално – без прерада (CC BY-NC-ND)

4. Ауторство – некомерцијално – делити под истим условима (CC BY-NC-SA)

5. Ауторство – без прерада (CC BY-ND)

⑥ Ауторство – делити под истим условима (CC BY-SA)

(Молимо да заокружите само једну од шест понуђених лиценци.
 Кратак опис лиценци је саставни део ове изјаве).

Потпис аутора

У Београду, 04. 09. 2020. год.

1. **Ауторство**. Дозвољавате умножавање, дистрибуцију и јавно саопштавање дела, и прераде, ако се наведе име аутора на начин одређен од стране аутора или даваоца лиценце, чак и у комерцијалне сврхе. Ово је најслободнија од свих лиценци.

2. **Ауторство – некомерцијално**. Дозвољавате умножавање, дистрибуцију и јавно саопштавање дела, и прераде, ако се наведе име аутора на начин одређен од стране аутора или даваоца лиценце. Ова лиценца не дозвољава комерцијалну употребу дела.

3. **Ауторство – некомерцијално – без прерада**. Дозвољавате умножавање, дистрибуцију и јавно саопштавање дела, без промена, преобликовања или употребе дела у свом делу, ако се наведе име аутора на начин одређен од стране аутора или даваоца лиценце. Ова лиценца не дозвољава комерцијалну употребу дела. У односу на све остале лиценце, овом лиценцом се ограничава највећи обим права коришћења дела.

4. **Ауторство – некомерцијално – делити под истим условима**. Дозвољавате умножавање, дистрибуцију и јавно саопштавање дела, и прераде, ако се наведе име аутора на начин одређен од стране аутора или даваоца лиценце и ако се прерада дистрибуира под истом или сличном лиценцом. Ова лиценца не дозвољава комерцијалну употребу дела и прерада.

5. **Ауторство – без прерада**. Дозвољавате умножавање, дистрибуцију и јавно саопштавање дела, без промена, преобликовања или употребе дела у свом делу, ако се наведе име аутора на начин одређен од стране аутора или даваоца лиценце. Ова лиценца дозвољава комерцијалну употребу дела.

6. **Ауторство – делити под истим условима**. Дозвољавате умножавање, дистрибуцију и јавно саопштавање дела, и прераде, ако се наведе име аутора на начин одређен од стране аутора или даваоца лиценце и ако се прерада дистрибуира под истом или сличном лиценцом. Ова лиценца дозвољава комерцијалну употребу дела и прерада. Слична је софтверским лиценцама, односно лиценцама отвореног кода.